Observation of Antineutrino Disappearance at the Daya Bay Experiment

by

Bryce Richard Littlejohn

A dissertation submitted in partial fulfillment of

the requirements for the degree of

Doctor of Philosophy

(Physics)

at the

University of Wisconsin – Madison

2012

Defended on 11 May 2012

Dissertation approved by the following members of the Final Oral Committee:

Karsten M. Heeger · Associate Professor of Physics

A. Baha Balantekin · Eugene P. Wigner Professor of Physics

Sebastian Heinz · Assistant Professor of Astronomy

Matthew Herndon · Associate Professor of Physics

Albrecht Karle · Full Professor of Physics

Dedication

For Amanda and Leona

Acknowledgements

I foremostly appreciate the guidance and patience of Karsten Heeger in teaching me how to be an effective scientist: focusing on and seeing to the end the important and pressing issues, asking the right questions in the right ways, staying organized, and keeping a constant lookout for new ideas on the horizon from all kinds of sources. In addition to teaching this through his own example, I also appreciate his push to help me realize these qualities in myself and providing the research and other opportunities in which to realize them. I also acknowledge the great help of my officemates, Mike McFarlane and Christine Lewis, as well as UW-Madison group members Wei Wang, David Webber, and Paul Hinrichs, in providing many ideas and insights and solving many puzzles through our frequent conversations. I appreciate the unbelievable array of technical experience and know-how I got to occationally bump up against and absorb a little of during work with Tom Wise, Jeff Cherwinka, Henry Band, and Lee Greenler. My IHEP colleagues, particularly Jun Cao and Liangjian Wen, must be thanked for supporting me during prolonged stays in China, and Soren Jetter, Victor Pec, and Logan Lebanowski, among others, must be thanked for making these periods much more than just weeks of work away from the comforts of home.

Being a member of the Daya Bay Collaboration during my years of graduate school has also benefitted me greatly, providing constant interaction and learning opportunities with too many top-notch scientists to mention all of them here. I greatly appreciate the diverse feedback I was able to receive about all of my good and not-so-good shared thoughts and ideas; without these years of consistent feedback and exchange, this thesis would not have been possible.

Finally, I thank my wife Amanda for her constant supply of support and love, and for putting up with me when she shouldn't have and talking me down when I

felt like quitting. The work represented in this thesis would have been infinitely less enjoyable and worthwhile without her. I also thank my little shrimpy baby Leona for providing me additional motivation when I needed it; maybe one day you will read this, or, well, at least this page!

Contents

List of Figures

List of Tables

Acryonyms

ACU	Automated Calibration Unit: A, B, or C
AD	Antineutrino Detector
ALEPH	A particle collider experiment at CERN
AV	Acrylic Vessel
ADC	Analog to Digital Converter
Chooz	A French km-scale oscillation experiment
CERN	European Organization for Nuclear Research
CP	Charge-Parity
EH	Experimental Hall: 1, 2, or 3
ESR	Enhanced Specular Reflector
ESum	Analog energy trigger
FEE	Front-End Electronics
GALLEX	Gallium Experiment
GEM	Muon to Electron Gamma Experiment

GC	Gamma Catcher
GdLS	Gadolinium-Loaded Liquid Scintillator
Geant	Geometry and Tracking Monte Carlo System
GPS	Global Positioning System
GSL	GNU Scientific Library
GW	Giga-watt
H/C	Hydrogen-to-Carbon
HEPA	High-Efficiency Particulate Arresting
H/Gd	Hydrogen-to-Gadolinium
IBD	Inverse Beta Decay
ILL	Institut Laue-Langevin Experiment
Kamiokande	Kamioka Nucleon Decay Experiment
KamLAND	Kamioka Liquid Scintillator Antineutrino Detector
K2K	KEK to Super-K Long-Baseline Oscillation Experiment
LAB	Linear Alkyl Benzene
LBNE	Long Baseline Neutrino Experiment
L/E	Experimental oscillation parameter: Length/Energy
LED	Light-Emitting Diode
LEP	Large Electron-Positron Collider

LS	Liquid Scintillator
LSND	Liquid Scintillator Neutrino Detector
MC	Monte Carlo
MiniBooNE	Mini-Booster Neutrino Experiment
MINOS	Main Injector Neutrino Oscillation Search Experiment
MO	Mineral Oil
MSB	1,4-bis[2-(2-methylphenyl)ethyl]-benzene
MSW	Mikheyev-Smirnov-Wolfenstein
n-Gd	neutron capture on Gadolinium
n-H	neutron capture of Hydrogen
NHit	Hit PMT trigger
NOνA	NuMI Off-Axis Electron-Neutrino Appearance Experiment
NuWa	Daya Bay Simulation and Analysis Framework
OAV	Outer Acrylic Vessel
PE	Photo-electron
PMT	Photomultiplier Tube
PMNS	Pontecorvo-Maki-Nakagawa-Sakata
PPO	2,5-di(phenyl)-1,3-oxazole
PSI	Paul Sherrer Institut, Switzerland

QA	Quality Assurance
RENO	A Korean km-scale oscillation experiment
RPC	Resistive Plate Chamber
SAB	Surface Assembly Building
SAGE	Soviet-American Gallium Experiment
SI	Spill-In
SNO	Sudbury Neutrino Observatory
SO	Spill-Out
SPE	Single Photo-electron
SST	Stainless Steel Tank
Super-Kamiokande	(Super-K) Neutrino Experiment in Kamioka, Japan
T2K	Tokai to Super-K Long-Baseline Oscillation Experiment
TDC	Time to Digital Converter
UV	Ultraviolet
UVA	Ultraviolet-Absorbing
UVT	Ultraviolet-Transmitting
WP	Water Pool

Chapter 1

Thesis Summary and Outline

1.1 The Oscillating Neutrino

The neutrino's ubiquitous presence portrays its importance in the Universe's evolution and present state. However, its exact role has not been completely determined, as the particle is not entirely understood or characterized. It is known that neutrinos are extremely light, neutral, spin-$\frac{1}{2}$, weakly interacting fundamental particles that play a vital role in nuclear processes and in the formation and evolution of the universe. As with charged leptons, they come in three flavors, called electron (ν_e), muon (ν_μ) and tau (ν_τ). They are known to be extremely abundant, comprising nearly as much of the universe's total mass (roughly 0.3%) as all stars put together (0.5%).

It is also known that neutrino mass and weak eigenstates are not orthogonal, as in the quark sector, causing oscillation of neutrino flavor during propagation. The differences in the mass states, as well as the amplitude of transition between mass states, have been well-measured by experiments detecting neutrinos and antineutrinos created in the Sun, the Earth's atmosphere, nuclear reactors, and particle accelerator beams. However, along with the absolute neutrino masses, some parameters govern-

ing oscillation are not known. In particular, the mixing amplitude between the first and third mass states, called θ_{13}, has not been measured. In addition, CP-violating effects arising from oscillations, governed by a parameter δ, have not been measured, as well as the absolute value of the difference between the second and third mass states.

Until all neutrino parameters are determined experimentally, the neutrino's role the Universe's development and current state cannot be certain. In particular, observation of CP-violation in neutrino mixing could provide clues about the mechanism responsible for producing matter-antimatter asymmetry in the universe.

1.2 Detecting Neutrinos at Daya Bay

The Daya Bay experiment is specifically designed to measure short-baseline disappearance of reactor antineutrinos emanating from six reactor cores at the Daya Bay Nuclear Generating Station, less than 50 km from Hong Kong in the Guangdong Province of China. The experiment is composed of eight functionally identical three-zone liquid scintillation detectors situated in underground experimental halls at near ($<$500 m) and far ($\sim$1800 m) distances from the reactor cores. Antineutrinos created by beta decays inside these reactors are detected via inverse beta decay interaction ($p + \overline{\nu}_e \rightarrow p + e^+$) in each detector.

Large 20-ton detector targets and high detection efficiency ensure neutrino detection statistics higher than any previous neutrino experiment. Reduction of reactor and detector-related uncertainties is achieved through simultaneous measurement of reactor neutrino flux with multiple functionally identical detectors at multiple baselines. Backgrounds and associated uncertainties are reduced by providing hundreds of meters water equivalent overburden, and doping the target with Gd to create a

high-energy neutron capture signal, and buffering the target region from radioactive photomultiplier tubes and the environmental surroundings with a mineral oil buffer in the detector and an active water muon veto. Sub-percent statistical precision and reduction and cancellation of experimental systematics will allow the Daya Bay experiment to achieve unparalleled sensitivity to the neutrino oscillation parameter θ_{13}.

1.3 Results From Side-by-Side Comparison of Near Site Detectors

First Daya Bay physics data taking began with two side-by-side detectors at the same Daya Bay near site from August to December 2011. These 70 live days of data have been analyzed to provide a measurement of detected inverse beta decay events in each detector. Inverse beta events consist of two time-coincident detector triggers, which contain a number of PMT hits and total charge corresponding to the energy ranges of a either positron or a neutron capture on Gadolinium. The energy responses of both detectors are established as identical to sub-percent precision by calibrating the detector with cosmogenic muon-produced spallation neutrons and gamma and neutron radioactive sources. Signal events are separated from backgrounds through a regimen of energy, timing, muon veto, and charge topology cuts.

The ratio of inverse beta decay event detection rates in the first two detectors have been compared to the predicted ratio based on the detector target masses, detector-reactor baselines, and reactor operation information. The differences of these ratios is $0.004 \pm 0.008(stat) \pm 0.003(syst)$, demonstrating the identical response of the detectors to neutrinos, as well as proper understanding of detector systematics to sub-percent precision.

1.4 Observation of Short-baseline Reactor Antineutrino Oscillations

All three experimental sites are online as of December 2011: the previously mentioned two near hall detectors continue to run, while one detector has been deployed at the second near site and three detectors have been deployed at the far site. The first 50 days of three-site live time have been analyzed with the same regimen applied to the side-by-side near-site analysis to determine the antineutrino interaction rate in each detector. These rates have been again compared to predictions based on precise measurements of reactor power, baselines, detector target masses and detection efficiencies. The ratios between expected and predicted rates have been compared between detectors to search for any relative differences that would indicate $\overline{\nu}_e$ disappearance. Such a difference is measured between near and far baseline detectors in 50 days of data taking, with a relative deficit at the far site of:

$$D = 0.06 \pm 0.011(stat) \pm 0.004(syst). \tag{1.1}$$

This relative rate deficit is the first unambiguous signature of short-baseline reactor $\overline{\nu}_e$ disappearance ever measured. If this deficit is interpreted within the existing framework of neutrino oscillations, it indicates a non-zero value of θ_{13} at greater than 5σ confidence level, with an exact value of

$$\sin^2 2\theta_{13} = 0.95 \pm 0.017(stat) \pm 0.005(syst). \tag{1.2}$$

This result provides the first positive measurement of θ_{13}. The result confirms the hints of non-zero θ_{13} from previous reactor, solar, and accelerator experiments and has since been reproduced by another reactor antineutrino experiment, RENO.

1.5 Implications of and Future Studies with Daya Bay

The non-zero and relatively large value of θ_{13} measured by Daya Bay has significant impacts on the future of experimental neutrino physics. Oscillation effects from CP-violation and the neutrino mass hierarchy, which have yet to be measured, depend on the value of θ_{13}. A confirmed large value of θ_{13} significantly increases the probability of measurement of CP-violation or the mass hierarchy at imminent accelerator experiments. In addition, it greatly increases the physics motivation for a next-generation long-baseline accelerator experiment, such as LBNE: it is now clear that such an experiment would be sensitive to a majority of the CP-violation parameter space and to the mass hierarchy.

Theoretical frameworks predicting neutrino mixing and masses are also impacted by a Daya Bay's measurement of θ_{13}. Currently preferred theoretical models of neutrino masses, particularly tri-bimaximal mixing, which predict highly symmetric mixing parameters and a zero value of θ_{13}, are clearly no longer supported by experimental data. In their place, theories utilizing more complex symmetries must be utilized to explain the measured value of θ_{13}.

The Daya Bay Experiment, only at the beginning of its operational life at the time of this discovery, will continue to run for multiple years, increasing the size of its dataset by at least an order of magnitude. During this time period, the precision of the experiment's θ_{13} measurement will improve by a more than a factor of two from the increase in statistics alone. In addition, systematic uncertainties will be reduced with increased background statistics and better detector calibration. Higher statistics and more well-understood systematics will allow the Daya Bay experiment to complete a combined spectrum/rate analysis, which will help to further constrain

θ_{13} and the atmospheric mass-squared splitting Δm^2_{32}. An absolute rate and spectral analysis of Daya Bay data can provide new understanding of neutrino production and fission in nuclear reactors and further tests of possible very-short baseline oscillations into sterile neutrinos. More direct sterile neutrino searches utilizing a high-intensity antineutrino source at the Daya Bay far site have also been proposed.

1.6 Thesis Outline

This thesis follows an outline similar to the sections above to present unequivocal observation of reactor antineutrino disappearance at the Daya Bay experiment. Chapter 2 begins by giving a description of the physical theory of neutrinos and neutrino oscillations, as well as a history of the development of this theory. Chapter 3 chronicles the development of reactor neutrino experiments and their search for short-baseline reactor neutrino interactions in the 1980s, 1990s, and 2000s. During this description, the detection methods, detector characteristics, and background subtraction methods used in reactor experiments, and in Daya Bay more specifically, will be introduced. Chapter 4 describes in detail the design of the Daya Bay Experiment.

Chapters 5 and 6 focus on the design, construction, and assembly of detectors with functionally identical physics response. This is accomplished in Chapter 5 by describing first how minimally non-identical target acrylic vessels are designed, fabricated, transported, and assembled. Chapter 6 will extend this discussion by using a detector simulation regimen to relate measured physical detector differences to differences in detector response. These simulations demonstrate that the small physical differences present in the as-built detectors should not introduce significant relative differences in detector response to antineutrino interactions.

Chapters 7, 8 and 9 will present analyses of the first Daya Bay physics data.

Chapter 7 will introduce event characterization methods as well as describing detector calibrations. Chapter 8 will use the first few months of Daya Bay data to show identical response to antineutrino interactions in side-by-side antineutrino detectors, and to demonstrate proper understanding of detector systematics. Chapter 9 will use the first three-site data from Daya Bay to show a deficit in antineutrino detection at the Daya Bay far site. This result is then interpreted in the current context of neutrino oscillations to determine a most likely value of θ_{13}.

Implications of this result are discussed briefly in the concluding chapter. The Appendix discusses possible future contributions of Daya Bay to the investigation of sterile neutrino oscillations.

Individual Contributions

As the Daya Bay collaboration consists of over 200 collaborators from three continents and 38 separate institutions, Daya Bay's exciting θ_{13} result is naturally the product of contributions from many different people. Construction of the experiment and development of the analysis framework was split up among institutions, with each institution producing or specializing in a specific detector or analysis component, or in the synthesis of these components. With the resultant data set, separate groups performed independent analyses for θ_{13} to ensure a proper cross-check of the experimental result. These analyses utilized many disparate background reduction, detector calibration, and efficiency calculation strategies to arrive at similar final measured oscillation values. These differences will be discussed in greater detail in Chapters 8 and 9.

In the same vein, the work presented in this thesis is one contribution of many to the final Daya Bay first result. This thesis provides the following additions to the body of Daya Bay development and analysis:

1. *Independent Relative Rate Analysis of $\overline{\nu}_e$ Disappearance:* The disappearance analysis presented here combines cuts and background estimations used widely by the collaboration with independently-developed cuts, efficiency calculations and systematics estimates to identify a 5σ relative deficit in detected-to-expected $\overline{\nu}_e$ ratios between near and far detectors. By fitting this relative rate deficit, a calculation of θ_{13} was produced, finding good agreement with the results of independent calculations by other Daya Bay groups.

2. *Independent Analysis Comparing $\overline{\nu}_e$ detection rates in side-by-side near site detectors:* The independent analysis developed for the disappearance measurement was also applied to Daya Bay's initial near site data to measure consistent detected-to-expected $\overline{\nu}_e$ ratios between side-by-side detectors. This analysis demonstrates functionally identical detector response between Daya Bay detectors, and shows a proper understanding of Daya Bay's relative detector systematics.

3. *Spallation Neutron-Based Energy Scale Calibration:* This calibration method utilizes Gd-captured spallation neutrons as a baseline, which, like inverse beta decay Gd-capture neutrons, are also uniformly distributed throughout the detector and peaked at 8 MeV. This method ensures that energy scale uncertainties are minimized for energy cuts on neutron Gd-captures, which were predicted to be a leading cause of systematic uncertainty for the experiment. In addition, this method allows for continuous monitoring of each detector's energy scale. This spallation-based calibration produces results in good agreement with calibrations based on radioactive calibration sources.

4. *Relative Energy Scale Calibration:* By investigating relative differences in calibrated detector response with time, position, and energy, cuts could be placed in

identical locations in each detector's energy spectrum with excellent precision. By utilizing this energy calibration method, rate analyses can avoid the comparative imprecision of absolute energy scale calibration, which is not necessary for a relative rate measurement of θ_{13}.

5. *Calculation of Relative Energy Cut Efficiency Uncertainties:* Differences in energy cut efficiencies arising from the small uncertainty associated with the relative energy scale calibration described above were also calculated. In addition, a method for calculating energy cut uncertainties arising from differences in relative spectral shape differences were developed and investigated. Using these calculations, the energy cut uncertainties used in Daya Bay relative rate analyses are significantly smaller than initially anticipated.

6. *A Simulation Programme to Investigate Identical Response of Daya Bay Detectors:* By simulating detectors with slightly varying detector parameters, effects of physical detector differences on detector response were elucidated. By comparing these results to detector characterization measurements, the degree of similarity in response to $\overline{\nu}_e$ of each detector was predicted to be very high. These simulations also demonstrate that the high degree of physical similarity between detectors implies negligible contributions to detector systematics from relative differences in inverse beta neutron spectral shapes, coincidence timing spectrum shapes, and contributions to the $\overline{\nu}_e$ event rate from interactions outside the target. These contributions to the relative detector systematics are nearly impossible to estimate in any other fashion.

7. *Design, Fabrication, Construction, and Characterization of the Daya Bay Acrylic Vessels:* Proper acrylic vessel construction and characterization measurements are crucial to ensuring the detector identicalness that is a central feature of the

Daya Bay Experiment's excellent θ_{13} sensitivity. By testing candidate materials, guiding component design via detector simulations, instituting and performing quality assurance and characterization measurements during fabrication, and overseeing cleaning and assembly of the outer acrylic vessels, I was able to help ensure the delivery of components meeting the strict requirements of the experiment.

8. *Acrylic R&D Studies:* Knowledge gained during the investigation of the optical, mechanical, and material properties of acrylic for vessel production and characterization are also applicable to other neutrino and dark matter experiments utilizing this material.

9. *Proposal for a Sterile Neutrino Oscillation Search at Daya Bay:* A highly radioactive source can be used to provide copious antineutrinos at very short baselines from the far site detectors. Observation of distortion of the energy or baseline spectrum of these antineutrinos could provide crucial new evidence in the ongoing investigation of oscillation hints at high Δm^2. Sensitivity studies presented in this thesis demonstrate the ability of this arrangement to rule out a significant portion of suggested very-short-baseline oscillation parameter space at high confidence level. This proposal provides a path for further extending the contributions of Daya Bay to fundamental neutrino physics discoveries.

Chapter 2

Introduction to Neutrinos and Neutrino Mixing

2.1 Discovery of the Oscillating Neutrino

Neutrinos were first theorized by Wolfgang Pauli in 1931 [1] as an explanation of the continuous electron kinetic energy spectrum observed in beta decay by Chadwick in 1913. The wide spectral shape, shown in Figure 2.1 for ^{210}Bi, was of great concern throughout the 1910s, 1920s, and 1930s, as beta decay was initially hypothesized to be the release of a single high-energy electron from a nucleus. Rather than sacrifice the symmetry of energy and momentum conservation, cornerstones of classical physics since the days of Newton, Pauli hypothesized that a three-body decay could produce such an experimental result. Later discovery of the neutron by Chadwick, the positron by Anderson, and development of spin statistics gave further theoretical impetus to support the existence of an additional light neutral fermion.

Reines and Cowan were the first to directly detect these neutral leptons, in their case antineutrinos [3, 4]. Their experiments captured $\overline{\nu}_e$ produced by fission products

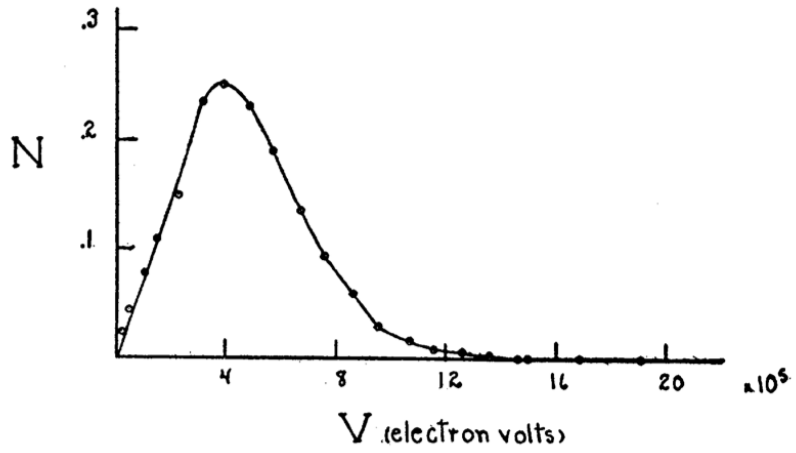

Figure 2.1: The beta decay spectrum of Radium E (now known as ^{210}Bi), as measured in 1935 by Scott [2]. Earlier measurements of similar result in the 1910s by Chadwick formed the initial crisis ultimately leading to hypothesis of the neutrino's existence by Pauli.

in reactor cores on protons in water via the inverse beta decay (IBD) reaction:

$$p + \overline{\nu}_e \rightarrow n + e^+ \tag{2.1}$$

Prompt gammas from positron-electron annihilation were converted to visible photons by liquid scintillator sandwiching the water region, which was then detected by photomultiplier tubes. The neutron, after thermalizing for a few microseconds, was captured on Cadmium dissolved in the water region. This higher-energy 9 MeV signal was detected in the same manner. The positron and neutron signals could then be linked using delayed coincidence circuits to form a distinct signature, allowing for significant background reduction. Backgrounds were further reduced in the Savannah River experiment by situating the neutrino detector 12 m underground to shield cosmic rays. Many of the techniques pioneered in these experiments form the basis of modern-day neutrino detection methods.

Even before the existence of the neutrino was experimentally verified, physicists began to develop theories describing neutrino properties, specifically those regarding

its mass and mode of interaction. The first theory of interaction behind beta decay was developed by Fermi in 1934. Fermi's inverse beta decay Lagrangian was a close analogue to quantum electrodynamics theories of the time [5], but with the exclusion of photons and the inclusion of neutrinos and a new weak coupling constant, G_F. This theory predicted the existence of the inverse beta decay reaction used by Reines and Cowan to detect neutrinos. Experimental observations of other phenomena, such as muon decay, resulted in the transformation of Fermi's description into a general theory of weak decay.

Theories of massless neutrinos began to surface with the observation of maximal parity violation in beta decays of spin-aligned ^{60}Co nuclei by Wu in 1957 [6]. For parity, or mirror symmetry to be preserved in the experiment, the number of electrons emitted in both directions relative to the spin should have been observed. However, electrons were only emitted in one direction, giving maximum parity violation. This led Yang and Lee to the conclusion that helicity, $\frac{\mathbf{s}\cdot\mathbf{p}}{|\mathbf{p}|}$ is only left-handed for neutrinos and right-handed for antineutrinos [7]. In order to be valid for all frames of reference, the neutrino must therefore be massless. Neutrinos were ultimately included as massless weakly interacting particles in the Standard Model of particle physics [8]. In addition, lepton family number is strictly conserved in the Standard Model, contrary to the quark sector.

While experimental evidence at that time supported the idea of a two-component and massless neutrino, no theoretical reason for assuming zero neutrino mass existed. Neutrinos could, for example, obtain mass in the same way other leptons were allowed, by coupling to the vacuum expectation value of the Higgs field. Likewise, no theoretical reason existed for assuming lepton flavor conservation. Non-standard theories were developed without these assumptions separately by Pontecorvo and Maki, Nakagawa, and Sakata [9, 10, 11]. These formulations focused on the phenomenon of

neutrino oscillation, which violated both mass and conservation assumptions. In this theory, quantum mechanical interference between neutrino mass states could allow for the possibility of neutrino flavor change, or for transition from neutrino to antineutrino, between final and initial states. Unfortunately, little to no experimental evidence to support this idea existed at the time.

Proponents of neutrino oscillations first found experimental promise in the discovery of a discrepancy between the observed number of neutrinos detected from the Sun and the number predicted by standard solar models [11]. A uniquely fascinating and thorough account of the inception of the solar neutrino problem can be found in [12]. Davis and his collaborators planned to detect the flux of pure electron neutrinos created by nuclear interactions in the Sun, particularly the high energy portion from ^{8}B decay, by way of the reaction

$$^{37}Cl + \nu \rightarrow \ ^{37}Ar + e^-, \tag{2.2}$$

which took place in a 390000 liter vat of liquid C_2Cl_4 [13]. By detecting the resultant radioactive ^{37}Ar, it was thus concluded that the solar neutrino interaction rate was less than 1 per day, significantly less than the 2-7 per day expected from solar model predictions of the time [12].

Despite new theoretical predictions and additional radiochemical solar neutrino experiments over the next few decades [14, 15, 16], this fascinating discrepancy persisted, remaining unexplained until the late 1990s and early 2000s, when detectors sensitive to multiple flavors of solar neutrinos, such as SNO, SuperK, and Borexino, would measure agreement with predicted solar neutrino fluxes [17, 18, 19]. These experiments demonstrated clearly the oscillation of neutrinos from electron-type at their point of production in the Sun to all three types in the detectors on Earth. These results, along with others in the intervening decade looking at other types of neutri-

nos, would provide thorough validation of the theory of neutrino oscillations. These experiments, including the Kamiokande and SuperK experiments [20][21], Chooz [22], Palo Verde [23], KamLAND [24], MINOS [25], K2K [26], and others, utilized neutrinos emanating from nuclear reactors, accelerators, and the atmosphere to identify parameters that characterized the phenomenon of oscillations. Many of these experiments, whose methods and results are germane to the topic of this thesis, will be described in detail in Chapter 3. These decades of intense investigation have yielded a coherent model of neutrinos and neutrino oscillation that describes nearly all measured instances of neutrino excess or deficit.

2.2 Neutrinos and their Properties

In order to properly understand the theory of neutrino oscillations, the properties and behavior of the neutrino within the Standard Model of particle physics should be overviewed. Since neutrino oscillations, on which this thesis is based, require non-zero neutrino mass, we should also briefly describe possible modes of neutrino mass generation and current neutrino mass limits.

Neutrinos Properties in the Standard Model

Neutrinos are included in the Standard Model of particle physics as spin-$\frac{1}{2}$ fermions, or leptons. Three chargeless neutrino generations are described, each serving as the partner of one of the three charged leptons is the three families of lepton isospin doublets:

$$\begin{pmatrix} e \\ \nu_e \end{pmatrix}, \begin{pmatrix} \mu \\ \nu_\mu \end{pmatrix}, \begin{pmatrix} \tau \\ \nu_\tau \end{pmatrix}. \tag{2.3}$$

The neutrino flavors are aptly named relative to their isospin doublet partners: the electron neutrino (ν_e), muon neutrino (ν_μ), and tau neutrino (ν_τ).

The Standard Model describes the interaction of fundamental particles via the strong, weak, and electromagnetic interactions. As chargeless leptons in this model, neutrinos do not interact with other particles via either the electromagnetic force or strong force. Thus, neutrino interactions proceed only via the weak interaction; the charged-current and neutral current Lagrangians describing these interactions are:

$$J_\mu^{W,CC} = \sum_i (\overline{\psi}\gamma_\mu(1-\gamma_5)\psi) \tag{2.4}$$

$$J_\mu^{W,NC} = \sum_i (\overline{\psi}\gamma_\mu(g_{v_i} - g_{A_i}\gamma_5)\psi) \tag{2.5}$$

These interactions conserve total lepton and lepton family number. Right handed neutrinos, which would be incapable of interacting even via the left-handed weak interaction, are excluded from the Standard Model.

The model described above has proven remarkably effective in describing experimental observations of neutrino-related interactions. The number of active neutrino flavors interacting with the Z-boson can be deduced from measurements of the total and visible partial widths of the Z-boson mass peak in electron-positron collider experiments. In particular, the collider experiments at the LEP accelerator at CERN have used this method to determine an active neutrino flavor number of [27]

$$N_\nu = 2.984 \pm 0.008, \tag{2.6}$$

in good agreement with the Standard Model. In addition to meeting this basic expectation of the Standard Model, weak interaction cross sections involving neutrinos, such as inverse beta decay, have been measured to good agreement with calculations based on the Standard Model (for example, [28]). In addition, searches for physics beyond the Standard Model, such as a neutrino magnetic moment, which would imply non-zero neutrino mass [29], rare lepton flavor-violating interactions involving

neutrinos [30, 31, 32], and decay of extra heavy neutrinos (for example, [33]) have yet to produce unexpected results.

Theories of Massive Neutrinos

The theory of neutrinos must be extended beyond the Standard Model description to include neutrino masses. Such an extension of neutrino theory is now known to be necessary with the observation of neutrino oscillations. In addition, as will be discussed in further detail in section 3.3, many theories unifying strong and electroweak interactions of quarks and leptons predict non-zero neutrino mass. While current preferred theories of neutrino mass generation exist, experimental observation has not definitively identified a mode of neutrino mass generation.

The Mass Lagrangian and Dirac and Majorana Particles

In a theory of massive interacting particles, the weak interaction Lagrangian described above must be accompanied by terms describing the mass of each particle. The theoretical formalism described here somewhat follows the presentation shown in [34]. The most general mass Lagrangian for a field ψ is:

$$-\mathscr{L}_m = \overline{\psi} m_D \psi + \overline{\psi} m_M \psi^c + h.c. \tag{2.7}$$

The number of terms in this Lagrangian is limited to these four by the requirement of Lorentz invariance and hermicity. If we further require global phase transformation invariance, only the first terms and its hermetian conjugate are allowed; these terms are referred to as 'Dirac' mass terms, while the other term and its hermitian conjugate are 'Majorana' mass terms. Since the Dirac masses allow for this additional symmetry, they can be associated with a conserved quantum number, while the Majorana terms, which are not invariant, do not conserve this quantum number.

For simplicity, the full Lagrangian can be re-arranged into a matrix formulation:

$$-\mathscr{L}_m = \begin{pmatrix} \overline{\psi} & \overline{\psi^c} \end{pmatrix} \begin{pmatrix} m_D & m_M \\ m_m^* & m_D \end{pmatrix} \begin{pmatrix} \psi \\ \psi^c \end{pmatrix} \tag{2.8}$$

This matrix can be easily diagonalized by requiring the off-diagonal elements to be zero. In this case, we have a quantum-number conserving Lagrangian with a single eigenvalue and eigenvectors that are not invariant under charge conjugation symmetry:

$$\psi \rightarrow \psi^C = C\overline{\psi}^T \tag{2.9}$$

Thus, we have fields with Dirac mass only whose interactions conserve quantum number and are not charge conjugation eigenstates, leading to two distinct states. If we do not require the off-diagonal Majorana mass terms of Equation 2.8 to be zero in this formulation, we have eigenvalues that are charge conjugation, or Majorana, eigenstates, which indicate equality between particle and antiparticle states. Interactions involving these Majorana eigenstates are quantum number-violating.

In order to describe a theory of neutrino masses, we must deal with weak flavor eigenstates of definite chirality ν_L and ν_R to distinguish between right-handed neutrinos and weakly-interacting left-handed neutrinos. In addition, we must include all three generations of neutrino flavor:

$$\nu_L^0 = \begin{pmatrix} \nu_L^e \\ \nu_L^\mu \\ \nu_L^\tau \end{pmatrix} \tag{2.10}$$

Given this consideration, Equation 2.8 can be re-organized and re-written to form mass Lagrangian terms that can be viewed as transitions between left- and right-handed states:

$$-\mathscr{L}_{m_\nu} = -\frac{1}{2} \begin{pmatrix} \overline{(\nu_L^0)^C} & \overline{\nu_R^0} \end{pmatrix} M_\nu \begin{pmatrix} \nu_L^0 \\ (\nu_R^0)^C \end{pmatrix} + h.c. \tag{2.11}$$

The mass matrix M_ν is composed of:

$$\begin{pmatrix} m_L & m_D^T \\ m_D & m_R \end{pmatrix}, \tag{2.12}$$

where the M_L and M_R contain left- and right-handed Majorana mass terms and M_D contains Dirac mass terms. The properties of these Majorana and Dirac terms are similar to those defined for the generic field ψ in the previous section.

Dirac Mass Generation

If all Majorana terms are zero, we have 'Dirac neutrinos,' with only mass Lagrangians of the form:

$$-\mathscr{L}_{m_\nu}^D = m_D \overline{\nu_R^0} \nu_L^0 + h.c. \tag{2.13}$$

This is the same form of Dirac mass Lagrangian that allows other standard model particles to acquire their mass through their coupling with the Higgs field. Additionally, this Lagrangian exhibits total lepton number conservation. This scenario is not the currently favored method of neutrino mass generation, as it would use the same mass generation mechanism as quarks and leptons to produce a drastically different neutrino mass scale.

The Seesaw Mechanism of Mass Generation

A favored theory of neutrino mass generation, called the See-Saw model, was proposed in 1979 by Gell-Mann, Raymond, and Slansky [35], as well as by Yanagida [36]. Unlike with quark and lepton mass generation, this mechanism is based on the Majorana masses, giving a possible explanation for the large difference between neutrino and other masses. The following discussion will describe Type I See-Saw model; other See-Saw models exist [37], but will not be discussed here.

Continuing with the general discussion in the previous sections, if Majorana terms in Equation 2.11 are not zero, we have 'Majorana neutrinos,' and must include additional mass Lagrangian terms of the following form,

$$-\mathscr{L}^{M}_{m_\nu} = \frac{m_R}{2}\overline{(\nu^0_R)^c}\nu^0_R + h.c. \tag{2.14}$$

which, since Majorana fields are charge conjugation eigenstates, indicates a lepton-number violating interaction. This full mass Lagrangian can then be diagonalized to obtain mass eigenstates, ν and N:

$$-\mathscr{L}_{m_\nu} = \frac{1}{2}\begin{pmatrix}\overline{\nu} & \overline{N}\end{pmatrix}\begin{pmatrix} m_D^2/m_R & 0 \\ 0 & m_R \end{pmatrix}\begin{pmatrix}\nu \\ N\end{pmatrix} \tag{2.15}$$

This transformation results in the formation of three states ν with mass of the scale $m_\nu = m_D^2/m_R$ and three states of mass scale $m_N = m_R$. If the Dirac mass terms are logically given the same mass scale m_D of the quarks and leptons and the Majorana terms are given a $m_R \gg m_D$, one obtains very small ν masses and very large N masses. Utilizing the top quark mass (173 GeV) as m_D and an order-of-magnitude estimate of 0.05 eV for the light neutrino mass scale, m_ν, one obtains a heavy neutrino mass m_N on the order of the GUT scale, 10^{15} GeV. Thus, this theory appears to conform well with experimental observations of three light left-handed neutrinos and three as-yet-unobserved heavy neutrinos that are well beyond the range of measurement of any particle accelerator.

To summarize, See-Saw neutrino mass generation properly produces very light active neutrino masses. This mechanism also ensures the existence of non-weakly-interacting right-handed neutrinos. Finally, seesaw-generated masses would require that neutrinos be Majorana particles, thereby excluding total lepton number conservation in some neutrino interactions. Observation of such interactions, particularly

neutrino-less double beta decay, would prove neutrinos are Majorana particles, and strengthen arguments in favor of See-Saw mass generation.

Neutrino Mass Limits

Current limits on the mass of the three light active neutrinos are provided by an array of different experimental techniques; these limits are shown in Table 2.1. Upper limits are provided by high-energy, beta-endpoint and neutrino-less double beta decay experiments, as well as by cosmological surveys. Beta-endpoint experiments use precise energy spectrometers to measure the shift in or spectral distortion of the beta decay endpoint resulting from the removal of kinetic energy because of non-zero neutrino mass. Neutrino-less double beta decay is an as-yet-unobserved lepton number-violating interaction in which two electrons and no neutrinos are released from a radioactive nucleus in successive beta decays. By experimentally limiting the decay's cross-section, one indirectly limits the scale of the effective neutrino mass. Cosmological and astronomical surveys measure anisotropy of matter in the universe or redshifts of distant stellar objects, which are dependent on the universe mass density. As neutrinos make up a significant portion of that matter, these measurements can also be used to limit neutrino masses, although these limits are dependent on the accuracy of cosmological models.

Lower limits on the neutrino masses come from oscillation experiments, which measure differences between the mass states. If the lightest neutrino has no mass, the heaviest neutrino must have mass identical to the largest neutrino mass splitting, about 0.04 eV.

Neutrino Mass	Limit	Experiment	Detection Method
m_{ν_e}	<2.3 eV	Mainz 2000	Tritium Beta Endpoint
m_{ν_μ}	<1.9 keV	PSI 1996	Pion Decay
m_{ν_τ}	<18.2 MeV	ALEPH 1998	Tau Decay
$\sum_i \nu_i$	< 0.3-1.3	Cosmology	CMB, Supernova, Lyman α
$m_{0\nu\beta\beta}$	< 0.3-0.6 eV	Various	$0\nu\beta\beta$ Decay
$m_{heaviest}$	> 0.04 eV	Oscillations	Largest Mass-Squared Splitting

Table 2.1: Current limits on neutrino masses. Some limits are from directly measuring the kinematic effects of flavored neutrino mass in particle decays, while others are indirect limits from cosmology or neutrinoless double beta decay, which depend on input cosmological models and neutrino mixing parameters and phases, respectively. Oscillation experiments provide a lower limit on the mass of the heaviest neutrino. All values from [38].

2.3 Mixing in the Lepton Sector

Now that the theoretical underpinnings and experimental limits of neutrino mass have been described, we will turn our attention to the particular property of neutrinos that is the focus of this thesis: neutrino flavor oscillation. This section will outline the theory behind the phenomenon of neutrino oscillations by starting with a simpler two-neutrino picture and then generalizing to the full three generations. Current known values of oscillation parameters will then be overviewed. Finally, the physical manifestations of neutrino mixing, appearance and disappearance of neutrinos at specific baseline and energy ranges, will be described for experimental situations sensitive to the mixing parameter θ_{13}.

Theory of Neutrino Oscillations

For simplicity, let us first simplify the full mass Lagrangian in Equation 2.11 to a theory with only two generations of type a and b, and explicitly write out the

individual left-handed lepton-number-conserving terms for each flavor:

$$-\mathscr{L}_{M_\nu} = m_{\nu_a}\overline{\nu}_a\nu_a + m_{\nu_b}\overline{\nu}_b\nu_b + m_{\nu_a\nu_b}(\overline{\nu}_a\nu_b + \overline{\nu}_b\nu_a), \tag{2.16}$$

which can be written in the matrix form

$$-\mathscr{L}_{M_\nu} = \overline{\nu}_l M_\nu \nu_l, \quad \text{with} \tag{2.17}$$

$$M_\nu = \begin{pmatrix} m_{\nu_a} & m_{\nu_a\nu_b} \\ m_{\nu_a\nu_b} & m_{\nu_b} \end{pmatrix} \quad \text{and} \quad \nu_l = \begin{pmatrix} \nu_a \\ \nu_b \end{pmatrix}. \tag{2.18}$$

By moving to a new basis, (ν_1, ν_2), using the unitary transformation matrix U,

$$\begin{pmatrix} \nu_a \\ \nu_b \end{pmatrix} = \begin{pmatrix} \cos\phi & \sin\phi \\ -\sin\phi & \cos\phi \end{pmatrix} \begin{pmatrix} \nu_1 \\ \nu_2 \end{pmatrix} \tag{2.19}$$

our matrix M'_ν is now diagonal, meaning that the states (ν_1, ν_2) have definite masses:

$$M'_\nu = \begin{pmatrix} m_1 & 0 \\ 0 & m_2 \end{pmatrix} \tag{2.20}$$

The physical masses m_1 and m_2 of these mass states have a direct relation to the coupling constants in the full Lagrangian.

An a-type neutrino created through the weak interaction will begin in a definite flavor state, which is a superposition of the two mass states:

$$|\nu_a\rangle = \sum_i U_{ai} |\nu_i\rangle = |\nu_1\rangle \cos\phi + |\nu_2\rangle \sin\phi. \tag{2.21}$$

To find the amplitude of a relativistic neutrino of energy E oscillating to a final b-type neutrino state at a distance L, one must apply the time evolution operator to the initial a-type neutrino state, and then apply this to the final b-type neutrino state:

$$A(\nu_a \to \nu_b) = \sum_i \langle\nu_i| U^\star_{ai} e^{-iE_i t} U_{bi} |\nu_i\rangle \tag{2.22}$$

After simplification and the inclusion of the correct factors of c and h, one gets a probability

$$P(\nu_a \to \nu_b) = \sin^2 2\phi \sin^2 \Delta, \text{where} \tag{2.23}$$

$$\Delta = 1.27\Delta m^2(eV^2)\frac{L(km)}{E_\nu(GeV)}. \tag{2.24}$$

In this two-neutrino case, the parameters governing the oscillatory behavior are the neutrino mixing angle ϕ and the difference between the masses of the neutrinos, Δm = m_1 - m_2. The same general features are reproduced with the inclusion of lepton-number violating mass terms, with the addition of a few phases that do not effect oscillations between neutrino flavors.

This basic picture is reproduced in extending to three neutrino flavors and mass states. In place of a single mixing angle, the mass and flavor states are related by the unitary PMNS matrix, which consists of three mixing angles and one CP-violating phase:

$$U_{PMNS} = \begin{pmatrix} c_{13}c_{12} & c_{13}s_{12} & s_{13}e^{-i\delta} \\ -c_{23}s_{12} - s_{13}c_{12}s_{23}e^{+i\delta} & c_{23}c_{12} - s_{13}s_{12}s_{23}e^{+i\delta} & c_{13}s_{23} \\ s_{23}s_{12} - s_{13}c_{12}c_{23}e^{+i/delta} & -s_{23}c_{12} - s_{13}s_{12}c_{23}e^{+i\delta} & c_{13}c_{23} \end{pmatrix} \tag{2.25}$$

$$= \begin{pmatrix} 1 & & \\ & c_{23} & s_{23} \\ & -s_{23} & c_{23} \end{pmatrix} \begin{pmatrix} c_{13} & & s_{13}e^{-i\delta} \\ & 1 & \\ -s_{13}e^{i\delta} & & c_{13} \end{pmatrix} \begin{pmatrix} c_{12} & s_{12} & \\ -s_{12} & c_{13} & \\ & & 1 \end{pmatrix}, \tag{2.26}$$

where s_{ij} and c_{ij} are $\sin\theta_{ij}$ and $\cos\theta_{ij}$. Two Majorana phases are also introduced into the matrix by Majorana mass terms, but cancel out in all flavor oscillation scenarios.

Table 2.2 lists the current knowledge of these parameters as well as the splittings between the three mass states. Using the same quantum mechanical process as for two flavor and mass states, one can write down a formula for the probability of oscillation

between flavor states:

$$P(\nu_l \to \nu_{l'}) = \sum_i \left| U_{li} U^{\star}_{l'i} e^{-i(m_i/2E)L)} \right|^2 . \tag{2.27}$$

Depending on the neutrino energy, the experimental baseline, L, and the value of the oscillation parameters listed in Table 2.2, certain terms in this equation will be vanishingly small, and others will dominate the probability equation. For instance, with an L/E of $\sim$0.5 km/MeV and a $|\Delta m^2_{21}| \ll |\Delta m^2_{32}|$, the ν_e disappearance probability approaches Equation 2.23, with θ_{13} in place of ϕ and Δm^2_{31} in place of Δm^2. Thus, an experiment measuring ν_e with this L/E is mainly sensitive to the value of θ_{13}. Similar equations exist for other neutrinos and other values of L/E, with each type of experiment having sensitivities to particular oscillation parameters [39].

Parameter	Best Fit Value	3σ Interval
Δm^2_{21} $(10^{-5} eV^2)$	$7.59^{+.20}_{-.18}$	$7.09 - 8.19$
Δm^2_{32} $(10^{-3} eV^2)$	$\pm 2.45^{+.09}_{-.09}$	$2.18 - 2.73$
$\sin^2\theta_{23}$	$0.51^{+0.06}_{-0.06}$	$0.39 - 0.64$
$\sin^2\theta_{12}$	$0.312^{+0.017}_{-0.015}$	$0.28 - 0.35$
$\sin^2\theta_{13}$	$0.013^{+0.009}_{-0.006}$	< 0.035

Table 2.2: Best-fit values for neutrino mixing angles and mass splittings. 3σ confidence intervals are given for all parameters with the exception of $\sin^2\theta_{13}$, where only a 3σ limit is given. In addition, the absolute value of the parameter Δm^2_{31} is not known. From [40].

Additions: Matter Effects and CP-Violation

This oscillation picture is complicated by electron neutrino interactions with dense matter during propagation, which introduces an additional effective potential to the Hamiltonian [41]:

$$V_c(\nu_e) = \sqrt{2} G_F N_e \quad \text{and} \quad V_c(\overline{\nu}_e) = -\sqrt{2} G_F N_e, \tag{2.28}$$

where N_e is the electron density of the material. This potential manifests itself as an additional phase in the evolution operator, causing a modification of the oscillation frequency and amplitude for certain values of L/E. This effect is especially important in solar neutrino oscillations: higher-energy ν_e created in the Sun must travel through high solar electron densities, causing their disappearance to be maximized despite a non-maximal solar mixing angle θ_{12} [42]. This matter-enhanced oscillation is called the MSW effect. By probing solar neutrinos from different energy regimes, the MSW effect can be detected and utilized to provide multiple constraints on the value of the solar mixing parameter θ_{12} in Table 2.2. In addition, the absolute value of the matter effect is determined by the sign of the difference between the involved mass states; thus, the MSW effect can also be used to determine the neutrino mass hierarchy for the two neutrino mass states m_1 and m_2. Earth matter effects are of lesser magnitude, as the electron density of the earth is far lower. The oscillation length and measured mixing angle would be expected to deviate by less than a few percent due to Earth-matter effects for long-baseline accelerator neutrino experiments, and has yet to be measured. Because of this, the hierarchy of the m_1 and m_3 mass states is unknown, as reflected in Table 2.2.

As in quark sector mixing with the CKM matrix, the unitary nature of the PMNS matrix ensures the inclusion of a complex phase, δ. This complex phase leads to CP-asymmetry as well as T-asymmetry in leptonic mixing:

$$\text{CP-Asymmetry:} \quad P(\nu_a \to \nu_b) \neq P(\overline{\nu}_a \to \overline{\nu}_b) \tag{2.29}$$

$$\text{T-Asymmetry:} \quad P(\nu_a \to \nu_b) \neq P(\nu_b \to \nu_a)) \tag{2.30}$$

Measurement of CP-violation is the lepton sector is one of the main current challenges in particle physics, as it may provide clues about matter-antimatter asymmetry in

the universe, which could be caused by large CP-violating effects of unknown origin in the early universe.

By measuring differences in mixing amplitudes between neutrinos and antineutrinos, this phase δ can be measured along with the remaining mixing parameters. An alternate method of obtaining this parameter is by measuring the area of the PMNS unitarity triangle; however, given the difficulty of creating large quantities of ν_τ, the former method is more likely to provide avenues for measurement of δ.

2.4 Measuring θ_{13}: Methods and Consequences

One particularly interesting feature visible in Table 2.2 is the small value of θ_{13}. At 3σ confidence level, its value is consistent with zero; however, the table shows that a non-zero θ_{13} value is favored at 90% confidence level. A further discussion of the experimental origins of this non-zero hint will be presented in Section 3.3. The parameter θ_{13} is of particular interest currently because it is the last undetermined neutrino mixing angle and because it plays a vital role in determining the magnitude of CP violation in the neutrino sector.

Two methods have commonly been used to directly probe the value of θ_{13}: reactor $\overline{\nu}_e$ experiments and long-baseline $\overline{\nu}_e/\nu_e$ appearance experiments. Reactor $\overline{\nu}_e$ experiments measure the survival probability of reactor $\overline{\nu}_e$; that is, they detect the number of $\overline{\nu}_e$ that do not oscillate into other flavors over the experimental baseline. The full disappearance probability for these neutrinos, using the sine and cosine abbreviations from 2.25 and 2.24, is

$$P(\overline{\nu}_e \to \overline{\nu}_e) = 1 - c_{13}^4 \sin^2 2\theta_{12} \sin^2 \Delta_{12} + c_{12}^2 \sin^2 2\theta_{13} \sin^2 \Delta_{13} + s_{12}^2 \sin^2 2\theta_{13} \sin^2 \Delta_{23}, \tag{2.31}$$

Given the near identity of Δ_{31} and Δ_{32}, the last two terms can be combined. In order

to maximize these last two combined terms, which are sensitive to the value of θ_{13}, it is preferred that

$$\Delta_{31} = 1.27\Delta m^2_{31}\frac{L(m)}{E_{\overline{\nu}_e}(MeV)} = \frac{\pi}{2} \tag{2.32}$$

Given the known value of Δm^2_{31} and the energy spectrum of the reactor $\overline{\nu}_e$, which peaks at 3-4 MeV, the detector baseline should be roughly 2 km. Conveniently, this choice of L/E assures that the first term in 2.31, which governs θ_{12}-related mixing is small, thus disentangling θ_{13} from any other oscillation parameters for this measurement. For this reason, reactor $\overline{\nu}_e$ experiments are considered a 'pure measurement' of θ_{13}.

Long-baseline accelerator ν experiments are sensitive to θ_{13} by detecting the appearance of ν_e ($\overline{\nu}_e$) in an accelerated beam of ν_μ ($\overline{\nu}_\mu$). With neutrino energies in the GeV range, baselines of several hundreds or thousands of kilometers are necessary to observe oscillations related to Δm^2_{32}. Including non-negligible Earth-matter effects with the attendant parameter $a = 2\sqrt{2}G_f N_e E_\nu$, the ν_μ transition probability for the accelerator L/E is [39]:

$$\begin{aligned}
P(\overline{\nu}_\mu \to \overline{\nu}_e) &= 4c^2_{13}s^2_{13}s^2_{23}\sin^2\Delta_{31} \\
&+ 8c^2_{13}s_{13}s_{23}c_{23}s_{12}c_{12}\sin\Delta_{31}[\cos\Delta_{32}\cos\delta - \sin\Delta_{32}\sin\delta]\sin\Delta_{21} \\
&- 8c^2_{13}s^2_{13}s^2_{23}c^2_{23}\cos\Delta_{32}\sin\Delta_{31}\sin\Delta_{21} \\
&+ 4c^2_{13}s^2_{12}[c^2_{12}c^2_{23} + s^2_{12}s^2_{13}s^2_{23} - c_{12}c_{23}s_{12}s_{13}s_{23}\cos\delta]\sin^2\Delta_{21} \\
&- 8c^2_{13}s^2_{13}s^2_{23}(1-2s^2_{13})\frac{aL}{4E_\nu}\sin\Delta_{31}\left(\cos\Delta_{32} - \frac{\sin\Delta_{13}}{\Delta_{13}}\right).
\end{aligned} \tag{2.33}$$

The first term is dominant and contains a dependence on θ_{13}. The ensuing terms are non-negligible and contain dependencies on a few additional unknown parameters: Δ_{31}, which has an unknown absolute value, and the CP-violating phase δ. Thus, while a non-zero measurement of ν_e appearance would demonstrate a non-zero value of θ_{13}, its sensitivity to neutrino mass hierarchy and CP violation would be greatly

hindered by this degeneracy of solutions. For example, a particular non-zero result could be explained equally well with two separate sets of parameters, (θ_{13},δ) or (θ'_{13},δ').

Given this parameter degeneracy in the accelerator neutrino oscillations, it seems clear that a pure θ_{13} measurement with reactor $\overline{\nu}_e$ is a primary concern in the development of neutrino physics. If the value of θ_{13} can be independently measured, long-baseline accelerator ν_e measurements can be used to provide more precise information about CP violation and the neutrino mass hierarchy. Also, because every CP-violating term in 2.33 also depends on θ_{13}, a large value of $\sin^2 2\theta_{13}$ would mean larger measurable CP-violating effects. Thus, measuring the size of θ_{13} is important in determining the necessary accelerator and detector technology required for the next generation of neutrino experiments. Given a large ($>$0.05) value of $\sin^2 2\theta_{13}$, conventional long-baseline neutrino beam experiments could be used to search for asymmetries between $\nu_\mu \rightarrow \nu_e$ and $\overline{\nu}_\mu \rightarrow \overline{\nu}_e$ [43]. Lower values may necessitate the need for more complex and expensive ν sources such as beta beams or muon storage rings.

Chapter 3

Reactor $\overline{\nu}_e$ and θ_{13}: An Experimental History

Nuclear reactors are useful sources of copious amounts of antineutrinos. Nuclear reactors provided neutrinos for Reines and Cowan during their groundbreaking neutrino detection experiments of the 1950s and 1960s. After the observation of the solar neutrino deficit, scientists were interested so see if they could detect similar deficits in reactor $\overline{\nu}_e$ fluxes, resulting in a number of reactor $\overline{\nu}_e$ detection experiments being conducted at short (<1 km) baselines. These experiments employed many similar methods to reduce experimental systematics, increasing their sensitivity to any $\overline{\nu}_e$ deficit. The main determinant of these experiments' baselines was their desire for high statistics and low statistical uncertainties. The selection of short baselines became more nuanced after early atmospheric results suggested mass-squared splittings in the vicinity of 10^{-2} to 10^{-3} eV^2, which would point to km-scale baselines as optimal for observing oscillation with reactor neutrinos.

The search for θ_{13} requires the proper selection of L/E as well as an experimental design that most effectively eliminates as much systematic and statistical uncertainty

as possible. The following sections will overview previous experiments whose designs, methods, and results provide motivation the Daya Bay and other experiments seeking to measure θ_{13}. Concurrent atmospheric and accelerator experiments that led the selection of reactor experimental baselines to higher values will also be overviewed.

3.1 Early Reactor $\overline{\nu}_e$ Experiments

After the first detection of reactor $\overline{\nu}_e$ at the Hanford and Savannah River reactors, further work was done in the 1960's and 1970's by Reines and his colleagues to measure the properties of the newly discovered particle, such as its neutral and charged current interaction cross sections and its decay time [44, 45]. In 1980, an unexpectedly low detected rate of charged current interactions, which can only be caused by $\overline{\nu}_e$, with respect to detected neutral current interactions, which can be caused by all flavors, led the collaborators to suggest oscillation of $\overline{\nu}_e \rightarrow \overline{\nu}_x$ governed by a large Δm^2, on the order of a few eV^2[46]. Further investigation of this oscillation parameter space was urged by the authors.

In the late 1970's, an experiment utilizing 10-55 MeV neutrino beams from the Los Alamos Meson Production Facility (LAMPF) also began looking for neutrino oscillations in the same Δm^2 parameter space [47]. The neutrino beam consisted largely of $\overline{\nu}_\mu$, ν_μ, and $\overline{\nu}_e$ from the decay of positive pions and their subsequent positive muons. A *Čerenkov* detector located a distance of 6.3 meters from the beam stop could be filled with either light water to look for inverse beta decay of $\overline{\nu}_e$ or heavy water to look for or the reaction:

$$\nu_e + d \rightarrow e^- + 2p. \tag{3.1}$$

A significant fraction of ν_e detected with respect to $\overline{\nu}_e$ would provide a clear

signature of $\nu_\mu \rightarrow \nu_e$ oscillations. The absence of such an excess resulted in ruling out large regions of high Δm^2 (>0.7MeV) parameter space. Thus, reactor antineutrino oscillations, if they were to occur, would likely happen at baselines in excess of a few meters.

Over the course of the next decade and a half, a number of experiments were induced by high neutrino fluxes and rumblings of oscillations at attainable short baselines to conduct very short baseline reactor $\overline{\nu}_e$ detection experiments. This following sections will discuss the design, detection method, systematics- and background-reduction strategies, and results of these experiments. An chronology and overview the various experiments is given in Table 3.1. One should particularly note the evolution of selected experimental baseline as a function of time, which, as previously mentioned, was guided by findings from concurrent atmospheric neutrino experiments. Also highlighted are the two principal analysis strategies undertaken by these experiments to probe $\overline{\nu}_e$ disappearance: absolute comparison of measured and predicted neutrino fluxes and spectra, and relative comparison of measured flux and spectra at multiple baselines. The difference between these two methods will be described below.

ILL: Absolute Measurement of Rate and Spectral Shape

The first of these experiments took place in 1980 at the Institut Laue-Langevin (ILL), which maintains a 57 MW thermal power reactor [48]. The ILL experiment searched for neutrino oscillations by comparing the measured inverse beta decay positron rate and energy spectrum directly to the predicted rate and spectrum at a baseline of 8.8 m between detector and reactor centers. The predicted values were based on another experiment done in 1980 at ILL which used thermal neutrons from the reactor to bombard nearby thin foils of a fissile isotope commonly found in nuclear reactors,

Experiment	Year	Baselines (m)	Absolute $\frac{N_{obs}}{N_{exp}}$	Relative $\frac{N_{obs,1}}{N_{obs,2}}$	References
ILL	1980-81	8.8	0.955±0.12	-	[48]
Goesgen	1981-1985	37.9 45.9 67.4	1.018 1.045±0.06 0.975±0.06	No Relative Deficit	[49, 50, 51]
Bugey	1982-84	13.6(18.3)	-	1.10±0.03	[52]
Rovno	1983-1991	18(25)	0.964±0.07	0.985±0.04	[53, 54, 55]
Krasnoyarsk	1987-94	57(231)	0.99±0.05	0.86±0.15	[56]
Bugey	1995	15 40 95	0.99±0.05 0.99±0.05 0.92±0.14	No Relative Deficit	[28]
Chooz	1997	1000	1.01±0.04	-	[22, 57, 58]
Palo Verde	1999	890(750)	1.01±0.10	-	[23, 59]

Table 3.1: Chronology and overview of short-baseline reactor $\overline{\nu}_e$ experiments. The double lines between the three different time periods indicate periods of gradual advancement in knowledge of the atmospheric Δm^2 parameter: the earliest period had no input from accelerator experiments, the middle period occurred as atmospheric results were surfacing from various experiments, and the late time period consisted of experiments with baselines tailored specifically to the Δm^2 values suggested by Kamiokande-II. Also outlined is any reported absolute or relative deficit.

^{235}U [60]. After the isotopes fissioned in the presence of the neutrons, the neutron-rich products of the reaction beta decayed, creating a spectrum of beta electrons whose energy and normalization were measured by a magnetic spectrometer. As the neutrino and the beta particle are the only products of the interaction, a conversion procedure was used to translate the beta spectrum into an expected $\overline{\nu}_e$ spectrum. The converted spectrum can be seen in Figure 3.1, along with the spectra of a few other common fissioning isotopes, ^{238}U, ^{239}Pu, and ^{241}Pu. As the ILL reactor was composed of a steady level of 95% ^{235}U, the converted $\overline{\nu}_e$ spectrum could be combined with the total thermal power of the reactor to provide an absolute expected $\overline{\nu}_e$ rate and spectrum for the ILL experiment.

For their direct $\overline{\nu}_e$ flux measurement, the ILL experiment used the same delayed-coincidence detection method used in the original Reines and Cowan experiments.

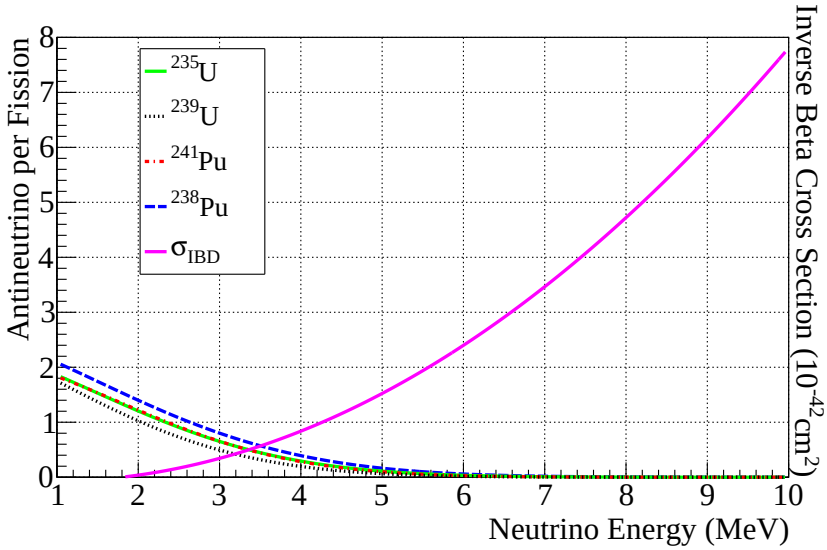

Figure 3.1: Converted $\overline{\nu}_e$ spectrum For ^{235}U, ^{238}U, ^{239}Pu, and ^{241}Pu. The spectra were measured for ^{239}Pu and ^{241}Pu in a similar manner to ^{235}U [61, 62]. the spectrum for ^{238}U has not been measured, and instead is arrived at via nuclear calculations. The spectra shown are commonly used parametrizations of these experiments and calculations elucidated by Vogel and Engel in [63]. The cross-section of inverse beta decay interaction, which is utilized in many reactor $\overline{\nu}_e$ experiments, is also pictured [64].

A diagram of their detector is shown in Figure 3.2. $\overline{\nu}_e$ interact with free protons in optically separated cells of liquid scintillator via inverse beta decay, whose interaction cross-section spectrum can be seen in Figure 3.1. The prompt scintillation light from the positron energy deposition was detected by photomultiplier tubes on the end of the cells; the time distribution of the scintillation light could be used to distinguish between positrons and heavier background particles, a process called pulse-shape discrimination, or PSD. After wandering during thermalization, some neutrons would be detected by ^{3}He wire counters sandwiched between the scintillator target cells. The ^{3}He wire counters would provide the delayed signal, allowing for large background reduction via delayed coincidence. In addition, the segmented nature of the detector could also rule out as background events with proper energy signatures but incorrect event topologies. Furthermore, periods of reactor-on data could be compared with

periods of reactor-off data to subtract any remaining backgrounds unrelated to the reactor.

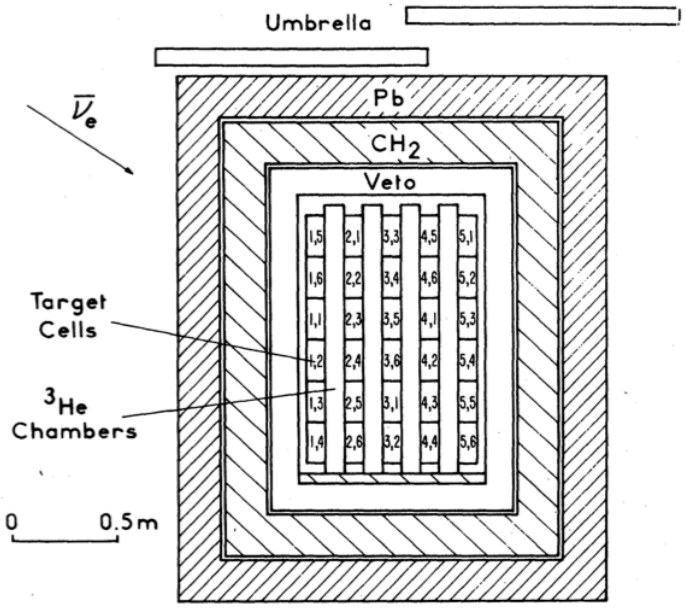

Figure 3.2: Diagram of the ILL detector. Pictured are the target scintillator cells, the neutron counters, and the surrounding shielding. From [48].

After 128 days of live time with reactors on, the detector recorded 4890 ± 180 counts. This corresponded to a ratio of detected to expected events of

$$\mathrm{R} = \frac{n_{obs}}{n_{exp}} = 0.955 \pm 0.035(\mathrm{stat.}) \pm 0.110(\mathrm{syst.})$$

This result was consistent with a no-oscillation hypothesis. In addition, the detected and expected $\overline{\nu}_e$ spectrum, reproduced in Figure 3.3, were compared assuming no oscillations via a χ^2 test; the result was consistent with the no-oscillation hypothesis for the regions of Δm^2 and θ parameter space suggested by the earlier Savannah River experiment. However, this measurement was limited in its ability to rule out larger regions of parameter space by systematics, particularly by the uncertainties in the normalization and shape of the reactor $\overline{\nu}_e$ spectrum as measured in [60].

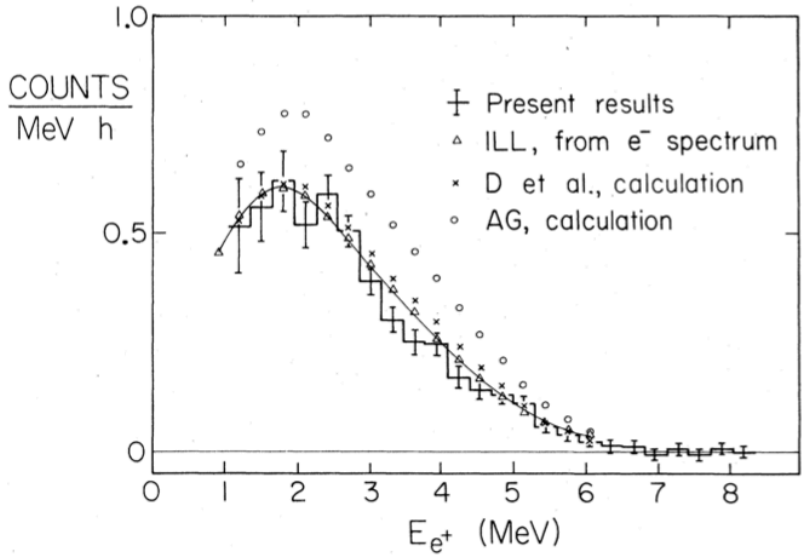

Figure 3.3: Measured and expected inverse beta positron spectrum in the ILL experiment. The triangles represents the expected result based on the beta spectrum measurement in [60], while the circles, and x's represent the expected result based on different nuclear calculations. Figure from [48].

Goesgen, Bugey, and Rovno: Relative Measurements

After the ILL experiment, numerous measurements were made with the same or similar detectors at the Goesgen and Bugey Pressurized Water Reactors (PWRs) [49, 50, 51, 52, 28]. The reactors at Goesgen and Bugey were commercial Pressurized Water Reactors (PWRs) with thermal power outputs of 2800MW, more than an order of magnitude higher than the ILL reactor. While this meant these reactors would provide higher fluxes of $\overline{\nu}_e$, the spectra of these reactors were less well known. The fuel for PWR reactors contain less than 10% ^{235}U that is depleted as operation and fission proceed. Simultaneously, significant amounts of ^{239}Pu, and ^{241}Pu are created out of the large amount of ^{238}U in the fuel, causing the contribution of $\overline{\nu}_e$ from these isotopes to steadily increase over time. This fuel burn-up, pictured in Figure 3.4, results in the introduction of additional systematics related to the shape and normalization of the reactor $\overline{\nu}_e$ spectrum for these three additional isotopes.

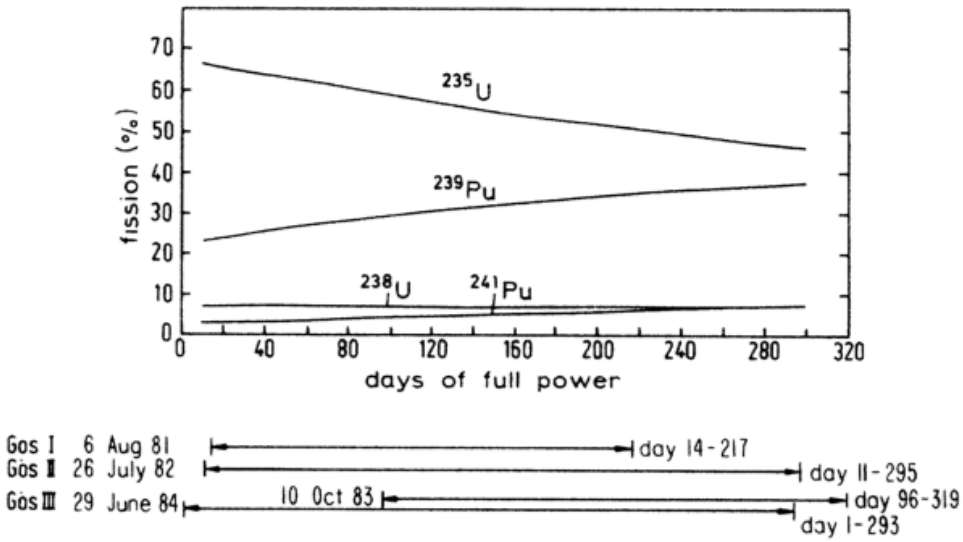

Figure 3.4: Reactor fuel burn-up at the Goesgen PWR reactors. Reactor fuel begins with less than 10% total ^{235}U and a much larger fraction ^{238}U. Initially a majority of fission comes from ^{235}U. As more ^{239}Pu and ^{241}Pu are created through capture of fission neutrons on ^{238}U, these isotopes will gradually contribute a greater percentage of fissions as burn-up proceeds. A small but consistent fraction comes from fast neutron-induced fission of ^{238}U. This figure also denotes the operation times of the detectors used the Goesgen experiment with respect to the point in the 12-month fuel cycle, and thus the fission fractions sampled by each individual detector. Figure from [51].

A simple re-conception of the experimental design was used to circumvent many of these and other systematics: neutrino interaction rates at two different baselines can be compared to yield information about oscillation that is largely independent of reactor information. In absence of neutrino oscillations, at two different positions, the $\overline{\nu}_e$ isotropically released from a reactor core should have the same spectral shape at any baseline and rates proportional to the inverse square of the distances from the reactor core. Without largely correlated reactor systematics at each baseline, neutrino oscillations could thus be identified through any deviation in the measured spectral shape or baseline-corrected detection rate between detectors. Of equal importance,

correlated detector systematics will also be cancelled by a two-site comparison. For example, in the Goesgen experiment, while the detection efficiency was uncertain to 3.8%, if the detector's efficiency was unaltered in the move from baseline to baseline, the contribution of this 3.8% uncertainty to a site-to-site comparison's systematic would be 0%.

The Goesgen experiment, run from 1982 until 1985, used one reactor and one ILL-like detector, moving the detector between baselines of 37.9 m, 45.9 m, and 67.4 m after a period of operation at each baseline. Despite the slight difference at each baseline in shape and rate because of changes in $\overline{\nu}_e$ production rates by each isotope from fuel burn-up, a site-to-site comparison greatly reduced the correlated reactor-related and detector-related systematics of the experiment. At Goesgen, an oscillation analysis comparing the absolute neutrino flux at each site to the expected $\overline{\nu}_e$ flux had a systematic uncertainty of 6.0%. For the site-to-site comparison, that uncertainty was reduced to 1.5% for the near baselines and 3.0% for the far baseline. As with the ILL experiment, the expected to measured rate and spectra for all three baselines were consistent with no oscillations. In addition, comparisons between all baselines yielded spectral and rate ratios that were also consistent with no oscillations.

The first reactor $\overline{\nu}_e$ experiment run at the Bugey reactors from 1982 to 1984 improved on the systematics cancellation of the Goesgen experiment by detecting $\overline{\nu}_e$ at two separate baselines of 13.6 m and 18.3 m simultaneously with two separate identical inverse beta decay detectors [52]. Simultaneous data-taking at two sites ensures more complete cancellation of reactor systematics, as the integrated burn-up and fission fractions are fully correlated in time for both detectors. The multiple detectors used a similarly segmented design to the ILL and Goesgen experiments, with a larger target region composed of a different scintillation medium. Utilizing this reactor and detector arrangement, the experiment reported an unexpected 10%

deficit in the detection ratio between the far and near detectors after baseline correction, giving a positive oscillation result in significant conflict with the Goesgen results. Later measurements made in 1986 with improved shielding to reduce cosmic and neutron-related backgrounds were reported to resolve this unexpected deficit (see [28]).

An additional Russian experiment, Rovno, running from 1983-1991, would then provide an additional systematic check of these short experimental baselines [53, 54, 55, 65, 66]. Rovno utilized two identical inverse beta decay detectors at similar baselines (18.3 m and 25.3 m), and attempted to maintain equal live time between detectors during all phases of reactor burn-up. Also, in addition to experimental runs with a ^{3}He proportional counters-based detector, some runs were done with identical detectors utilizing Gd-dopant in the liquid scintillator to create a high-energy the delayed signal necessary for low-background coincidence detection. This improvement allowed an increase in detection efficiency from less than 10% for ILL to around 30% for Rovno. Rovno reported no measurement of unexpected rate or spectral deviations between detectors, providing a null result in agreement with the Goesgen experiment.

Constraining Oscillation Parameters at Short Baselines

These oscillation results can be used in the context of a two-neutrino mixing scheme to rule out or identify feasible values for the mixing parameters $\sin^2 2\theta$ and Δm^2. As discussed in Chapter 2, oscillation is maximized for a particular value of Δm^2 at one experimental L/E parameter. Thus, for these experiments of roughly point-like baseline distribution and wide energy spectrum, any involved Δm^2 would result in a peak in the spectral distortion between detectors or between prediction and measurement. The amplitude of that distortion can be used to constrain possible

values of $\sin^2 2\theta$. Similarly, a relative rate deficit provides similar but less precise information on the mixing parameters. An absolute rate deficit between predicted and detected events can be interpreted as evidence for mixing from a large Δm^2, whose oscillation effects have averaged out over excessive baseline to reduce the $\overline{\nu}_e$ flux to half its maximally oscillated value at all energies. Absence of any relative or absolute rate deficits or spectra distortions removes possible mixing parameter values from consideration.

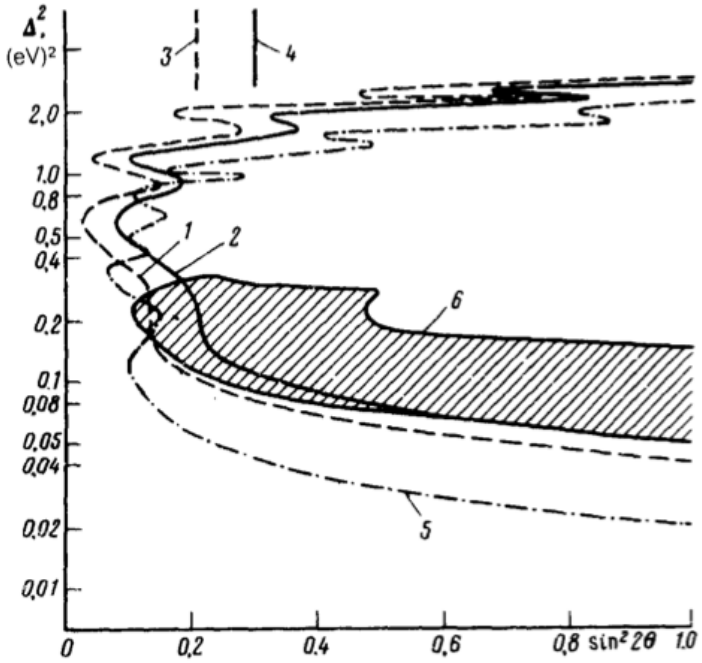

Figure 3.5: Sensitivity contours of early reactor $\overline{\nu}_e$ experiments to oscillation parameters $\sin^2 2\theta$ and Δm^2: 1) Rovno [54], 68% CL; 2) Same, 90% CL; 1) Rovno [53], 68% CL; 2) Same, 90% CL; 5) Goesgen, 90% CL; 6) Bugey, 90% CL. The suggested parameter space of Bugey is almost completely ruled out by both Goesgen and Rovno. 3) and 4) Demonstrate the parameter space exclusion from a rough absolute comparison of detected and expected flux at a single baseline.

The constraint placed on oscillation parameters by these short-baseline experiments is best represented on a two-dimensional plot of Δm^2 versus $\sin^2 2\theta$, as shown in Figure 3.5. On this plot one can see contours defining the regions of this pa-

rameter space excluded by the experimental results to varying degrees of confidence (68% and 90% for two separate Rovno incarnations, 90% for Goesgen, and 90% for Bugey). The regions to the right of the curves are excluded, while the regions to the left remain untested space where oscillation could occur. In the case of Bugey, which reported a non-null oscillation result, the shaded region represents the suggested parameter space for Δm^2 and $\sin^2 2\theta$. This result is clearly at odds with all Rovno and Goesgen measurements, suggesting the possibility of systematics problems with the Bugey result. Bugey would re-test these regions of parameter space with a subsequent experiment, which will be discussed in the following sections.

3.2 The Move to Longer Baselines

In the 1990s, the search for oscillation of reactor $\overline{\nu}_e$ was redirected to a different region of Δm^2 parameter space by hints of neutrino oscillations in atmospheric ν experiments. Only recently has the original short-baseline region of high Δm^2 received renewed interest from theorists and experimentalists; this renewed investigation is discussed further in the Appendix.

Nucleon Decay Experiments and Atmospheric Oscillations

During the 1980s and early 1990s, hints of neutrino oscillations began to emerge from experiments built to search for proton decay as tests of baryon number conservation. These detectors, Kamiokande-II [20] and IMB [67], were kiloton-scale lined underground caverns filled with highly purified water and instrumented with thousands of photomultiplier tubes to detect Čerenkov light from high-energy particles travelling in the detector. In searching for a high-energy proton decay signal 938 MeV, experiments needed to understand and properly subtract backgrounds from interac-

tions of high-energy neutrinos created in the atmosphere by cosmic ray interactions. Atmospheric neutrinos are created in the following interaction:

$$\pi^+ \rightarrow \nu_\mu + \overline{\nu}_\mu + \nu_e + e^+ \quad \text{or} \quad \pi^- \rightarrow \nu_\mu + \overline{\nu}_\mu + \overline{\nu}_e + e^-. \tag{3.2}$$

Given that these neutrinos are created in the atmosphere all around the Earth by fairly well-known mechanisms, their production and propagation could be simulated to yield a prediction of zenith-angle dependence for each neutrino type. In addition, the expected ratio between muon- and electron-type neutrinos could be simulated, and, based on the above interaction, was expected to be close to 2. After performing such simulations, IMB in 1986 and Kamiokande in 1988, reported anomalously low numbers of detected muon-like neutrinos. Kamiokande-II followed this with further evidence in 1992, showing an unexpected deficit of muon-type to electron-type neutrinos showing a significant zenith-angle dependence. Using this result, Kamiokande-II suggested a region of best-fit oscillation parameter space in the vicinity of 10^-2 eV^2. A summary of the results from these early atmospheric neutrino experiments are shown in Table 3.2.

While somewhat at odds with later atmospheric muon-type to electron-type results from IMB [78] and other iron spectrometer proton decay detectors, Frejus and NUSEX [79, 68, 69], this hint, along with a hint from the MACRO collaboration [73], were enough to attract the attention of reactor neutrino experimentalists across the globe: disappearing atmospheric muon-type neutrinos could be oscillating into electron-type neutrinos, opening up a possible suggested Δm^2 for reactor $\overline{\nu}_e \rightarrow \overline{\nu}_\mu$ oscillations. The SuperK experiment [76, 77] would later unequivocally demonstrate a non-zero oscillation result, and will be discussed later. In addition, the Soudan-2 experiment would present as early as 1997 the first measured muon neutrino deficit in an iron spectrometer detector [74].

Experiment	Year	Muon $\frac{Obs}{Exp}$	Additions	Δm^2 (eV^2)	References
IMB	1986	0.76±0.09	-	NR	[67]
Kamiokande-II	1988	0.59±0.07	-	NR	[20]
Frejus	1990	0.94±0.22	-	No Osc.	[68]
NUSEX	1991	0.88±0.2	-	No Osc.	[69]
Kamiokande-II	1992,94,98	0.57±0.07	Zenith-angle	$2\times10^{-}2$	[70, 71, 72]
MACRO	1995	0.73±0.16	-	NR	[73]
Soudan-2	1997,99	0.64±0.12	-	NR	[74, 75]
Super-Kamiokande	1998-present	0.65±0.05	Full L/E	$2\times10^{-}3$	[76, 77]

Table 3.2: Chronology and overview of early atmospheric neutrino experiments. The horizontal line indicates the separation between those atmospheric experiments that influenced some the reactor experiments discussed in this chapter (top), and SuperK and Soudan-2, whose findings greatly influenced the current reactor neutrino experiments like Daya Bay. Also listed are reported muon deficits with respect to Monte Carlo simulations, and best fit Δm^2 (eV^2), if reported. If not reported, NR is listed. Note only publications and oscillation results from the 1980s and 1990s are historically relevant here, and thus are included.

Intermediate Baselines: Bugey and Krasnoyarsk

If one took this hint at a smaller Δm^2 on the order of 10^{-2} eV^2 as a guide, a reactor experiments' oscillation maximum would be located at a baseline of approximately 500 m. A few experiments designed slightly before or around the time of the appearance and solidifying of this hint were able to utilize the presence of multiple reactors in their vicinity to probe oscillations at higher baselines.

The Krasnoyarsk experiment from Russia utilized one detector at a distances of 57 m and 57.6 m, and 231 m from three separate nuclear reactors [56]. The detector design was similar to the ILL and Goesgen detector, with higher efficiency and large volume. As the various reactors were turned on and off, the experiment would sample the resultant change in flux. By creating a system of equations describing the expected flux for each of the various reactor on-off configurations, a measured rate from each of the three reactors could be effectively measured and compared to prediction. By doing this, Krasnoyarsk was able to utilize the far baseline, albeit with limited statistical

precision, to probe smaller values of Δm^2 than were accessible at any of the previously mentioned reactor experiments. It also saw no evidence for neutrino oscillations based on the comparison of event rates and spectra for different reactor on-off configurations.

A new incarnation of the Bugey experiment also was able to test oscillations at baselines as long as 95 m [28]. One near detector was placed underneath a reactor at a distance of 15 m, and two were placed at a distance of 40 m from the reactor. When the primary reactor was turned off, the detectors would sample neutrinos from a further adjacent reactor, providing the longer desired baselines. All detectors were identical, and utilized a segmented design, with 98 optically separated compartments within a 600-liter cube of Lithium-doped liquid scintillator. The delayed signal of inverse beta decay coincidences were formed by neutron capture on Lithium, which created an α particle and a compact energy deposition with unique timing characteristics amenable to pulse shape discrimination. Heavy particles, such as alphas and protons, interacting with the scintillator caused creation of scintillation light over a broader time range than for light particles like positrons and electrons. In this way, prompt-delayed time coincidence could be used in tandem with the ability to discriminate the IBD-signature positron and alpha from other backgrounds. With the larger target mass and higher neutron detection efficiency achieved in this detector design, Bugey generated higher neutrino statistics than any previous reactor $\overline{\nu}_e$ experiment. In addition, multiple detectors were deployed at different baselines to take reactor data simultaneously, removing some reactor-related uncertainties involving fuel burn-up over time.

Low statistical uncertainty, lower reactor and detector systematics from their site-to-site comparison, and wider variations in baseline allowed Bugey to examine a large region of oscillation parameter space. A reproduction of the relative near-far neutrino energy spectral ratios from the 15 m, 40 m, and 95 m baseline datasets can be seen

in Figure 3.6. As the event ratio between sites followed the square of the ratios of the baselines at all energies, within the bounds of the statistical and systematic uncertainties, the no-oscillation hypothesis was once again confirmed.

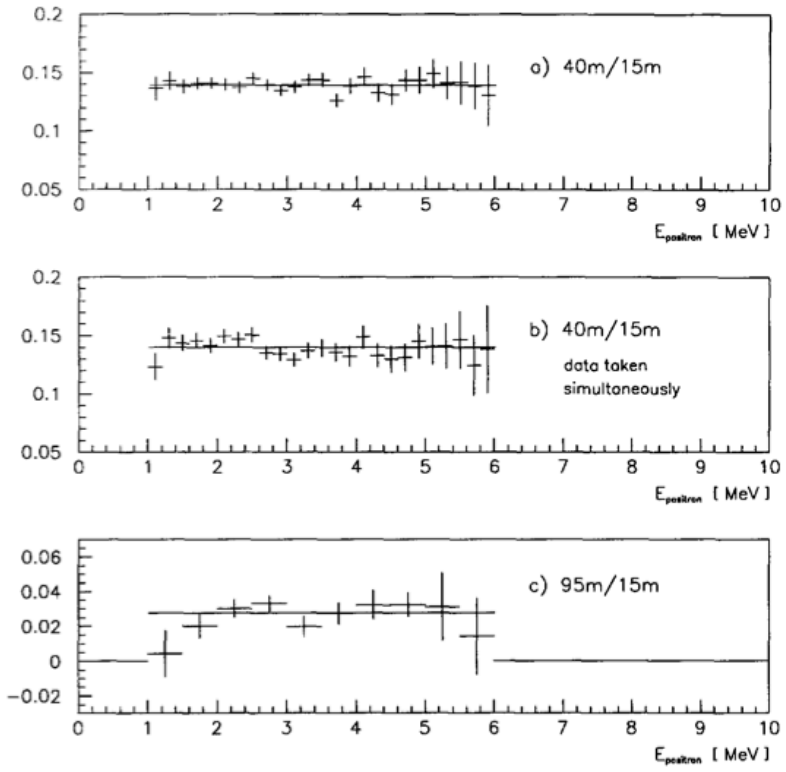

Figure 3.6: Ratios of measured positron spectra between detectors at the three Bugey baselines. a) 15/40 ratio follows the expected value of $(15/40)^2 = 0.14$. b) 15/40 ratio from data taken simultaneously at both sites. c) 15/90 ratio follows the expected value of $(15/90)^2 = 0.028$. Figure from [52].

The regions of parameter space ruled out by these short-baseline reactor $\overline{\nu}_e$ experiments can be seen in Figure 3.7. After a decade and a half of detection by experiments at five different nuclear reactor stations making successively more sensitive measurements with improved detection and measurement techniques, no consistent evidence was uncovered to support the existence of reactor $\overline{\nu}_e$ oscillations at very short baselines.

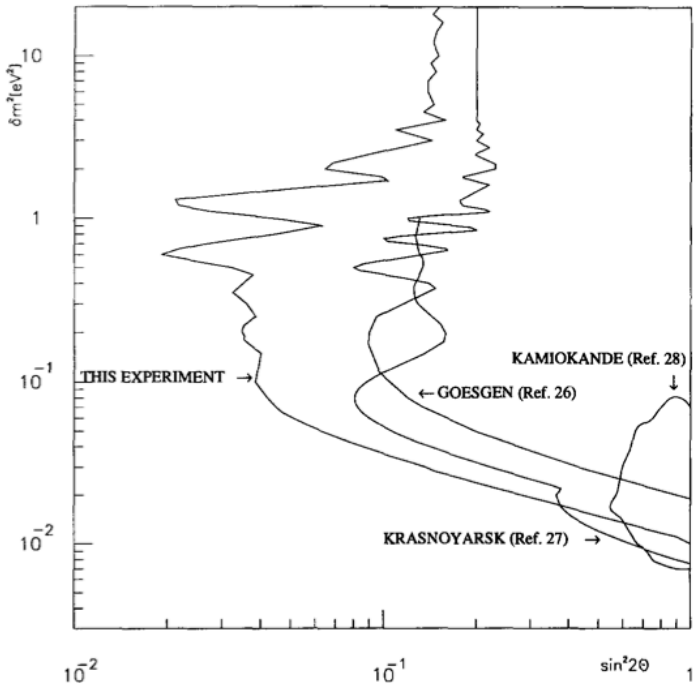

Figure 3.7: The area to the right of the curves is the neutrino oscillation parameter space ruled out at 90% CL by short-baseline reactor $\overline{\nu}_e$ experiments. 'This Experiment' refers to the Bugey experiment, from which this Figure is reproduced [52]. The 'Kamiokande' region represents the parameter space hinted at by the Kamiokande collaboration, as discussed in the previous section.

Designing for the Atmospheric Oscillation Length: Chooz and Palo Verde

With hints for non-zero neutrino mixing at Δm^2 of $2{\times}10^{-2}$ at Kamiokande, new reactor $\overline{\nu}_e$ experiments proposed in the mid-1990's aimed to tailor their sensitivity specifically to smaller mass-squared differences by building detectors at farther baselines than previous reactor experiments. The atmospheric experiments showed evidence of $\nu_\mu \rightarrow \nu_x$ oscillations with a large value of θ_{23}. If these ν_μ oscillated to ν_e, a large $\overline{\nu}_e \rightarrow \overline{\nu}_\mu$ component, and thus a large deficit at a km-scale baseline, could be expected. However, if ν_μ oscillated largely into ν_τ, any leftover $\overline{\nu}_e \rightarrow \overline{\nu}_\mu$ component would be quite small. Given the long baselines and possibility of a small

disappearance signal, design of larger, more precise detectors for $\overline{\nu}_e$ experiments was necessary.

Chooz

The Chooz experiment was done at the Chooz power station in the Ardennes region of France; this station contained two PWR reactors with a total output of 8.5 GW thermal power. A detector was placed at a baseline of 1 km in an underground cavern beneath a hill providing 300 meters water equivalent (mwe) overburden to reduce muon-related backgrounds. A mechanical drawing of the detector can be seen in Figure 3.8. The detector was composed of a 5 ton target region of Gadolinium-doped scintillator, surrounded by a 17-ton scintillating region equipped with 192 PMTs facing the central target region. For reference, the ILL experiment's target, at 0.3 tons, was 6% the size of Chooz's target region. These two regions were located inside a 90-ton muon veto region isolated optically from the central regions and filled with water and 48 muon veto PMTs.

$\overline{\nu}_e$ interactions taking place in or near the target region would deposit a prompt energy signal from the positron thermalization and annihilation and then a delayed energy signal approximately 20 μs later from the thermalized neutron capture on Gd. The position of the signals were roughly reconstructed by analyzing the hit pattern of scintillation light emitted isotropically when the positron and neutron interact and deposit their energy. These signals were detected in time coincidence, which greatly reduced the background of the measurement. Background was further reduced by making cuts on the coincidence of reconstructed position in the delayed and prompt signals. After signal selection cuts, the efficiency of this detection method was 70%, with an energy resolution of $12\%/\sqrt{E}$. This detection efficiency was nearly 60% higher than the ILL detector, and about twice as efficient as later detectors like

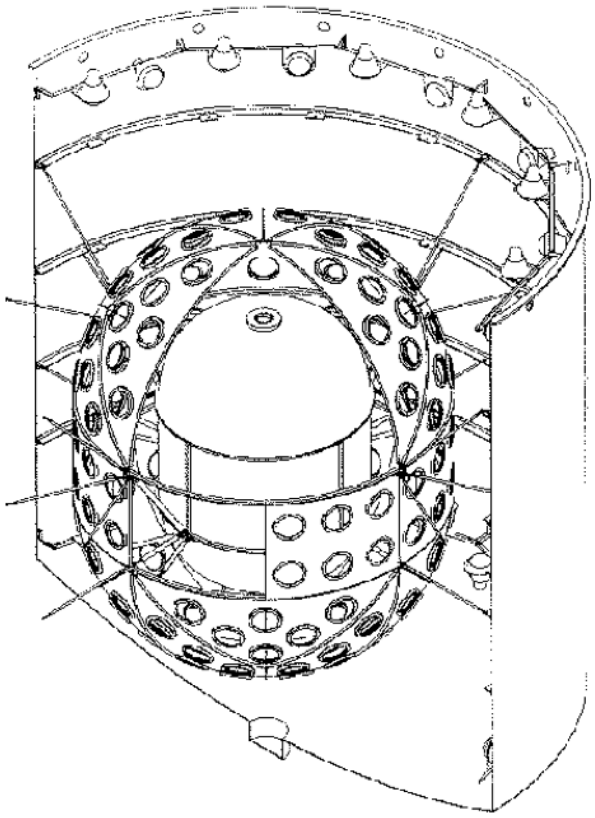

Figure 3.8: Mechanical drawing of the Chooz detector. Pictured are the inner target region, the intermediate region containing the target PMTs, and the outer veto region. From [22].

Karsnoyarsk. By utilizing a larger target, a more powerful reactor complex, and high detection efficiency, Chooz was able to overcome the lowered statistics from a longer baseline while still maintaining excellent energy response and resolution.

The Chooz detector made an absolute measurement of the reactor $\overline{\nu}_e$ spectrum and rate with one detector. In a method similar to that done in the ILL analysis and one of the Goesgen analyses, the experiment compared the observed event rate to that expected based on knowledge of detector size and energy response, reactor power levels, fuel composition, and corresponding reactor $\overline{\nu}_e$ spectral shape. The experiment also began taking data during a reactor-off period, giving it a well-measured

background spectrum to subtract from the reactor-on period. In its analysis, the collaboration did not see any evidence of a rate deficit or spectral distortion above the experimental uncertainties. Unfortunately, the collaboration collected only 200 days of usable data because of a problem with the scintillator in their target region: over time, the clarity of the scintillator was degraded, causing an exponential loss of scintillation light yield with a decay constant of 720 days. This corresponded to a 35% light yield loss over the life of the experiment. Despite this problem, the statistical uncertainty of the measurement was matched by experimental systematics; the error budget for the oscillation analysis is given in Table 3.3. Because it utilized an absolute measurement, systematics were dominated by the uncertainty in the $\overline{\nu}_e$ spectrum normalization from the 1980's ILL beta measurements and by the uncertainty in the detection efficiency.

Parameter	Uncertainty (%)
$\overline{\nu}_e$ spectrum normalization	1.9
Number of protons	0.8
Detection efficiency	1.5
Reactor power	0.7
Energy released per fission	0.6
Total Systematic	2.7
Total Statistical	2.8

Table 3.3: Overview of uncertainties for the Chooz experiment. Statistical and systematic uncertainties were of similar magnitude. Systematics were largely limited by the knowledge of the reactor $\overline{\nu}_e$ flux and spectrum. Values from [22].

With this relatively low error budget compared to previous experiments and the new longer baseline, Chooz was able to exclude large new regions of oscillation parameter space [22, 57, 58]. The regions of allowed parameter space after Chooz can be seen in Figure 3.9. One can clearly see that the increased baseline allowed Chooz to probe vast new expanses of parameter space. In particular, one can see the disagreement in result between the excluded Chooz parameter space and the suggested

Kamiokande parameter space, which provided strong evidence that atmospheric ν_μ were oscillating principally into ν_τ rather than ν_e.

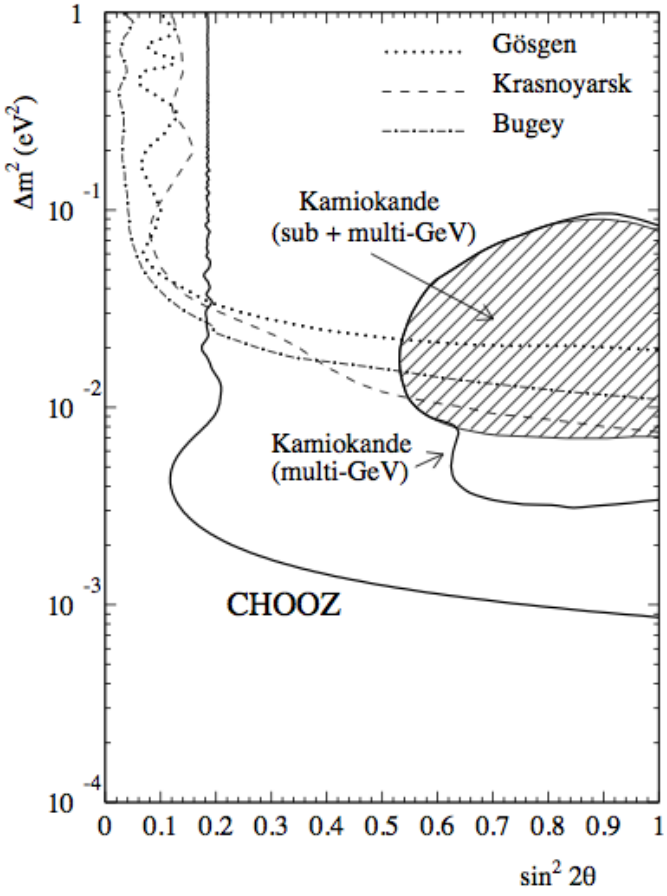

Figure 3.9: The area to the right of the curves is the neutrino oscillation parameter space ruled out at 90% CL by short-baseline reactor $\overline{\nu}_e$ experiments. One can clearly see that the increased baseline allowed Chooz to probe vast new expanses of parameter space. In particular, one can see the disagreement in result between the excluded Chooz parameter space and the suggested Kamiokande parameter space, which provided strong evidence that atmospheric ν_μ were oscillating principally into ν_τ rather than ν_e.

Palo Verde

A larger, longer-baseline reactor $\overline{\nu}_e$ experiment was also done at the Palo Verde 11.6 GW nuclear reactor complex in Arizona [23]. This detector utilized a segmented

design similar to that employed in the Bugey experiment, but on a much larger scale: Palo Verde's detector contained 11 tons of Gd-doped liquid scintillator, while Bugey's detectors each contained only ∼0.5 tons of Li-doped scintillator. As a result of greater background reduction from the segmented design, the detector was built with only 32 mwe overburden. However, the $\overline{\nu}_e$ detection efficiency of the Palo Verde detector was markedly lower than Chooz's, around 10%. Palo Verde also saw no evidence for spectral distortion or a rate deficit, allowing it to rule out a similar region of oscillation parameter space as Chooz.

Summary of Experimental Results and Techniques

Two decades of reactor neutrino measurements have used a wealth of fascinating and diverse reactor sampling and background reduction methods to detect inverse beta decay and arrive at the same general oscillation result: namely, that many neutrinos are created by reactors, but very few of them, if any, appear to be disappearing. The various background reduction and reactor sampling techniques are summarized in Table 3.4, along with the experiments utilizing that particular method.

Using these various methods, these experiments have achieved a wide range of systematic uncertainty and statistical precision. These experimental uncertainties are summarized for each experiment in Table 3.5, along with each detector's detection efficiency.

Clearly, inspired neutrino physicists wishing to construct a new neutrino detector have many possible tools at their disposal. The Daya Bay experiment, which is the main subject of this thesis, utilizes a number of these techniques, including significant overburden, a high-energy delayed signal for background reduction, time coincidence, and simultaneous reactor sampling with multiple identical detectors. An optimal combination of these techniques will allow for excellent background and systematics

Category	Technique	Experiments
Background Reduction	Prompt-Delayed Time Coincidence	IL, GO, RV, BG1, BG2, PV, CZ
	Significant Overburden	all, but especially CZ
	Detector Segmentation	IL, GO, RV, BG1, BG2, KY, PV
	High-Energy Delayed Signal	RV, CZ, PV
	Pulse-Shape Discrimination	ILL, GO, BG1, BG2
	Cosmogenic Veto Systems	All
Reactor Sampling	Single-Detector: Absolute	ILL, CZ, PV
	Multiple Baselines	GO, RV, BG1, KY, BG2
	Multiple Identical Detectors	RV, BG1, BG2
	Simultaneous Sampling Detectors	RV, BG1, BG2

Table 3.4: An overview of background reduction and reactor sampling techniques and the experiments using each technique. The experiment abbreviations are as follows: ILL - Institut-Laue-Langevin; GO - Goesgen; BG1 - Bugey, 1980s; BG2 - Bugey, 1990s; RV - Rovno; KY - Krasnoyarsk; CZ - Chooz; PV - Palo Verde.

Experiment	Systematic Unc. (%)		Statistical Unc. (%)	Det. Efficiency. (%)
	Absolute	Relative		
ILL	3.5	-	11	<5
Goesgen [51]	6.0	1.5	1.9; 1.9; 3.6	17
Bugey: 1980s [80]	6.9	2.8	1.4	4.6
Rovno [54]	6.8	4.7	0.3	40
Krasnoyarsk [56]	5.0	2.0	1.0, 15	30
Bugey: 1990s [28]	5.0	2.0	0.4, 1.0, 13	49
Chooz [22]	2.8	-	2.7	70
Palo Verde [23]	5.3	-	2.4	11

Table 3.5: An overview of the ultimate systematic and statistical uncertainties achieved by each short-baseline reactor antineutrino experiment. For some experiments, multiple values are given for each individual detector or baseline. In these cases, statistical uncertainties are quoted in order from lowest to highest baseline. Overall detection efficiencies are additionally provided for comparison.

reduction in the search for ever-greater sensitivity to short-baseline reactor neutrino oscillations.

3.3 Honing the Search For θ_{13}

After two decades of mostly null results, the search for short-baseline reactor neutrino oscillations was brought into sharp focus by a number of new experiments in the late 1990s and 2000s. These experiments clearly spelled out the oscillation picture for atmospheric neutrinos, identifying precise values for the atmospheric mixing parameters Δm^2_{32} and $\sin^2 2\theta_{13}$. With these values firmly cemented through tests from multiple independent experiments, a clear picture of short-baseline reactor neutrino oscillations was presented based on the unmeasured mixing parameter $\sin^2 2\theta_{13}$.

Super Kamiokande and Atmospheric Neutrino Oscillations

Hints of atmospheric neutrino oscillations were further investigated with an upgrade of the Kamiokande detector in the late 1990s into what was called the Super-Kamiokande (Super-K) detector. The upgraded detector consisted of a 50 kiloton cylindrical water tank, separated into two regions by a steel framework close to the edge of the tank. The inner region was lined with 11,000 inward-facing PMTs for detecting Cherenkov radiation from energy depositions between 4.5 MeV to over 1 TeV. The pattern of Čerenkov radiation from ν interaction products could be analyzed to reconstruct the positions, energies, and trajectories of ν passing through the detector. The outer region consisted of ∼1900 outward-facing PMTs used as a background veto system for events taking place in the inner region [81]. This improved setup and additional outer veto system allowed for greatly improved response over a broad range of energies.

In this newly upgraded detector, ν_μ/ν_e ratios were once again measured to be anomalously low, while excesses of ν_e were not observed [76], indicating

$$P(\nu_e \to \nu_e) \sim 1 \quad \text{and} \quad P(\nu_\mu \to \nu_e \sim 0). \tag{3.3}$$

Given the parametrization in equation 2.25, and this result of likely transition of ν_μ to ν_τ, the atmospheric oscillations appeared to be a result of oscillation between the third and second mass states. Oscillation parameters could be precisely probed by using the detector's excellent directional reconstruction to construct precise zenith-angle distributions of the neutrino flux at various energies and checking them against Monte Carlo predictions [77]. Δm^2_{32} would be indicated for each energy range by looking for the zenith angles, and hence baselines, at which ν_μ deficits were occurring. The best fit Δm^2 was found to be 2×10^-3, roughly an order of magnitude lower than that suggested by Kamiokande. The value $\sin^2 2\theta_{23}$ was indicated to be maximal by the amplitude of the ν_μ deficit. This result gave SuperK the first strong evidence for the existence of neutrino oscillations, and thus non-zero neutrino mass.

Accelerator ν Experiments

The K2K and MINOS experiments are long-baseline accelerator experiments built to confirm the atmospheric oscillation parameters reported by the Super-K collaboration [25, 26]. These experiments created high-energy beams of ν_μ and tuned their baselines such that the atmospheric Δm^2_{32} oscillation maximum coincided with the peak of the ν_μ beam's energy spectrum; by doing this, the statistical uncertainty of the oscillation signature was minimized. The resulting experiments produced 0.5-30 GeV ν_μ that were detected and near sites and at far distances of 250 km or 735 km for K2K and MINOS, respectively, giving the proper L/E for observation of atmospheric oscillations. The experiments detected ν_μ interactions by looking for signatures of muons created by the charged current interaction:

$$\nu_\mu + n \rightarrow \mu + p. \tag{3.4}$$

These experiments were able to make better measurements of Δm^2_{32} than Super-K

because they were able to precisely observe the spectral distortion of the expected ν_μ energy spectrum. Such a distortion measured at MINOS is visible in Figure 3.10; at some energies, there is good agreement between the expected and detected event number, while at others there is a deficit of observed events. Given the 735 km baseline and the energy of the largest observed event deficit, the frequency of oscillation and value for Δm^2_{23} can be precisely determined. The value of the mixing parameter θ_{23} can be taken from the magnitude of the observed spectral distortion.

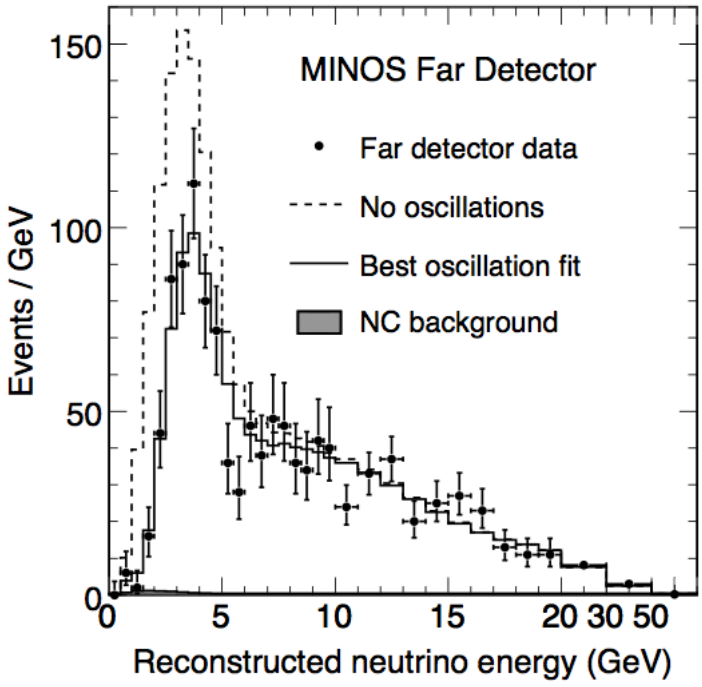

Figure 3.10: Evidence of spectral distortion in the MINOS experiment due to neutrino oscillations [25]. The expected ν_μ energy spectrum without oscillations is pictured along with the observed reconstructed energy spectrum and the best fit to the data including neutrino oscillations.

The currently allowed parameter space from all atmospheric and accelerator experiments is shown in Figure 3.11; the central value for Δm_{32} is located at 2.4×10^{-3} eV^2, while the best-fit value for $\sin^2 2\theta_{13}$ is maximal. Given the energy of reactor neutrinos, this value of Δm_{32} calls for a baseline of roughly 2 km to achieve the proper L/E to

observe oscillations.

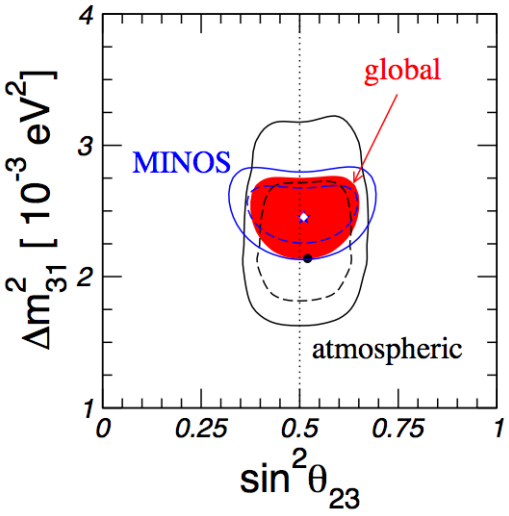

Figure 3.11: Confidence regions for atmospheric oscillation parameters. Dotted lines are 90% CL and solid are 99.73% CL. The red region is 99.73% CL for the global analysis. The dot, star and diamond are the best fit for atmospheric, MINOS, and global data, respectively. From [40].

In addition to looking for ν_μ disappearance by identifying muon-like events, K2K and MINOS could also search for ν_e appearance in the beam by identifying electron-like events [82, 83]. No positive identification of ν_e appearance was seen in the detectors, supporting the evidence from Super-K and reactor experiments that the ν_μ must be oscillating mostly to ν_τ. In addition, the lack of ν_μ to ν_e oscillation also constrained the value of $\sin^2 2\theta_{13}$ in the PMNS mixing formulation. Along with the Chooz and Palo Verde results, which showed a lack of the CPT-conjugate oscillation $\overline{\nu_e}$ to $\overline{\nu_\mu}$ in the same L/E region, this result pointed to a relatively small (<0.1) or possibly zero value of $\sin^2 2\theta_{13}$

The result of oscillations between neutrinos and antineutrinos could only be assumed to be equal with the additional assumption that CP- and CPT-violating effects are minimal. Given that Chooz, Palo Verde, MINOS, and K2K measured such small

values of θ_{13}, which closely accompanies the CP-violating phase δ, as shown in the PMNS matrix (see Equation 2.25), this assumption appears to be well-founded.

Current Limits and Hints at Non-Zero θ_{13}

The parameter space for θ_{13} oscillations, as a result of the many experiments described in this chapter, has been narrowed to a select range of θ_{13} and Δm^2_{31} values, which can be see in Figure 3.12. The main limiter of parameter space in the θ_{13} direction in this figure is the Chooz $\overline{\nu}_e \rightarrow \overline{\nu}_e$ limits, while the Δm^2_{13} space is limited mainly by a combination of atmospheric and accelerator experiment results.

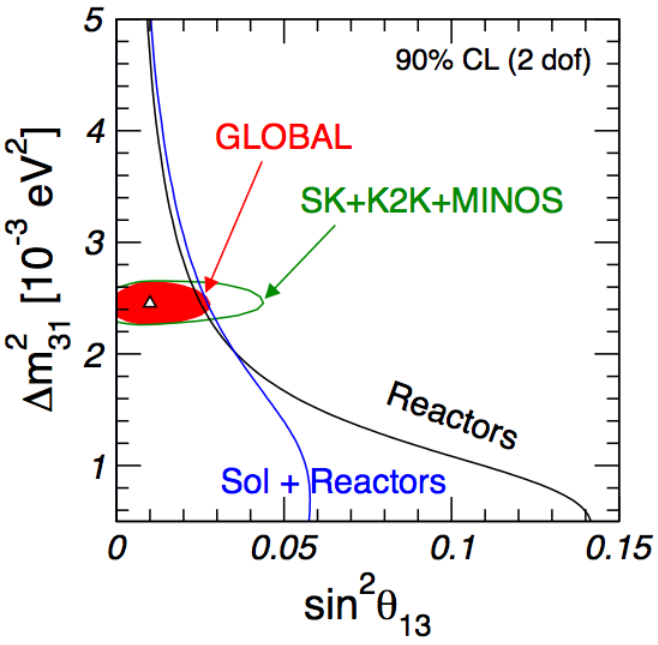

Figure 3.12: 90% CL constraints on θ_{13} from various sources. Chooz provides the strongest constraint on the mixing angle, while atmospheric and accelerator experiments highly constrain the mass difference. From [40].

Recently, new experimental results and global fits of oscillation data have strongly hinted at the existence of a nonzero value of θ_{13}, with best-fit values for $\sin^2 2\theta_{13}$ in the vicinity of 0.08.

The first set of hints comes from the difference in the best fit values for θ_{12} and Δm^2_{12}, the solar mixing parameters, between solar neutrino detection experiments and the results of KamLAND, a recent long baseline reactor $\overline{\nu}_e$ experiment [40, 84, 85, 86]. Both the solar experiments and reactor experiment KamLAND [24] look for mixing at a much smaller Δm^2 of 10^{-5} eV^2. Solar experiments attain the necessary large L/E by observing oscillations of neutrinos coming from the sun, while KamLAND attains a high L/E by looking at reactor neutrinos at distances of hundreds of kilometers, rather than a km or less for the previous discussed reactor experiments. The two experiment types' allowed regions of parameter space overlap, but their best fit points are offset from one another. While both experiments are sensitive to the same solar mixing parameters, the two experiment types have small but different dependences on θ_{13}: if the value of θ_{13} is increased the allowed regions and best fit points shift with respect to one another. The best fit points are aligned for a non-zero value of θ_{13}. While this result is not significant to more than 2σ, it is a hint nonetheless.

The most direct hints are recent results from both reactor and accelerator experiments. The T2K experiment, a long-baseline ν_e appearance experiment, observed 6 clean ν_e events above an expected background of 1.5 events, an excess of 2.5σ, before a large earthquake forced shutdown of the experiment [87]. In addition, the MINOS experiment also observed a slight excess of ν_e events above background, repeating its previous reported result with higher statistics [88]. A combined analysis, given in [84], shown in Figure 3.13, indicates a non-zero value of θ_{13} at 3σ confidence level. Note that this result is true for both mass hierarchies, which both experiments are somewhat affected by because of significant Earth-matter effects from the long baselines.

An additional tantalizing hint comes from the Double Chooz experiment, whose experimental design will be discussed in more detail in the following chapter. With

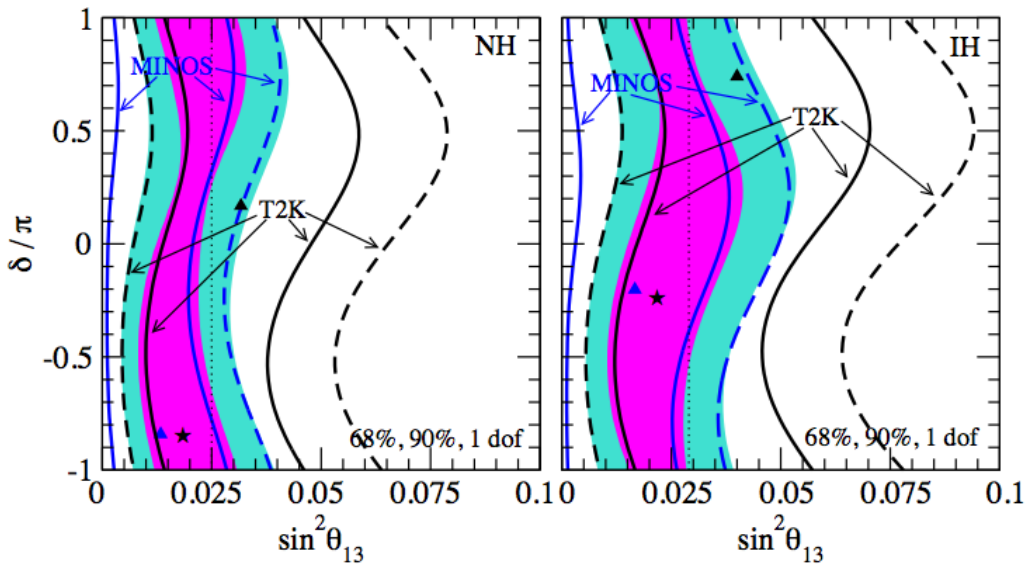

Figure 3.13: Allowed parameter space from a combined analysis for of the most recent T2K and MINOS ν_e appearance results.

one-half year of data from one 10 ton detector at the location of the original Chooz experiment, the collaboration reports a 5% deficit in measured events below the predicted rate [89]. The experiment claims an absolute systematic uncertainty of 2.75% and statistical uncertainty of 3.75%, leading to a 94.5% CL exclusion of the θ_{13}=0 hypothesis, and a $sin^2 2\theta_{13}$ value of 0.08.

All of these enticing results underscore the urgency and excitement about prospects for an unequivocal, high-significance θ_{13} measurement. The Daya Bay experiment will make this high-significance measurement in a short timescale by detecting relative disappearance of reactor neutrinos at its operational near and far sites. In the long-term, the Daya Bay experiment's setup will also allow it to make the most sensitive measurement of θ_{13}.

Neutrino Mixing Models and Predictions of θ_{13}

Since Georgi and Glashow in 1974, theorists have attempted to develop a single grand unified theory that describes all particle properties and interactions [90]. In particular, these theories attempt to unify the strong, weak, and electromagnetic forces, and predict the masses and interactions of all standard model particles. As the evidence for massive neutrinos and neutrino oscillations have developed and solidified, many models have been developed to predict neutrino masses and mixings. Many of the simplest GUTs, such as the SU(5) symmetry group discussed by Georgi and Glashow, are unable to properly incorporate massive neutrinos, while others, such as SO(10) [91, 92], remain relevant even with increased experimental constraints.

In addition to these types of first-principles predictions, theorists also utilize a bottom-up approach, using the results of mixing experiments to serve as a guide to suggesting particular lepton flavor symmetries. One such formulation that has received significant attention is tri-bimaximal mixing [93]. This model follows the result of atmospheric and accelerator experiments, which showed $\sin^2\theta_{23} \sim 0.5$ and $\sin^2\theta_{13} \sim 0$, and solar experiments, which showed $\sin^2\theta_{13} \sim 0.333$. Such a prediction leads to a highly symmetric mixing matrix with $\mu - \tau$ symmetry:

$$M_{PMNS} = \begin{pmatrix} \frac{2}{3} & \frac{1}{3} & 0 \\ \frac{1}{6} & \frac{1}{3} & \frac{1}{2} \\ \frac{1}{6} & \frac{1}{3} & \frac{1}{2} \end{pmatrix} \tag{3.5}$$

Various tri-bimaximal lepton flavor models and related permutations predict very small values (<0.01) for $\sin^2 2\theta_{13}$.

Neutrino mass and mixing models fitting the requirements defined by the known neutrino mixing parameters presented in Table 2.2 are overviewed in [94], providing predicted values of θ_{13} for each model. Of these 86 models, two-thirds predict values of $\sin^2 2\theta_{13}$ between 0.01 and 0.2, while the remainder are zero or nearly zero and

beyond the range of the Daya Bay experiment to detect. In addition, a quarter have $\sin^2 2\theta_{13}$ at large values of >0.1 [95].

It is clear that regardless of its outcome, the Daya Bay experiment will have significant power to constrain possible neutrino mass and mixing models. A null result at Daya Bay will rule out two-thirds of existing models, while a large θ_{13} measurement will narrow down the possible candidates even further.

Chapter 4

Daya Bay Experiment

The Daya Bay Experiment is being built to make a precision measurement of θ_{13} by measuring relative differences in $\overline{\nu}_e$ flux between identical detectors at two different baselines [96]. By doing a relative rather than an absolute measurement, most correlated reactor and detector systematics are cancelled; the remaining uncertainties are those uncorrelated between detectors and reactors. In order to achieve the experiment's desired sensitivity, the Daya Bay $\overline{\nu}_e$ detectors must have well-understood uncorrelated detector systematics well below 1%. An unequivocal measurement of θ_{13} benefits greatly from a relative measurement: the largest systematics related to the reactor $\overline{\nu}_e$ flux and absolute detection efficiency are cancelled, allowing a comparatively simple low-systematics measurement.

4.1 Experimental Overview

The Daya Bay Reactor Antineutrino Experiment, heretofore referred to as Daya Bay, is a short-baseline neutrino oscillation experiment being built at the Daya Bay nuclear power complex in Shenzhen, China. Currently, three pairs of Pressurized Water

Reactor (PWR) cores, named Daya Bay, Ling Ao I and Ling Ao II, generate 17.4 GW of thermal power using conventional PWR low-enriched uranium fuel. Eight antineutrino detectors will be situated at three experimental halls (EHs), two near the Daya Bay cores, two near the Ling Ao and Ling Ao II sites, and four at a far distance from all three sites. All eight detectors are designed to be functionally identical to allow maximal cancellation of detectors systematics. At least 2 detectors are deployed at each site to allow for high-statistics comparisons of detector response between ADs and to demonstrate understanding of detector systematics.

Hundreds of meters water equivalent (mwe) overburden for reducing backgrounds related to cosmic ray muons are provided by mountains bordering the generating station. Table 4.1 provides more specific site information including baselines, overburdens, backgrounds, and expected event rates at each underground detector site. A map of the experimental site can be viewed in Figure 4.1. Because of the experiment's layout and short baselines, the high $\overline{\nu}_e$ flux from the reactors, the large target volume, and high detection efficiency, the Daya Bay experiment's $\overline{\nu}_e$ detection rate will be higher than that of any previous experiment's.

Detector Site	DB Near	LA Near	Far Hall
Baseline (m)	363	481 from Ling Ao 526 from Ling Ao II	1985 from Daya Bay 1615 from Ling Ao
$\overline{\nu}_e$ rate (evts/day)	840	740	90
Overburden (m)	98	112	350
Muon rate (Hz)	36	22	1.2
Accidental Bkg/Signal (%)	<0.2	<0.2	<0.1
Fast Neutron Bkg/Signal (%)	0.1	0.1	0.1
^{8}He+^{9}Li Bkg/Signal (%)	0.3	0.2	0.2

Table 4.1: A summary of detector baselines, overburdens, and expected signal, and background rates. 'DB' is the near hall in the vicinity of the two Daya Bay reactor cores, also called EH1, while 'LA', also called EH2, is the near hall in the vicinity of the four Ling Ao reactor cores. From [96].

The detectors at each detector site will be surrounded by a light water pool,

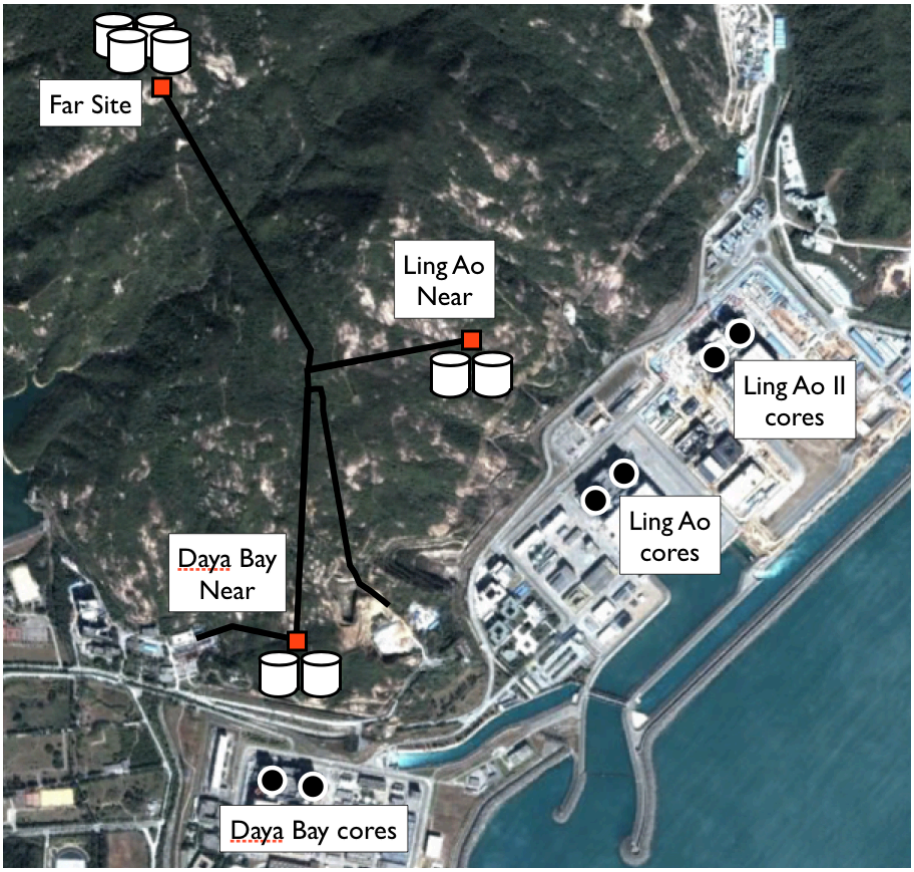

Figure 4.1: A diagram of the Daya Bay experimental site. The three experimental halls and three reactor sites are pictured. Event and background rates given in this table are expected values based on calculations and Monte Carlo simulations. They include expected neutron detection efficiencies. From [96].

which provides at least 2.5 meters of shielding from natural radioactivity in the rock surrounding the pool. In addition, the pool serves as a water Cherenkov detector for studying and vetoing cosmogenic backgrounds. By combining this system with an RPC muon veto system on the surface of the tank, muon tagging efficiency will be better than 99.5%, reducing muon-related backgrounds to less than 1%, as can be seen in Table 4.1.

Using the near-far detector arrangement provided by the three experimental halls of the full experiment, the Daya Bay experiment will be able to perform a high-

precision oscillation measurement. $\overline{\nu}_e$ created by decaying fission products of U and Pu isotopes, whose compositions are shown in Figure 3.4, will radiate from the cores isotropically, with $\overline{\nu}_e$ flux decreasing as $1/r^2$. An expected $\overline{\nu}_e$ flux obtained from a measurement at the near site can be compared with the number of detected neutrinos at the far site. $\overline{\nu}_e$ oscillation would manifest itself in a negative difference greater than the statistical and systematic uncertainties of the experiment.

4.2 Antineutrino Detection

The Daya Bay antineutrino detectors (ADs), pictured in Figure 4.2 are three-region cylinders 5 m in diameter and height. This shape was chosen for its ease of transport and construction: the large size still allows for assembly at the surface and transport through the construction tunnels. The innermost region, called the target, is a 20-ton cylinder of 0.1%-doped gadolinium-loaded liquid scintillator (GdLS). Outside of this is a 0.43 m thick region of liquid scintillator (LS) used to capture gammas from the target volume. The outermost region, filled with mineral oil (MO), also contains stainless steel ladders, which hold 192 PMTs. Top and bottom reflectors on the barrels of the cylinder reduce the number of PMTs needed while still maintaining high effective photocathode coverage. On top of the vessel are three calibration boxes containing calibration sources and equipment, and tanks for holding overflow volumes of LS, GdLS, and MO. Monitoring of the overflow tank liquid levels, along with monitoring during filling allows for measurement of the detector target mass to 0.1%. The following sections will describe each detector component and its operation in more detail.

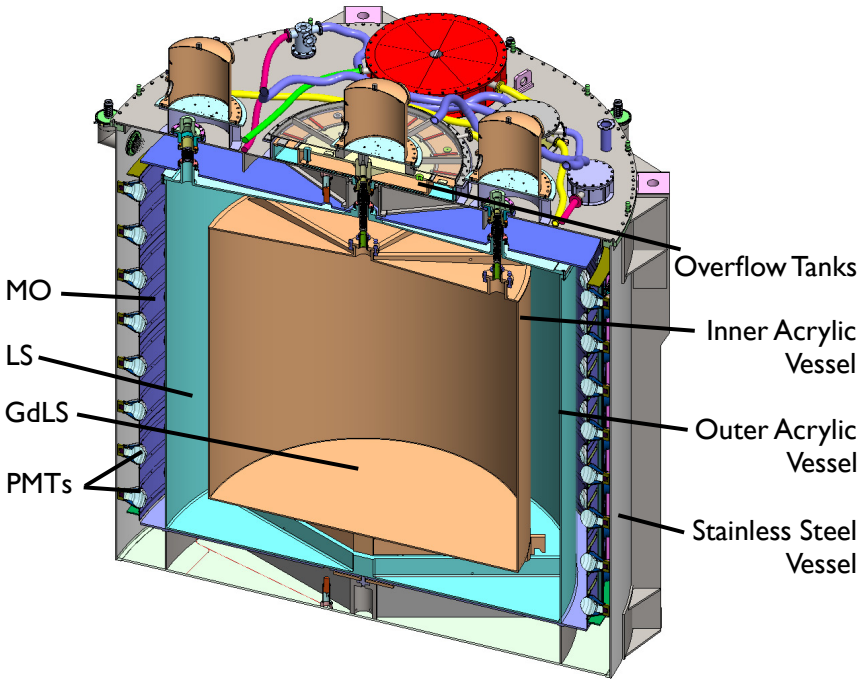

Figure 4.2: A cross-section of a Daya Bay AD. The liquid Gd-loaded scintillator (GdLS), gamma catcher (LS), and mineral oil (MO) regions are bounded by the inner and outer acrylic vessel (IAV and OAV) and the stainless steel tank (SSV), respectively. PMTs are located in the MO regions. Overflow tanks and calibration units are attached to the top of the SSV.

Detection Method

As with many of the previously discussed $\overline{\nu}_e$ experiments, in the Daya Bay detectors, $\overline{\nu}_e$ interact with protons in the target region via inverse beta decay (IBD), creating a neutron and a positron. By multiplying the energy spectrum of the $\overline{\nu}_e$ flux by the $\overline{\nu}_e$-proton cross-section, one can obtain the expected energy spectrum of detected antineutrinos, as pictured in Figure 4.3. The kinematics of the interaction dictates that the positron will carry away most of the excess kinetic energy. The positron will annihilate quickly, depositing $\sim$1 MeV of rest mass energy plus the excess kinetic energy from the $\overline{\nu}_e$. The neutron will thermalize over the course of a few microseconds

and mainly capture on free protons or gadolinium in the target volume, releasing 8 MeV in the case of Gd-capture or 2 MeV in the case of hydrogen-capture.

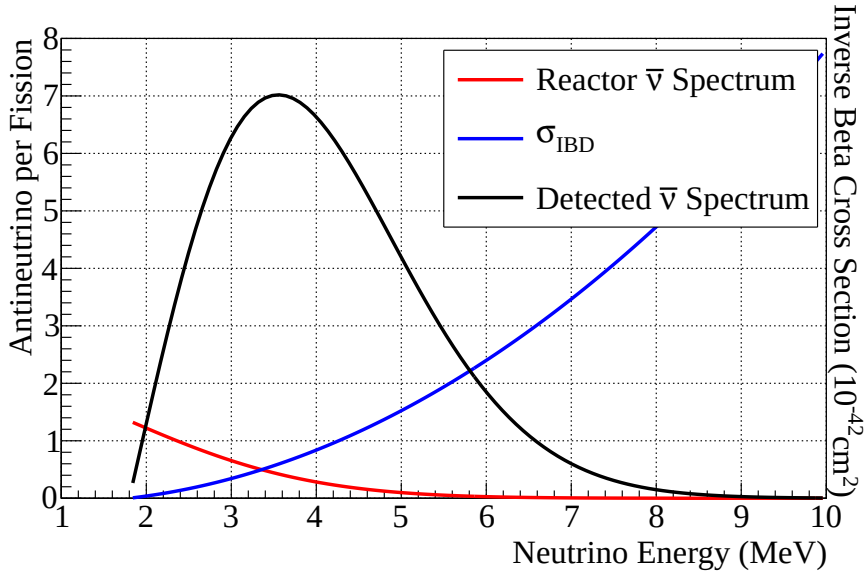

Figure 4.3: Reactor $\overline{\nu}_e$ flux and $\overline{\nu}_e$ - proton cross section as a function of energy. Multiplication of the two yields the expected $\overline{\nu}_e$ energy spectrum in the Daya Bay ADs.

Both the prompt positron and delayed neutron energy depositions will be partially converted to visible light and wavelength-shifted by scintillation and other processes undergone by the linear alkyl benzene and organic fluors in the GdLS and LS. Monte Carlo simulations predict ∼160 photoelectrons/MeV will be detected by the PMTs in the mineral oil (MO) region, with an energy resolution of $\sim 9\%/\sqrt{\mathrm{E}}$. PMT signals are then fed through the experiment's electronic and data acquisition systems, which are used to detect delayed coincidence between the prompt positron energy signal and the high-energy delayed Gd-capture signal. By calibrating the ADs with gamma and neutron sources, the energy scale of the detector can be determined so that particle energies can be identified. Utilizing charge topology along with the energy scale calibration, energy and position reconstruction of each neutrino event will also

be done. Signal events can then be selected through possible cuts on particle energy and time correlations between events in the AD, and position and time correlations between triggers in the AD and muon veto systems. A prototype detector built to test these detection principles as well as detector component and building material candidates is described in [97].

GdLS Target Region

The Daya Bay gadolinium-loaded liquid scintillator region is a cylinder 3.1 m in diameter and 3.1 m in height with a flat conical region at its top. The size of the GdLS was designed to be large enough to meet the statistics goals of the experiment at the far baseline given the expected power of the nuclear reactor complex. The entire region contains 20 tons of GdLS.

The 0.1%-doped GdLS itself is composed mainly of the organic scintillator linear alkyl benzene (LAB). This scintillator was chosen because of its low volatility, high flash point and good compatibility with a wide range of building materials. The GdLS was made in 50 separate 4 ton batches in a clean underground liquid production hall at the Daya Bay site in a multi-step process. First a gadolinium salt is combined with an organic ligand; the use of the ligand is essential to getting the inorganic Gd salt to stay in solution with a non-polar organic solvent. After combining a small batch of LAB to the Gd-ligand product to create a 0.5% Gd-LAB solution, this result is combined with a larger amount of LAB and the fluor PPO and wavelength-shifter MSB to create a final 0.1%-doped GdLS product. After production of each batch, the product GdLS was transferred to one of five GdLS storage tanks. The emission spectrum of the GdLS peaks in the 400-450 nm range. Prototype batches of the GdLS have been tested for stability and have exhibited no degradation of optical clarity after 2 years of testing. More information about the Daya Bay GdLS can be

found in [98] and [99].

LS Gamma Catcher Region

Compared to positrons, the interaction length in the target of the γ products of the neutron capture are quite long, causing some of them to travel tens of cm from their origin before depositing their energy. This is why smaller early reactor $\overline{\nu}_e$ experiments attempted using ^{3}He neutron counters rather than detecting the gamma product of neutron capture. To address this problem and ensure a high detection efficiency in the Daya Bay experiment, a 0.43 m-thick 'gamma catcher' (GC) region of LS was used to surround the GdLS region. With the addition of this zone, $\overline{\nu}_e$ interacting at the edge of the target region will have their neutron-capture gammas largely detected. This effect is illustrated in Figure 4.4, which shows the simulated neutron detection efficiency as a function of gamma catcher thickness. A 0.43 m thick gamma catcher ensures that the neutron detection efficiency will be more uniformly high throughout the target region.

The 25 tons of LS filling the GC region are composed largely of LAB, with PPO and MSB additives to shift the peak of the LS emission spectrum into the 400-500 nm range. Because the LS region does not contain any Gd, most $\overline{\nu}_e$ interacting in the LS region will result in neutron captures on hydrogen. These delayed signals will not be high-energy enough to pass the delayed neutron energy cut that Daya Bay applies to reduce backgrounds, as in the Rovno and Chooz experiments, causing most interactions in the GC region to not contribute to the total event rate. This design effectively creates a clean, easily-identifiable fiducial volume with low systematic uncertainty. However, some events from the GC region will have neutrons that wander into the target during thermalization and capture on Gd. Likewise, some target events will have neutrons that wander out of the target region and capture

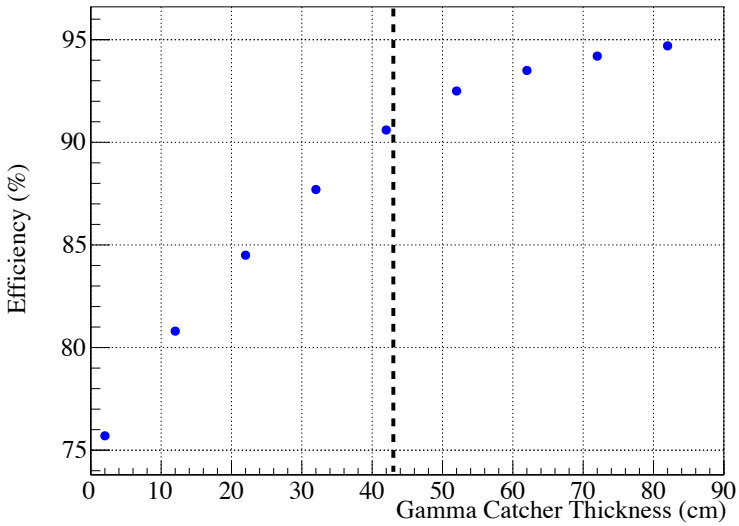

Figure 4.4: Change in n detection efficiency versus change in gamma catcher radius resulting from OAV radius variation. The chosen gamma catcher thickness is indicated by the dashed line. From [96].

on H rather than Gd. These events are called spill-in and spill-out, respectively, and their effect is pictured in Figure 4.5. Their effect on the detector systematics will be further discussed in Chapter 8.

Acrylic Vessels

The GdLS and LS regions of the detector are separated from each other and from the outer regions of the detectors by cylindrical acrylic vessels with conical tops [100]. These vessels are made of UV-transmitting non-scintillating acrylic that has greater than 90% transmittance to all light above 360 nm. The inner acrylic vessel (IAV) is designed to be 10 mm thick on its sides and 15 mm thick on its bottom and top. The 4 m diameter and 4 m height outer acrylic vessel is designed to be 18 mm thick on its sides, bottom and lid. The vessels were designed to be thin to minimize

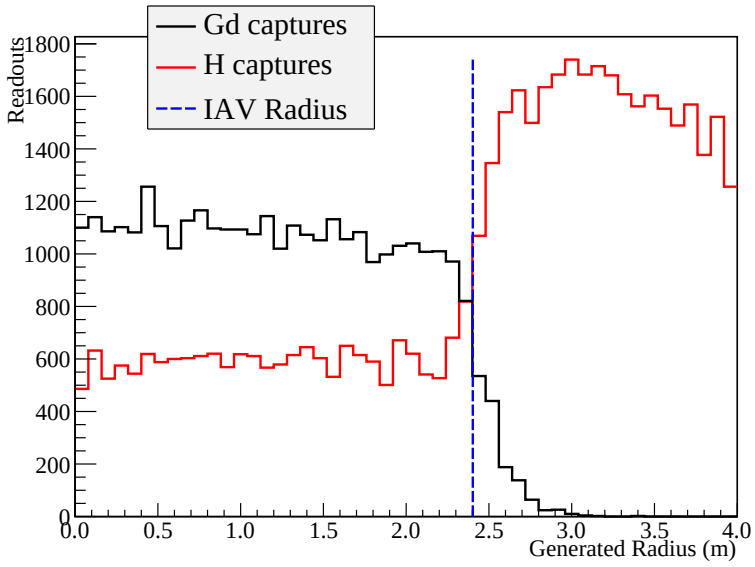

Figure 4.5: Generated radius of neutron captures on hydrogen and gadolinium in Monte Carlo. The tail of Gd-captures outside the IAV radius define the spill-in effect, while the increased H-captures at the GdLS edge define the spill-out effect.

the amount of non-scintillating material near the target volume, and thus maximize the detection efficiency. The vessels are thick enough to ensure their mechanical stability during construction, filling, transport, and operation of the ADs; to further mechanically stabilize the vessels, ribs are included on the tops and bottoms of each vessel, effectively reducing the gamma catcher volume by a few percent.

The acrylic vessels are also designed to allow for filling and calibration of the detectors. To that end, the IAV has 2 calibration ports located on its top that allow for calibration along a central and side axis. The OAV has 3 calibration ports to allow for the 2 GdLS calibration axes and one off-center LS calibration axis. The calibration ports are also used to deliver the flow of GdLS and LS during filling of the detectors. The top of the OAV is detachable to allow for separate manufacture of the IAV and OAV. The design, fabrication, transport, and assembly of the AVs will be described in more detail in the Chapter 5. The technical details are available

in [100].

Mineral Oil Buffer Region, PMTs and Associated Components

Outside of the OAV is the 45 cm thick buffer region. The region is filled with low-scintillating mineral oil that provides an additional shield and background absorber between the low-radioactivity inner region and the outer components of the AD and the AD exterior. 192 Hamamatsu model R5912 8" PMTs are arrayed in 8 equally spaced rings of 24 PMTs facing inwards at the outer edge of the buffer region [101]. The ∼18 cm of space between the beginning of the buffer region and the PMT photocathodes provides shielding to attenuate the radioactive backgrounds coming from the PMT glass. The R5912 PMTs have quantum efficiencies of >10% between 320 nm and 500 nm and gains of $>10^7$ and nanosecond timing capabilities. The quantum efficiency spectrum of the PMTs can be combined with the emission spectrum of the scintillator, the transmittance spectrum of the scintillator and acrylic, and the reflectance spectrum of the reflectors to yield the wavelength profile of detected photons in the Daya Bay detector. Such a plot can be seen in Figure 4.6.

The PMTs are clipped into position in frames that are connected to 4 m tall stainless steel ladders. The eight PMT ladders each hold three columns of eight PMTs, for a total of 192 PMTs. The ladders are bolted into place around the outer edge of the buffer region;. Mu-metal shields are wrapped in a conical shape around the backs of each PMT to minimize the effect of the Earth's magnetic field on the trajectory of photoelectrons and secondary electrons. Also affixed to the front of the ladders are black acrylic radial panels with holes through which the PMT photocathodes stick out. Rather than allowing optical photons to reflect in unpredictable ways off PMT

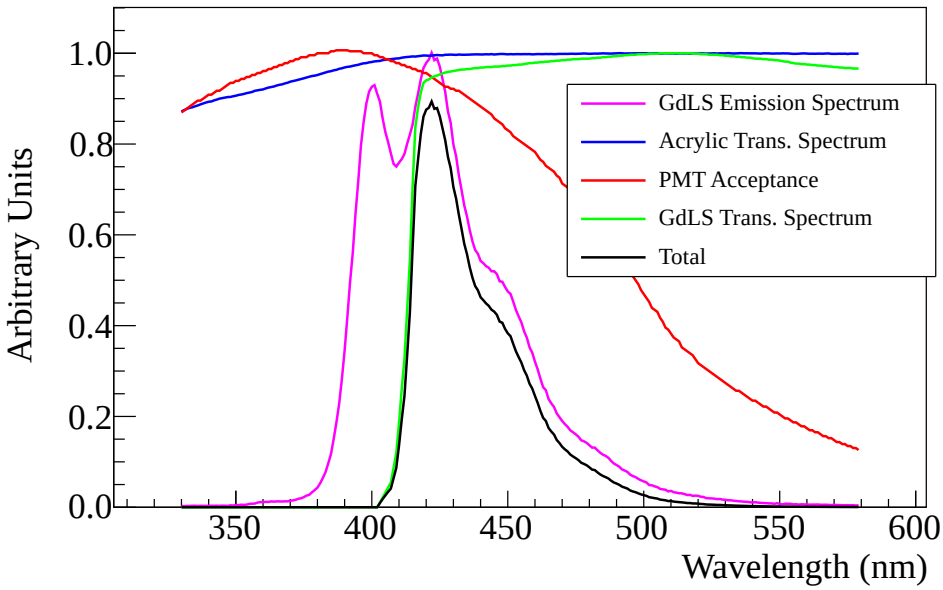

Figure 4.6: The light production and transmittance spectra of the various AD optical components. Multiplication of all curves yields the 'total' spectrum accepted by the PMTs. Reflector reflectance is not pictured as it is nearly maximal for all concerned wavelengths.

cables, ladders, and other hard-to-model shapes, these panels absorb most of that light, while reflecting a small portion of it in a predictable way.

Top and Bottom Reflectors

The top and bottom reflectors are located just beyond the top and bottom of the OAV. The reflectors are composed of a 4.35 m diameter circle of specular ESR reflector sandwiched between two 10 mm thick acrylic sheets. The use of reflectors instead of top and bottom AD PMTs lowers costs and reduces radioactive backgrounds while maintaining good effective photocathode coverage and a uniform light yield as a function of height in the detector. The principal drawbacks of using a reflector rather than PMTs on top and bottom are the reduced ability to make meaningful cuts on scintillation light timing because of reflected light, and some loss of power to reconstruct

the vertex of an event in the target region due to the more complicated modelling of multiple reflections and significant detection of indirect light. A demonstration of vertex reconstruction in the presence of reflectors in the Daya Bay prototype is discussed in [102]. Since Daya Bay does not use reconstructed vertex cuts for inverse beta decay selection, this should not impact the sensitivity of a θ_{13} measurement.

Additional 2" PMTs are located on mounts above the top reflector, behind small circular gaps in the reflector's ESR surface. These PMTs can be used in tandem with small directional light sources to calibrate the optical properties of the detector liquids in-situ.

Stainless Steel Tank

A 5 m stainless steel tank is used to enclose the rest of the regions of the detector and provide structural support to the rest of the detector components. As the surface of the tank is optically isolated from the central region by the radial shield, its optical properties are not important. Special low-background steel was selected for the fabrication of the stainless vessels. U, Th, and K backgrounds in the tank are shielded by the buffer region and contribute only moderately to the singles rate of the detector.

Overflow Tanks

One of the critical systematics in the Daya Bay experiment is related to the number of protons in the target region. In order to reduce this systematic, the Daya Bay experiment has connected the target region via a system of bellows to an external overflow tank system on top of the AD, where liquid levels can be closely monitored. In addition, the overflow tanks allow for thermal expansion and contraction of the

detector liquids. The AD and half of the overflow tank system is initially filled with liquid that is measured to less than 0.1% accuracy for the GdLS and to 0.1% and 0.3% for the LS and MO. Any changes in target protons as a result of temperature and density changes or shape changes during running will result in a change in the liquid levels of the overflow tanks, which will will be monitored by a number of redundant liquid level sensor systems. These sensors will ensure knowledge of the target mass to within 0.01% after the initial filling of the detector. The design, fabrication, transport, and assembly of the overflow tank system will also be discussed in greater detail in Chapter 5.

Calibration System

In order to properly calibrate individual PMTs and electronics channels, and to accurately determine the energy scale of the ADs, an automated calibration system has been designed and attached to the top of each AD. The calibration system consists of 3 dome-shaped automated calibration units (ACUs), one above each of the three OAV calibration ports. Each ACU consists of a water-tight stainless steel shell enclosing a rotary system on which a number of different calibration sources and attendant deployment mechanisms are attached. These sources can be lowered into the target region via bellows systems running from the bottoms of the ACUs to the OAV and IAV calibration ports.

Table 4.2 overviews the calibration sources in the ACUs and the purpose of each calibration source. LED sources can be used to calibrate the timing and gain of each PMT and FEE channel. By combining the calibration data from radioactive sources with other detected events of well-known energy such as neutron-capture peaks, energy scales for the different particle types can be constructed to properly calibrate each AD. The goal precision of the energy scale calibration of each AD is

1%; furthermore, the calibrated energy scales of all detectors will be identical to less than 1%.

Source	Calibrations
Am-C: neutron source	H-Capture: 2.223 MeV; Gd-Capture: ∼8 MeV; H/Gd Ratio; absolute efficiency
^{68}Ge: positron source	0.511 + 0.511 MeV (annihilation)
^{60}Co: gamma source	1.173 + 1.333 MeV
LED source	PMT gain

Table 4.2: Sources to be used for calibration in the Daya Bay ACUs. The possible calibrations provided by each source are also listed.

Electronics and Trigger

Analog charge signals from from a PMT are fed into a front-end-electronics (FEE) module, providing time and charge information on which physics events can be reconstructed. Each FEE module services 16 PMTs. The circuit diagram for the FEE can be seen in Figure 4.7. TDC timing values are determined for channels with analog signals that pass above a reference voltage level; these threshold crossings also provide a 100 ns wide pulse to the trigger system to keep track of the number of hit channels. In order to ensure a charge dynamic range that extends below 1 MeV for low-energy $\overline{\nu}_e$ to GeV for high energy AD muon events, two separate amplifiers are used: low-energy signals are fed into a 10× amplifier, while high-energy signals are additionally put through a 1× channel. These are referred to as the 'fine' and 'coarse' ranges of the electronics. The output of these amplifiers is then filtered, shaped, pedestal-subtracted, and finally fed into the ADC to receive digitized charge information.

For physics runs, the base trigger level contains two main independent conditions:

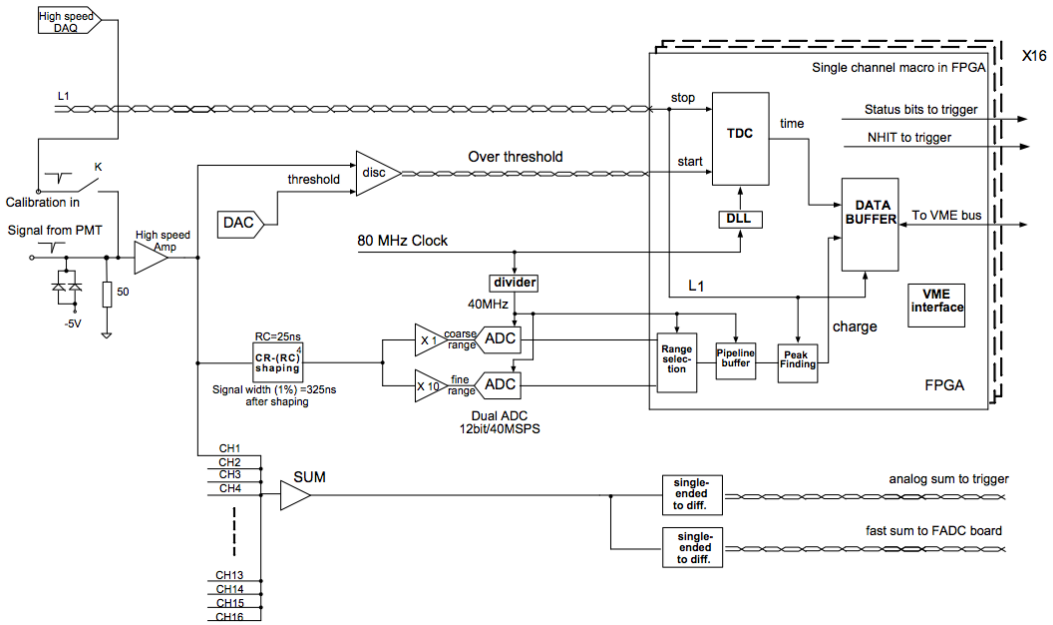

Figure 4.7: A block diagram of a front-end electronics (FEE) module. From [96].

an NHit trigger is issued if the total number of 100 ns threshold crossings at any given time is above a certain value, while an ESum trigger is issued if the total shaped analog charge of all channels is above a certain value [103]. These two triggers can be used to cross check the total trigger efficiency and ensure that trigger-related systematics are well-understood. If either or both of the trigger conditions are met, the ADC and TDC information for all channels within a 1200 ns readout window is delivered to higher level triggers. A trigger time latency is set such that the peak number of TDC values is located near the beginning of the readout window. ADC and TDC information from triggers is ultimately sent to the readout system for offline data processing, storage, and analysis.

4.3 Muon Veto System

The Daya Bay muon veto system consists of three independent active detectors: inner and outer water Čerenkov detectors, and a resistive plate chamber array. These systems in tandem provide a muon detection efficiency of >99.5%, as well as the ability to cross-check detection efficiency between systems, allowing for low-uncertainty background identification and reduction for a $\overline{\nu}_e$ measurement. A diagram and photograph of the system are visible in Figure 4.8.

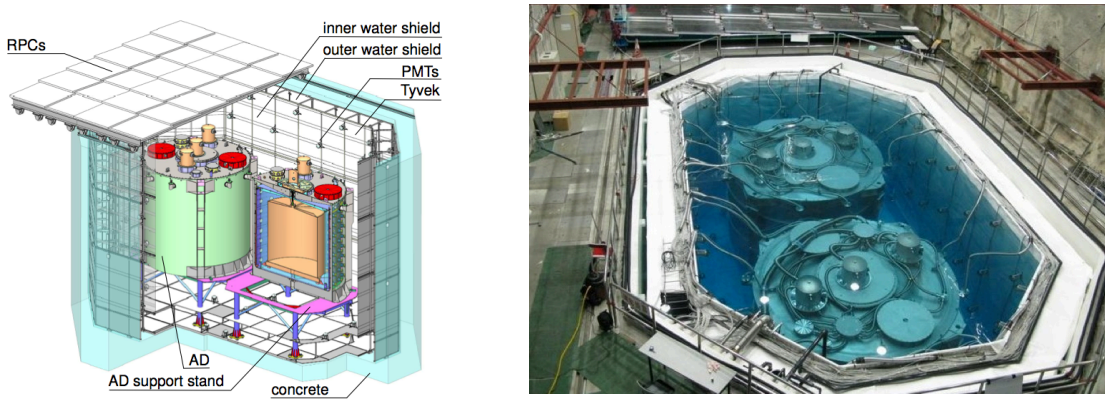

(a) A diagram of the muon veto system and ADs. From [104].

(b) A photograph of a filled near site pool with ADs. RPCs are visible at the photo top, rolled off to the side of the pool. Photo courtesy of Daya Bay.

Figure 4.8: The inner and outer water pool and RPC muon veto systems.

Water Pool Veto

The Daya Bay water pools provide a minimum of 2.5 m of ultra-clean water shielding for the ADs. For the near halls, the pool is 16 m long × 10 m wide × 10 m deep, while the far hall pool is 16 m long × 16 m wide × 10 m deep. These pools are separated into two optically decouple regions by a support structure near the floor and walls of the pool that is lined with white Tyvek. For 1 m wide outer water pool, 8" PMTs are secured to frames along the pool wall facing into the pool, and

to the structure that separates the water pools, facing the wall of the pool. For the inner pool, 8" PMTs are secured to the inside of the support structure facing inward towards the ADs. The far hall uses 384 PMTs, while the inner hall uses 288, resulting in 0.6% photocathode coverage. The water pool PMTs' time and gain characteristics are calibrated by LED sources located at numerous positions in the water pool.

Water pools serve as both a passive shielding system and an active muon detector. They shield detector backgrounds from the rock surrounding the pool, reducing AD single trigger rates by five orders of magnitude. Cosmic ray muons passing near and through the ADs will create Čerenkov light in the water, which will be detected by PMTs in the two water pools. This muon signal can be used to veto time-correlated events in the ADs. The water also shields the detectors form fast neutrons originating from muon spallation in the rock surrounding the detector.

RPCs

RPCs consist of a region of highly ionizable gas sandwiched between resistive plates [105]. Muons traversing the detectors will ionize the gas, which will cause a charge avalanche under high voltage, which can be read out by pickup strips running along the outside the of the plates. By stacking four RPCs with alternating x-y orientation, the position of the thoroughgoing muon can be identified, while assuring high detection efficiency and low noise trigger rates.

The RPCs for the Daya Bay experiment are fully installed and undergoing commissioning and characterization testing [106]. For this reason, they were not used for the analysis presented in this thesis. Redundancy in muon detection for this analysis is instead provided by the inner and outer water pool detectors.

4.4 Experiment Systematics

The systematics involved in the Daya Bay experiment can be best summarized by considering the variables describing the number of detected events. For a single detector, the equation for the absolute number of detected events is

$$N_{det} = \frac{N_p}{4\pi L^2} \int \epsilon \sigma P_{sur} S dE, \tag{4.1}$$

where N_p is number of protons in the detector, L is the reactor-to-detector baseline, ϵ is the detection efficiency, σ is the inverse beta decay cross-section, P_{sur} is the survival probability resulting from neutrino oscillation over the baseline L, and S is the reactor flux. Each of these variables contributes its own systematic uncertainty, whose goal magnitudes of contribution to the absolute flux measurement systematic can be seen in Table 4.3. For an absolute measurement, the dominating contributors to the systematic uncertainty are reactor-related: the spectrum and normalization of the $\overline{\nu}_e$ flux from the reactor cores are both only known to a few percent. The largest expected contributor to detector systematics is the uncertainty in the number of protons in the scintillator: even if the target mass of the scintillator is known to 0.1%, the number of protons per unit mass of the scintillator can only be measured to $\sim$0.5%.

As was demonstrated by a number of previous reactor experiments such as Goesgen and Bugey, and illustrated in Table 3.5, sensitivity to θ_{13} can be enhanced by making a relative measurement of the $\overline{\nu}_e$ at simultaneously at two different baselines with identical detectors. The power of using this technique, km-scale baselines, and proper background reduction strategies to rule out large new regions of θ_{13} parameter space were spelled out specifically in 2000 by Mikaelyan and Sinev [107]. The

Variable	Systematics Description	Absolute (Correlated) Systematic (%)	Relative (Uncorr.) Systematic (%)
N_p	Target Mass Measurement	0.1	0.1
	Free Protons Per Unit Mass	0.5	-
ϵ	Detection Efficiency	0.38	0.38
σ	IBD Cross-Section	0.2	-
S	$\overline{\nu}_e$/Fission	~ 2	-
	$\overline{\nu}_e$ Spectral Shape	~ 2	<0.1
	Reactor Power	0.5	<0.1
L	Detector Baseline	0.02	0.02
Goal Total Systematic		3.2	0.4

Table 4.3: Goal correlated and uncorrelated systematics for a relative or absolute measurement of $\overline{\nu}_e$ flux at the Daya Bay Experiment. These systematics predictions are based on Monte Carlo simulation of the Daya Bay detectors and on systematics quoted by previous reactor experiments [96]. The analysis of the full Daya Bay Experiment shown in Chapter 9 will outline the actual experiment systematics.

equation describing the ratio of detected events between two different detectors is

$$\begin{aligned} R = \frac{N_f}{N_n} &= \frac{\frac{N_{p,f}}{4\pi L_f^2}\int \epsilon_f \sigma P_{sur,f} S dE}{\frac{N_{p,n}}{4\pi L_n^2}\int \epsilon_n \sigma P_{sur,n} S dE}, \\ &= \left(\frac{N_{p,f}}{N_{p,n}}\right)\left(\frac{L_n}{L_f}\right)^2\left(\frac{\epsilon_f}{\epsilon_n}\right)\left(\frac{P_{sur}(E,L_f)}{P_{sur}(E,L_n)}\right). \end{aligned} \tag{4.2}$$

where n and f refer to the near and far detectors, respectively. For the remaining ratios of N, L, and ϵ, uncertainties that are correlated between detectors are fully cancelled, while only those uncertainties that are uncorrelated between detectors remain. By taking data simultaneously at one far site and two near sites adjacent to the six reactor cores, the reactor power and spectral shape and normalization uncertainties are almost entirely cancelled. The resulting contribution of these uncorrelated uncertainties to the systematic for a relative ratio measurement can also be seen in Table 4.3. Notice that the total detector systematic is reduced from over 3% to 0.38%.

With the relative measurement, minimized reactor-related systematics give way to uncorrelated detector systematics as the dominant contributor to the experimental

systematic. Table 4.4 lists the individual contributors to the experiment's goal relative detector systematics.

Detector Systematic	Goal Relative (Uncorrelated) Systematic (%)
Proton Number	0.3
Energy Cuts	0.2
Timing Calibration	0.1
Electronic Effects	0.01
Multiplicity Cuts	0.05
Clock Effects	0.01
Total Relative Detector Systematic	0.38

Table 4.4: Magnitude of uncorrelated detector systematics for a relative measurement of $\overline{\nu}_e$ flux at the Daya Bay Experiment.

Detector-related uncorrelated systematic uncertainties are the dominant uncertainty in the Daya Bay experiment, limiting its sensitivity to θ_{13}. If the Daya Bay experiment is able to lower this value through a better designing, construction, calibration, and monitoring of the ADs, the overall sensitivity of the experiment can be lowered considerably. It is particularly beneficial to improve the volume monitoring system and to reduce the detection efficiency uncertainty through better calibration and understanding of detector identicalness.

4.5 Other Contemporary θ_{13} Experiments

Two other reactor $\overline{\nu}_e$ experiments are also currently taking data, and also hope to use this data to measure a non-zero value of θ_{13}.

Double Chooz

The Double Chooz experiment is located at the same nuclear power station that was host to the Chooz experiment [108]. The experiment will ultimately utilize

two identical 10-ton-target three-zone detectors similar in design to Daya Bay's, one located in the location of the detector in the original Chooz experiment at a baseline of 1 km, and another a very short distance from the two reactor cores. The experimental parameters can be seen in Table 4.5. The Double Chooz baseline is not optimized to the known parameter space of Δm^2_{31}, and as a result, the experiment will be less sensitive to θ_{13} mixing. In addition, the total target mass for the Double Chooz experiment will be lower, meaning that the experimental sensitivity will improve more slowly over time than Daya Bay's.

Experiment	Reactor Thermal Power (GW)	Baseline Near/Far (m)	Overburden Near/Far (mwe)	Target Mass Near/Far (ton)
Double Chooz	8.6	280/1050	80/300	10/10
RENO	16.4	292/1380	110/450	16/16
Daya Bay	17.4	363(480)/1910(1540)	260/910	2×20/80

Table 4.5: Overview of experimental parameters for the three new high-precision θ_{13} experiments. The Daya Bay experiment include two numbers for near and far baselines because of the two different near sites and the two different clusters of reactor cores.

The Double Chooz far detector began taking data in December 2010 and has presented its first results, as described in the Chapter 3. The near detector is still under construction and is slated to be brought online in the middle of 2013. Double Chooz's goal is to be sensitive to values of $\sin^2 2\theta_{13}$ as low as 0.03 at 90% CL after 3 years of running.

RENO

Another collaboration, named RENO, is constructing a high-precision θ_{13} experiment at a power plant in Yonggwang, South Korea [109]. The nuclear power plant at Yonggwang consists of 6 PWR reactors with a total power of 16.4 GW, slightly

smaller than the total output of the Daya Bay power plants. The reactors are equally spaced in a line spanning 1.3 km. Two identical three-zone detectors will be built to do a near-far relative measurement of the neutrino flux, as in the Daya Bay and Double Chooz experiments. The site parameters of the RENO experiment can also be seen in Table 4.5. The baseline of the RENO far detector is more optimal than the Double Chooz experiment, but less optimal than Daya Bay. In addition, the RENO site provides less overburden. which will increase the levels of cosmogenic backgrounds in the measurement and limit the sensitivity of the experiment to θ_{13}.

The full RENO experiment is currently up and running. First results were presented in April 2012 [110]. After 3 years of running RENO hopes to reach a 90% CL $\sin^2 2\theta_{13}$ sensitivity of 0.02.

Chapter 5

The Daya Bay Acrylic Vessels

5.1 Introduction

The bulk of the hardware component of my graduate research was spent participating in the design, fabrication, transport, characterization and assembly of the Daya Bay acrylic vessels, which are vital components that determine many of the properties of each AD's target region. In order to ensure identical detector response and well-understood relative detector systematics, acrylic vessels must be built as identically as possible. This chapter will give a detailed overview of how this is achieved during the production of the first two Daya Bay inner and outer acrylic vessels. Further information on design, construction, characterization, and assembly of the AVs can be found in [100].

5.2 Vessel and Overflow Tank Design

The Daya Bay acrylic target vessel system is composed of three main elements: the inner acrylic vessel (IAV), the outer acrylic vessel (OAV), and the overflow tank

system. A complete acrylic vessel (AV) system is pictured in Figure 5.1. The IAV contains the GdLS volume, and is visible in Figure 5.1 as the inner nested cylinder. The OAV holds LS, and is visible in Figure 5.1 as the outer cylinder. The overflow tank system rests on top of the stainless steel vessel (SSV) that encapsulates the AVs, PMTs, reflectors, and AD liquids. This subsystem contains extra separated LS and GdLS volumes to ensure that both AVs are completely filled at all times during running despite environmental temperature and pressure changes.

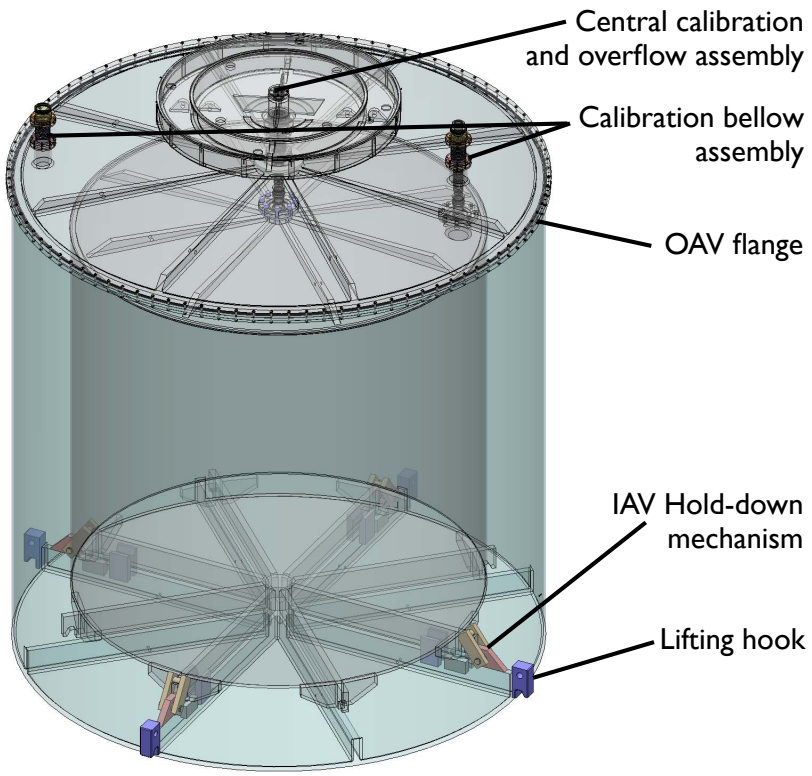

Figure 5.1: Transparent model of the complete OAV, IAV, and overflow tank system. The IAV is nested inside the OAV, with the overflow tank appearing above both AVs. The overflow tanks are outside the main detector volume and above the steel lid. The mineral oil overflow tanks are part of the stainless lid and not shown here.

The AV structures must satisfy a wide range of design requirements. The main purpose of the the AVs is to maintain the target and gamma-catcher liquid regions

as separate nested volumes of well-defined size. Thus, the design of the OAV must accommodate the nesting of the IAV within it. In addition, the vessels must be structurally sound while filled or unfilled and leak-tight. The vessels must always be completely full, with any excess liquid volume closely monitored in overflow tanks. There must also be a leak-tight liquid pathway between the vessels and the overflow tank system. To maintain design simplicity, these pathways should also accommodate the processes of filling and calibrating the liquid regions inside the vessels. The position of the two vessels with respect to one another should also be consistent to maintain these pathways and the liquid regions' shapes.

The proper physics response of the AD places other design constraints on the vessels. They must be sufficiently optically clear such that anti-neutrino signals from the center regions can be detected by PMTs in the outer regions of the detectors. They must also have low radioactivity so as not to contribute significant background to the experiment.

Further design requirements are imposed by the shipping and assembly processes. The vessels' design must include a method of being lifted during transportation and installation. They should also be designed to maintain their shape and integrity during and after experiencing stresses during these processes. The design should additionally allow for all parts to fit together properly in the presence of minor misalignments or dimensional flaws.

Finally, the vessels must be designed to ensure that the AD will function properly for the entire planned length of the experiment. This means that the materials used for the acrylic vessels and overflow tanks must be compatible with LS, GdLS, and mineral oil over long time periods. The materials compatibility issues are also important for the stability of the GdLS. Extensive testing and special care has been taken to ensure that the wetted materials that come in contact with the detector

liquids meet these requirements.

Vessel Design

Figure 5.1 provides an overview of the acrylic vessel design. The IAV and OAV are composed of a main cylindrical section approximately 3 m and 4 m in diameter, and 3 m and 4 m in height, respectively, and a conical top of 3% gradient. The walls are kept thin, 10 mm for the IAV and 18 mm for the OAV, to reduce the amount of non-scintillating absorptive material in the inner detector. The vessels encapsulate a volume of 23 tons of GdLS in the target and 25 tons of LS in the gamma-catcher region. The vessels are manufactured from ultraviolet-transmitting (UVT) acrylic, which allows for maximal transmission of near-UV and optical scintillation light emitted by the AD liquids. Acrylic is the vessel material of choice because it is stronger, cheaper, lower in radioactivity, and easier to fabricate than most other optical window materials. Fabrication and construction of large acrylic objects is a common practice: acrylic is the material of choice for commercial aquariums and other applications, and was also used to build the 12 m diameter sphere inside the Sudbury Neutrino Observatory [111].

The nested design of the inner and outer acrylic vessels in Daya Bay poses an interesting challenge. The OAV is manufactured in the US and shipped to Daya Bay, while the IAV is fabricated in Taiwan. The vessels are assembled together into the AD in the Surface Assembly Building (SAB) at Daya Bay. To accommodate this fabrication plan, the conical top of the OAV has been designed as a detachable lid that connects to the rest of the vessel via a double o-ring seal to a 4 m-diameter flange on top of the OAV walls. A cross-section of this OAV flange-lid connection can be seen in Figure 5.2, along with a photo of a production OAV flange seal and accompanying leak check port plug. The o-rings are compressed by stainless bolts

torqued into nitrogen-allowed nuts at 60 foot-pounds. The bolts are separated from the acrylic by viton washers and teflon bolt-hole sleeves.

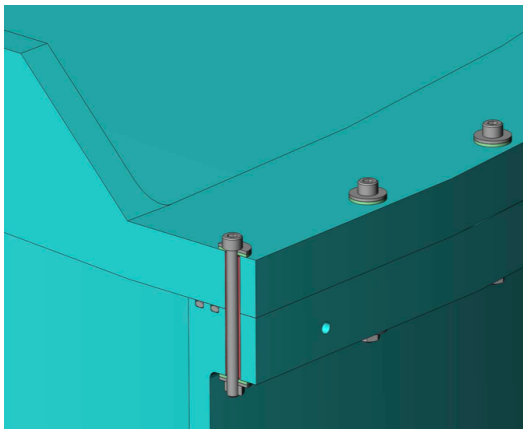

(a) Drawing of the OAV flange double o-ring seal, including leak check port.

(b) Photograph of the as-built OAV flange-lid seal, including leak check port and plug.

Figure 5.2: Close-up drawing and photograph of the OAV flange double o-ring seal connecting the OAV lid to the rest of the OAV vessel. Also pictured in the photograph is the OAV leak-check port and the plug used to seal the leak-check port and the space between o-ring grooves. A teflon-covered stainless wire is used to hold the port plug in place.

The top of the IAV and the OAV lid have two and three ports, respectively, which will serve as the entry point for liquids, and entry and exit points for calibration sources. A close-up view of the off-center calibration ports can be seen in Figure 5.3. The off-center ports accommodate delivery of LEDs and radioactive sources during calibration and liquids during filling, while the central port allows delivery of calibration sources and allows the flow of liquids between the AVs and the LS and GdLS overflow tanks. The IAV ports are connected to semi-flexible teflon bellows that run up to connection hardware on the stainless steel tank lid. While traversing the OAV region, the IAV teflon bellow runs inside a larger-diameter teflon bellow that connects the OAV ports to a related set of connection hardware on the stainless steel vessel lid. The calibration sources are housed in and lowered from slightly elevated automated calibration units directly above the stainless steel vessel connection hardware. All

the connecting parts are made of acrylic, teflon, or viton, and utilize single or double o-ring seals to prevent liquid leakage. To allow for proper connection despite minor radial and height misalignments, the calibration tubes are capable of sliding up and down with respect to other parts while maintaining leak-tightness. The flexibility of the teflon bellows also helps assure connection in spite of slight misalignments.

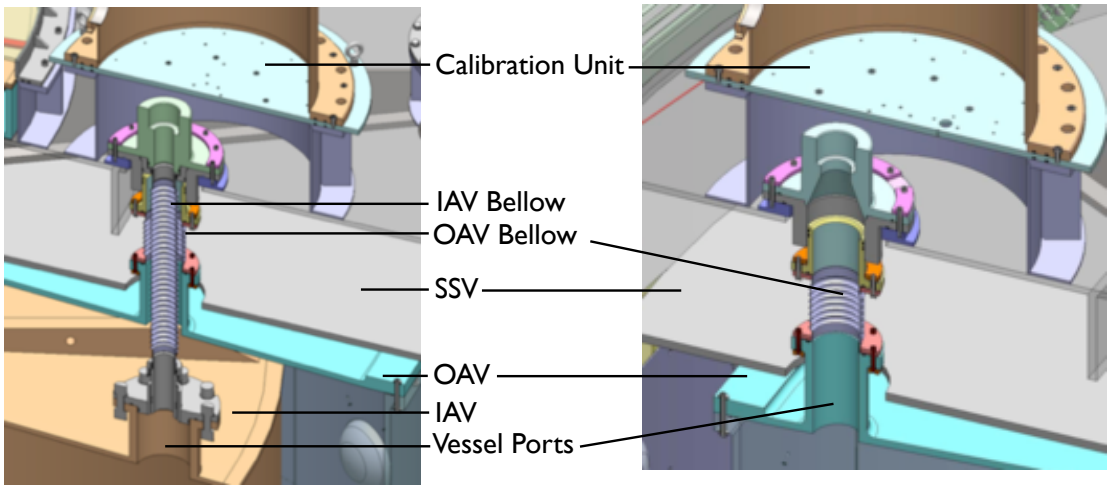

Figure 5.3: Detailed close-up of connections between the off-center IAV calibration port (left), off-center OAV calibration port (right) and connection hardware on the top of the stainless steel tank lid. Parts are color-coded to help differentiate between individual pieces. O-ring locations are also pictured. Acrylic vessel ports connect to flexible teflon bellows that seal to the stainless detector housing underneath the calibration box.

The bottoms of the AVs provide structural support, facilitate the alignment of the acrylic vessels, and make a mechanical link between the inner and outer vessels through the hold-down mechanisms. 5 cm-thick supporting ribs can be seen in Figure 5.1 on the bottom outside of the IAV and the bottom inside of the OAV, as well as on the outside of the IAV and OAV lids. The ribs provide a support structure that allows the vessels to withstand stresses experienced during lifting, transport, and filling. Finite element analysis (FEA) was carried out on the vessel designs to determine the necessary wall thickness and structural support. The highest stress

risk occurs during the filling process if liquid levels become uneven: Figure 5.4 shows that expected stresses for a 30 cm level difference inside and outside the OAV are as high as 10 MPa. To avoid these stresses, liquid levels will be matched to 5 cm during filling.

The long-term design stress limits for the acrylic vessels is 5 MPa. Short-term stress exposures up to 10 MPa are considered safe. The filling process, which takes 4 days to complete, is considered a short duration compared to the nominal 5-10 year lifetime of the acrylic vessels. Stress characterization tests that validate these tolerances are discussed in Section 6.1.4.

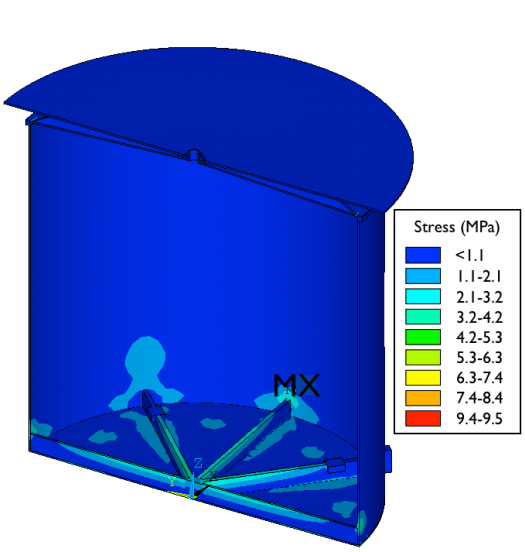

(a) Results of FEA calculation. The small region of maximum stress at 9.5 MPa is labelled "MX". Another high-stress region can be seen at the bottom middle of the OAV.

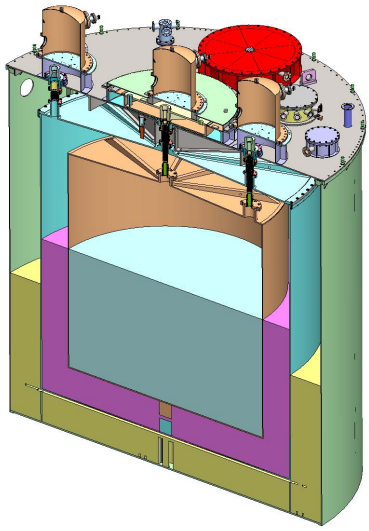

(b) A depiction of the filling scenario giving rise to the stresses calculated via FEA in the adjoining figure.

Figure 5.4: FEA results for a scenario in which the liquid level is 30 cm higher on the inside of the OAV than on the inside.

A few other design features located at the bottom of the vessels can be seen in Figure 5.5. Lifting hooks on the IAV and OAV can be seen in Figure 5.5(c); four hooks are located on the outside of each AV, one every 90°. Rigging and lifting of

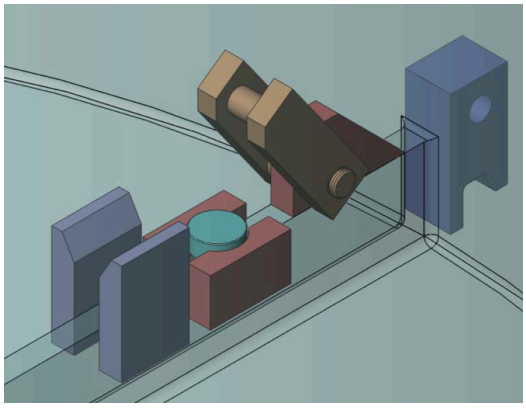

(a) A close-up of the lateral alignment guide, support puck, IAV hold-down mechanism, rib stop, and lifting hook without an IAV present.

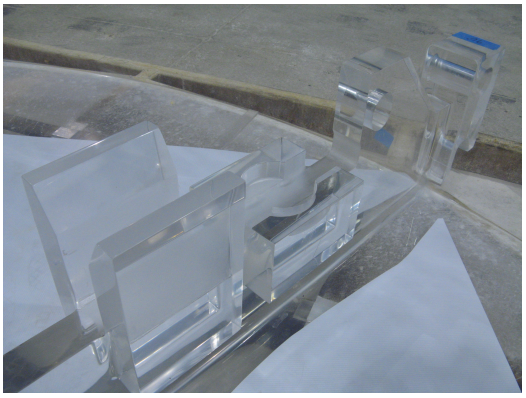

(b) A close-up of the as-built components pictured to the right. Not present in this picture is the support puck and IAV hold-down latch.

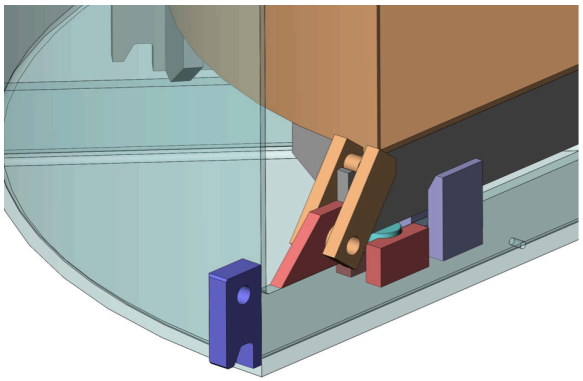

(c) A close-up of an engaged IAV hold-down mechanism. IAV and OAV lifting hooks are also visible, along with the engaged lateral alignment guide.

Figure 5.5: Close-up views of the IAV/OAV interface. The IAV rests on the teflon puck (blue), which is shimmed beforehand to ensure IAV levelness, The latch (brown) is rotated to secure the IAV with respect to the OAV. The lateral alignment guide directs azimuthal placement while the IAV is being lowered onto the shimmed puck.

the vessels using these hooks will be discussed further in Section 5. Figure 5.5 also demonstrates the hold-down mechanism which latches the IAV to the OAV. The IAV is lowered into the vessel and four of its ribs are rested on four teflon pucks that rest on the ribs of the OAV. A latching mechanism connected to the OAV is then rotated into place over a hook on the end of the IAV rib. This mechanism is designed to constrain the IAV's movement upward. The latch can only be disengaged by applying upward

force to the bottom of the latch, minimizing the risk of accidental disengagement from vibration during transport. The rib stops atop the OAV ribs beyond the IAV rib ends constrain the IAV's movement in the radial direction. One set of rotational stops attached to either side of one OAV rib, along with the rib stops, constrain motion about the axis of the vessel.

Material	Compatible With:		
	LS	Gd-LS	MO
Acrylic	Y	Y	Y
Teflon	Y	Y	Y
Viton	Y	Y	Y
Nitrogen Gas	Y	Y	Y
Stainless Steel	N	N	Y

Table 5.1: Material compatibility between AV and overflow system construction materials and AD liquids.

Table 5.1 lists all the materials present in the AVs, overflow tanks, and connection hardware, and overviews the level of compatibility between these materials and the AD liquids. Materials are non-compatible if one causes the mechanical or optical degradation of the other when the two are in contact. Further documentation of compatibility QA measurements are detailed in Section 6.1.3. The vessel and port connections only use materials compatible with all AD liquids.

Overflow Tank Design

Overflow tanks are connected to the central detector volumes for Gd-LS, LS, and MO to allow for the thermal expansion of the detector liquids during filling, transport, and storage. A close-up view of the overflow tanks can be seen in Figure 5.6. The overflow tanks consists of two separated nested spaces bounded by acrylic. The innermost region, the Gd-LS overflow tank, is 1.3 m wide and 13 cm deep, and is surrounded

by an LS overflow tank of 1.8 m diameter and 13 cm depth. This corresponds to an overflow liquid volume of 167 liters Gd-LS and 151 liters LS.

These overflow spaces are created by three large acrylic structures, which can be see in Figure 5.6. The first is a 0.9 m-radius flat-bottom cylindrical tank with no top that serves as the base of the LS overflow region. The next is a 0.65 m-radius cylinder with an extra elevated flared ring of material on its outside top that rests on top of the outer cylinder. Raised areas on the underside of this piece allow it to rest on the bottom of the outermost cylinder, while still allowing liquid to pass below it inside the outermost cylinder. This second piece is the base of the Gd-LS overflow region and the flared covers the LS overflow region on top. The third piece is a lid for the Gd-LS overflow region. Polyurethane is applied to the interfaces between these three pieces to provide a seal between the overflow tank volumes and the outer cover gas region of the detectors. A stainless steel ring with spokes, or spider ring, is fastened down on top of these acrylic pieces to hold them together without the need of screws in acrylic. Finally, a stainless steel shell surrounding the apparatus provides an air- and liquid-tight seal to enclose the nitrogen gas and AD liquids in the overflow tanks and separate them from the water outside the detector.

The AD is filled with liquid by pumping Gd-LS and LS in through the off-center IAV and OAV ports, respectively, displacing nitrogen gas that is circulated through the AD before filling. The liquid fills up through the volume of the detector, then through the bellows and into the overflow tanks. Filling was stopped with the liquid levels at 4.6 cm and 6.4 cm above the bottom of the Gd-LS and LS overflow tanks, respectively. An approximate 3°C rise in temperature and subsequent expansion of the AD liquids would cause the complete filling the LS and Gd-LS overflow tanks. In addition, if the temperature is lowered by 2°C, the liquid will contract out of the overflow tank and begin emptying the target volume, causing unknown changes in

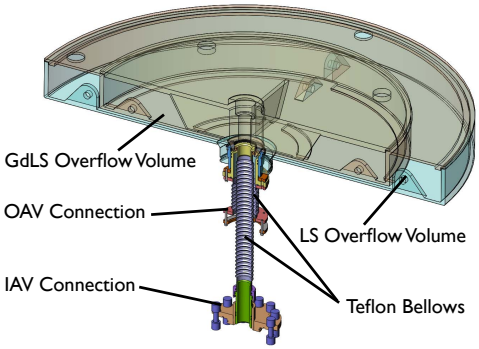

(a) Drawing of overflow tank and connection hardware.

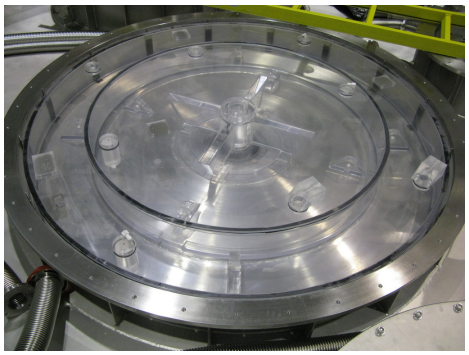

(b) Photograph of an as-built overflow tank. The two overflow regions are clearly visible.

Figure 5.6: Close-up view and photograph of the overflow tank system, including OAV/IAV connection hardware. The parts are color-coded to emphasize the individual pieces. The stainless steel overflow tank cover and spider ring are not pictured in either drawing or photograph.

optical properties at the top of the detector. Because of this, a 2°C temperature change is the operational limit that can be experienced by the AD during filling and operation of the detectors.

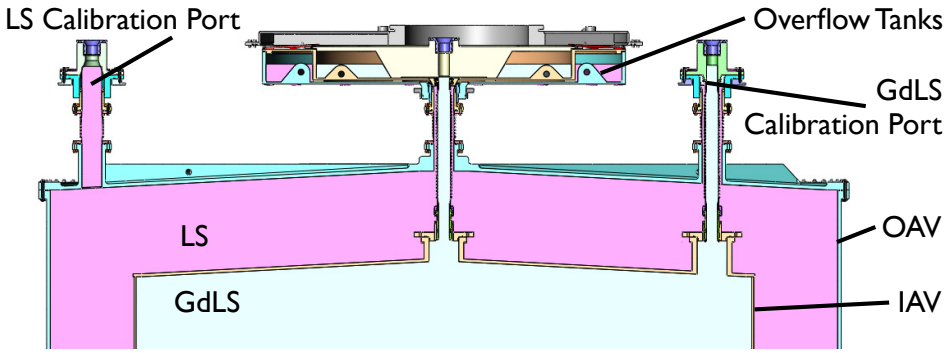

Figure 5.7: Cross-section of a filled AD. The path from the LS and Gd-LS bellows through to the overflow tanks are visible in this figure. Also note the LS and Gd-LS filling up their respective calibration ports.

The locations of LS and Gd-LS liquid levels in the AVs and overflow tanks for a filled AD are illustrated in Figure 5.7. During detector operation, the liquid level is monitored in the overflow tanks by ultrasonic and capacitance sensors and in the

off-center calibration ports with cameras to determine changes in the target and gamma-catcher mass resulting from changes in temperature and density the liquids.

5.3 Material Selection

Initial quality assurance and R&D measurements were done during the design stage before vessel fabrication to determine the correct material with which to build the acrylic vessels. Of particular concern were the optical, radioactive, and mechanical properties of candidate materials, and their compatibility with prospective target and gamma catcher liquids.

Optical Properties

The transparency requirements of the acrylics used in the IAV and OAV are dictated by the emission and transmittance spectrum of the AD liquids, as well as by the quantum efficiency spectrum of the Daya Bay PMTs [112, 101]. From these inputs, it was determined that the IAV and OAV acrylic needs to be highly transparent to photons with wavelengths from 360 nm to 500 nm. The specifications on transmittance for a 10-15 mm sample in air for IAV and OAV acrylics for Daya Bay were 84% at 360 nm, 88% at 380 nm, 90.5% at 400 nm, and 91.5% at 500 nm. These values mirror those used in the SNO experiment. Acrylic sheets with transmittances of a few percent below specifications for lower wavelengths were also deemed acceptable as a majority of the scintillation light propagated in the Daya Bay liquids is above 400 nm.

During the design phase, a variety of samples were tested using an SI Photonics Model 440 UV-Vis Spectrometer [113] to identify acrylic types that met these transmittance specifications. UVT acrylic meets these requirements, while standard

UV-absorbing (UVA) acrylics only begin transmitting light appreciably at 400 nm. Eventually, thin UVT acrylic sheets from Polycast were selected for the OAV walls, cast blocks of UVT acrylic from Reynolds were selected for the OAV lid and bottom, and PoSiang UVT acrylic was selected for the IAV. UVA acrylic was used for the overflow tanks and connection hardware, as these components are either small or far removed from the detector target. Transmittance data from the UVT acrylics are presented in Section 6.3.

Acrylic Radioactivity Testing

Acrylic is an organic compound and does not contain many of the long-lived radioactive isotopes that are present in other optical window materials, such as glass. To ensure that radioactive backgrounds from the selected production acrylic types were acceptably low, samples of each type of acrylic were counted for radioactivity using a high-efficiency HPGe detector situated inside a low-background external radioactivity shield. Measurements were made with similar setups at either a concrete-shielded surface facility at Berkeley National Laboratory or at an underground laboratory at the Oroville Dam in Oroville, California [114]. Radioassay results are listed in Table 5.2. Note that the value for all measurements is only an upper bound, which is limited by the sensitivity of the equipment, the size of the sample, and the duration of the assay.

In order to keep singles rates and correlated backgrounds at an acceptable level, it is desired that the intrinsic bulk radioactivity contribution from each AV component be lower than the radioactivity requirement for the 20 kg of Gadolinium salt used to manufacture the GdLS. Table 5.2 includes the measured radioactive isotope concentration upper limits for each acrylic type, as well as the isotope concentrations that will achieve the radioactivity requirement. For Polycast acrylic and for ^{40}K

concentrations, these requirements have been met by the measurements. More precise measurements have been planned to lower the limits for Reynolds and PoSiang acrylics, so that low backgrounds in these acrylics can be confirmed.

Acrylic Type	^{238}U (ppb)		^{232}Th (ppb)		^{40}K (ppm)	
	Measured	Goal	Measured	Goal	Measured	Goal
Reynolds	<3	0.1	<3	0.3	<1	13
Polycast	<0.07	0.09	<0.2	0.2	<0.1	9
Posiang	<0.2	0.1	<0.4	0.2	<0.3	11

Table 5.2: Measured and required limits on concentration of radioactive isotopes in the production AV acrylics.

Mechanical Characteristics

To ensure that the AVs are structurally sound over the life of the experiment, the vessels, like most other large acrylic structures, are designed for a maximum stress of 5 MPa and a lifetime of 10 years. A setup was constructed to independently test these limits by stressing acrylic samples at known amounts and observe the effects over time. A photograph of the setup is shown in Figure 5.8(b). Long, thin acrylic pieces of well-known cross-section are hung from a frame from one end while known weights are hung from the bottom of the acrylic, which creates uniform, well-known stresses in the main length of the acrylic.

The first trial consisted of an acrylic strip stressed to 24 MPa. Significant crazing was viewed in the piece within 24 hours, and the piece broke after 48 hours. The second strip was stressed to 15 MPa, and moderate crazing was visible after 8 days of hanging. This piece was then removed and replaced with another strip that was stressed to 10 MPa. Minor crazing appeared after about 6 months and has persisted but not worsened appreciably after 2 full years of hanging. From these trials, the figure of 5 MPa over 10 years seems acceptable; vessels were designed to be supported such

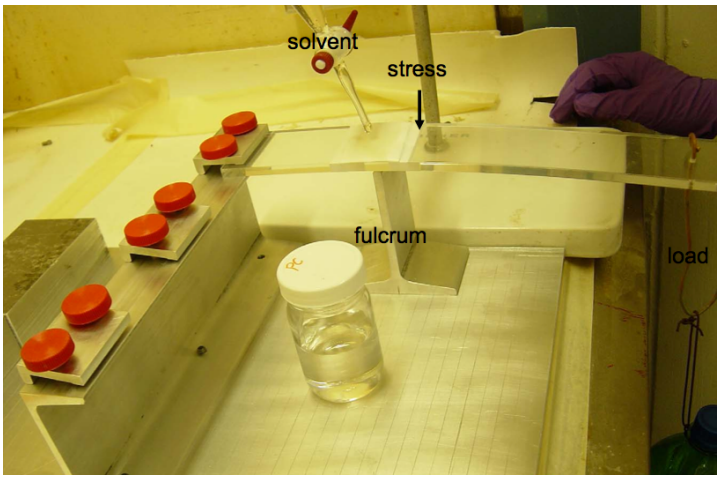

(a) Setup of mechanical compatibility tests of various candidate target liquids with acrylic.

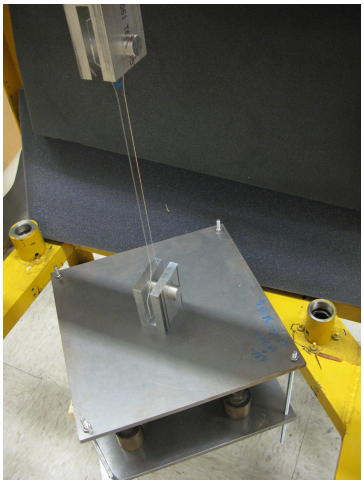

(b) Photograph of an acrylic stress testing setup. The acrylic is the long clear bar connecting the top metal hitch to the bottom weight

Figure 5.8: Photographs of two different stress testing setups, one for testing material compatibility, and one of testing maximum stress limits.

that stresses were well below the 5 MPa limit for all parts of the vessel structure. In addition, these tests show that short-term (on the order of a few days) stresses around 10-15 MPa are acceptable; this figure provides a guide to acceptable maximum stresses allowed during short-term processes such as shipping, lifting, and filling.

Materials Compatibility

It is important to test optical and mechanical compatibility between acrylic and candidate detector liquids, as many solvents and some liquid scintillators are known to cause crazing in stressed regions in acrylic. Mechanical compatibility testing was carried out in a manner described in the Handbook of Acrylics, the standard reference text on acrylics [115]; figures of the test setup can be seen in Figure 5.8(a). Strips of acrylic of well-known dimensions were held in position at one end and stressed on the other with a known weight. A fulcrum was placed underneath the middle of the

acrylic strip; above the acrylic in the area of the fulcrum a filter paper was placed and saturated with the test liquid. The stressed acrylic was then observed over a period of time to observe any changes resulting from the liquid-acrylic contact. Pseudocumene, a liquid scintillator solvent used in other experiments such as KamLAND, caused the stressed acrylic piece to break within one hour of loading the acrylic. Linear alkyl benzene (LAB), a commonly used solvent for detergents, did not have any appreciable effect on the acrylic after 30 hours of stressing, making it a good candidate use at Daya Bay.

Optical compatibility testing was done by placing acrylic samples into samples of candidate liquids for extended periods of time at elevated temperatures, to accelerate any possible leaching or other chemical interactions between the acrylic and liquid. The degradation rate with time of the LAB transmittance when exposed to acrylic was negligibly small after 21-28 days of testing at 40°C. as LAB was the most optically and mechanically compatible liquid with acrylic, it was selected as the liquid scintillator for the production target and gamma catcher liquids.

5.4 Fabrication

OAV Fabrication

OAVs are manufactured at Reynolds Polymer Technology, Inc., in Grand Junction, Colorado, USA [116]. The walls of the OAVs are constructed from 16 sheets of Polycast UVT acrylic [117]. The bottom, lid, and flange are cut from two large, thick blocks of Reynolds-cast UVT acrylic. The bottom ribs are made from 50 mm-thick sheets of Reynolds UVT acrylic and a central hub piece machined from a block of Reynolds UVT acrylic. The vessel elements were bonded using a proprietary UVT bonding syrup from Reynolds; the bond material appears in approximately 1/8" wide

regions between bonded sheets. A drawing showing the placement of acrylic sheets and bond lines on an OAV can be seen in Figure 5.9.

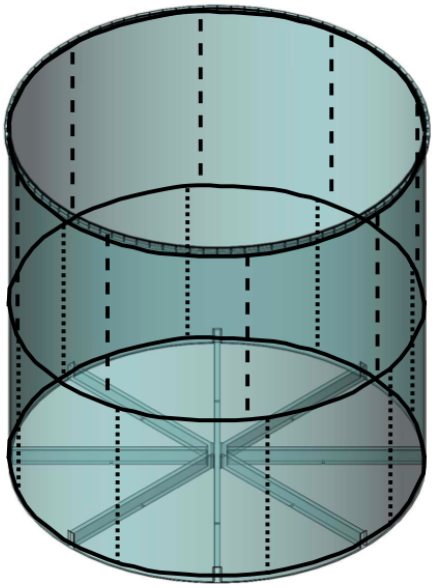

(a) Bond locations on the OAV barrel. Top cylinder bonds are dashed, bottom cylinder bonds are dotted, and circumferential bonds are solid.

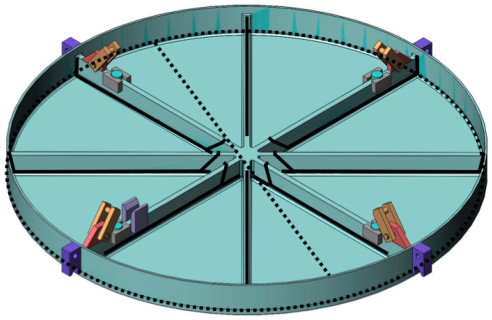

(b) Bond locations on the OAV bottom. Solid lines indicate bonds connecting the ribs and hub to the main vessel. Dotted lines indicate the bottom-barrel bond and the bond joining the two bottom sheets. All colored parts are also bonded onto the main structure.

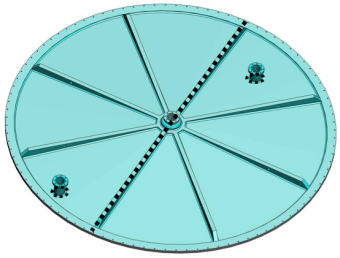

(c) Bond locations on the OAV top: directly through the lid middle and around the OAV lid ports.

Figure 5.9: Approximate bond locations on the OAVs.

OAV fabrication was preceded by the construction of a prototype OAV at the same facility, as well as a round of prototype acrylic optical testing to determine an acceptable acrylic for the production OAVs. Radioactivity, compatibility, stress, and

optical testing results for a range of acrylics are presented Section 6.1.

The cylindrical OAV walls are composed of two 4 m-diameter acrylic cylinders, each created by bending and bonding together eight acrylic sheets. The OAV top, bottom, and flange are machined out from two thick blocks of bonded UVT acrylic. Rib sections and a central hub are bonded to the bottom, dividing it into octants. Additional acrylic pieces for the IAV support structure and hold-down mechanisms are bonded to four of the ribs.

Annealing is done on the individual lid, wall, and bottom components to cure bonding material and to clear residual stresses introduced during fabrication. Care was taken to fully support the shape of acrylic components during annealing to avoid permanent deformation from components becoming more plastic at high annealing temperatures and sagging under their own weight. Such sagging was experienced during annealing of the OAV lid prototype. Annealing of subsequent OAV lids was done on a conical frame, while annealing of the OAV bottoms was done on precision-cut flat surfaces to ensure flatness of the OAV base and flange.

Bonding of OAV components is done using proprietary bonding syrup mixed by Reynods. After setting dams along the intended bond against the joining acrylic pieces, syrup is injected between the pieces and cured using a proprietary heating regimen. The OAV flange and bottom structure are bonded to the top and bottom cylinders, respectively. The top and bottom cylinders are then bonded together to complete the vessel construction. A final anneal is done after bonding to clear residual stresses introduced during bonding.

Vessel surfaces and bond lines are sanded and polished after bonding to remove excess syrup and discontinuities and to improve the clarity of the vessel surface. The OAV and IAV are polished down to 1 to 3 micron grit using aluminum oxide polishing powder, buffing wheels and water. A fully fabricated OAV's top and bottom can be

seen in Figure 5.10.

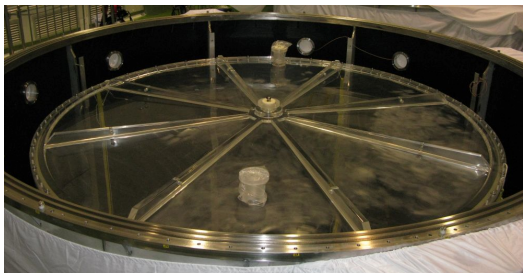

(a) Image of fabricated OAV top after cleaning. Notice the extra calibration port for the LS region.

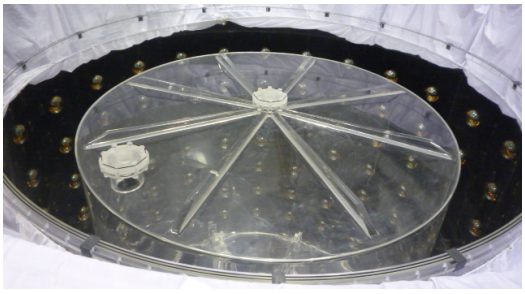

(b) Image of fabricated IAV top during installation. Notice in particular the bonded lid, unlike the OAV.

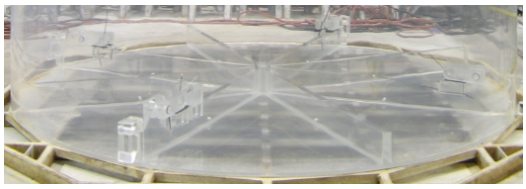

(c) Image of an OAV bottom after finishing fabrication. Notice that the ribs and extra features are on the OAV inside.

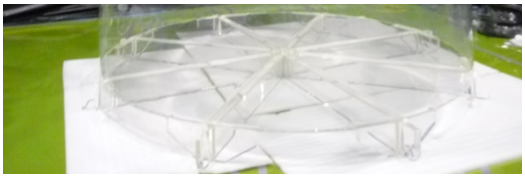

(d) Image of a fabricated IAV bottom during cleaning. Notice that all structural support is located on the IAV outside.

Figure 5.10: A comparison of the tops and bottoms of production OAVs and IAVs.

IAV Fabrication

IAVs were constructed at Nakano International Limited, in Taipei, Taiwan [118]. Nakano used PoSiang UVT acrylic for all parts: six 10-mm thick sheets for the walls, four 15-mm thick sheets for the top lid, four 15-mm sheets for the bottom lid, two 55-mm sheets for the ribs, and two UVT acrylic calibration ports. Sheets are joined together by approximately 1/8" wide bonding regions made out of a cured UVT syrup. A drawing showing the placement of acrylic sheets and bond lines on an IAV can be seen in Figure 5.11.

As with the OAVs, quality assurance measurements are done on candidate IAV materials to ensure the suitability of the production acrylic for the Daya Bay detector.

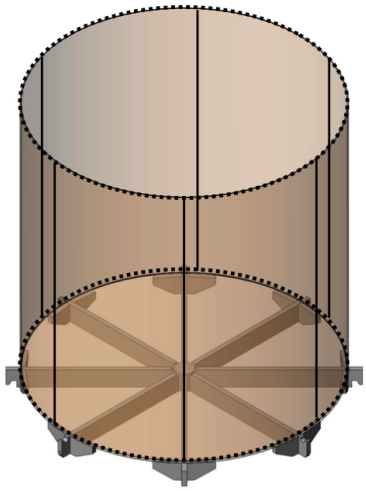

(a) Bond locations on the IAV barrel. Vertical bonds are solid and circumferential bonds are dotted.

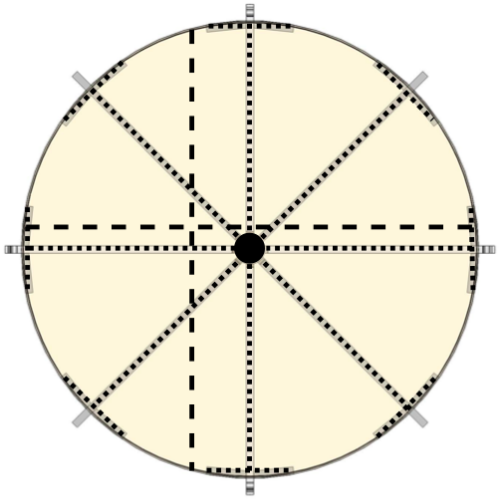

(b) Bond locations on the IAV bottom. Dotted lines indicate bonds connecting the ribs and hub to the main vessel. Dashed lines indicate the bonds joining the four main bottom sheets.

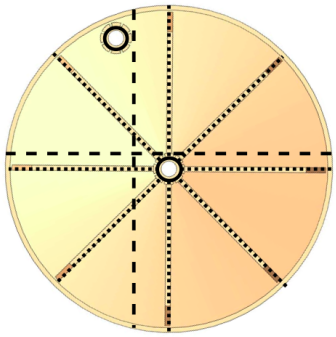

(c) Bond locations on the OAV top. Bond line indications are similar to that of the IAV bottom, with the addition of IAV top ports bonds.

Figure 5.11: Approximate bond locations on the IAVs.

Details of these measurements are discussed in Section 6. In addition, a prototype IAV was fabricated to test the construction processes and vessel design.

Vessel construction begins by forming the six wall sheets and then bonding them together using the UVT syrup and a system of dams to keep the syrup in place while the bonds undergo UV-curing. During this process, the top and bottom of the vessels

are constructed separately in the same manner, with the top being baked on a mold to achieve a conical shape. In addition, ribs are bonded onto the IAV bottom and top, and center and off-center calibration ports are bonded to the IAV top. Following construction, each separate component's surfaces are polished in a similar manner as described in the OAV construction. After polishing, the top is bonded to the walls. The inside of the vessel must then be cleaned before the final bond is made, as after this point no further access to the inside of the IAV exists. The cleaning of the IAV will be described in greater detail in Section 5.1. After cleaning, the bottom is bonded to the rest of the vessel, completing construction. The IAV bottom edge must be properly shaped to encourage excess bonding syrup to flow out of the vessel during curing rather than into the vessel where it cannot be removed or polished out. A picture of a fabricated IAV's top and bottom is visible in Figure 5.10.

In Figure 5.10 one can identify contrasting features on the IAV and OAV top and bottom . On the top, the major differences are the presence of the extra OAV flange seal and an extra calibration port. On the bottoms, the major difference is that the OAV's support structure is inside the OAV, while the IAV's support structure is on the outside of the IAV.

Overflow Tank Fabrication

The three main acrylic components for the overflow tanks are the LS overflow tank, the Gd-LS overflow tank, and the tank lid. The acrylic pieces that comprise each of these three components are fabricated by subcontractors of Reynolds by cutting and forming sheets of UV-absorbing acrylic into designed shapes. The component sub-pieces are then sent back to Reynolds to be bonded into the three separate overflow components using Weld-on 40 acrylic cement. Other smaller acrylic parts from the overflow tank system and connection hardware are also manufactured by Reynolds'

subcontractors.

5.5 Transport and Shipping

After fabrication, the IAVs and OAVs are transported from their respective locations to the Surface Assembly Building at Daya Bay, where they are assembled into the antineutrino detectors. The OAVs are manufactured at Reynolds Polymer Technology in Grand Junction, CO and are transported by truck to Long Beach, CA, by ship to Yantian Port, and finally by truck to Daya Bay. The IAVs must be trucked from the Nakano factory in Taipei to port, and then shipped to Yantian, where they are then brought by truck. The entire shipping route of the vessels can be seen in Figure 5.12.

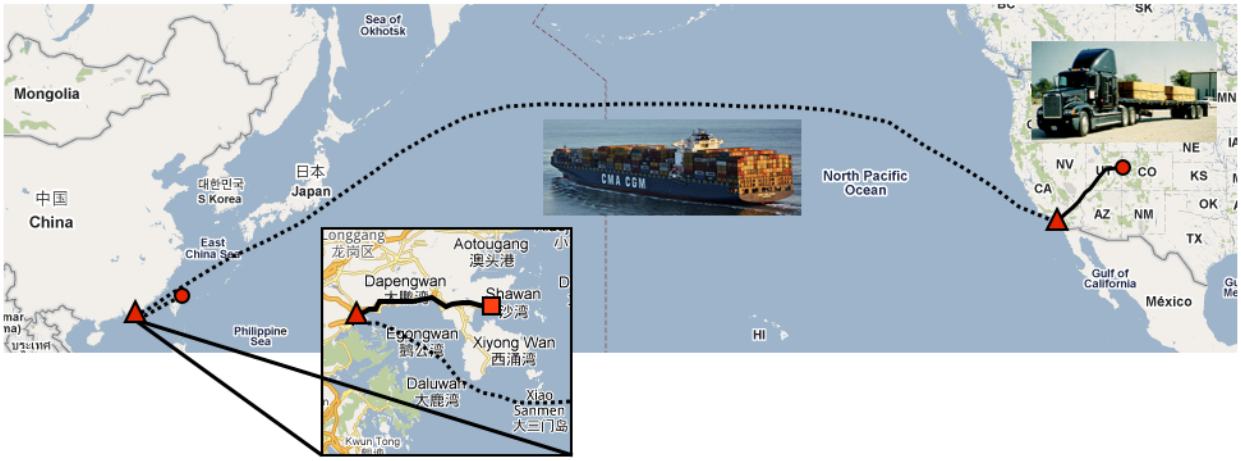

Figure 5.12: A map of the entire shipping route for OAVs and IAVs. Circles indicate the origin locations of OAV (Grand Junction, CO, USA) and IAV (Taipei, Taiwan), triangles indicate the ports of Yantian and Long Beach, through which the AVs travel, and the square indicates the final destination, Daya Bay, China.

Shipping Crates

For transport, the vessels are packed into shipping frames and containers that support the structure of the AVs and minimize their exposure to light and environmental

conditions. The OAV shipping frame can be seen in Figure 5.13. The sealed OAV rests on a steel square base and is secured by fastening hold-down pieces over all four OAV lifting hooks. A steel A-frame structure rises on each side of the base. A steel OAV lid support structure is lowered onto the top middle of the four A-frames and is attached to ears located there. A plug in the central OAV port is screwed upward into the center of the lid support structure, providing extra structural support for the lid during shocks and preventing resonant vibrations in the lid during shipping. The OAV is protected from impacts by casing made of polystyrene and kiln-treated wood and plywood. Underneath this casing are layers of self-adhesive plastic film and Coroplast [119] to preserve the surface quality of the OAV. To ensure that the inside of the vessel remains somewhat isolated from the surrounding environment, a hose and HEPA filter is connected to both off-center ports.

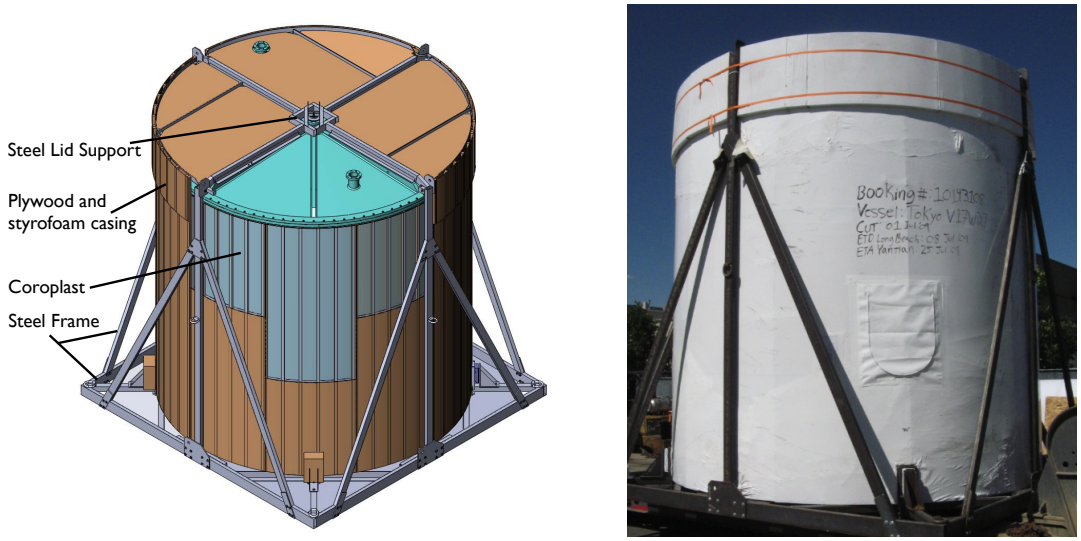

(a) ISO drawing of an OAV in its shipping container. The lifting frame is also included in this drawing.

(b) A photograph of a production OAV in its shipping frame.

Figure 5.13: An isometric drawing and photograph of the OAV shipping frame.

The IAV shipping container can be seen in Figure 5.14. The container consists of six steel-framed panels lined on the inside with wood panels. These panels are bolted

together to form the cubical shipping crate. Foot-thick styrofoam panels are placed inside these outer panels to support the IAV on all sides and to absorb shocks during shipping. Lid support is less crucial for the IAVs, as they are smaller in diameter that the OAVs. To protect its surfaces, the IAV is coated in plastic wrap and then covered with black plastic sheeting. The IAV ports are covered with flanges containing HEPA filters to ensure that the IAV insides retain their cleanliness.

Figure 5.14: Photograph of a partially-unpacked IAV in its container. Some of the styrofoam packing has been removed, but the IAV remains in its black plastic casing with styrofoam in front and behind it.

Shipment Monitoring

Several devices are used to monitor OAV location, acceleration, temperature, humidity, pressure and light exposure during shipment. Customs issues in shipping prevented the application of the same monitoring regimen for the IAVs; as a result, no shipping data is available for IAV1 and IAV2.

For the OAVs, acceleration data is collected every 9 seconds by MSR 145W dat-

aloggers [120] mounted on the base of the shipping frame and the OAV lid. Additionally, the MSRs on the base recorded temperature and pressure readings every 90 seconds. The lid-mounted MSR had a pressure sensor on an external cable, which allowed measurement of the pressure inside the OAV. The largest pressure changes correspond to changes in altitude as the OAVs are trucked from ∼1400 m to sea level. Trackstick Pro GPS data loggers are also mounted on the shipping frame to provide location information while the OAVs are in the United States [121]. To measure shocks, such as would occur if the AV is dropped, Shock Timer 3d loggers are mounted along with the MSRs on the shipping frame and OAV lid [122]. These sensors recorded the date and time of all shocks over 3 g and took additional temperature and humidity readings every hour. Finally, a pair of HOBO Pendant Dataloggers are mounted from a threaded rod suspended inside each AV to monitor light levels [123]. These are expected to be low as the OAVs are shipped with opaque coverings to shield them from UV.

The first pair of OAVs left Colorado on June 25, 2009 and arrived at Daya Bay on August 5 and August 6. Just outside of Grand Junction, metal lifting tabs attached to the top of the OAV lid support structure were bent down by impact with a low bridge; this impact was recorded by the shock timers. The truck was returned to Reynolds to ensure that the vessels were not damaged. Other shocks greater than 3 g were recorded 10 times on the base sensors on each side of the OAVs, although most shocks did not correlate in time between sensors. The few sensor-correlated shocks seem to correspond to periods of loading or unloading. Periodic vertical acceleration measurements are shown in Figure 5.15; during the trip, typical accelerations were between 0.2 g and 0.4 g in excess of gravity. The changes in acceleration patterns give a picture of the status of the vessel, whether it was moving on the road, at rest, moving on a ship, or being loaded and unloaded.

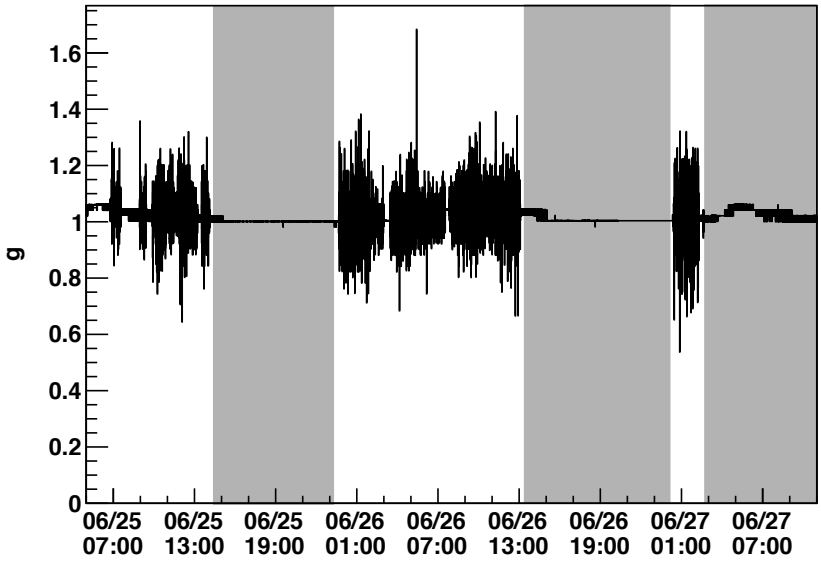

Figure 5.15: Periodic acceleration measurements, measured in g. The measurement period begins in Grand Junction, Colorado and ends at port in Long Beach, California. The gray-shaded periods of low acceleration correspond to times when the OAVs and transport truck were at rest.

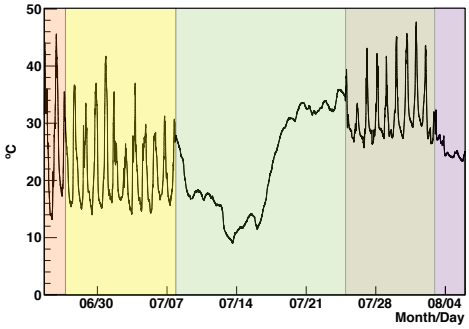

(a) Temperature measurements during OAV transport. The figure is split into five periods: by truck in USA (red), at port in Long Beach (yellow), at sea (green), at port in Yantian (gray), and en route to and in the SAB (purple).

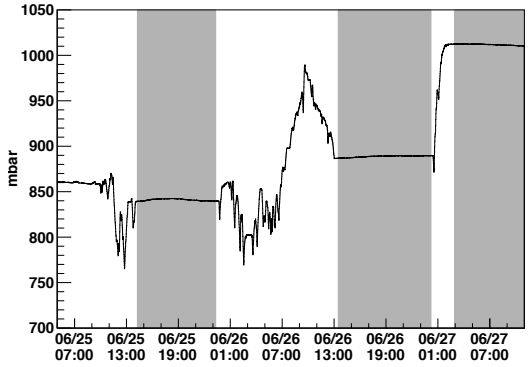

(b) Pressure measurements during OAV trucking transport in the US. Pressure changes are due to altitude variations along the trucking route shown in Figure 15. The gray-shaded periods correspond to times when the OAVs were at rest.

Figure 5.16: Temperature and pressure of the OAV environment during transport. Note that the changes of temperature and pressure with time convey the vessel's current general location.

The temperatures over time recorded by one sensor on the OAV shipping frame base is shown in Figure 5.16(a). Periods of rapid temperature fluctuation correspond to time spent outside on the road or in port, while the smoothly varying period corresponds to time spent on the ocean. The temperature sensor recorded variations between 8 °C and 48 °C, with a maximum of 29 °C change over the course of 12 hours. Another temperature sensor located within the OAV packaging on its lid experienced temperature variations of only 20 °C.

This 20 °C temperature fluctuation, if also experienced by the OAV, corresponds to a 4 mm variation in radius of the OAV from thermal expansion and contraction. It was not clear from the available temperature data how much temperature fluctuation, and thus acrylic expansion and contraction, varied over the surface of the OAV. Excessive or uneven expansion and contraction of the OAV is a concern as it is not known if such behavior will affect the mechanical strength of the OAV appreciably. Temperature tests have been conducted that ensure acrylic and bond optical and mechanical stability in the presence of these environmental fluctuations. As an added precaution, future OAVs were shipped with extra insulation to flatten out these temperature fluctuations.

The recorded pressure history during the driving portion of the trip is shown in Figure 5.16(b); the rise in pressure at the end of the trip is the result of the transport truck coming down to sea level. Differences in pressure inside and outside an OAV were never greater than 1 mbar. The light sensor data did not show any unexpected periods of brightness. In addition, a light-sensitive acrylic monitor sample mounted by the OAV1 lid sensors did not show any signs of optical degradation, as would be expected if it had experienced any moderate exposure to sunlight.

5.6 Assembly

Cleanliness and Cleaning

When they reach Daya Bay, acrylic vessels must be cleaned to ensure that the amount of radioactive contaminating material inside the detector's target region is minimized. In addition, cleaning improves the optical quality of the IAV and OAV surfaces and removes contaminants that are incompatible with the AD liquids. The quantitative cleanliness goal is to ensure that the radioactivity rate from contaminants in the IAV and OAV is less than 10% of the expected radioactivity from the GdLS liquid. This corresponds to a contamination radioactivity of 1 Hz. Table 5.3 presents rough estimates for acceptable amount of possible contaminants based on their activity.

Contaminant	Source	Isotope	Acceptable Amount
Al_2O_3 Powder	Spot-Scrubbing	^{40}K	36 kg
Fingerprints	Human Contact	^{40}K	$>$ 1000 handprints
Human Sweat	Human Contact	^{40}K	< 1 cm^3
Bamboo or Wood	Used for Scaffolding	^{40}K	< 3 cm^3
Dirt	Surrounding Environment	^{40}K,^{232}Th,^{238}U	2 g
Paint Chips	Semi-Cleanroom Crane	^{40}K,^{232}Th,^{238}U	< 50 g

Table 5.3: Possible radioactive contaminants in the OAVs and IAVs, listed with their maximum acceptable post-cleaning presence.

Cleaning of the IAV insides was done over the course of two days at Nakano. Cleaning of the IAV outsides was done in the course of a day per IAV at the Daya Bay SAB. OAV cleaning took 4-5 days per vessel at the SAB.

Cleaning of the OAVs is done in the SAB semi-cleanroom, a climate-controlled, low-particulate environment. The top of the vessel is removed, and the top flange and lid are then spot-scrubbed with Al_2O_3 powder, water, and a microwipe cloth to remove salt water residue, rust, and plastic wrap residue. The entire lid is washed on top and bottom with a 1% Alconox solution and fresh microwipes and rinsed with a

pressure washer using 10 MΩ water. The conductivity of the rinse water is measured with a conductivity meter. When the rinse water conductivity matches that of the water directly from the pressure washer, rinsing is considered complete. The lid is then dried with microwipe towels and covered with a clean tarp. This same process is applied to the inside and outside of the OAV. After cleaning the vessel inside and walls, the lid is then reconnected and the vessel is lifted onto blocks so that the bottom can be spot-scrubbed and cleaned. A few pictures of the cleaning process can be seen in Figure 5.17.

(a) Scrubbing the OAV inside with 1% Alconox solution.

(b) Testing rinse water conductivity with a conductivity meter. All conductivity meters used were accurate to 0.1 μS.

Figure 5.17: Photographs taken during IAV and OAV cleaning in the SAB at Daya Bay.

The same general procedure is applied during the cleaning of the outside of the IAV and the acrylic overflow tank parts in the SAB semi-cleanroom. The inside of the IAV is also cleaned in the same manner, but in a class 10,000 clean tent at the Nakano factory before the vessel is completely bonded together. AV tube connection hardware parts are cleaned using an ultrasonic cleaner first in a 1% Alconox solution, and then in water.

Leak-Checking

Vessels are leak-checked to ensure that the target volume remains well-known to better than 0.1% after five years of detector operation. In addition, the leaking of non-scintillating liquids like water or mineral oil into the scintillating regions will reduce the detector's light yield.

The leak requirements for the inner volumes are listed in Table 5.4; if these requirements are met, the uncertainty in target mass resulting from leakage will be <0.013%. Leak rates of argon in cc/sec at a given pressure differential are calculated from the 5-year acceptable leakages to serve as specifications for the leak-checking process. While the entire AD is surrounded by water, no single direct water-to-LS junction exists. Because of this, a water-to-LS leak rate specification is not applied.

Leak Type	ΔP (cm H_2O)	5 yr Leakage (l)	Argon Leak Rate (cc/sec)
LS to or from GdLS	15	3	3.8×10^{-2}
MO to LS	15	5	6.4×10^{-2}

Table 5.4: Leak rate specifications for the central liquid volumes, given for argon and for the AD liquids. As the leak rate is dependent on the pressure differential between zones, a conservative estimate of the zone pressure differential is also given.

Each AV pair has numerous seals in four main locations: on the OAV lid, on the IAV calibration/overflow tube stacks, on the OAV calibration/overflow tube stacks, and near the stainless steel lid connections. Some leak-testing procedures are done at Reynolds, and some are done on-site at the Daya Bay SAB using varied procedures that depend on the type and location of the seal.

Double o-ring seals are used facilitate high-precision leak checking of the critical OAV flange connection. This seal can be checked by pressurizing the region between the o-ring seals with argon using a special gas input port, and then monitoring any change in pressure over time. The maximum leak rate on the main seal of OAV1 and OAV2 was 4.4×10^{-2} cc/sec at a pressure of around 5 psi. This is well below 0.1 cc/sec,

the maximum acceptable argon leak rate from MO to LS given in Table 5.4, corrected to a pressure of 5 psi.

The OAV port single o-ring seals were tested at Reynolds by placing a tight seal at the bottom of the port, as in Figure 5.18, and then pressurizing the entire sealed port to 5 psi and monitoring any change in pressure with a pressure gauge. The maximum change in pressure for any OAV port was 3.2×10^{-2} cc/sec, significantly below the 0.1 cc/sec leak-rate limit.

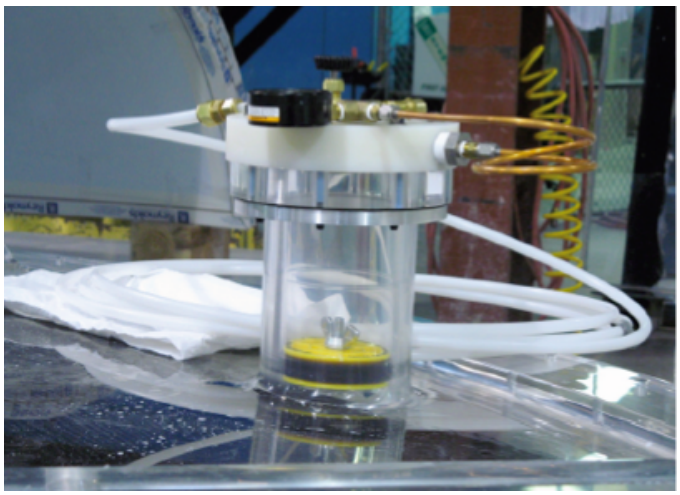

Figure 5.18: Photograph of the double o-ring seal leak-checking setup for the OAV ports. The yellow seal at the bottom of the port is clearly visible, as is the gas input.

For single and double o-ring seals that cannot be easily accessed or isolated, a different leak-checking procedure is used. The calibration tube stacks are assembled and attached to the AV, which is then pressurized to 10-15 cm water column with argon gas. Gas input routing and pressure control are centralized in a gas rack located in the SAB cleanroom. Gas output from the AD is run through an exhaust system to the SAB exterior. To prevent AV over-pressuring from line kinks and other gas system malfunctions, safety relief valves are also placed at a number of locations in the gas system. A diagram of the gas system circuit can be seen in Figure 5.19(a). When the AVs are sufficiently pressurized, an argon sniffer can be used to check for

leaks along the tube stack. The appearance of the IAV lid area during IAV tube stack leak checking can be seen in Figure 5.19(b). The sensitivity of this method is a minimum leak rate of 10^{-3} cc/sec and is limited by the stability of the gas sniffer.

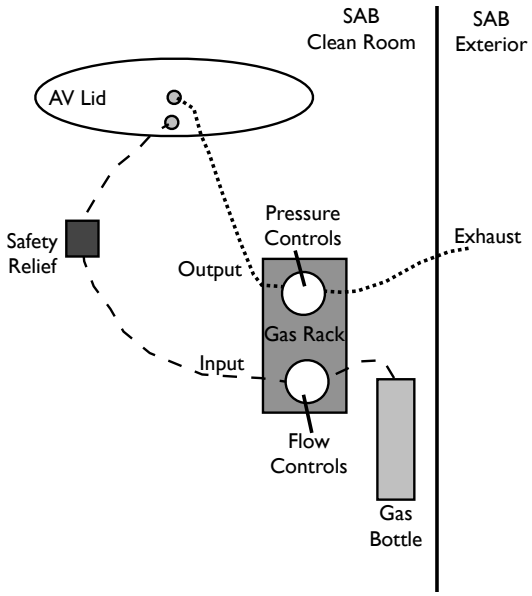

(a) Diagram of the gas circuit for AV leak checking. Gas is fed from bottles through a gas control rack and the into AV. Output air is pushed out of the AV and through an exhaust line to the exterior of the SAB. AV gas pressure is controlled through the use of pressure relief bubblers.

(b) Photograph of the IAV tube stack leak-checking setup. An argon sniffer is run up and down the tube stack, which is pressurized with argon gas.

Figure 5.19: An overview of the gas circuit and appearance of the leak-checking system in the Daya Bay SAB cleanroom.

The maximum measured leak rate measured using this method was 3×10^{-3} cc/sec at one location on on OAV1, well within the maximum specified GdLS-to-LS leak rate listed in Table 5.4. The leak rates in all other areas were below the sensitivity of the gas sniffer. The same method is used for measuring the leak rates in the OAV calibration tube stacks with similar sensitivity and results.

A final test of the aggregate leak-tightness of the AVs was made after completing installation of the IAV and OAV tube stacks and SSV lid. Using the same gas circuit

from the previous test, the GdLS and MO regions were pressurized with argon at 10 cm water pressure, while the LS region was filled with freon at 1 cm water pressure, to ensure minimal freon leakage during filling. Freon and argon concentrations were verified by measuring the lowered oxygen content of the exhaust air from the regions with an oxygen monitor. Once the LS region was composed of >75% freon, the pressure differentials were reversed, leaving the freon-filled LS volume pressurized with respect to the GdLS and MO volumes; this maximized any possible freon leakage. After 20 hours, the freon concentration of the AD1 GdLS and MO region exhausts were measured at 66 ppm and 52 ppm with a freon sensor; similar values were found for AD2. These values are below 159 ppm and 133 ppm, the maximum values of acceptable freon concentration in the GdLS and MO exhaust based on the AD leakage requirements.

As was mentioned before, the acrylic overflow tank components are contained in a nitrogen gas environment. The leak-tight stainless steel housing that separates this gas volume from the water volume surrounding the AD and overflow region will not be discussed in this paper. Any possible leakage or splashing between overflow tank volumes is minimized by the acrylic covers on each volume.

Installation

After the OAV is cleaned in the semi-cleanroom, the OAV lid is temporarily reattached and the OAV is moved into the cleanroom. Using the 40 ton cleanroom crane and proper rigging, pictured in Figure 5.20, the OAV is lifted and lowered into a cleaned SSV located in the AD assembly pit. The OAV is set down on the bottom reflector, a 4.5 m diameter circular sheet of specularly reflecting material sandwiched between two 10 mm thick acrylic sheets. The reflector rests on the SSV bottom ribs. Surveys are then done on the OAV lid using a Leica System 1200 Total Station to de-

termine if the OAV is level and if the OAV ports line up with the previously surveyed locations of the SSV ports [124]. The vessel is shimmed, re-situated, and re-surveyed until the SSV and OAV ports are acceptably aligned and levelled. Survey details and results will be further discussed in Section 6.3.6. When surveys are complete, stainless steel hold-down mechanisms are installed over the OAV lifting hooks to hold the OAV in place during all future AD activities.

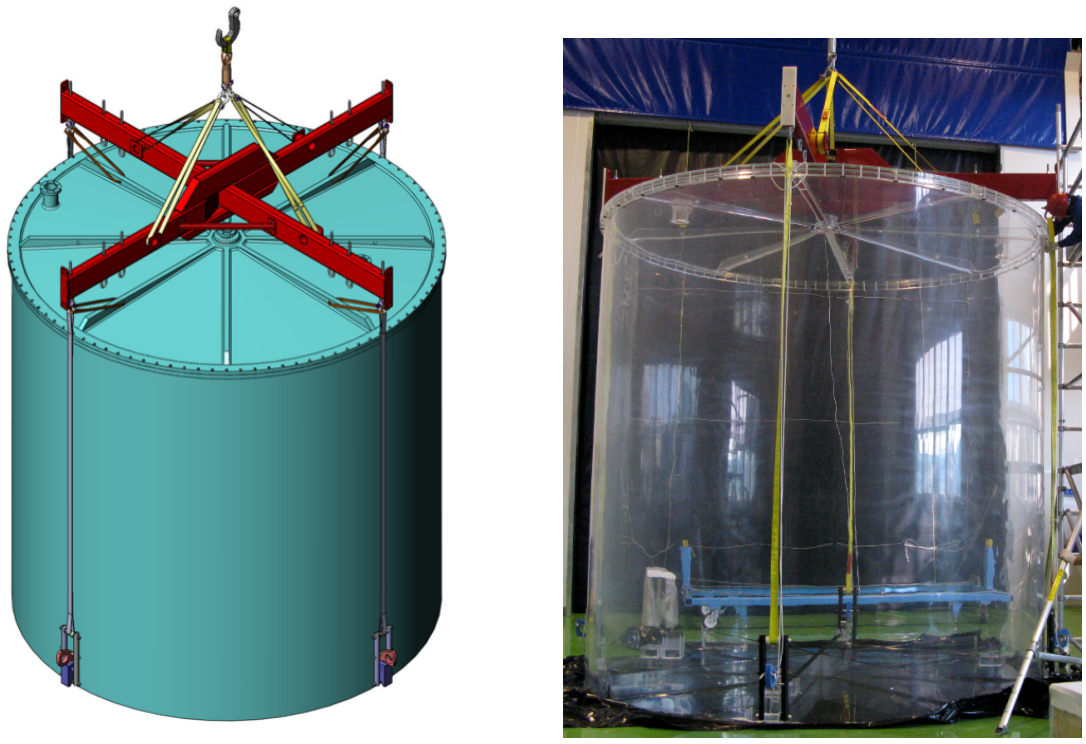

(a) Drawing of a lifted OAV.

(b) Photograph of the OAV just before lifting in the SAB.

Figure 5.20: A drawing and photograph of the OAV rigged for lifting. Visible are the lifting fixture and the rigging connected to the OAV via the OAV lifting hooks.

Once the OAV is in place, its lid is removed and the OAV flange is surveyed. Shims are then installed along with the IAV support pucks, to ensure that the IAV is level when installed. A cleaned IAV is lifted using the same lifting frame and slightly different rigging, and lowered into the OAV until it is resting on the pucks.

The IAV ports and top are then surveyed to check if they are concentric with the other OAV and SSV ports, and repositioned and shimmed if necessary. This data is also included in the Section 6.3.6. Once proper alignment has been achieved, the hold-down mechanisms are engaged to secure the IAV to the OAV. A final survey of the IAV top is recorded to provide flatness and concentricity data for geometric characterization. A photo of the nested acrylic vessels can be seen in Figure 5.21. Assembled ladders of PMTs are installed after the securing of the vessels.

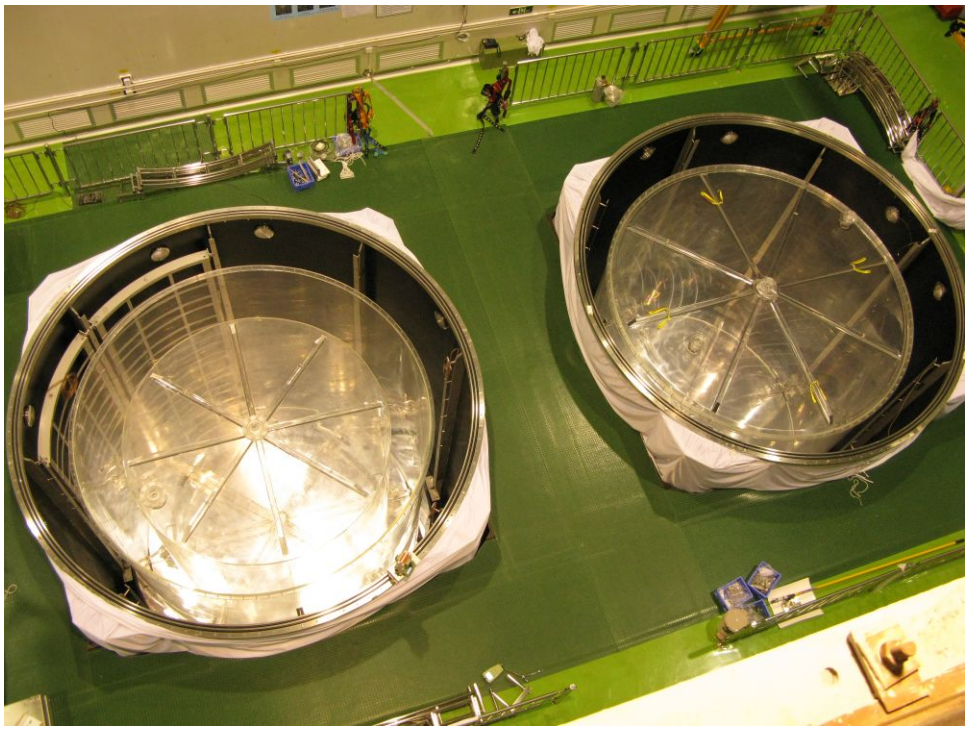

Figure 5.21: A photograph of the assembly of a pair of ADs in the cleanroom. Assembly for the two vessels is at different stages in the photo: AD1, on the left, is shown with a nested IAV and OAV, while AD2, on the right, is shown with an OAV with lid attached.

At this point, the IAV connection tubes are installed, leak-checked, and removed so that the OAV lid can be installed and its double o-ring seal leak-checked. The top AD reflector, which rests on top of the OAV lid, can then be installed. Next, OAV connection tubes are installed onto the OAV lid and are leak-checked. If all

seals pass their leak-checks the SSV lid can then be installed. Once the SSV lid is secure, off-center OAV connection tubes are secured to the SSV, and IAV connection tubes are fed down through the OAV tubes and connected to the IAV ports. With the the lid and connection tubes properly installed, the final three-zone leak check can be performed. The overflow tank assembly is then assembled and connected to the central OAV and IAV tubes and SSV lid, completing the AV and overflow tank installation. A picture of overflow tank installation can be seen in Figure 5.6(b).

Chapter 6

Expected Identicalness of AD Response

6.1 Introduction

In the previous discussions of the near-far relative measurement of reactor $\overline{\nu}_e$ flux, we have assumed that all detectors are physically identical, having the same geometric, optical and mechanical properties, and thus having functionally identical detector response. In practice, this will not be the case; possible geometric, optical and other parameters that can vary from detector to detector are listed in Table 6.1. By varying these detector parameters individually in detector simulations, any differences in detector response arising from differences in as-built AD parameters can be estimated. This mapping between as-built differences and detector response can then be compared to the observed differences in as-built ADs found during construction and assembly via characterization and QA measurements. In addition to demonstrating the proper assembly and functionality of the detectors, this process will provide some guidance in thinking about the degree of detector response difference and systematics

for the first two ADs. Ensuring sufficient identicalness of detector response is a critical part of understanding the detector-related systematic in a relative measurement between near and far detectors.

Further, this process will help determine how similar each of the ADs in the first detector pair will be to ADs from the other three detector pairs, which will be assembled and filled with liquids at a different time. If differences between pairs are minimal, efforts to reduce detector systematics by pair-wise installation or detector swapping may produce little benefit. Lastly, it will provide some guidance in thinking about which AD components are more likely to contribute to differences in detector response, and which are not likely causes. This knowledge can help in tuning detector simulation parameters and identifying sources of unexpected detector response.

Component	Parameter
AVs	Shape and dimensions Thickness Positioning Optical Properties
AD Liquid Regions	Shape Optical Properties H/Gd Ratio H/C Ratio
Reflector	Shape and dimensions Positioning Reflectivity
PMTs	Distance from AD center Distance from radial shield Dead PMTs
Radial Reflectors	Reflectivity Shape
All	Radioactivity Spill-in/out Effects Opaque Inclusions

Table 6.1: A list of detector components and parameters that are subject to physical variation or non-identicalness between detectors.

For each detector component, this chapter will outline:

1. The possible parameters that can vary.
2. The change in detector response demonstrated by simulations arising from variation of each parameter.
3. What variation in that parameter was seen between the first two as-built ADs.
4. What level of variation can be expected between ADs from different detector pairs based on the AD group's experience in constructing the first two detectors.

6.2 Simulation Overview and Identicalness Metrics

To examine the effect of each source of physical non-identicalness on detector response, detector simulations were carried out using the simulation and analysis software framework NuWa, which is based on the Gaudi framework developed by LHC [125]. Detector simulations utilize Geant4 as a basis for detector geometry definition, vertex generation, and particle simulation [126]. The results of Geant4 simulation are then run through electronics and trigger simulations developed by the collaboration to create simulated detector triggers and readouts. Simulated data from NuWa has a final structure identical to that of the Daya Bay DAQ output. Because of this, real and simulated data can be analyzed using the same tools in NuWa. NuWa analysis modules and root file output are identical for real and simulated data, excepting the additional presence of generation and particle history handling and information for simulated data.

For identicalness simulation studies, a sample of events of a specific particle type and vertex distribution is generated using the baseline detector design; for example, one can generate 10^6 IBD neutrons uniformly throughout the target region. Then, the same event sample can be run with different random seeds in an AD where one detector parameter is altered in the NuWa detector description. This can be done repeatedly to obtain samples for numerous values of the one altered parameter. Finally, in order to concretely quantify differences in all aspects of detector response, the data is analyzed to compare standard AD performance metrics:

1. **Neutron Detection Efficiency and Related Uncertainty:** For this metric, a small sample of simulated calibration data is run and the resulting PE spectrum is used to determine the calibrated 6 MeV energy cut value in PE. The neutron detection efficiency is defined as the number of events above that PE value over the total number of Gd-captured neutron events. The neutron energy cut uncertainty is defined by the energy scale uncertainty of the detector, which is estimated to be 1% for the purposes of this simulation. To determine the energy cut uncertainty, the number of events within 1% of the calibrated 6 MeV peak is divided by the total number of events. As the uncertainty is only a fraction of a percent, large statistics and long simulation times are needed to detect statistically significant numbers of events in the $\pm 1\%$ uncertainty bin. These metrics are especially important, since they are directly related to the experimental sensitivity.

   The Daya Bay experiment will not be able to accurately determine its absolute energy cut efficiency to better than 0.5% without extensive special calibration deployments. Thus, small variations in detection efficiency demonstrated by these studies will not be measurable between the real detectors, and thus will

contribute directly to detection efficiency uncertainty. This point underscores the crucial importance of designing and building detectors that are as identical as possible, as well as the importance of these variation simulation studies in ensuring that detector response will be acceptably identical.

2. **H/Gd capture ratio:** The fraction of neutrons capturing on Gd. This metric is also directly related to the experimental sensitivity. This quantity can be measured in-situ, relatively between detectors to better than 0.1% by comparing the detectors' neutron capture times on Gd.

3. **Light Yield:** Light yield is defined as the average number of photoelectrons per MeV of visible energy created by a particle. The relative change in light yield from the baseline detector design is also commonly cited in this thesis. This metric is not directly related to the experimental sensitivity, and as such is less powerful in determining identicalness of detector systematics. However, it can be used as an easy proxy for other light yield-related metrics, like detection efficiency and its uncertainty: if the light yield of the detector is not impacted significantly by a detector variation, then detection efficiency and its uncertainty will almost certainly not be affected. The relation between light yield and efficiency uncertainty is explored in detail in the simulation studies.

4. **Detector Resolution:** By fitting the peak of the PE spectrum from a given event with a Gaussian, the width of the fit can be obtained and used as a measure of detector resolution. This metric is also not directly related to detector sensitivity.

5. **Light Yield Non-Uniformity:** This metric compares the light yield of events generated in different locations in the detector. It typically consists of a 2D histogram in R or X and Z showing the light yield relative to the detector

center for different detector location bins. This metric is useful in determining if isolated regions of the detector are especially impacted by a particular detector variation.

6. **Reconstruction Efficiency and Biases:** Specific methods of vertex and energy reconstruction will be discussed in detail in Chapter 7. Complex event reconstruction algorithms may fail to return reconstructed values or return excessively biased values for non-ideal detectors. Reconstruction efficiency, the total number of successfully reconstructed events over the total number of events, defines how well the reconstruction algorithm processes correctly. Reconstructed position and energy biases can be found by plotting the generated minus reconstructed energy and position for each bin on a 2D histogram in X versus Z or X versus Y.

7. **Radioactivity Singles Rates:** In order to gauge changes in the rate of single radioactivity-related triggers, or singles, resulting from a detector variation, a set number of backgrounds events can be generated for a baseline and varied detector; the relative difference in detection rates above the 1 MeV prompt energy cut between the two cases determines the percent change in singles rate expected from that detector variation.

6.3 AV Non-Identicalness

Shape and Dimensions

The shape of the OAV and IAV were changed in simulation by varying the height and width of the cylinder, as would be the result of out-of-tolerance AV fabrication, or by applying a concave hyperbolic profile to the AV walls or a spherically convex

shape to the AV top, as could be the result of pressure differentials between different AD liquid regions. The effect of these changes in shape and the resultant change in target volume on neutron detection efficiency and related uncertainty are shown in Figure 6.1(a) and 6.1(b). In addition, the change in detection efficiency as a function of LS thickness (which changes as the result of OAV shape variations) is pictured in Figure 4.4. All shapes appear to have a similar effect on these metrics, with the main determinant of change in metric being the change in target volume. For example, a 4% change in target volume as a result of shape variations results in a 0.4% change in detection efficiency and a 0.01% change in detection efficiency uncertainty.

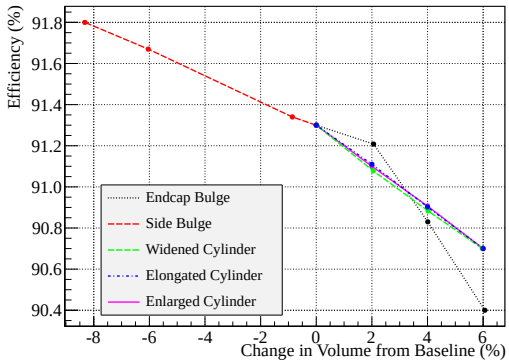

(a) Change in n detection efficiency versus change in target volume resulting from IAV shape variation.

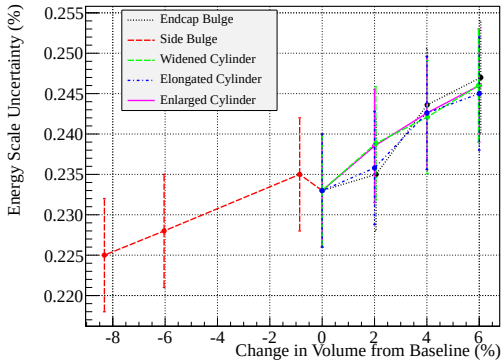

(b) Change in n detection efficiency uncertainty versus change in target volume resulting from IAV shape variation.

Figure 6.1: Changes in AD metrics resulting from changes in AV shape. Detector response changes appear to depend more on target volume than on the shape of that volume.

In the as-built detectors, the height and diameter of the AVs were measured during quality assurance testing. Outer diameters were measured at various heights on all four AVs using a pi tape measure; heights were measured with a tape measure. Outer-diameter and height data and design tolerances for all four of the first two AVs can be seen in Figure 6.2 (height) and Figure 6.3 (diameter). The cross-sectional shapes of the vessels were obtained for the the OAVs by doing inner diameter measurements

at a number of angular locations, and for the IAVs by measuring the angles between ribs on the IAV outside. The measured cross-sections for the first AVs were circular to within 1 cm. Diameter and height varied by as much as a few mm from place to place on the same AV; the average diameter difference was 5 mm between OAV1 and OAV2 and 0 mm between IAV1 and IAV2. The IAVs showed a relative difference in height of 5 mm, which corresponds to a 0.3% difference in target volume.

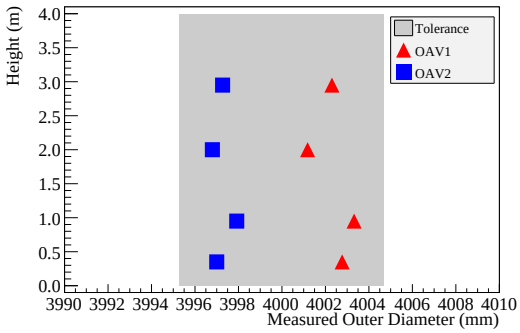

(a) Measured OAV diameter variations with height.

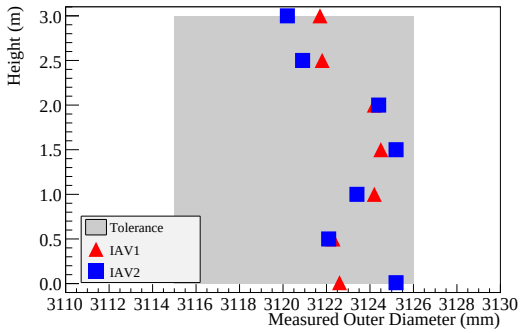

(b) Measured IAV diameter variations with height.

Figure 6.2: IAV and OAV diameter measurements for both vessels, measured at various heights on the AVs. Only one measurement was taken at each height. Tolerances are indicated by the grey band in each figure.

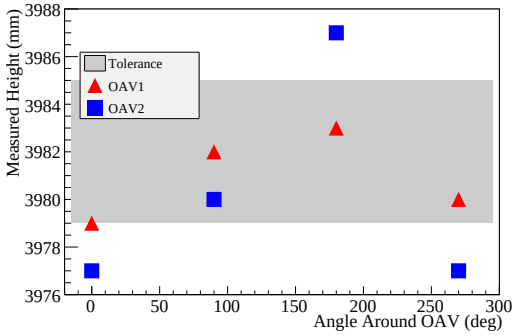

(a) Measured OAV height variations with angle around the OAV outside edge.

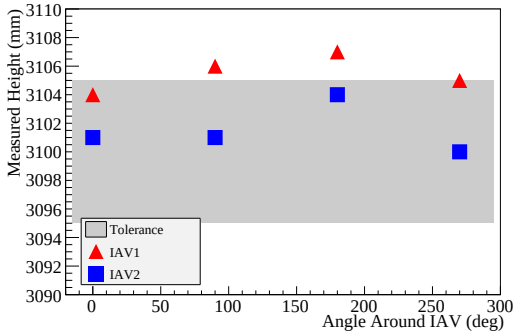

(b) Measured IAV height variations with angle around the IAV outside edge.

Figure 6.3: IAV and OAV height measurements for both vessels, measured at various angles on the AVs. Only one measurement was taken at each height. Tolerances are indicated by the grey band in each figure.

The AVs may bulge during operation from pressure differentials between detector zones, changing the volume of the target region. However, this change in volume is limited by the amount of liquid in the overflow tanks, which is 0.3% of the total target volume. In addition, the size of the target volume, which is the main determinant of change in detector metrics, will be known to better than 0.1%.

Comparing these physical differences of 0.3% in target mass to changes in detector response from the above results, one can conclude that efficiency will be similar between detectors to <0.1%. The efficiency uncertainty will be more or less identical for both detectors.

Engineering constraints require sub-cm level tolerances on AV height and diameter, so future vessels will closely match the AD1 and AD2 ADs in this parameter. In addition, all ADs will undergo the exact same filling regimen. Thus, little detector response difference will arise from this parameter either between 2 ADs in a pair, or between 2 ADs in different pairs.

Positioning

Shifting the IAV or OAV with respect to one another or the AD results in altered gamma catcher and buffer region shapes and is straightforward to simulate with NuWa. Shifts of up to 5 cm were simulated, with no resultant change in either neutron detection efficiency or its related uncertainty.

In the as-built detectors, the locations of the X-Y center of the IAV and OAV were calculated by analyzing AD survey data taken during the AD assembly process. The surveys are done using a Leica System 1200 Total Station [124]. Surveys were done of various points on the SSV and OAV bottom, sides, and lid, and on the IAV top. In addition to helping in the AV centering process, the survey data also ensures that calibration ports are properly aligned and that the AVs are sufficiently level.

The survey data is analyzed to give the horizontal and vertical positions of the calculated centers of specific surfaces on the AVs and SSV relative to the calculated center of the SSV lid. These dimensions correspond to the horizontal and vertical distances between point A and points B, C, D, and E in Figure 6.4. Table 6.2 presents an overview of the surveyed vessel offsets between point A and points B, C, D, and E in cylindrical coordinates: magnitude of Z offsets of the centers of given vessel surfaces are presented along with magnitudes of X-Y offsets. In addition, levelness is described by the difference in absolute Z-coordinate between one side of a vessel and the other. The vessels are largely concentric, having less than 5 mm offset in most cases. Z-positions of the various surfaces are in close agreement between ADs, and tilts of these surfaces are all around 5 mm or less.

Vessel	Magnitude (mm)	Angle (deg)	Height (mm)	Tilt (mm)
SSV1 Top	-	-	0	4
SSV2 Top	-	-	0	2
OAV1 Flange	2	257	542	<4.4
OAV2 Flange	7	39	546	<4
IAV1 Lid Edge	3	256	970	5
IAV2 Lid Edge	2	259	964	6
OAV1 Bottom	2	0	4515	4
OAV2 Bottom	4	231	4514	3
SSV1 Bottom	3	352	4556	3
SSV2 Bottom	5	186	4557	2

Table 6.2: As-built vessel surface offset data, listed in cylindrical coordinates as X-Y offset magnitude, X-Y offset angle, and Z offset. The coordinate system is set such that the top of the SSV lid center is (0,0,0). Values are obtained from aggregating data from numerous survey locations. Uncertainties on these aggregated values are ± 3 mm.

Unexpected shifts between AVs can also effectively exist if AV walls are not perpendicular to the AV bottoms, or if the AV walls bulge outward or inward. Perpendicularity and flatness of each vessel's wall was measured via a plumb bob test conducted at the AV's fabrication site in either Taipei, Taiwan or Grand Junction,

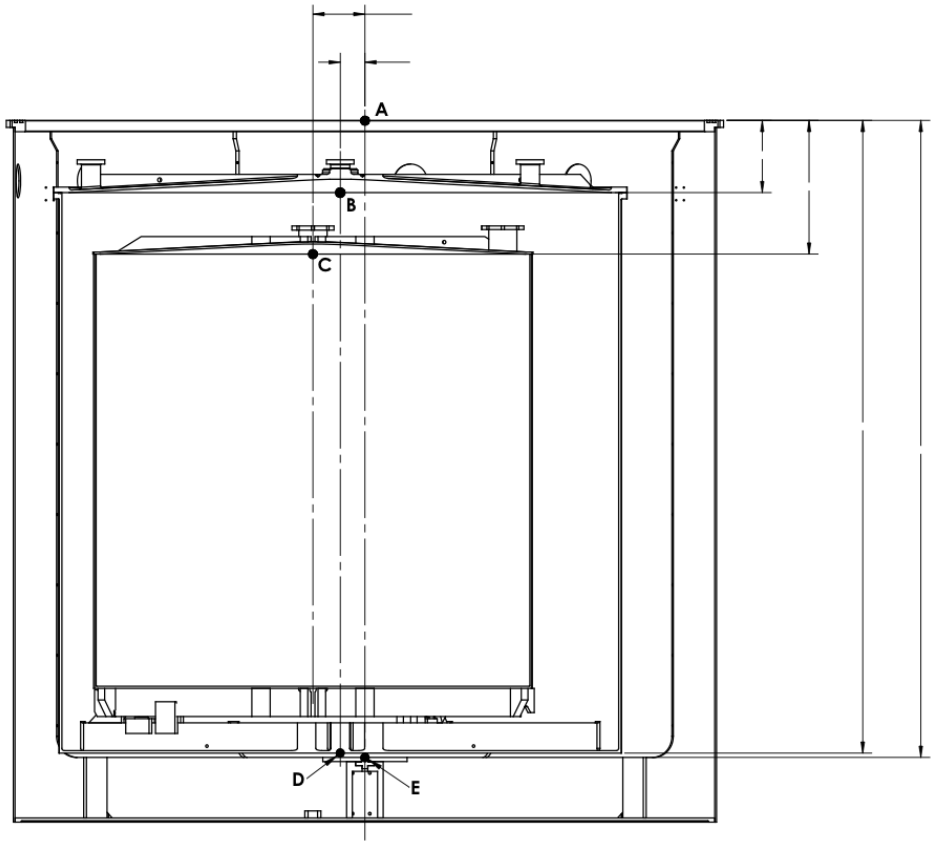

Figure 6.4: Depiction of an AD with offset AVs that shows key reference points (B, C, D, and E) whose vertical and horizontal distances from the calculated SSV lid center (point A) are calculated from the AV survey data. The AV offsets pictured here are exaggerated for illustration and not shown to scale.

Colorado, USA. The walls were seen to be flat and perpendicular to within 2 cm from top to bottom despite suboptimal flatness of the surface beneath the AV, which can induce non-perpendicularity of the vessel walls.

Since no change in detector metrics was seen with 5 cm AV shifts, the as-built level of concentricness, levelness, and perpendicularity will result in negligible differences in detector metrics between ADs. Engineering constraints require alignment at the sub-cm level, so no possible detector response differences between ADs in a pair or different pairs of ADs should arise from this parameter.

Thickness

As the inner acrylic vessel provides the bulk of the non-scintillating material in the center-most region of the ADs, the thickness of an as-built IAV can have a significant effect on an AD's behavior. For this reason, variations in the thickness of the IAV were simulated using NuWa. Changes in efficiency and its related uncertainty with changes in IAV thickness are shown in Table 6.3 [127]. According to these simulations, 5 mm of difference in average wall thickness between ADs results in a difference of 0.9% in efficiency and a 0.03% change in efficiency uncertainty. The outer acrylic vessel thickness will affect the efficiency of the detector to a much smaller degree, as it is located >40 cm away from the target volume; an increase in the thickness of the OAV by a few mm at the expense of gamma catcher thickness will have a very minimal effect on neutron detection efficiency, as demonstrated in Figure 4.4.

IAV Wall Thickness	n Detection Efficiency	n Detection Eff. Uncertainty	Statistical Uncertainty
10	90.7	0.29	0.04
15	89.8	0.29	0.04
20	89.1	0.29	0.04

Table 6.3: Change in n detection efficiency and its uncertainty as a function of IAV thickness.

After AV fabrication, AV barrel wall thickness measurements were made at various heights and angles around the vessel with an ultrasonic thickness gauge. Data for the IAV and OAV barrels can be seen in Figure 6.5. Wall thickness varies by a few mm over the surface of each IAV because of uneven levels of sanding and polishing, but the pattern of variation is consistent between ADs. The average thickness differed by less than 1 mm between OAV1 and OAV2 and less than 0.5 mm between IAV1 and IAV2. Thus, relative differences in detection efficiency between the two ADs resulting from as-built IAV thickness differences should be less than 0.1%. Relative differences

in physics arising from OAV thickness differences should be negligible.

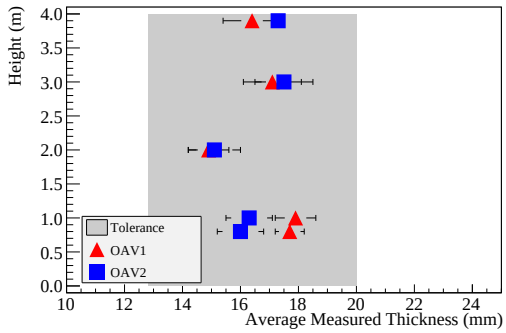

(a) OAV thickness deviation with height on the OAV.

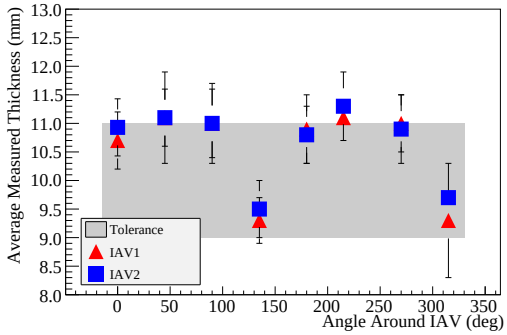

(b) IAV thickness deviation with angular position around the IAV edge.

Figure 6.5: IAV and OAV thickness measurements for both vessels, measured at various AV heights and angles. The error bars indicate the standard deviation of all thickness measurements made at the given height or angle. Tolerances are indicated by the grey band in each figure.

As the IAVs are all constructed using the same procedure, the thickness is not expected to differ significantly for any of the future IAVs. In an effort to meet production deadlines, the OAVs may not be polished to optical clarity but only to 600 grit, and will result in OAVs that are thicker on average by on the order of 1 mm. However, this should not result in any detrimental physics effects, since the effect of varying OAV wall thickness is negligible and the acrylic will become optically clear once immersed in liquids of similar indices of refraction.

Optical Properties

Any variation in the attenuation length and index of refraction of the IAVs will cause differences in how light interacting with the AVs is absorbed, transmitted and reflected. The percent transmittance of light through a material is determined by the Beer-Lambert law,

$$T = e^{-x/\Gamma}, \tag{6.1}$$

where x is the light's pathlength in the material and Γ is the material's attenuation length. The reflected and transmitted percentage of light at the material surface is determined by the Fresnel equation; at normal incidence, Fresnel's equation for reflected light reads as

$$R = \frac{(n_1 - n_2)^2}{(n_1 + n_2)^2}, \tag{6.2}$$

where n is the material's index of refraction.

However, R and T are often hard to directly measure. In the case of parallel-plane interfaces, such as the acrylic vessel walls and testing samples of the production acrylic, the picture is complicated by multiple internal reflections. In these cases, the measured transmittance and reflectance of a sample with parallel surfaces is

$$T^* = \frac{(1 - R)T}{1 - R^2T^2} \tag{6.3}$$

$$R^* = R(1 + TT^*), \tag{6.4}$$

with T and R as given in Equations 6.2 and 6.1. To complicate things further, both Γ and n are wavelength-dependent. By measuring some combination of T^*, R^*, T, and R at multiple wavelengths, one can determine the optical properties Γ and n for each acrylic sheet used in each acrylic vessel.

In order to measure the Daya Bay AVs' optical properties, a number of different techniques were used. In one study, T^* and R^* as a function of wavelength were measured for a PoSiang acrylic sample using a Perkin-Elmer Lambda 650 UV-Vis spectrometer with a 60 mm integrating sphere [128]. These values were then used to solve numerically for R and T, and thus Γ and n; this method is called the RT method, and has been used previously in the SNO experiment [129]. In another study, samples of the same acrylic type, along with acrylic samples manufactured by Polycast and Reynolds, were sent to Schott North America, a glass manufacturer and developer, to have their indices of refraction measured at a few characteristic wavelengths via

V-block refractometry [130]. The resulting measured n values for these two studies can be seen in Table 6.4; these values are in good agreement with those measured in [129]. These studies indicate that indices of refraction for acrylic vary less than 0.001 between acrylic samples and types for a given wavelength. Using Equation 6.2, this difference corresponds to 0.01% extra reflected light at an air-acrylic interface, which is certainly negligible. This means that all acrylics in all ADs can be treated as having identical indices of refraction.

Acrylic Type	Wavelength (nm)	RT-Measured n	Schott-Measured n
PoSiang	365	1.512	-
PoSiang	405	1.504	-
PoSiang	480	1.495	1.4966
Polycast 1	480	-	1.4970
Polycast 2	480	-	1.4974
Reynolds	480	-	1.4973
PoSiang	546	1.491	1.4922
Polycast 1	546	-	1.4926
Polycast 2	546	-	1.4929
Reynolds	546	-	1.4928
PoSiang	587	1.490	1.4902
Polycast 1	587	-	1.4906
Polycast 2	587	-	1.4910
Reynolds	587	-	1.4909

Table 6.4: Index of refraction measurements using the RT method and measurements procured from Schott North America. Systematic uncertainties on the RT and Schott measurements are 0.006 and <0.001, respectively.

Using this measured reflectance spectrum, T and Γ can calculated from T^*, which was measured for parallel-surface acrylic samples with the previously mentioned Perkin Elmer spectrometer or an SI Photonics 400-Series UV-Vis spectrometer [113]. This was done for one acrylic sample from every sheet used in the first two IAVs and OAVs to determine every sheet's attenuation length. The differences between the highest and lowest attenuation length spectrum can be seen in Figure 6.6. Keep in mind that these high and low values are the result of both actual variations in the

attenuation length of the acrylic as well as the systematic limitation of the UV-Vis spectrometer, which is 1%.

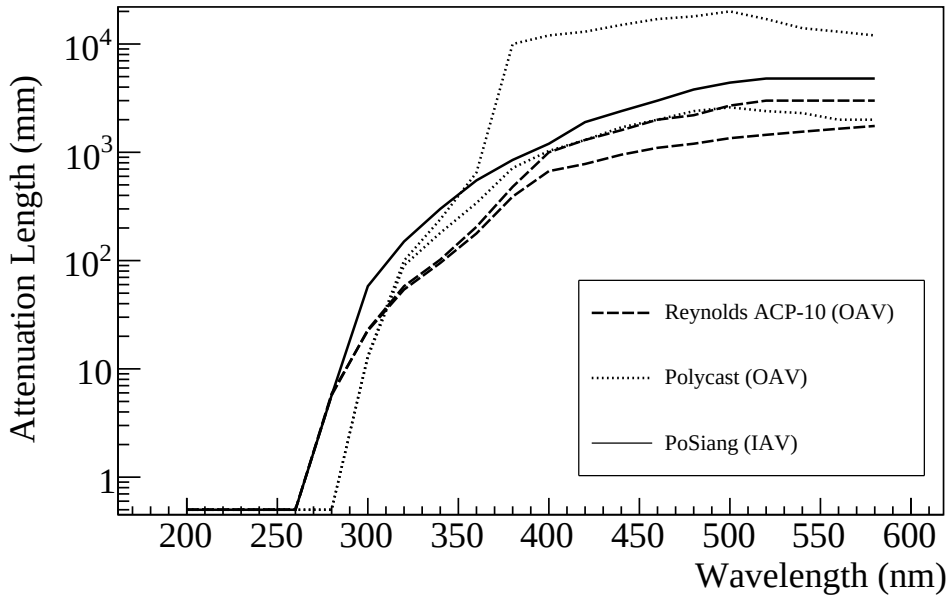

Figure 6.6: Best and worst case attenuation length spectra for each type of IAV or OAV acrylic. The best and worst values are the product of the transmittance measurement uncertainties as well as actual variations in acrylic attenuation length. Only one PoSiang attenuation length value is shown here.

To determine the effect of varying attenuation lengths on detector performance metrics, the highest and lowest measurements for each acrylic brand were inputted as the attenuation length spectrum for the entire simulated OAV in the NuWa simulation. Resulting changes in detector metrics are shown in Table 6.5. The difference in light yield between the highest and lowest attenuating OAVs was 4.4%. The maximum observed variation in efficiency was 0.2% $\pm$ 0.13%, and the change in the associated efficiency uncertainty was statistically insignificant. When all acrylics in the AD were varied from highest to lowest of any type, efficiency changed by 0.3% $\pm$ 0.18% and the associated efficiency uncertainty change was statistically insignificant.

This result does show a statistically significant variation in the relative detection

Acrylic Type	Light Yield (% Change)	n Detection Efficiency (%)	Stat. Unc. (%)	n Det. Eff. Unc. (%)	Stat. Unc. (%)
Raychung Best	1.8	92.00	0.09	0.23	0.01
Raychung Worst	-2.7	91.89	0.09	0.22	0.01
Polycast Best	1.8	92.09	0.09	0.22	0.01
Polycast Worst	-0.8	91.97	0.09	0.22	0.01
Reynolds Best	-0.9	91.96	0.09	0.23	0.01
Reynolds Worst	-2.9	91.98	0.09	0.21	0.01
PoSiang	1.2	91.95	0.09	0.22	0.01

Table 6.5: Change in n detection efficiency and its uncertainty when the OAV attenuation length is changed to the best and worst attenuation length of various UVT acrylic brands. The percent change in light yield is quoted with respect to the baseline attenuation length model in the NuWa simulation.

efficiency between detectors with different acrylic optical properties. However, in order for such a variation in response to occur in an as-built detector, all sheets of acrylic for one AD must be the worst performers, while all the sheets for another AD must be the best performers. QA transmittance measurements have shown this to not be the case for the first two ADs, and would identify such a scenario were it to occur in any subsequent ones. Thus, differences in detection efficiency because of optical properties should be negligible.

This result does also demonstrates the possibility of percent-level variations in light yield (energy scale) between different detectors. This is not too large of a concern, however, as light yield is not directly tied to the experiment's sensitivity: the light yield differences will be corrected for during the energy scale calibration of the detectors. This study also suggests the possibility of percent-level differences in light yield with position within one detector as well as between detectors. This could cause an increase in the relative energy scale uncertainty between detectors, and will be measured precisely during energy scale calibration using real data in the following chapters.

It is also interesting to note in this study that a small change in light yield was

not accompanied by a significant change in efficiency or efficiency uncertainty. This observation will be used to support conclusions in other studies.

Acrylic optical properties can vary not only between different sheets, but also over time in the same sheet if the optical properties of the acrylic degrade significantly. In particular, acrylic is known to undergo significant optical degradation with exposure to ultraviolet radiation, generally from sunlight [112]. The degradation rates as a function of UV dosage for the Daya Bay acrylics have been measured and applied to determine the acceptable exposure time of the AVs in various environments. These values are given in Figure 6.6; acceptable exposure is defined as the length of exposure time necessary to cause 2% light yield loss in the AD from AV degradation. Precautions have been taken to minimize UV exposure of the Daya Bay acrylic, which should prevent any significant variation of the acrylic optical properties with time: UV-screens have been installed in the Daya Bay surface assembly buildings, and vessels are covered at all times with tarps or UV-absorbing film when outside or in storage.

Acrylic Part	Outdoor Limit (d)	Factory Limit (d)	UV-Filtered Limit (d)
OAV Lid and Base	0.5	16	205
OAV Barrel	1.2	40	527
IAV	3.5	122	1590

Table 6.6: Acceptable exposure times for the OAV and IAV in various environments. The factory limits are quoted with and without UV-filtered windows.

In summary, it appears likely that differences in acrylic optical properties between ADs will result in negligible differences in detector performance between all ADs.

Surface Quality

The surface quality of the acrylic vessels can affect light propagation in the detector. Reflections can occur at acrylic-liquid interfaces, as well as diffusion of light if acrylic

surfaces are rough. If the amount of reflection and diffusion from acrylic are significant in the AD, optical photon pathlengths could be significantly increased or decreased in different parts of the detector, resulting in altered light yields and worse position reconstruction. Thus, the magnitude of acrylic surface reflection and diffusion must be quantified to determine if the first two ADs will have similar detector performance.

The surface of OAVs and IAVs in ADs 1 and 2 experienced the same surface preparation regimen, being polished to 1 to 3 micron grit by the AV manufacturers Reynolds and Nakano. In air, this gives the vessels a largely transparent finish with small halos of diffusely reflected light visible from certain perspectives. Visual inspection of the vessel reveals that a large majority of the total incident light is specularly transmitted or reflected. The IAVs appear to have a slightly more diffusive surface than the OAVs. However, these surface effects, along with surface reflection, largely disappear when the vessels are immersed in liquids on either side of the AV walls. This is because of the excellent index of refraction matching between the AD liquids and acrylic. Figure 6.7 illustrates the disappearance of surface features and excess light reflection when the AVs are filled with liquids. The same effect can be seen on the installed AVs by viewing the AD inside before and after liquid filling with a camera installed inside the AD; such a comparison is shown in Figure 6.8. The amount of light diffusion caused at an interface of LS and a 3 micron grit finish acrylic sample was consistent with zero using a UV-Vis spectrometer with a 1% measurement uncertainty. This data supports the conclusion that surface reflection and diffusion effects from acrylic will be negligibly different between detectors.

The only minor surface defect present in the acrylic vessels was on OAV1: brass brushes were used to abrade the surface of the OAV and remove sticky residue left from the OAV packing materials whose compatibility with the AD liquids was unknown. The surfaces in these abraded areas is more diffusive than other areas, while

(a) Acrylic sample polished to 400-grit, in air.

(b) Acrylic sample polished to 400-grit, immersed in mineral oil.

Figure 6.7: A comparison of acrylic surface appearance when surrounded by two mediums of different refractive index, air (n∼1) and mineral oil (n∼1.36). Acrylic has n∼1.50

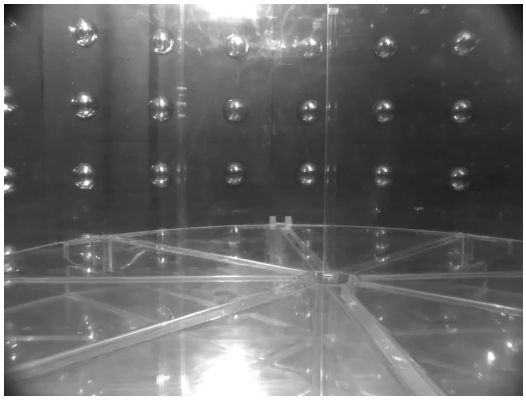

(a) Photo of the AD inside before AD liquid filling.

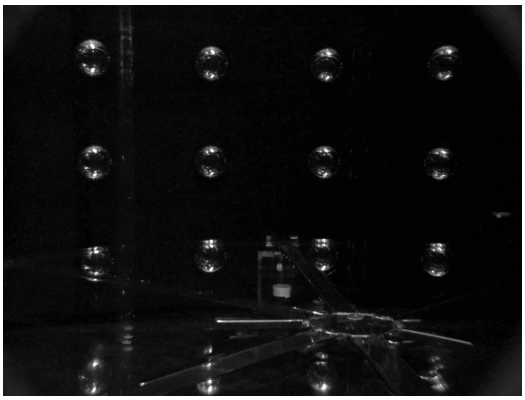

(b) Photo of the AD inside after AD liquid filling.

Figure 6.8: Photos of the AD insides before and after filling. Visible in the dry AD are PMTs, the IAV bottom and ribs, filling probes, and many reflections. Still visible in the wet AD photo are the outlines of the AV ribs, PMTs, and a white teflon IAV support puck previously obscured by reflections on the AV. Reflections are clearly decreased after filling.

still mostly transparent. We qualitatively estimate that 10-20% of the bottom surface of OAV1 is abraded. By measuring similarly abraded samples with a UV-Vis spectrometer, it appears that 4-8% of the light traversing this MO-acrylic will be diffused. Considering the total surface area of the OAV and the small size of the effect, this surface defect should have a negligible impact on total light propagation in the AD.

In summary, this data supports the conclusion that surface reflection and diffusion effects from acrylic will cause negligible detector performance between different detectors.

6.4 AD Liquids Non-identicalness

Shape

The shape of the AD liquid regions are mainly governed by AV shape and concentricness, which has already been discussed. To a smaller degree, it is also affected by the shape of the AV support structures. Detector simulation was done to determine changes in AD response metrics in response to changes in the volume of non-scintillating (dead) material in the gamma catcher. Changes in detector metrics with gamma catcher dead volume percentage is shown in Figure 6.9(a) and Figure 6.9(b). The efficiency and efficiency uncertainty change by 1.25% and 0.015%, respectively, when dead volume is increased from 0% to 5% of the gamma catcher region.

The total designed dead volume in the gamma catcher from the AV support structures is 2.5%. The difference in total acrylic dead volume in the ADs can be quantified by comparing the weights of the different ADs. AVs were weighed during AD assembly with a crane scale of resolution 7 kg; The total measured masses are 1847±7 kg (OAV1), 1852±7 kg (OAV2), 907±7 kg (IAV1), and 916±7 kg (IAV2). The 9 kg difference between IAV1 and IAV2, if completely the result of support

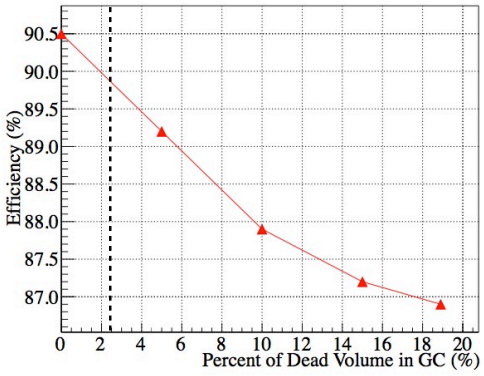

(a) Changes in neutron detection efficiency with gamma catcher (GC) dead volume.

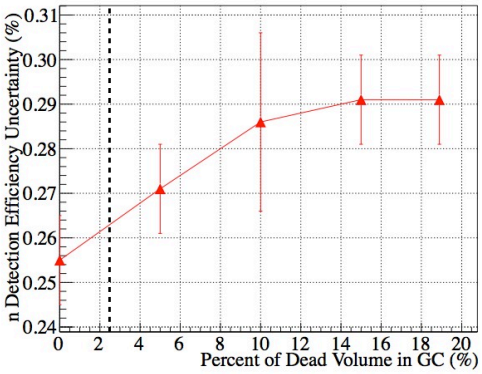

(b) Changes in neutron detection efficiency uncertainty with gamma catcher (GC) dead volume.

Figure 6.9: Changes in neutron detection efficiency and its uncertainty as a function of gamma catcher dead volume. The dashed lines indicate the designed level of gamma catcher dead volume, which comes largely from the acrylic support structures for the IAV and OAV.

structure volume differences, corresponds to a 0.03% dead volume difference. Thus, a difference in non-scintillating material in the gamma catcher is not expected to cause any differences in detector response.

Optical Properties, H/Gd Ratio, and H/C Ratios

A change in the H/Gd ratio changes the number of neutron captures on hydrogen, which will not be classified as detected events once energy cuts are applied. Changes in the H/Gd ratio were simulated with NuWa to ascertain the resultant changes in the Gd-capture fraction. A 1% variation in the H/Gd ratio results in a 0.13% difference in Gd captures. Thus, if the relative H/Gd ratio between detectors is unknown to 1%, this parameter will contribute a 0.13% uncertainty to the total IBD event rate.

A change in the H/C ratio directly effects only the total number of protons in the experiment: the more H in the AD liquids, the more $\overline{\nu}_e$ interactions. Thus, a 1% uncertainty in the H/C ratio leads to a 1% uncertainty in the total IBD event

rate. By filling all ADs with the same AD liquids, this uncertainty will be correlated between all detectors and will cancel in a near-far measurement.

A change in the attenuation length of the AD liquids will effect the light collection capability of the detector. Simulation studies have been done in NuWa to determine changes in detector metrics with changes in LS and GdLS attenuation length. Results are shown in Table 6.7. It appears that as long as the LS and GdLS attenuation length remain above 8 m, light yield will change by less than 10%, neutron detection efficiency should be stable within ±0.2%, and energy reconstruction biases for Daya Bay's maximum likelihood reconstruction will remain below a few percent for all detector regions if not properly corrected.

GdLS Attn. Length (m)	Light Yield (%)	Detector Resolution (%)	n Detection Efficiency (%)	Max. Reconstructed Energy Bias (%)
5	77.8	7.94	91.8	5
8	89.6	7.02	91.5	3
11	95.0	6.84	91.3	2
13	97.7	6.74	91.4	2
15	100	6.64	91.2	2

Table 6.7: Change in detector metrics as a result of changes in LS and GdLS attenuation length. Light yield is given in reference to 15 m liquid attenuation length.

The GdLS has been produced and is stored in 5 different acrylic storage tanks in the filling hall. Each storage tank is the product of different GdLS production batches, each of which may have percent-level differences in optical properties, H/C ratios, and H/Gd ratios. This could result in percent-level or less differences in properties between GdLS storage tanks. In order to ensure identicality in AD liquid properties despite this, each AD will be filled equally from each of the five different storage tanks. This filling process ensures that differences in properties between ADs will be more dependent on uncertainties in measured volumes, which are <0.1%, than on storage tank-to-storage tanks property differences. For example, this filling method

can ensure identical H/Gd ratios between all detectors to 0.04% even with H/Gd variations of 2% between storage tanks by filling each detector with liquid from each GdLS storage tank to 0.1% precision. AD-to-AD H/C ratio and attenuation length differences would be reduced in a similar manner.

Other sources of non-identicalness between detector liquid may exist, but can be mitigated by the detector filling scheme and subsequent detector calibrations during data taking:

1. **Time-dependent changes in AD liquid properties:** If the liquid in one detector experiences changes in liquid properties uncorrelated with any of the other AD liquids in other ADs or in the storage tanks, this could cause differences between detectors. Any changes would need to be larger than the limits determined via simulation mentioned above if they are to create differences in physics response. If all liquids in all ADs experience equal time-dependent changes in liquid properties, then non-identicalness between detectors would not be observed in the ratio of near and far event rates. Although such changes are possible and have been experienced in previous experiments, such as Chooz, there is no evidence from out QA testing of prototype or production AD liquids that this scenario will occur. Production batches of LS have been monitored for more than a year and the measured transmission is found to be stable. Over the timescale of years for the prototype AD liquids, no precipitation has been observed, meaning a constant H/Gd ratio, while measured absorbance of the liquids as measured by UV-Vis spectroscopy has remained constant.

2. **The successive nature of the AD filling:** After filling AD1 and AD2, the liquid for subsequent detectors still remains in the storage tanks. Because of this, if all liquids experience similar time-dependent changes, such as gradual

precipitation, significant differences between detector pairs could arise. In addition, non-identicalness between detectors could arise from any time-dependent evolution of the liquids triggered by the filling process or contact with AD materials, as ADs filled at different times would be at different stages of liquid property evolution. Thorough compatibility tests have been done between the AD liquids and all filling and AD materials, and no problems have been observed. Even if these unlikely types of changes were to occur, their effects on systematics of detector pairs would be minimal, as ADs are filled in pairs and would evolve as pairs in time.

3. **Stratified differences in liquid properties in one storage tank:** Individual 4 ton batches of GdLS with percent-level batch-to-batch variation in H/Gd ratios, as well as differences in optical properties, are pumped sequentially into the 40 ton storage tanks. As a result, layering of the storage tanks by batches is possible, which, if not corrected, could cause AD-to-AD differences in liquid properties. To remedy this, before withdrawing fluids for filling an AD there will be a 5-volume recirculation performed on each 40 ton storage tank to thoroughly mix the contents of each storage tank.

To summarize, detector simulations show that if H/Gd ratios are different by less than 1% between detectors and H/C ratios are different by less than 0.1%, we can expect that the Gd-capture percentage and number of protons for detectors of equal target mass will be identical between detectors to within their respective baseline systematics values of 0.1%. If the attenuation length of LS and GdLS remain above 8 m in all detectors, all detector performance metrics should remain acceptably identical between detectors. The only possible scenarios that would cause such changes or differences in AD liquid properties seem unlikely to occur based on AD liquid

characterization and AD assembly and filling techniques.

Spill-in/out Effects

While the inner acrylic vessel separation between GdLS and LS establishes a finite fiducial volume for the AD, cross-over of particles between regions does occur; neutrons from $\overline{\nu}_e$ interacting in the LS region can travel as they thermalize and capture on Gd in the GdLS region, inflating the total number of events. Simultaneously, neutrons from $\overline{\nu}_e$ interacting in the GdLS region can travel outwards while thermalizing in the LS region, totally eliminating their ability to be detected as target $\overline{\nu}_e$ interactions. These processes are termed spill-in and spill out effect, respectively. Spill-in events account for approximately 6% of the Gd-captures in the AD, while approximately 2% of $\overline{\nu}_e$ interactions in the target volume have neutrons that escape the GdLS. Spill-in and spill-out effects should not affect the sensitivity of a relative measurement, as detectors should experience those effects to an identical degree.

Variations in the density of the GdLS, LS, and IAV, Gd concentration in the GdLS, and thickness and shape of the IAV can effect the number of spill-in and spill-out (SI/SO) events in a detector, however. This directly effects the detector's effective target mass and thus the experimental sensitivity. Each of these parameters is either known to vary minimally or is assured in the detector design plan to vary within a certain range. These values have been measured as part of liquid and AV quality assurance.

Simulations have been conducted by inputting the expected variation of each of these parameters and looking for any change in the SI/SO contribution to total event rates. Expected variations of detector parameters and their effect on spill-in/out contributions to total event rates are shown in Table 6.8. Parameters that have been measured, like IAV thickness, shape, and density will cause negligible changes in

SI/SO-related Gd-captures. If AD liquid parameters remain comparable over time to those quoted in QA documents [96], their attendant changes to SI/SO rates will contribute at most 0.05% uncertainty to total Gd-capture rates.

Parameter Varied	Level of Variation	Variation in Spill-in (%)	Variation in Spill-out (%)
GdLS Density	1%	0.05 ± 0.02	0.01 ± 0.01
LS Density	1%	0.03 ± 0.02	-0.02 ± 0.01
H/Gd Ratio	1%	0.03 ± 0.02	-0.01 ± 0.01
IAV Density	1%	<0.01	0
IAV Thickness	10%	0 ± 0.02	-0.01 ± 0.01
IAV Shape	6% in volume	0.02	0

Table 6.8: Change in the IBD Gd-capture rate, and thus effective detection efficiency resulting from changes in spill-in/out rates from varying relevant detector parameters. The 6% volume change for IAV shape corresponds to an excessive 0.35 m bulge of the IAV endcap. All changes are much smaller than 0.1%.

Ultimately, more important than uncertainties in spill-in/out rates is the uncertainty in detector response directly from the change itself. For example, the uncertainty in detection efficiency from the changes in GdLS density are more the result of attendant changes in hydrogen capture rates than from any changes in spill-in/out rates.

6.5 Reflectors

Dimensions

The change in light yield resulting from a change in the radius of the reflector can be calculated easily by knowing the amount of reflected light in the detector, which was measured via simulation to be 41%. Lowering the 2.25 m radius of the reflectors by 1 cm changes the surface area by 1%, lowering the light yield of the reflected portion of light by 1%. Given that reflected light is less than half of the total light,

this change will induce less than 0.5% change in detector light yield. Referring back to the AV optical properties study, it is clear that this small change in light yield will result in negligible changes in systematics-related or reconstruction-related AD metrics. Reflector radius for all reflectors are consistent to within 2 mm. Clearly, reflector radius will not contribute to differences between any ADs.

Change in AD response from acrylic thickness variation between reflectors is indirectly examined by the AV acrylic thickness studies. As there is a smaller reflector surface area than AV surface area in the detector (roughly a 4-to-1 ratio), changes in detector response from a change in reflector thickness will be smaller than a that from a change in AV thickness. Thus, AV thickness should be more of a concern than reflector thickness.

Optical Properties

The reflectivity of reflector samples has been measured, and variability of reflectivity between ADs or between different locations on a single AD is likely to be on the order of a few percent [131]. Changes in light yield as a function of reflectivity variation is easy to calculate knowing that 41% of light is reflected: if reflectivity is reduced by 2%, then light yield is lowered by $< 1\%$, a negligible change. This figure once again assumes the worst-case scenario, in which an entire reflector from one AD has the lowest measured reflectivity, while one from another AD has the best measured reflectivity; the detector QA regimen assures that this has not happened. Changes to reconstruction resulting from this minor variability in reflectivity would also be negligible. Finally, there is no evidence in any of the long-term QA testing done on the reflectors to suggest time-dependent changes in reflectivity of the reflectors.

Shape

A roughly hyperbolic 2 cm sag from the edge to the middle of the top reflector of AD1 was measured during surveys of the ADs. As the reflector shape is an important possible input into some event reconstruction algorithms, reconstruction-related AD response metrics should be examined as well as the previously used metrics.

To address this, changes in the shape of the reflector to a roughly hyperbolic profile were simulated using NuWa. Light yield decreased by 0.4% as a result of 2 cm sagging. In addition, reconstructed energy bias is increased by a percent or less in isolated areas of the detector. Position reconstruction biases are increased by at most a centimeter. Changes of this magnitude in isolated areas of the detector are negligible.

By using the same survey regimen on future ADs, reflector sag greater than this magnitude will be identified and corrected, meaning this parameter will not contribute significant non-uniformity between ADs.

6.6 PMTs

Distance to AD center

PMT positions have been surveyed for the first ADs and are known to exhibit position-dependent variations on the order of a few cm. Some PMT rings are systematically further in than others by at most a centimeter. As the PMT mounting method and ladder production and transport method is the same for all PMTs and ladders, these variations will likely be of similar magnitude on all ADs.

Changes in PMT ring positions were simulated using NuWa [132]. Distance to the AD center for each ring of PMTs was adjusted to mirror the measured values. An

additional cm of difference between the farthest-in and furthest-out rings was added in to make the simulation a worst-case scenario. This altered detector experienced a light yield increase of 0.5% with respect to the baseline design. As mentioned before, this will result in negligible changes in AD response metrics directly to the detector systematic. No changes in light yield uniformity in the detector were visible.

A cm-order shift of PMTs inwards would also decrease the amount of MO buffer between the PMTs and the scintillating region, increasing the singles rate by $\sim$1 Hz.

If future ADs have PMT position variations of the same order of magnitude as the first ADs, this parameter should not contribute any significant non-uniformity.

Distance to Radial Reflector

The distance from the top of the PMT photocathode to the radial shield also varies between PMTs by as much as 3 mm. This variation causes the radial shield to shield the back end of some PMT photocathodes more than others, affecting the detector light yield.

Simulated shifts inward and outward of all PMTs with respect to the radial shield have been done [133]. Changes in light yield as a function of position with respect to radial shield are shown in Figure 6.10. A 3 mm shift with respect to the radial shield changes light yield by approximately 2%. This is a greater magnitude effect than variations in PMT position with respect to the AD center. However, one AD will not have all its PMTs closer to the radial shields than another AD, so the actual change in response between ADs will be much lower.

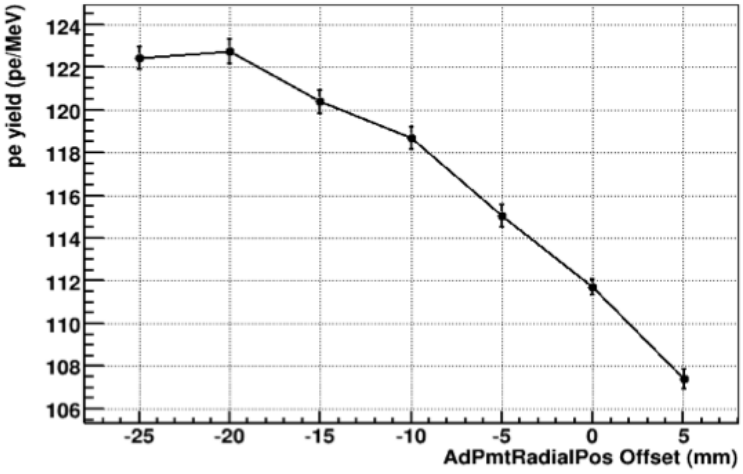

Figure 6.10: Changes in light yield as a function of distance between the radial shield and the PMT photocathode top. A negative offset indicates PMT movement inward towards the detector center. Figure provided by [133].

Dead PMTs

The effect of dead PMTs on light yield is easy to calculate: if 5% of PMTs are dead, light yield decreases by roughly 5%. Changes in detector resolution are not so straightforward and must be simulated [133]; detector resolution increases by less than 0.5% when 5% of PMTs die, and increases by 2% with 50% PMT loss. If the failure is random with position and the number of dead PMTs is much less than the total number of 192 PMTs per AD, detector uniformity will not be affected. Over months of data running, no AD PMTs have died.

Radial Shields

The surface area of the black radial shields are approximately twice that of the reflectors, with a reflectivity approximately 10% that of the reflectors; this means reflected light from the radial shield contributes approximately 8% of the AD's total detected light. Thus, variations in the reflectivity or dimensions of the radial shield must be

greater than 10% to cause changes in light yield or light yield uniformity of greater than 1%. This magnitude of variation of radial shield parameters between ADs seems extremely unlikely. The conclusion of these simplified calculations are reinforced by simulation studies performed in which extra holes were cut in the radial reflector to look for AD-wide and localized changes in light yield.

The surface area of the radial reflectors will vary minimally: gaps between reflector panels are known to with a few mm and panel dimensions are known to within a few mm. This represents an uncertainty of <0.5% in the radial reflector surface area. This will contribute a completely negligible change in light yield.

6.7 Other Sources of Variation

Non-transparent Inclusions

A small fraction of light created by particle interactions in the AD will be blocked or absorbed by the semi-opaque materials in the AD optical region, such as teflon or viton shims, support pucks, port covers, o-rings, or small imperfections in the acrylic vessels. The effect of these small inclusions on light yield can be easily calculated by comparing the solid angle of the inclusions to the total detector solid angle at various points in the detector. Based on these calculations, such inclusions will not reduce light yield by more than 1% if the inclusion have surface areas on the order of 0.25 m^2 or smaller. Inclusions can be even larger without deleterious effect if they are transparent or reflective. This is overwhelmingly true of all semi-opaque inclusions in the AD.

Radioactivity

Every material in each AD has been radio-assayed to measure its concentration of radioisotopes. This vetting process is designed to ensure radioactivity rates of all materials in all AD building materials are at acceptable levels.

Besides radioactivity in building materials, radon daughter implantation on and contamination of AD components post-manufacture is also a contributor to radioactivity of the as-built detector. Radon concentration will be mitigated in AD liquids by storing them in teflon-lined plastic storage bags before being put into the AD. No mitigation has been done regarding radon implantation in acrylic. Fortunately, implantation of radon daughters in acrylic, studied comprehensively in Ref [134], is slow enough that this should not be a concern for the Daya Bay ADs, even given the high radon concentrations (>100 Bq/m^3) in the SAB assembly pits during the year of AD1 and AD2 assembly.

6.8 Summary

A table summarizing the effects of each detector parameter variation on detector response metrics can be seen in Table 6.9.

After reviewing detector variation simulations and as-built AD characterization data, the possible sources of differences in detector systematics between ADs appear to be quite limited. This is not to say that data from all ADs will look exactly the same. For example, light yields, and thus energy scales, could be different between ADs for a number of reasons discussed above; also, PMT and FEE properties will cause raw data from different ADs to look different. Intrinsic radioactive backgrounds, while within acceptable tolerances, may exhibit some spectral or rate differences between detectors.

Many physical differences in production can be cited between any 2 ADs. However, this study shows that in all cases observed in the construction and assembly process, these differences are smaller than the levels that would cause significant differences in systematics between detectors. There are also many noteworthy differences between the life cycles of different pairs of ADs, including different lengths of assembly and exposure to radon backgrounds, different lengths of storage of AD components at various locations, different shipping and repair histories, different AV polishing regimes, different raw material production batches, and so on. However, the summarized simulation studies and AD component characterization data all show that despite these differences, we expect an AD's detector systematics to be similar to that of any other AD.

Component	Parameter	Variation between ADs	Resultant Variation in Response Metric			
			n Det Eff. (%)	n Eff. Unc. (%)	Light Yield (%)	Other
AVs	Shape/dimensions	Target volumes vary by <0.3%	0.1	<0.01	-	-
	Thickness	Avg. thickness same to <1 mm	0.1	<0.01	-	-
	Positioning	Concentric to <5 mm	<0.1	<0.01	-	-
	Optical Properties	Attn. length from 1 to 10 m	<0.1	<0.01	4.4	-
AD Liquids	Addl. Shape	Dead volume varies by 0.03%	Negl.	Negl.	-	-
	Optical Properties	< 1 m Attn. Length Variation	0.1	0.03	2-3	-
	H/Gd Ratio	<0.04% with fill procedures	Negl.	-	-	
	H/C Ratio	<0.04% with fill procedures	-	-	-	<0.04% Event rate
Reflector	Dimensions	Diameter <2 mm	Negl.	Negl.	0.01	-
	Reflectivity	<2%	Negl.	Negl.	<1	-
	Shape	<2 cm sag	Negl.	Negl.	0.4	Energy Bias: 1% Position Bias: 1 cm
PMTs	Dist. to AD center	<2 cm	Negl.	Negl.	0.5	-
	Dist. to radial shield	<3 mm	Negl.	Negl.	2.0	-
	Dead PMTs	No Dead PMTs	-	-	1	-
Rad. Shield	Reflectivity	Likely <10%	Negl.	Negl.	<1.0	-
	Shape	Surface area >0.5%	Negl.	Negl.	<0.1	-
All	Radioactivity	All materials pass QA testing	-	-	-	Minor Variations
	Opaque Inclusions	Less than 30 cm diameter	Negl.	Negl.	<0.3	-
	Spill-in/out Effects	Result of other variations	-	-	-	Spill-in: ±0.06% Spill-in: ±0.03%

Table 6.9: A table summarizing the variations of parameters measured in the as-built ADs, along with the attendant expected changes in detector response. "Negl." means that the change in light yield accompanying an as-built variation is so small that the other metrics will exhibit negligible change.

Chapter 7

Calibration, Reconstruction, and Event Classification

7.1 Introduction

In order to perform a relative rate-only θ_{13} analysis with the Daya Bay detectors, PMT signals in the ADs must be converted into physics quantities that be can be used to reliably and precisely separate inverse beta events from other event types. The fundamental unit of analysis is a *hit*, which consists of one ADC and one TDC value recorded when a PMT's voltage crosses a set threshold. Hit-level calibrations must be done to standardize the charge and timing information from each channel.

Physics quantities, such as reconstructed energy and trigger time, are calculated for each *trigger*, which is a collection of all ADC and TDC values in one detector in a 1.2 μs readout window. In turn, triggers closely spaced in time can be grouped to form *coincidences*, which can be closely examined to select a clean and well-defined set of inverse beta decay candidates.

The timing and charge calibrations described here are based on algorithms devel-

oped by other collaboration members and used collaboration-wide to provide consistent low-level physics quantities for all analyses from all collaborators. Two separate energy calibration and reconstruction schemes have been developed, one based on radioactive calibration sources, and another based on spallation neutron captures. This thesis will focus on the spallation-based calibration and reconstruction, as a significant portion of my analysis work was spent helping develop this calibration scheme and investigating relative differences in spallation-based energy scale between detectors.

7.2 Timing and Charge Calibration

Initial low-level gain calibrations convert each channel's ADC values into a standard measure of detected photoelectrons, or charge. Gain calibrations for the fine-range ADC are based on low-intensity ACU LED source runs, where a majority of PMT hits are caused by single photoelectrons (SPE). For each channel, the SPE triggers' ADC values are recorded, along with the average of the previous 4 ADC values before the SPE trigger, called the preADC. The preADC is then subtracted from the SPE trigger's ADC value to obtain a noise- and baseline fluctuation-subtracted ADC-to-PE conversion, or gain. The distribution of the measured gains in all AD1 channels is shown in Figure 7.1(a); the average value of this distribution exhibits some time-dependence, as shown in Figure 7.1(b). The coarse-range ADC is calibrated by inputting pulses of known amplitude into the electronics and recording the produced coarse range ADC value.

These gain constants are stored in a database that is updated on a weekly basis as new calibration runs are performed. Further corrections are added to properly calibrate the charge of closely spaced hits. These constants and corrections are applied

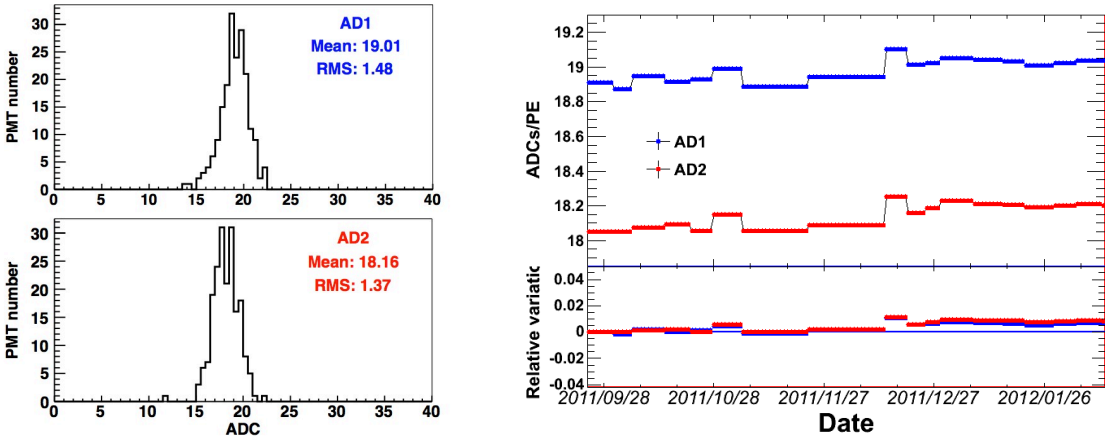

(a) Distribution of AD1 and AD2 PMT gains.

(b) Time dependence of PMT gains.

Figure 7.1: Distribution and time-variation of calibrated PMT gains for ADs 1 and 2.

to raw data in the NuWa processing chain to provide stable and standardized PE values from each PMT, which are essential to achieving stability in higher-level energy calibrations.

In order to exclude the charge of hits in the readout window unrelated to the triggering physics event, only hits within a specific TDC time range are accepted. To maximize the efficiency of this cut, the average TDC times of all individual channels, which can vary because of differences in geometry and PMT transit-time spread, must be calibrated by fitting the leading edge of their TDC time spectra. The calibrated TDC time spectrum for a 6-minute subset of AD1 data is shown in Figure 7.2. One can see that the main physics event forms a sharp peak around -1530 ns before trigger time. The excess TDC hits following the main peak can be caused by reflected light or by flashers, which exhibit a wide TDC time spectrum. The flat continuum in the spectrum is caused by random excitations on the PMT photocathode or dynode chain. In order to select only the signals originating from a real physics event, the

total nominal charge, Q_i of each channel is calculated as follows:

$$Q_i = \sum_{j=-1600}^{-1200} q_{ij}, \tag{7.1}$$

where q_{ij} is the calibrated charge of each hit in TDC time bin j. After this step, basic timing and charge quantities for the ADs are established, and can be used to perform higher-level physics analysis.

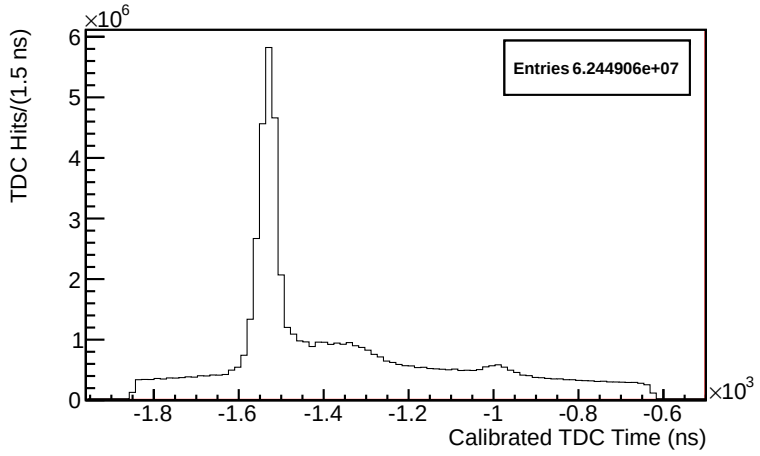

Figure 7.2: TDC spectrum for all PMT hits in a 6-minute run period. Tails are largely caused by dark hits in the PMTs and post-event electronics effects. The large number of entries in this 6-minute period demonstrates the significant volume of channel readout.

7.3 Event Types

By looking at charge and timing information from each AD, classifications of events can be made. By classifying events using low-level metrics, initial classifications can be independent of reconstruction method and any associated biases or efficiencies.

Low Level Classification and Filtering

A good measure for the total energy deposition of an event in an AD is its total number of detected photoelectrons,

$$N_{PE} = \sum_i Q_i, \tag{7.2}$$

where Q_i is the calibrated total charge in each PMT discussed in the previous section. It is also useful to calculate the degree of anisotropy of the light collection for each event, as physics events in the scintillating AD should release light isotropically. A good measure of anisotropy is the ratio of the highest-charge PMT to the total charge collected in the AD:

$$R_{max} = \frac{Q_{max}}{N_{PE}} \tag{7.3}$$

By looking at N_{PE} versus R_{max} for all AD triggers in a 24 hour period, as in Figure 7.3, one can separate triggers into a number of different event categories:

- **AD Candidate Events (Section A):** This region contains many types of physics events, including radioactive singles, muon-related backgrounds, and inverse beta signal events, as well as noise triggers caused by electronics effects after high-charge events. Further classification must be done to separate IBD further from these other events.

- **AD Muons (Section B):** High-charge events caused by mostly minimum-ionizing muons traversing the AD, causing significant scintillation and Cerenkov light emission. The wide charge range is indicative of the varied pathlengths of muons in the AD's scintillating region.

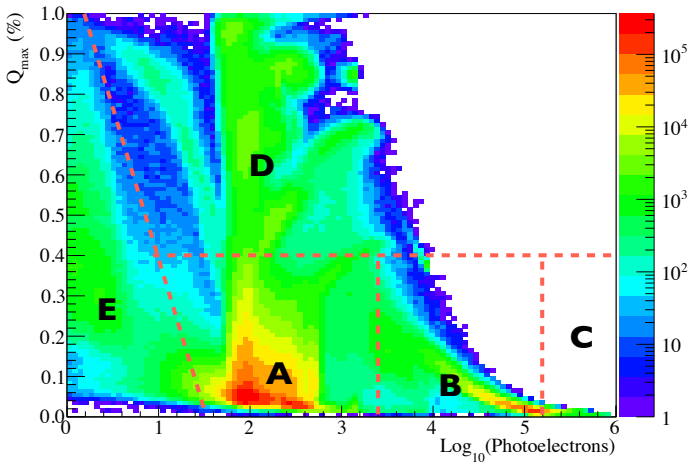

Figure 7.3: Distribution of all triggers for a 24-hour subset of data for AD1. The total charge and charge anisotropy separate the events into a number of categories: (a) AD candidate events, (b) AD muons, (c) Showering AD muons, (d) PMT flasher candidates, and (e) forced random triggers.

- **Showering Muons (Section C):** Very high-charge events caused mostly by inelastic collisions of muons with the active detector region. Because of the large energy deposition, many channels' total recorded incident PE is limited by PMT charge saturation, resulting low R_{max}.

- **Flasher Candidates (Section D):** Events that produce light anisotropically in the detector. This section is overwhelmingly comprised of instrumental backgrounds from the PMTs in which semi-periodic light pulses of varying intensity are emitted from PMT bases. These events are called flashers. Further classification can be done to further separate these events from those in sections a and b.

- **Random Triggers (Section E):** Periodic forced triggers used to study the rate of random PMT charge collection and other electronics effects. These events are excluded from physics analysis.

As the triggers in regions d and e are unrelated to particle interactions in the ADs, they should be excluded from any further classification. Region e can be removed by considering only events with NHit or ESum trigger types. In order to more fully separate region d, an additional measure of anisotropy must be introduced. The PMTs in the AD can be split into 8 high by 6 wide quadrants with respect to that trigger's highest-charge PMT. One can then take the ratio of the total charge in the quadrant directly across from the highest-charge PMT, Q_2, to the total charge in the regions adjacent to the highest-charge PMT's quadrant, Q_3 and Q_4:

$$R_{quadrant} = \frac{Q_2}{Q_3 + Q_4}. \tag{7.4}$$

A cut on this variable will remove events in which light is transmitted directionally across the detector. Physics events will not exhibit this topology, while many flashers have demonstrated this characteristic behavior. The efficiency of these two flasher discriminators in removing flashers from physics events will be discussed in future chapters.

The final group of non-physical AD triggers that should be removed are those caused by ringing and after-pulsing of the electronics after high-charge AD events. These events can be removed with high high efficiency by disregarding triggers within 20 μs after a high-charge AD event.

Water Pool (WP) event classification should also be briefly mentioned. The NHit trigger threshold for each water pool, which is set at 6, allows for frequent triggers from random PMT triggering and electronics noise. To remove these non-physics triggers, WP events are defined as any water pool trigger having greater than 12 hit PMTs.

Physics Event Classification

After the removal of these non-physical events, further discrimination is necessary to separate inverse beta candidates from other physics events. Some very useful tools in such a discrimination are the expected time coincidence between prompt and delayed signals and the expected energies of the prompt positron (1-12 MeV) and delayed neutron-Gd capture (6-12 MeV). Figure 7.4 shows the energies of the prompt and delayed signals for triggers occurring within 400 μs of one another.

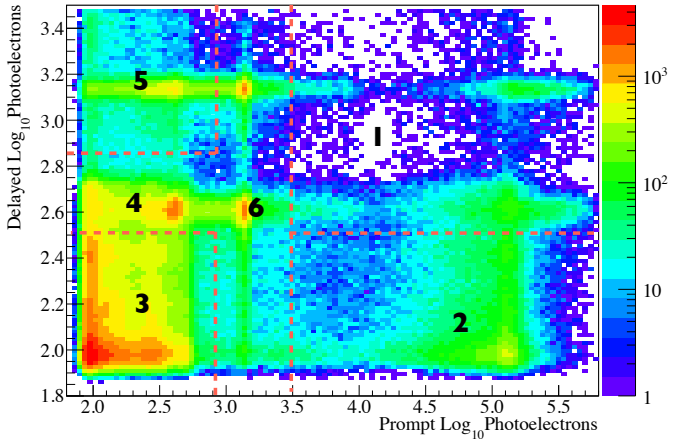

Figure 7.4: Distribution of time-coincident physics-related triggers for a 24-hour subset of data for AD1. The energies of the prompt and delayed triggers divide the space into a number of generalized categories: (1) Random coincidences of radioactive singles, (2) Hydrogen-capture coincidences, (3) Gadolinium-capture coincidences, (4) Multiple-neutron coincidences, (5) fast neutrons or spallation neutrons following AD/Showering Muons, (7) muon-related coincidences. Significant overlap can exist between some of these regions/event types.

Various event types can be identified in this plot:

- **Spallation and Fast Neutrons (Region 1)** As muons pass through the AD, they scatter inelastically off nuclei in the target, creating spallation neutrons that can subsequently capture on other nuclei in the target, such as Gd or H. These two signals will be correlated in time. Spallation neutrons from

muons passing through the water pool or the AD's buffer region will not be accompanied by very-high-energy prompt signals, but can instead create random coincidences with other event types, resulting a coincidence of high delayed energy and varied prompt energy. In addition, neutrons with high kinetic energy, called fast neutrons, can create their own prompt signals by producing recoil protons as they interact with the scintillator. These last two neutron types can make their way into region 5, which contains many of the signal events.

- **Muon-related coincidences (Region 2)** AD Muon and AD Shower triggers are relatively common and will form random coincidences with other common event types, such as radioactive backgrounds. It is interesting to note that these coincidence occur at lower average prompt energy than the spallation neutrons, indicating that AD Showers produce a disproportionately large share of spallation neutrons.

- **Accidental backgrounds (Region 3):** Radioactive decays from ^{238}U and ^{232}Th create alphas, betas, and gammas dozens of times per second that produce little resultant charge. These frequent depositions can cause random or correlated coincidences where both triggers have low total charge.

- **Hydrogen-capture coincidences (Region 4):** Neutrons capturing on hydrogen create a characteristic signal of around 400 PE. n-H captures can provide the delayed signal in an inverse beta decay, which is visible at slightly higher prompt energy. This inverse beta decay signal is contaminated by accidental coincidences of radioactive backgrounds with themselves and with spallation n-H captures.

- **Gadolinium-capture coincidences (Region 5):** Neutrons capturing on Gadolinium create a characteristic signal of around 2500 PE. This region pro-

vides the cleanest sample of inverse beta candidates, as the higher capture energy separates the signal from much of the accidental background. Spallation n-Gd captures coincident with radioactive backgrounds or other neutrons can still create backgrounds in this region. Cosmogenically-produced β-n emission isotopes and (α,n) reactions in the target can also create backgrounds in this region.

- **Excess-neutron events (Region 6):** Muon-produced neutrons in the raw physics sample can capture on Gd, providing prompt and delayed signals for accidental backgrounds. Many muons will create multiple neutrons that will capture closely in time, creating additional background coincidences. This group of events indicates the need for a muon veto that will remove from the IBD candidate dataset all coincidences occurring closely after a WP or AD muon trigger.

After completing this classification, the many possible event types should be well-established, as well as their relation to the inverse beta signal and its possible backgrounds. This classification has also given some hints for possible inverse beta event selection cuts, which will be more precisely defined and discussed in the following chapters.

7.4 Energy Calibration and Reconstruction

As the Daya Bay experiment plans to measure θ_{13} by comparing relative rates between near and far detectors, reconstruction and energy calibration focus primarily on establishing an energy scale that is consistent between detectors at the near and far sites. A consistent AD-to-AD energy scale ensures that the various energy cuts will

produce identical detection efficiencies for all ADs and that the detected antineutrino event rates would be identical in the absence of neutrino oscillations. The absolute value of these efficiencies, as well as the absolute energy scale of the prompt spectrum, are not necessary inputs to a relative rate-only measurement of θ_{13}. They will only be relevant for an absolute measurement of the reactor spectrum and flux for the comparison with MC predictions, which will be discussed briefly in the Appendix.

To achieve the smallest possible relative energy scale uncertainty, the Daya Bay detectors are calibrated by establishing a linear energy scale based on a common source in each detector. To ensure that this scaling remains consistent between detectors for all positions, energies, and particle types, calibrated energy peaks of known position and particle type are compared between detectors. Any variation in energy, position, and time dependence between detectors determines the relative energy scale uncertainty of the detectors.

Identical energy reconstruction is also applied to all ADs to even out energy response with position and to reduce each detector's energy resolution.

Energy Calibration with Spallation Neutrons

Spallation neutrons produced by cosmic muon interactions with the water pool and AD are excellent candidates for a relative energy scale calibration basis. Spallation neutrons can capture on H or Gd, giving energy peaks at 2.22 and 8.05 MeV. Because the uniform spatial distribution and neutron capture energy signature of spallation n-Gd captures mirror those of inverse beta n-Gd captures, they can be used to determine with low uncertainty the relative energy scale of each AD's delayed signals, which is the main determinant of the experiment's ultimate systematics-limiter, the delayed energy cut.

To select spallation neutrons, the following criteria are applied:

1. Flasher rejection: $\mathrm{Log}_{10}\left(\frac{R^2_{max}}{0.45^2} + R^2_{quadrant}\right) < 0$

2. The event must occur within 300 μs of an AD muon and WP muon

3. The event must occur greater than 20 μs after an AD muon to exclude noise triggers.

After these cuts, the high-energy Gd-capture peak is easily distinguishable. Triggers in the period between between 320 and 600 μs after an AD muon are statistically subtracted to remove background events and obtain a clean hydrogen-capture peak. Using this method, over 6×10^3 Gd-captures and 8×10^3 H-captures are detected daily in the near site detectors, while the over 500 Gd-captures and 800 H-captures are observed daily per far site AD. This high event rate allows for precise calibration of detector response during normal physics data taking.

The high-energy portion of the the spallation neutron photoelectron spectrum is fit well by a double Crystal Ball function, which describes well the energy response of a detector with finite resolution and non-negligible energy leakage to gammas:

$$f(x;\alpha,n,\overline{x},\sigma) = N\cdot\begin{cases} exp(-\frac{(x-\overline{x})^2}{2\sigma^2}) & \text{for } \frac{x-\overline{x}}{\sigma} > -\alpha \\ A\cdot(B-\frac{x-\overline{x}}{\sigma}) & \text{for } \frac{x-\overline{x}}{\sigma} \leq -\alpha \end{cases} \tag{7.5}$$

where

$$A = (\frac{n}{|\alpha|})^n\cdot(-\frac{|\alpha|^2}{2}), \tag{7.6}$$

$$B = \frac{n}{|\alpha|} - |\alpha|. \tag{7.7}$$

The two Crystal Ball functions fit individual contributions to the peak from the two Gd isotopes, ^{157}Gd and ^{155}Gd. The properties and relative contribution of each peak to the total n-Gd peak are shown in Table 7.1. The combined peak value is determined by taking the weighted average of the two crystal ball means. A visible

energy calibration constant is then defined for each AD by dividing this mean peak value of photoelectrons by the true mean energy, 8.05 MeV.

Isotope	^{155}Gd	^{157}Gd
Isotopic Abundance (%)	14.80	15.65
Neutron Capture Cross-section (barn)	60900	254000
Contribution to n-Gd captures (%)	18.5	81.5
Neutron Capture Peak (MeV)	7.937	8.536

Table 7.1: Contributions of Gd isotopes to the Gd-neutron capture peak. These two main contributors provide more than 99.9% of all Gd-captures. The detected n-Gd capture spectrum is combination of the energy peaks from these two separate isotopes. Isotope information from [135].

The relative uncertainty associated with this fit is 0.1%. The PE-energy conversion factor is around 165 PE/MeV for both ADs. The time deviation of this parameter, shown in Figure 7.5, ensures a stable energy scale despite minor fluctuations and time drift of the PMT and FEE gain calibration. The absolute variation in this parameter is around 1% for all ADs.

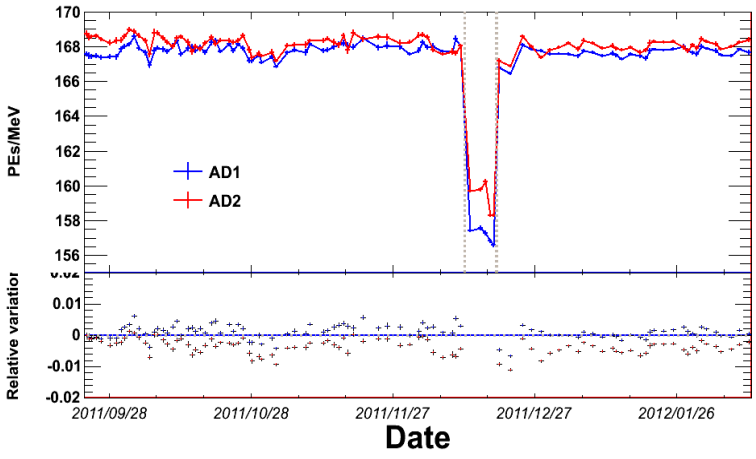

Figure 7.5: Variation in spallation n-Gd capture energy calibration constant with time. The calibration constants show variations on the order of 1% in both ADs. The significant dip in calibration constant in December is the result of an instrumental test in which a fraction of PMTs in each AD were switched off. Figure from [104].

Any physics event is converted to visible energy, E_{vis}, by multiplying by this time-dependent function. Figure 7.6 shows the background-subtracted spallation neutron E_{vis} spectrum for AD1 and AD2 after applying this calibration. Both capture peaks are clearly visible. In order to establish good agreement between ADs, the asymmetry of the two spectra are also examined:

$$A = \frac{N_{AD1} - N_{AD2}}{(N_{AD1} + N_{AD2})/2} \tag{7.8}$$

A flat asymmetry indicates that the peaks are well-aligned, while a slanted or humped asymmetry indicates a small energy scale shift between the two peaks. One can see in Figure 7.6 that the n-Gd peaks are almost perfectly aligned, while the n-H peaks exhibit an energy scale shift. This shift is caused by small differences in position-dependence between ADs, which will be discussed in section 7.4.

Position Reconstruction

Position reconstruction is not used directly in the Daya Bay θ_{13} analysis, since position cuts are not applied at any point. However, reconstructed position can be used to cross-check the purity and spatial distribution of inverse beta decay candidates in the target, and to evaluate detector spatial non-uniformity with continuously distributed event sources, such as spallation neutrons. The positions of particle interactions in a detector are fairly well-estimated by the center of charge of the event,

$$x_{COC} = \frac{\sum_i^{PMTs} Q_i x_i}{N_{PE}}, \tag{7.9}$$

where Q_i and N_{PE} are the per-channel and total charge defined in the previous section, and x_i is the physical location of the ith PMT. However, this metric tends to cluster events in the center of the detector. A more accurate reconstructed position can be calculated by applying a correction table to the center of charge variable based on

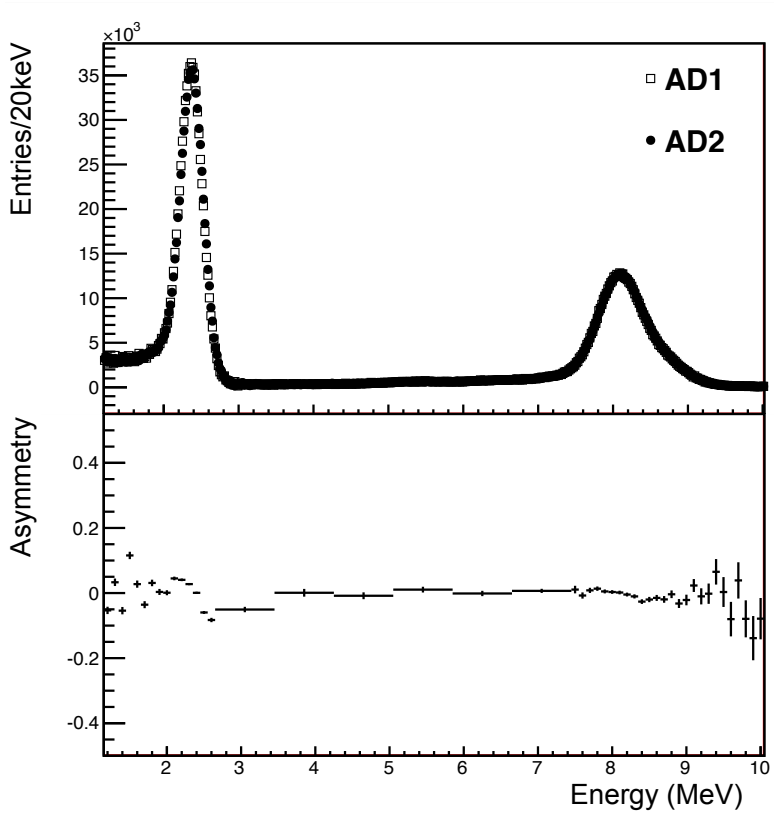

Figure 7.6: Spallation neutron energy spectrum and asymmetry. Asymmetry is defined in Equation 7.8. After background subtraction, the n-H and n-Gd capture peaks are clearly visible. The bottom panel shows a flat asymmetry at the n-Gd peak, indicating little relative energy scale shift between detectors. The n-H peak at lower energy shows a distorted asymmetry, indicating a small relative scale shift.

a comparison between true and center-of-charge vertices of a Monte Carlo AD event sample.

The bias of this position reconstruction can be evaluated by comparing the reconstructed and true positions of ^{60}Co ACU calibration source deployments, whose positions are well-known. Biases at all positions are less than 15 cm at locations for all detectors, with a resolution of around 20 cm at all locations. This degree of resolution is sufficient for the AD-to-AD spallation neutron energy non-uniformity comparisons necessary for relative energy scale calibration.

Energy Reconstruction

In order to ensure that the n-Gd peak will appear at the same energy at all locations in an AD, a further position-dependent energy correction is applied to the data. Figure 7.7 demonstrates the variation in visible energy as a function of reconstructed position for both the spallation n-Gd and n-H peaks. The variation in E_{vis} with position along calibration axes is shown by splitting the AD into bins of 0.54 m in Z and 0.31 m^2 in R^2, which provide sufficient statistics in each bin, splits the target evenly in Z and R^2. One then can select events in the first, seventh and ninth center-most bins in $R^2$to compare to ACU A, B, and C, respectively. Peak values are given along the ACU axes to allow an easy comparison between spallation neutrons and ACU source ^{60}Co z-scans, which are shown in Figure 7.7(c) for AD1 and AD2.

There is a clear increase in energy scale with increasing R^2 and decreasing energy scale with Z-distance from the AD center. The Z-distribution is slightly offset from the detector center, as the PMT and reflectors are not geometrically symmetric about the detector Z-center. Z- and R^2- trends appear to be consistent between the different capture targets and between spallation and calibration source data.

One can provide a more uniform detector response by reconstructing event energies to correct for this variation. A correction function based on the average non-uniformity of the n-Gd peak in AD1 and AD2 was applied to the visible energy:

$$E_{rec} = 8.05/F(R) \times 8.05/F(Z) \times E_{vis}, \tag{7.10}$$

where $F(R)$ and $F(Z)$ are the energy response functions in terms of the cylindrical radial coordinate R and height coordinate Z respectively (both in units of meters):

$$F(R) = 7.74687 - 0.129958R + 0.355034R^2 - 0.0337578R^3, \tag{7.11}$$

$$F(Z) = 8.09949 - 0.11702Z - 0.124515Z^2 + 0.0245703Z^3. \tag{7.12}$$

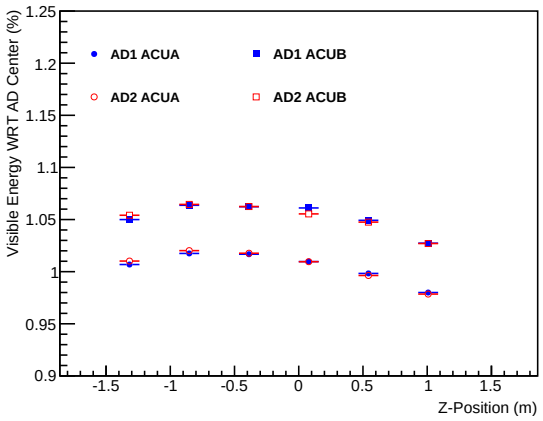

(a) Variation of AD1 n-Gd visible energy peak with Z-position along ACUA and ACUB.

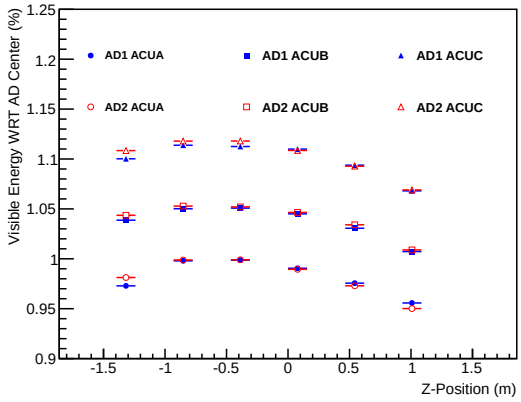

(b) Variation of AD1 n-H visible energy peak with Z-position along ACUA, ACUB, and ACUC.

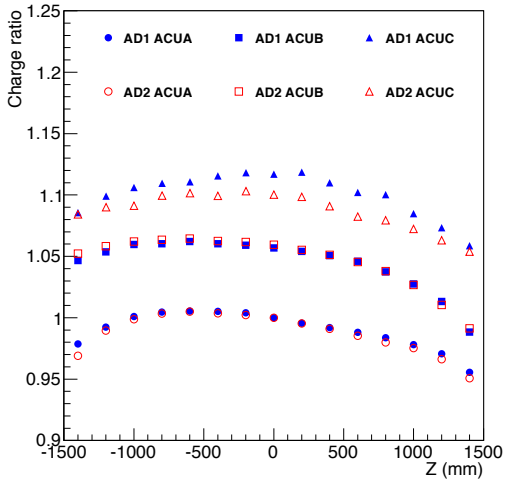

(c) Variation of AD1 ^{60}Co visible energy peak with Z-position along AUCA, ACUB, and ACUC.

Figure 7.7: Variation of the spallation n-Gd and n-H visible energy peaks as a function of position in AD1. Peaks values are given along the ACUs to facilitate easy comparison between spallation neutrons and ^{60}Co ACU calibration source z-scans, also pictured here. The R-positions of each ACU are 0 m (ACUA), 1.35 m (ACUB), and 1.77 m (ACUC).

This same reconstruction was applied to all detectors to avoid introducing detector-to-detector biases in the reconstruction. Thus, any difference in the position-variation of the visible energy scale between detectors remains uncorrected in the reconstructed

energies.

Figure 7.8 shows the position variation of the reconstructed energy. As expected, the non-uniformity of the energy scale is greatly reduced in each detector. Since the correction function is based on n-Gd captures, non-uniformity correction in the LS region, where no n-Gd captures are produced, is not complete, and leaves a few percent difference with respect to the target region.

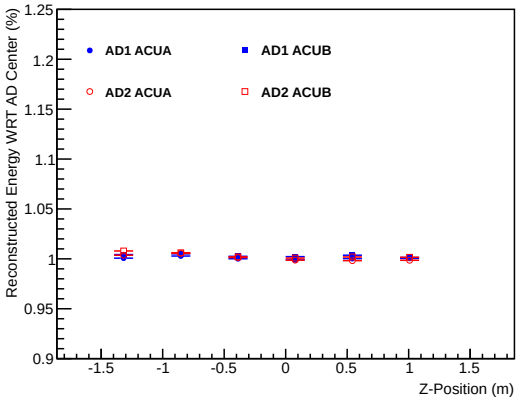

(a) Variation of AD1 n-Gd reconstructed energy peak with position.

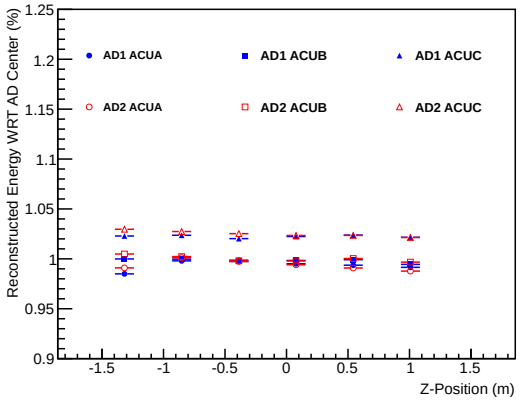

(b) Variation of AD1 n-H reconstructed energy peak with position.

Figure 7.8: Variation of the spallation n-Gd and n-H E_{rec} peak as a function of position in AD1. The variation in energy with R^2 and Z is clearly reduced from that seen in the visible energy, as pictured in Figure 7.7. One can also see the excellent agreement in the E_{rec} peak between ADs.

The energy resolution of the detector after reconstruction was measured by calculating the energy peak widths of the ^{60}Co, ^{68}Ge and AmC calibration sources. This resolution, demonstrated in Figure 7.9, is found to be $(7.5/\sqrt{E}+0.9)\%$. The neutron capture peak widths from spallation neutrons on Gd and H, as well as the inverse beta decay neutron captures, fit this resolution curve within a few tenths of a percent.

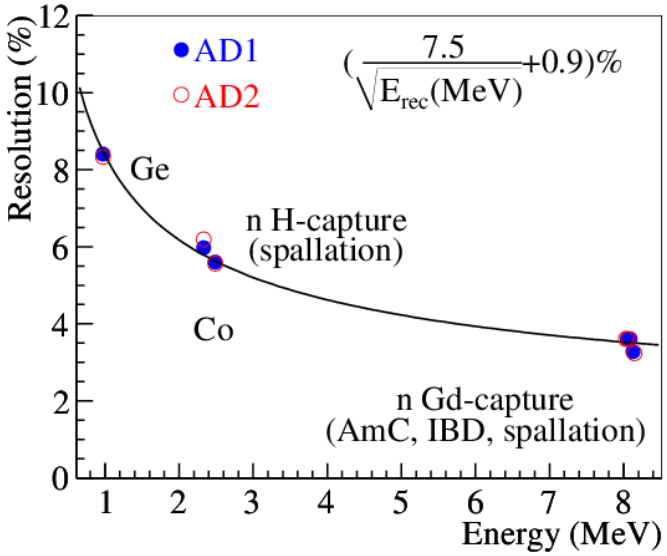

Figure 7.9: Post-reconstruction energy resolution for AD1 and AD2. Figure from [104].

Relative Position, Time, and Energy Differences

With the reconstructed energy and position of events established for all ADs, AD-to-AD differences in time, position, and energy dependence can be investigated to provide a relative energy scale uncertainty associated with the energy calibration.

The uncertainty due to the energy calibration constant's time-variation, which would be zero if this parameter could be instantaneously measured and applied, can be estimated by looking at an independent sample. Figure 7.10 shows the time-variation of the reconstructed ^{60}Co ACUA E_{vis} peak in the period of interest. The reader will notice that the mean asymmetry is not zero, but rather -0.13%. This is due to differences in position dependence between the two detectors, which are taken into account in the corresponding section below. The relative time variation difference between ADs, quantified by the RMS of the asymmetry about its mean, is 0.20%, which contributes directly to the relative energy scale uncertainty.

Variations in the detector energy scale with position were observed for all detector

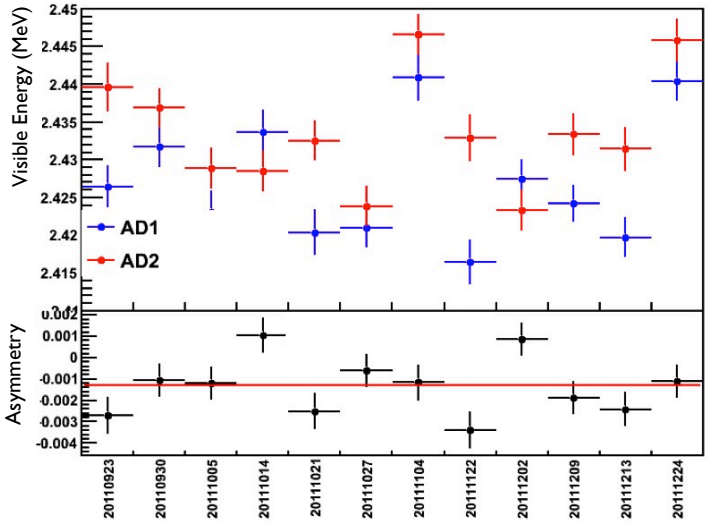

Figure 7.10: ^{60}Co ACUA E_{vis} peak at $z = 0$ vs time, after calibration with spallation neutrons. Also pictured is the asymmetry of this quantity between ADs. The RMS of this asymmetry about its mean is 0.20%, indicating a small difference in time-dependence between ADs.

locations by splitting the spallation neutron dataset into pixels in Z and R^2, as shown in Figure 7.11(a), and comparing the location of the n-Gd energy peaks between detectors for each pixel. The energy scale asymmetry between AD1 and AD2 for each pixel is shown in Figure 7.11(b). The energy scale is similar for all position bins to within 0.5%. The RMS deviation between detectors is 0.22%, which can be used as the contribution to the relative energy scale uncertainty from detector non-uniformity differences.

For an ACU source-based energy calibration, a non-linearity correction based on the AmC source must be applied in order ensure that neutron captures are reconstructed to the correct absolute energy. This step is not necessary for a calibration based on spallation neutrons. However, differences in non-linearity between detec-

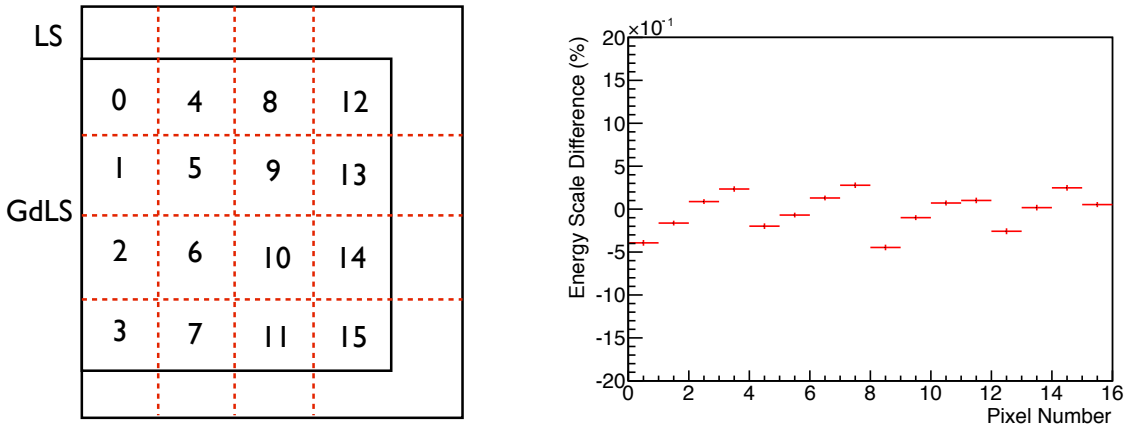

(a) Schematic cross-section view of the detector GdLS and LS targets and Labelling scheme of pixels for various detector positions.

(b) Difference in n-Gd energy scale between AD1 and AD2 for the detector position pixels shown in 7.11(a).

Figure 7.11: Difference in spallation n-Gd energy scale between AD1 and AD2 at all detector locations. n-Gd captures reconstructed to positions in the LS are included in the adjacent target pixel. Variation between detectors at all positions is less than 0.5%, with an RMS difference of 0.22%.

tors should still be characterized by comparing relative differences in E_{rec} between detectors for events of varying particle type and energy. For an eventual θ_{13} analysis, an absolute non-linearity calibration must be done to ensure that the inverse beta decay positron spectrum is properly reconstructed. However, for a high-precision comparison of near-site rates and spectra, this step is not necessary.

The comparison of relative non-linearity can be done by comparing detector-wide E_{rec} asymmetries for various particle types and energies. For this check, n-Gd and n-H gamma peaks are used, as well as alpha peaks gleaned from the decay chains of U-Th backgrounds in the detector. ^{212}Po from ^{232}Th, ^{214}Po from ^{238}U, and ^{215}Po from ^{235}U are created in small amounts uniformly in the detector target, creating low-energy correlated backgrounds. The energy peaks of these alphas can be identified with high efficiency by applying the correct time coincidence, energy, and position cuts, as shown in Table 7.2. Tight cuts ensure a high-purity sample, which is more crucial to

determining an unbiased alpha peak value than well-understood cut efficiencies.

Alpha Source	^{212}Po	^{214}Po	^{215}Po
Energy Cut (MeV)	1.05<E<1.5	0.7<E<1.3	0.65<E<1.3
Time Coincidence Cut (μs)	0.3< Δt<3	10< Δt<400	10< Δt<2000
Position Cut (m)	Radius < 1.5 and |Z| < 1.5		
Spatial Coincidence Cut (m)	Distance between signals < 1.5 m		

Table 7.2: Cuts used to isolate alpha background peaks in the detector at visible energies of around 1 MeV. These peaks can be compared between detectors to identify possible relative non-linearity differences.

While these alphas are created with energies exceeding 6 MeV, the E_{vis} spectra of these peaks, some of which are shown in Figure 7.12, exhibit energy quenching on the order of 85%, which is expected based on their large dE/dx. For this reason, any relative non-linearity difference between detectors would be highlighted in the alpha peak value asymmetries.

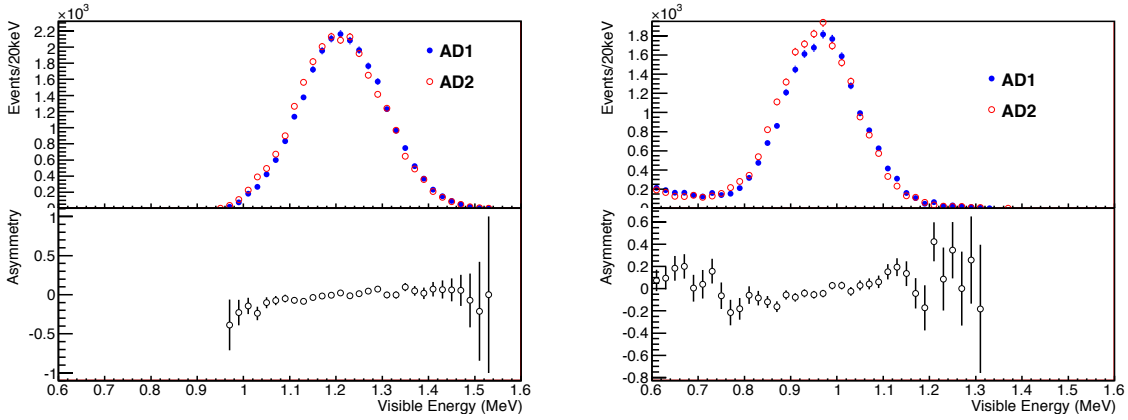

(a) ^{212}Po decay E_{rec} spectrum.

(b) ^{214}Po decay E_{rec} spectrum.

Figure 7.12: E_{rec} spectrum and AD1-AD2 asymmetries for ^{214}Po and ^{212}Po alpha decays. Asymmetry is defined in Equation 7.8. The flatness of the asymmetry spectra indicate relatively good agreement in energy scale between ADs for these highly-quenched peaks.

Relative energy scale differences between detectors for these alphas and the neutron capture peaks are shown in Figure 7.13 along with the spallation n-Gd as a

reference. All alphas exhibit asymmetries of less than 0.45%; the RMS deviation from zero for all points and detectors is 0.23%. It should be noted that for the ACU and alpha sources, asymmetries also derive from relative differences in position correction, so this uncertainty will be highly correlated with that arising from position non-uniformity.

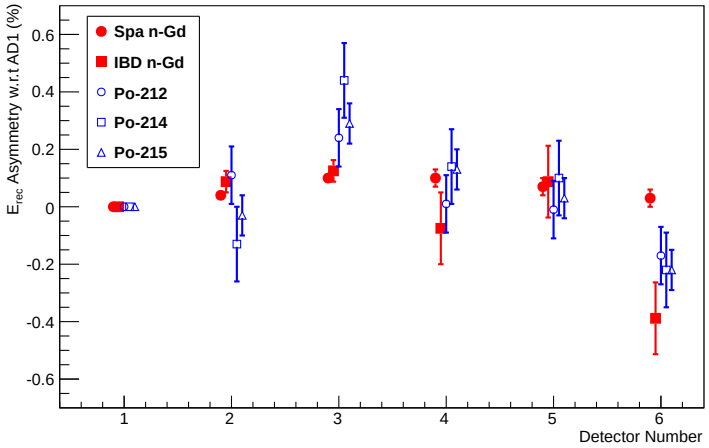

Figure 7.13: Variation in reconstructed energy asymmetry between each detector and AD1 for different particle types. It should be noted that for the ACU and alpha sources, asymmetries also derive from relative differences in position correction. The RMS of these values can provide a conservative measure of the relative uncertainty in the energy scale arising from non-linearity differences.

This value of 0.23% can be used as an conservative estimate of the contribution of non-linearity to the relative energy scale uncertainty for any particle type and energy. In the case of the n-Gd peak energy scale uncertainty, this value is made effectively zero by calibrating directly with spallation neutrons.

By combining the differences in time, position, and energy dependence, one can calculate the relative energy scale uncertainty associated with Daya Bay's energy calibration. The calibration will provide different values generally for all particle types/energies and for the specific n-Gd capture peak. A summary of the size of each

contribution to the total energy scale systematic for each of these two cases can be seen in Table 7.3. The estimated relative energy scale uncertainty for all particle types is 0.38%, while the uncertainty for the n-Gd peak is 0.30%, in perfect agreement with the ACU-based relative energy scale calibration presented in [104]. This information can be utilized to estimate relative differences in energy cut efficiencies between detectors, which comprise a significant portion of the expected systematic uncertainty of the Daya Bay experiment.

Systematic Source	n-Gd Unc. (%)	All Particle Type Unc. (%)
Relative Position Dependence	0.22	0.22
Time Dependence	0.2	0.2
Relative Non-Linearity	0	0.23
Total	0.30	0.38

Table 7.3: A summary of relative energy scale systematics for all particle types and energies, as well as specifically for the n-Gd peak energy scale. As the spallation neutron peak is the basis of the calibration and n-Gd position dependence is very well-characterized, its relative energy scale uncertainty is lower than for a generic particle and energy.

Chapter 8

Side-by-Side Comparison Of Near-Site Detectors

8.1 Introduction

In the initial phase of the Daya Bay experiment, two detectors were installed at the Daya Bay near site, also called experimental hall 1 or EH1, and operated while the remainder of the experimental halls were commissioned. This data period consists of 70.3 live days of physics data running, which are distributed as seen in Figure 8.1. The analysis time was split into runs of varying length as data-taking progressed. Approximately 77% of the total calendar time during September 23 and December 23 was used in this analysis. This initial data was used to compare inverse beta detection rates and single background rates in the two near site detectors.

As the first two detectors are located in the same experimental hall, the correlated effects of baselines and site-related backgrounds will largely cancel, allowing for a targeted comparison of detection efficiency between detectors. By using near detectors, which detect approximately 700 events per day, the statistical uncertainty

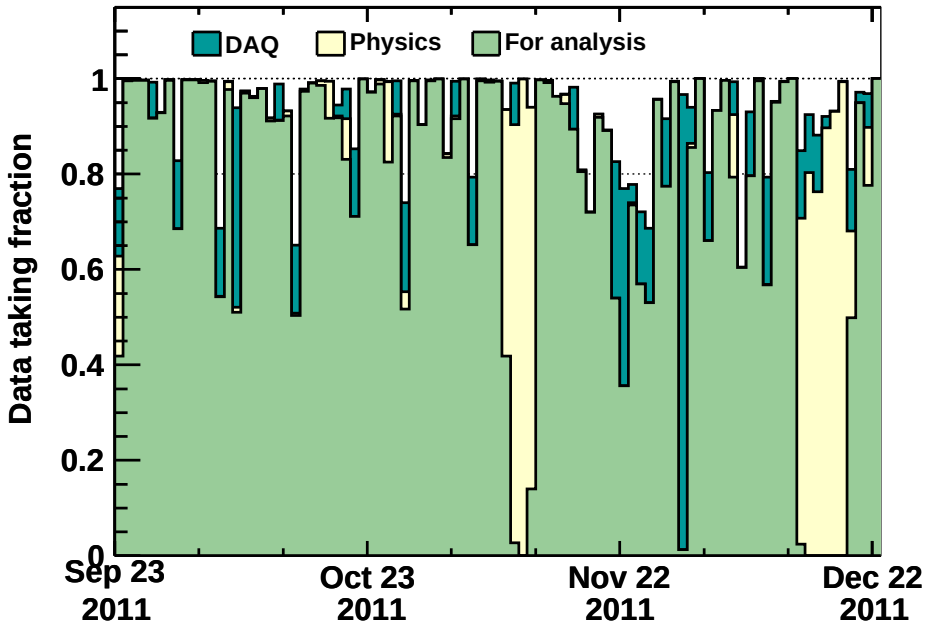

Figure 8.1: The data period from which the side-by-side comparison of EH1 detectors was made. The light green indicates time periods used in the physics analysis. Yellow physics data periods were generally dedicated to instrumental tests, while the blue DAQ periods consisted of weekly calibration runs and other electronics tests. Figure provided by [136].

of the comparison will be very low. If this targeted measurement is consistent between detectors, it will be an excellent demonstration of proper understanding of the Daya Bay experiment's relative detector systematics, which will lead to a reliable sub-percent precision measurement of oscillation effects for the full experiment.

The data for a Daya Bay near site AD is composed of approximately 60 triggers per second above 0.7 MeV, 22 of which are above 20 MeV and qualify as AD Muons. The Daya Bay water pool data consists of hundreds of water pool triggers per second distributed between the inner and outer water pool detectors. In contrast to this high event rate, a neutrino interaction is expected once every few minutes in each AD. Thus, a number of selection cuts must be applied to the processed data in order to obtain a high-purity sample of inverse beta candidates. The applied cuts

must produce highly consistent efficiencies between detectors in order to maintain a low detector-related relative systematic uncertainty. After selecting inverse beta candidates, residual backgrounds must are estimated, measured, and subtracted to yield a total number of inverse beta detections that can be compared between near-site detectors.

Analysis cuts and background estimations were developed and studied by a wide array of Daya Bay collaborators, resulting in analyses utilizing different efficiency cuts and background estimation techniques. For the collaboration's first physics result [104], multiple analyses were completed by different institutions, utilizing, in particular, differing muon veto and multiplicity cuts, energy calibration, and background estimations.

A portion of my analysis work focused specifically on the study of efficiencies and uncertainties related to energy, timing, and muon cuts, spill-in/out effects, and H/Gd ratios. The analysis presented in this thesis is a synthesis of these personal contributions as well as techniques and cuts explored by other collaborators. These pieces are brought together and applied to a full dataset of tagged time-coincident triggers in personally-developed analysis algorithms, which output a background-subtracted set of inverse beta decay detections for each AD.

8.2 Inverse Beta Selection

The inverse beta decay interactions undergone by $\overline{\nu}_e$ in each AD create time-correlated triggers between a prompt positron energy deposit and a delayed neutron capture. In order to reduce backgrounds and energy cut uncertainties, this analysis focuses specifically on those IBD events whose neutrons capture on Gd. By generally categorizing the various physics event types in Chapter 7, we uncovered a number of

possible discriminators that could be used to separate Gd-capturing IBD-like events from other types: event topology, time coincidence, prompt and delayed energy, time since muon, and event multiplicity. For this analysis, the following cuts are applied to obtain a high-purity IBD candidate sample:

- Flasher Removal: $\log_{10}((\frac{R_{max}}{0.45})^2 + (\frac{R_{quadrant}}{1})^2) < 0$, where $R_{max} = \frac{Q_{max}}{N_{PE}}$ and $R_{quadrant} = \frac{Q_3}{Q_2+Q_4}$. In addition, for any 2" calibration PMT, Q <100.
- Water Pool Muon: Veto all coincidences whose delayed signal is within (-2 μs, 600 μs) of a water pool trigger with > 12 hit PMT channels
- AD Muon: Veto all coincidences whose delayed signal is within 1400 μs of an AD trigger with >20 MeV in the same AD
- Showering Muon: Veto all AD coincidences whose delayed signal is within 0.4 s of an AD trigger with >2.5 GeV in the same AD
- Prompt Energy: 0.7 MeV < E_{prompt} <12 MeV
- Prompt Energy: 6 MeV < $E_{delayed}$ <12 MeV
- Prompt-Delayed Time Coincidence: 1 μs < Δt < 200 μS
- Event Multiplicity: Remove all coincidences with excess triggers:
  - one prompt-like trigger within (-200 μs,0 μs) of coincidence's delayed signal
  - no prompt-like trigger within (-400 μs,-200 μs) of coincidence's delayed signal
  - zero delayed-like triggers within (0,200 μs) of a coincidence's delayed signal

The following section will describe each of these cuts in more detail, and demonstrate the efficiency and systematic uncertainty introduced by each cut.

Flasher Removal

As described in Chapter 7, many AD triggers are caused not by physics events, but by flashes of light emitted periodically by the electronics inside particular PMTs. These 'flasher' triggers produce a topologically distinct charge pattern in the AD, depositing light primarily in the flashing PMT and in a beam of light across the AD. Other collaborators have demonstrated that this distinct pattern makes them easy to separate from real physics events with cuts on R_{max} and $R_{quadrant}$. For example, Figure 8.2 shows the distribution of events in flasher variable space for various energy ranges, as well as the applied flasher cut. A clear separation can be seen between physics and flasher events above 6 MeV, while the two types are largely separated for energies above 0.7 MeV. Flashing from a special 2" calibration PMT can be removed by cutting any trigger in which the 2" PMT has more than 100 PE charge.

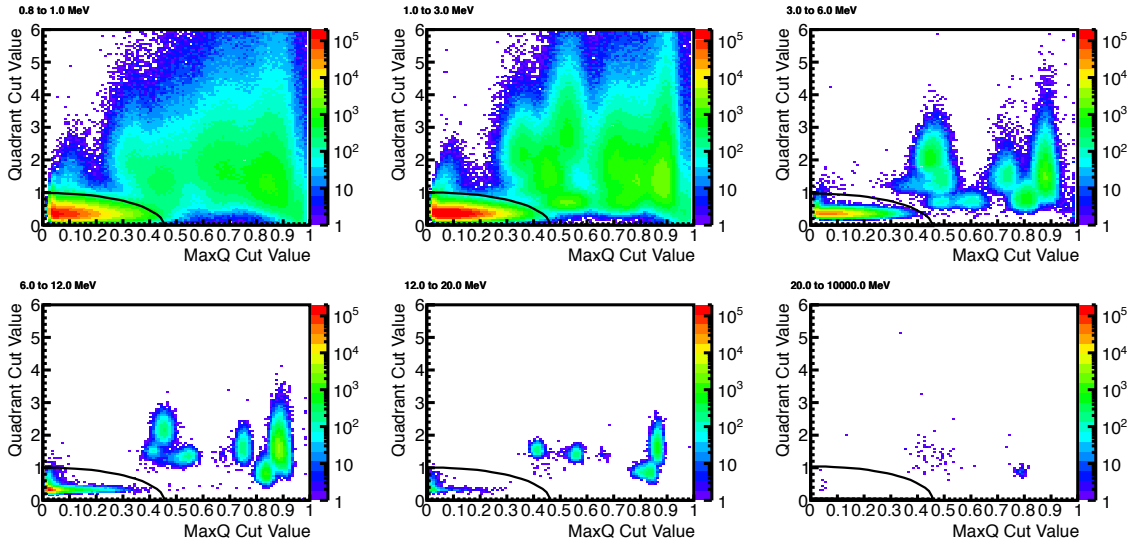

Figure 8.2: R_{max} versus $R_{quadrant}$ for AD1 triggers of different energy ranges. The plotted energy range is listed above each subfigure. The region in the bottom left-hand corner is comprised of physics triggers, while the flashers appear mainly at higher R_{max} and $R_{quadrant}$. Separation between physics events and flashers increases with trigger energy. The ellipse flasher cut is indicated by the solid black line.

An ellipse cut in flasher variable space is applied with maximum values of 0.45

and 1 for R_{max} and $R_{quadrant}$, respectively. By conducting Monte Carlo simulations of IBD events and observing how many MC event fall outside these cuts, one can determine the inefficiency of this topological cut. Using this method, an IBD detection inefficiency of 0.001% was calculated. One can also cross-check this inefficiency for various energy regions by tracking the maximum-charge PMT for each event not passing these flasher cuts. If the inefficiency is 0%, the highest charge PMT in a flasher event should not be a non-flashing PMT. One can plot the energy of the subset of events whose maximum-charge PMT is a non-flasher, and estimate the fraction of these inefficient events that follow the prompt energy spectrum of an IBD event. This method produces an estimated inefficiency of 0.002%.

Flasher contamination of the signal can be estimated by looking at the flasher variable for IBD candidate sub-events passing all but the flasher cut, shown in Figure 8.3. This plot shows clear separation of IBD and flasher events.

A conservative estimate of flasher contamination assumes that all events in the gap between the cut value of zero and the main peak beginning at about -0.25 are contaminating flasher-related coincidences. This estimate gives a 0.04% relative difference in IBD candidates between detectors. Given the small expected inefficiency of the flasher cut, this value of 0.04% can be treated as the total relative and absolute uncertainty contributed by the flasher cut.

Muon Veto

Muon-related activity in the detectors, particularly spallation neutrons, are rejected by vetoing all coincidences whose delayed event is within a certain time window surrounding a muon trigger. The rate of each type of muon trigger is shown in Table 8.1. Muon-created spallation neutrons created in the GdLS will mostly capture within 100 μs. Absent the presence of Gd in the MO and LS, spallation neutrons will

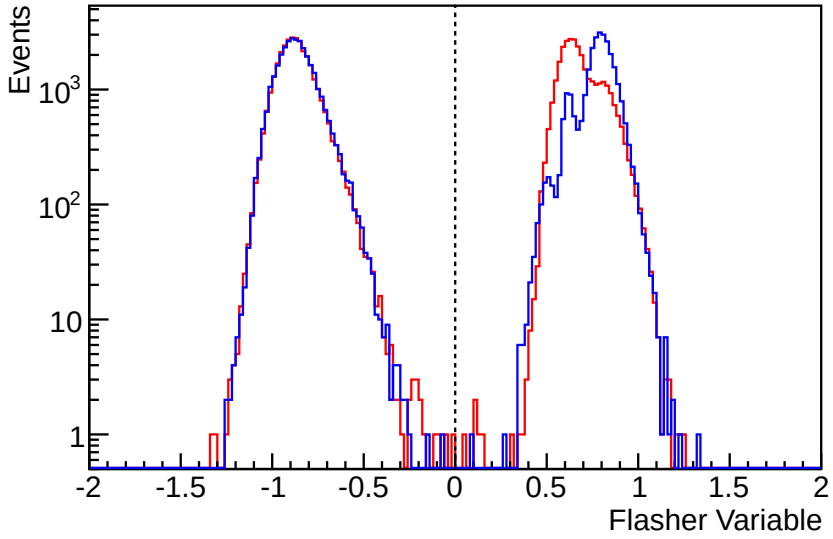

Figure 8.3: Flasher discriminator for all IBD delayed candidates. The events to the right of the illustrated cut value of 0 are flashers; these are rejected as IBD candidates. A few candidates appear in the gap between this cut and the main peak. If these are assumed to be flashers, they contribute 0.04% contamination of the IBD sample.

have a capture time of around 200 μs. Many of the spallation neutrons thermalizing in these regions can spill into the GdLS, causing Gd-captures many hundreds of μs after a muon trigger. Veto periods must be long enough to reject these spallation neutrons with high efficiency, but short enough to ensure high IBD detection efficiency.

Muon Type	Definition	Trigger Rate (Hz)
Water Pool	>12 NHit in Water Pool	360
AD Muon	>20 MeV in AD	22
Showering Muon	$>3\times10^5$ PE in AD	0.1

Table 8.1: The definition and rate of various muon triggers in Experimental Hall 1.

A 600 μs post-muon cut on the water pool highly rejects these neutrons while maintaining an efficiency of around 88%. In addition to vetoing time after WP muons, the 2 μs before a WP muon must also be vetoed because of an observed time latency between AD and WP triggers: WP energy depositions occurring before AD

energy depositions will create triggers with a slightly later timestamp than the AD trigger.

Because the AD muon rate is much lower than the WP muon rate, a longer muon veto window, around 1400 μs can be afforded for AD muon triggers, producing an approximate 98% efficiency. Showering muon triggers, which are even more rare, can be afforded a veto time window of 400 ms, during which many of the beta-neutron decay isotopes created by the showering muon will decay away.

The total efficiency of these cuts can be calculated by calculating the total time spanned by the many overlapping veto windows, and comparing this to the total live time of each detector. The veto time span for each of the three veto types was calculated first individually, taking into account the known overlap of the different veto types:

1. The first 1400 μs of every showering muon veto window are also defined as an AD Muon veto window. For this reason, showering muon veto windows only add a maximum of 398.4 ms in length to the showering muon's veto time span.

2. The first 600 μs of an overwhelming majority of AD muon veto windows are also defined as a WP Muon veto window. For this reason, AD muon veto windows only add a maximum of 800 μs in length to the showering muon's veto time span.

With these corrections in mind, the overlapping veto windows of each individual type are counted for all runs in the entire physics data period, and then compared to the total running time to get the efficiency for each of the three vetoes. By adding the above corrections, the calculated efficiencies are entirely uncorrelated with one another in time, so multiplication of the three efficiencies will give a total muon veto efficiency for each detector. This method of calculating the muon veto has

small uncertainties on the order of 0.1% resulting from the uncertainties in the time-correlation assumptions listed above. The total muon veto efficiency for each physics run in AD1 and AD2 as a function of time is shown in Figure 8.4. The average muon veto efficiency is 81.3% and 81.0% for AD1 and AD2, respectively. As expected, there is little change in efficiency with time.

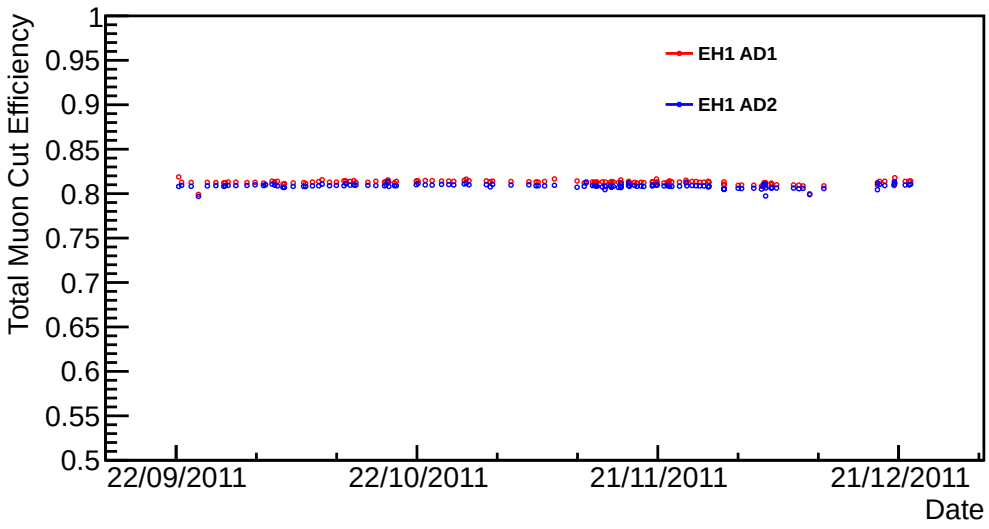

Figure 8.4: Muon veto efficiency as a function of time for AD1 and AD2. Included in this efficiency are the water pool, AD, and showering muon cuts. This efficiency for each physics run remains stable as a function of time.

One can also notice a difference of 0.3% in muon cut efficiency between ADs: this is caused by different shower muon cut efficiencies. The PE spectrum of AD2 extends to higher ranges, likely from differences in PMT gain at high charge and non-linearity in the coarse range ADC, effects which only impact high-energy, muon-like triggers. This means that more triggers in AD2 will be identified as showering muons, leading to more veto periods and lower IBD efficiency. As mentioned above, this difference is known negligible uncertainty, as veto windows are exactly counted.

Multiplicity Veto

A multiplicity cut is used to reject any events in which an extra prompt- or delayed-like AD trigger is in the vicinity of a coincidence's delayed trigger. For these groups of three or more events, it is hard to determine which triggers are caused by an inverse beta positron and neutron. These ambiguous coincidence groups are rejected, as they can distort the IBD positron and time coincidence spectrum.

The efficiency of this cut is determined by the prompt and delayed singles rate in each detector. The set of singles triggers are defined by the same set of cuts applied to IBD prompt set, with the exception of the time coincidence cut: singles events are required to be isolated in time by 200μs before and after. The singles spectrum for AD1 and AD2 are shown in Figure 8.5, along with the prompt-like and delayed-like singles rates as a function of time. This rate is corrected for the efficiencies of the applied muon veto and the multiplicity veto itself. One can see a small difference in prompt singles rates between ADs: this likely arises from slight differences in intrinsic detector radioactivity. The small decrease in prompt singles rate follows an exponential distribution, and is indicative of the gradual decay of a short-lived radioactive background in the detector.

The absolute multiplicity cut efficiency is calculated statistically assuming Poisson distribution of singles events in time,

$$\epsilon_{mult} = e^{-400\mu s \cdot R_p - 200\mu s \cdot R_d} \approx 1 - 400\mu s \cdot R_p - 200\mu s \cdot R_d, \tag{8.1}$$

where R_p and R_d are the rate of time-isolated prompt and delayed signals. The first term represents the accidental coincidence of an additional prompt-like single within 400 μ before a delayed-like trigger, and the second term the coincidence of another delayed-like trigger within 200 μs after a delayed trigger. Using this formula, the multiplicity cut efficiency for both detectors is determined to be 0.974. The change

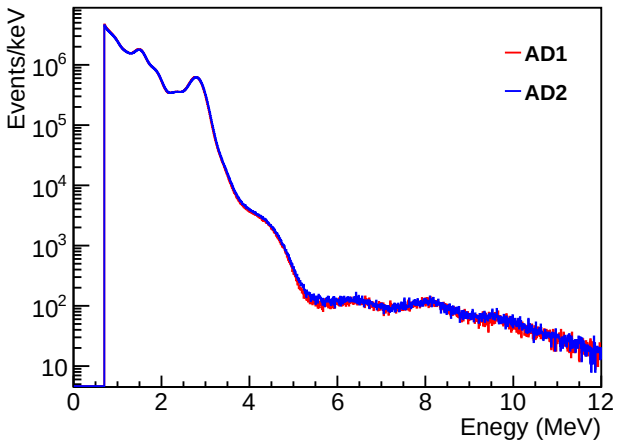

(a) Time-isolated singles spectrum. The low-energy analysis threshold of 0.7 MeV is clearly visible.

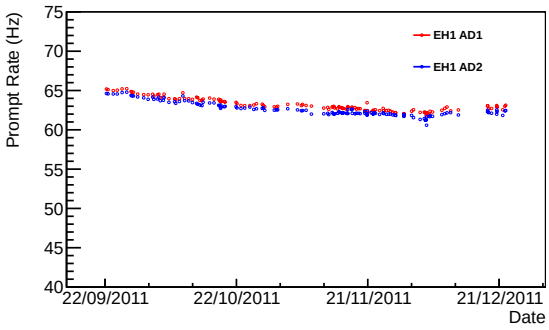

(b) Prompt-like singles rate for each physics run versus time.

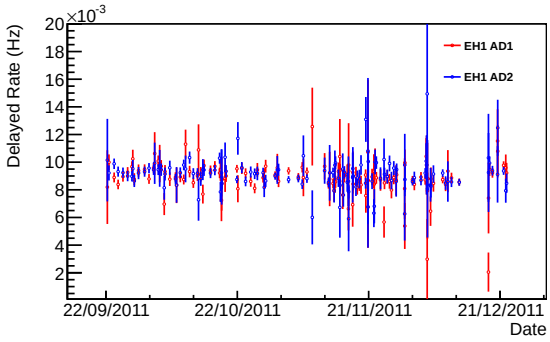

(c) Delayed-like singles rate for each physics run versus time. Fluctuations in this rate are statistical.

Figure 8.5: The rate and spectrum of singles in ADs 1 and 2. Singles triggers are required to be isolated in time, with no other triggers occurring within 200 μs. Prompt-like singles are singles triggers with energies above 0.7 MeV, while delayed-like singles have energies between 6 and 12 MeV.

in this efficiency as a function of time can be seen in Figure 8.6; a gradual total increase of around 0.1% can be seen as a function of time, which is caused by the decreasing prompt singles rate. The total absolute and relative uncertainty associated with this efficiency, <0.01%, is defined by the statistical uncertainties of the prompt and delayed singles rates, which are very low.

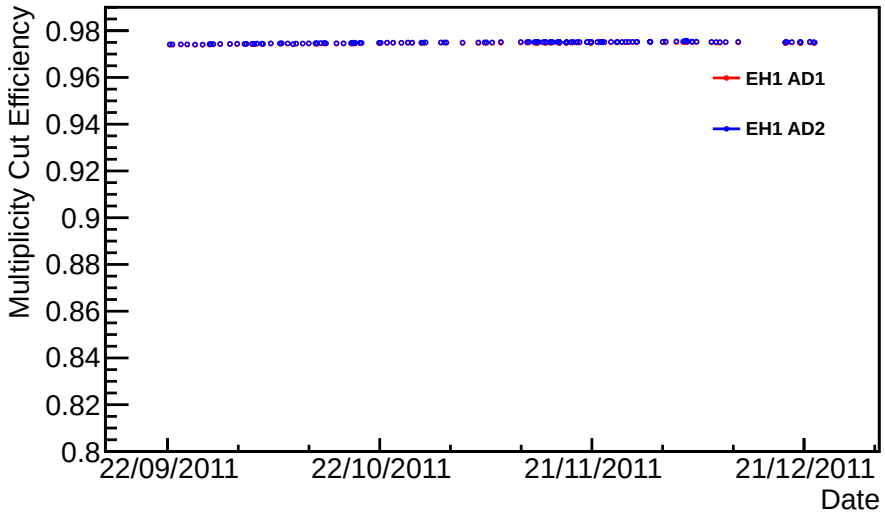

Figure 8.6: Multiplicity cut efficiency as a function of time for AD1 and AD2. On can see a slight upward trend in the multiplicity efficiency on the order of 0.1% resulting from the gradual depletion of singles rates.

Energy Cuts

The prompt and delayed energy of AD1 coincidences passing all except the IBD energy cuts are shown in Figure 8.7, along with the applied energy cut values. These energy cuts, particularly the 6 MeV delayed energy cut, reject an overwhelming majority of accidental backgrounds, which dominate the lower delayed energy region. However, as one can see by looking directly at the delayed energy spectrum in Figure 8.8, this cut passes through the middle of an energy range populated largely by IBD Gd-captures whose full energy was not deposited in the scintillating detector region, creating some inefficiency in detection of IBDs with n-Gd captures.

In a relative comparison of IBD detection rates between ADs, the absolute efficiency and uncertainty are not important, as their impacts cancel in the near-far comparison of detectors. The only portion that does not cancel is any relative difference in efficiency between detectors. A relative difference in efficiency can arise from

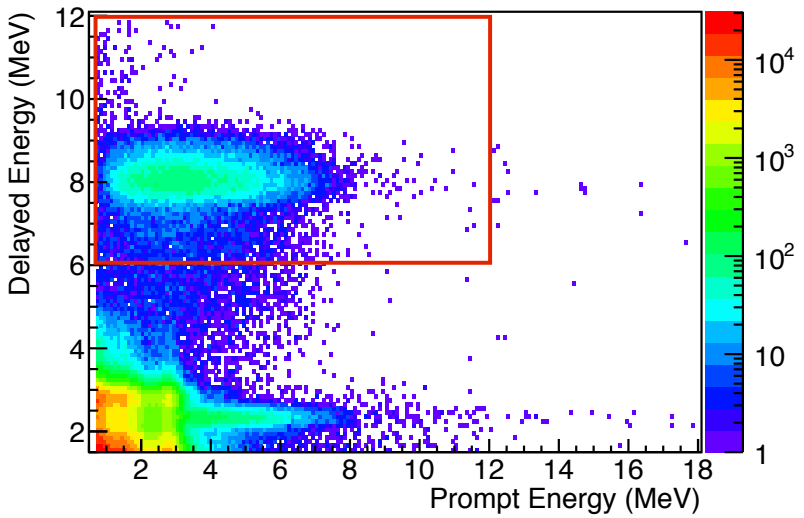

Figure 8.7: The prompt and delayed energy of all IBD candidates. The prompt and delayed energy cuts are indicated by the red box surrounding the signal region.

two possible sources:

1. **Relative energy scale differences:** If uncertainties in the energy scale calibration cause one detector's n-Gd peak and tail to be reconstructed to a higher energy than the other detector, a larger portion of that detector's events will pass the 6 MeV cut.

2. **Tail shape differences:** Physical detector differences can cause relative differences in the shape of the n-Gd tail between detectors. The 6 MeV cut will reject more signal events of an AD with a relatively larger tail, causing a difference in efficiency.

The relative contribution to the 6 MeV cut efficiency uncertainty from 1) can be easily estimated using the relative uncertainty in the energy scale calculated in the previous chapter, 0.3% . One can count the number of events in this 0.3% uncertainty window around 6 MeV and divide it by the total detected number of n-Gd captures passing the cut to calculate the relative energy cut uncertainty. Before

doing this, one must account for the fact that the outer GdLS regions at high R^2 and Z contribute more events to the delayed energy spectrum tail than do inner regions. As demonstrated in Figure 7.11, these outer pixels, particularly the AD bottom, have a larger relative energy difference than inner regions. The relative energy scale uncertainty value should be slightly inflated to account for this. In the calculation of relative non-uniformity differences, each pixel's energy scale difference should be properly weighted by its relative contribution to the total events in the 6 MeV region. This recalculation of the relative energy scale uncertainty yields a value of 0.37%, leading to an energy cut uncertainty of 0.12%. Using the same method, the relative uncertainty from the 0.7 MeV prompt energy cut is estimated to be 0.02%.

In Chapter 6, MC simulations were used to demonstrate that differences in detection efficiency (effectively differences in tail shape) resulting from differences in the physical detector parameters of the ADs would be less than 0.1%. This similarity in tail shape can also be demonstrated by counting the tail events in a high-purity sample of inverse beta candidates. Figure 8.8 shows the delayed energy spectrum of IBD candidates with prompt energy above 4 MeV. This strict cut removes a large majority of accidental backgrounds in the delayed energy tail above 3.5 MeV, leaving a reduced sample overwhelmingly composed of real IBD events. One can then count to determine the percentage of IBD n-Gd captures between 3.5 and 6 MeV. For AD1 and AD2, these tail percentages are 93.4% and 93.5%, with 0.23% statistical uncertainty. This result supports the conclusion first drawn from the MC simulation.

Although it is of less importance, the absolute efficiency of the 6 MeV cut can be estimated using a combination of MC and this high-purity IBD n-Gd sample. The spectrum of the MC n-Gd tail below 6 MeV can be adjusted with a linear scaling until its shape matches that of the IBD sample, as shown in Figure 8.8. This MC spectrum, which now contains the proper full tail shape for only n-Gd events, can

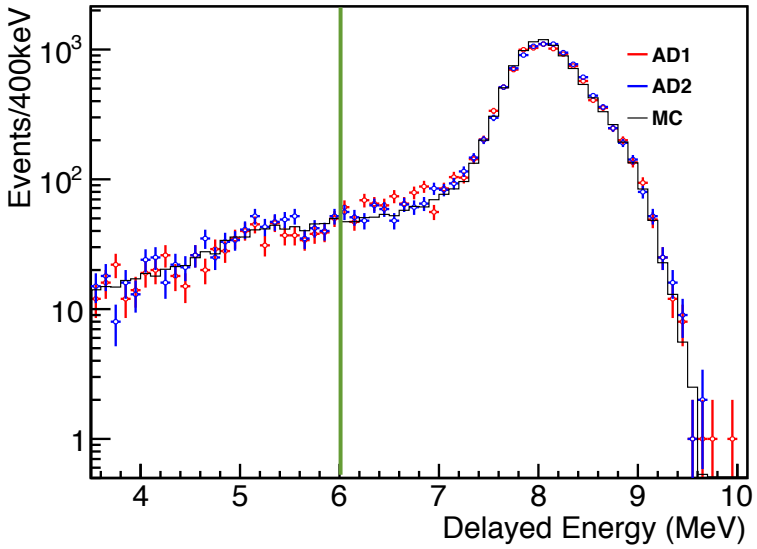

Figure 8.8: IBD candidate delayed energy spectrum. The low prompt energy cut is applied at 4 MeV, which removes accidental backgrounds while leaving the n-Gd peak and tail shape unchanged. A comparison between spectra and tails for ADs and Monte Carlo are also pictured.

then be used to calculate the absolute cut efficiency, which is calculated to be 92.0%. The associated absolute uncertainty, originating from uncertainties in the detected tail shape and MC tail modelling, is estimated to be 0.6%.

Gd Capture Fraction

In addition to rejecting some n-Gd tail events, the 6 MeV cut also rejects all IBD interactions whose neutron captures on hydrogen. Thus, relative differences in the ratio between Gd and H captures will result in relative differences in efficiency between ADs.

The relative Gd capture fraction between detectors can be determined by comparing the capture time spectrum between detectors: if one AD has a lower Gd to H concentration, it will exhibit a higher H-capture fraction as well as a capture time

more influenced by the longer n-H capture time. The exact relationship between capture time and Gd-capture probability is the following:

$$P_{Gd} = \frac{1}{1 + \Gamma_H/\Gamma_{Gd}} \tag{8.2}$$

where Γ_{Gd} and Γ_H are the n-Gd and n-H capture times of roughly $1/(30\ \mu\text{s})$ and $1/(200\ \mu\text{s})$, respectively. Thus, in order to know the Gd-capture percentage difference between detectors to a precision of 0.1%, the Gd-capture times must be measured to a precision of 0.5%.

This capture time comparison can be made using AmC neutron sources deployed at the center of each detector. These sources produce fast neutrons, which, as described in the previous chapter, produce a prompt proton recoil and delayed neutron-capture coincidence and an associated coincidence time spectrum. This dataset provides a high-statistics sample that is well-separated from the LS region, thus avoiding possible contamination of the timing spectrum by spill-in neutrons, which will spend longer times thermalizing in a region devoid of Gd.

The timing spectrum of AmC coincidences is shown in Figure 8.9. Each AD's full spectrum is fitted the following function:

$$N(t) = \frac{N_{th}}{\lambda_{th}} e^{-\lambda_{th} t} - \frac{N_u}{\lambda_u} e^{-\lambda_u t} + N_{bg}, \tag{8.3}$$

where N and λ describe the normalization and capture time of the thermalized (th) and unthermalized (u) neutrons, and N_{bg} describes the accidental backgrounds, which should exhibit no characteristic decay time. This function takes into account the energy-dependent variations in the Gd-capture cross-section which cause the capture time spectrum to peak at around 5 μs. The fitted capture times λ_{th} are 28.70 and 28.60 μs for AD1 and AD2, respectively. The uncertainty in the capture times, 0.15 μs or 0.5%, translates to an uncertainty in the Gd-capture percentage of 0.1%.

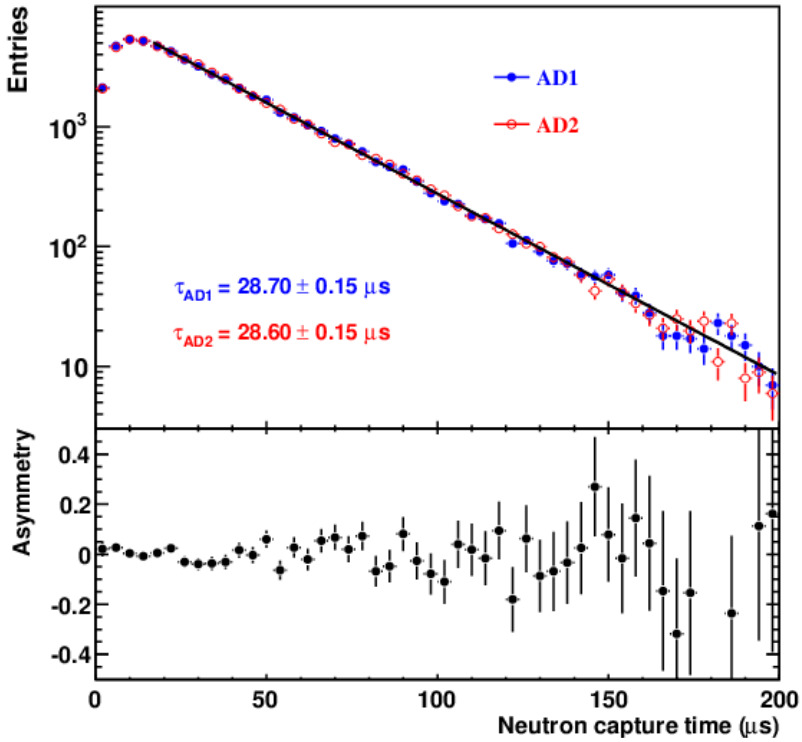

Figure 8.9: Capture time spectrum for an AmC source deployed at the detector center in AD1 and AD2. The prompt signal is provided by proton recoils, while the delayed signal is from neutron capture. From [104].

The absolute H/Gd capture ratio for each detector was also measured by comparing the sizes of the background-subtracted n-H and n-Gd spallation peaks in the center of the detector. The measured H/Gd capture ratios were 85.6%±0.5%, with uncertainties resulting mainly from statistical limitations.

Spill-in/out Events

The uncertainty in the total number of Gd-captures can also vary because of relative spill-in/out differences between detectors. The number of spill-in/out events is very hard to precisely compare between detectors with data. However, in Chapter 5, we noted using Monte Carlo simulations that very little relative difference in spill-in/out

was to be expected as a result of the measured variations of detector parameters. Table 6.8 shows in particular what variations could be expected. The only detector parameters exhibiting differences above systematic measurement uncertainties are the differences in IAV thickness, which were as large as 1 mm. This thickness variation could cause as much as 0.02% difference in the total number of detected Gd. This figure will be used as the relative spill-in/out systematic uncertainty.

The absolute size of the spill-in and spill-out effects are currently estimated by Monte Carlo simulations to be 5.0 and 1.8% of the total IBD detection rate, respectively. An absolute associated uncertainty of 1.5% originates from the uncertainty in IBD neutron transport modelling in NuWa.

Timing Cuts

Similar to energy cuts, relative uncertainties from timing cuts can be caused by relative uncertainties in the location of the timing cut from TDC calibration and by differences in detectors' coincidence time spectrum tail shape. The capture time spectrum of all IBD events, is shown in Figure 8.10. It resembles the AmC capture time spectrum with an additional tail at long capture time from spill-in Gd-captured IBDs, which have additional time to thermalize and wander in the absence of Gd in the acrylic and LS. This capture time spectrum can be fit using the capture time function for AmC with an additional exponential added to fit the additional component from spill-in events. By varying the fitted capture time constants, one finds that the number of events within the cut bounds remains consistent to $<0.01\%$.

The timing calibration discussed in Chapter 7 has a conservative associated uncertainty of 10 ns. Counting the events in the 10 ns window around the timing cut values yields a relative uncertainty of $<0.01\%$, which, when combined with the negligible uncertainty from differences in capture time spectral shape, give a total relative

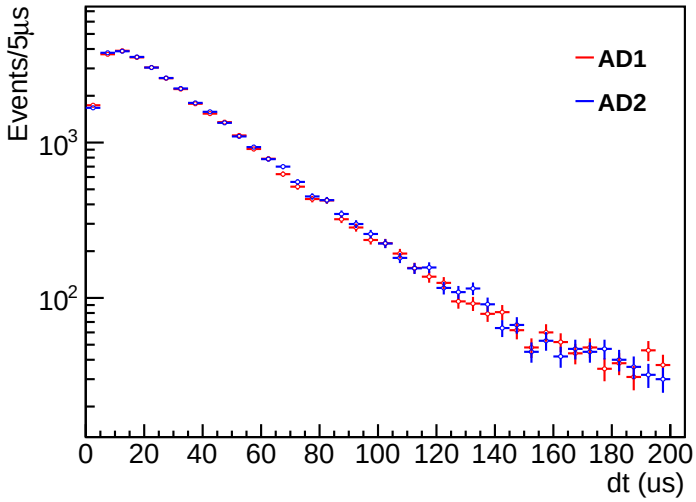

Figure 8.10: The spectrum of coincidence times between prompt and delayed signals for IBD candidates. The spectrum is similar to the one for AmC, with the addition of a larger flat continuum from backgrounds and an elongated tail from spill-in events.

timing cut uncertainty of <0.01%.

The absolute efficiency of this timing cut has not been measured with this data set, but has been estimated with Monte Carlo to be 98.7%. Absolute uncertainties are driven by spill-in rates and their absolute uncertainties. Since an overwhelming majority of the IBD events with capture times >200 μs are from spill-in events, a 5% spill-in effect with an uncertainty of 1.5% would produce roughly a 0.1% uncertainty in the absolute timing cut efficiency.

Summary

A summary of all calculated efficiencies and their associated absolute and relative uncertainties is shown given in Table 8.2. The total efficiency of all cuts is 63.3% and 63.1% for AD1 and AD2. Uncertainties in the timing cut and spill-in effects are correlated, as are the delayed and prompt energy cut uncertainties. Taking this

into account, AD1 and AD2 have total detector-correlated uncertainties of 1.8% and detector-uncorrelated uncertainties of 0.21%. Detector-correlated uncertainties will cancel in a ratio between the two detectors, while uncorrelated uncertainties will contribute an attendant uncertainty of 0.3%.

Category	Efficiency (%)	Corr. Unc (%)	Uncorr. Unc. (%)
Flasher Cut	99.9	0.04	0.04
Muon Veto Cut	81.3/81.0	0.1	0.1
Multiplicity Cut	97.4	<0.01	<0.01
Prompt Energy Cut	99.9	0.1	0.02
Delayed Energy Cut	0.92	0.6	0.12
H/Gd Ratio	85.6	0.5	0.1
Spill-in/out Effects	103.2	1.5	0.02
Time Cut	98.6	0.1	<0.01
Total	63.3/63.1	1.8	0.21

Table 8.2: A summary of all inverse beta cut efficiencies and their associated absolute (correlated) and relative (uncorrelated) uncertainties. If two numbers are given, the first is for AD1, and the second is for AD2.

8.3 Background Subtraction

The event selection criteria outlined above define a high-purity sample of inverse beta decays with relatively high efficiency and low systematic uncertainty. However, residual background events in this sample must be characterized and estimated to ensure sub-percent precision in the measurement of IBD rate differences between detectors. The major backgrounds in the experiment come from three main sources: uncorrelated triggers, correlated triggers from muon products, and correlated triggers from the AmC calibration source. While the muon- and AmC-related backgrounds are likely to be fully correlated for both detectors, they are still examined and subtracted to obtain a pure sample of IBD coincidences. This section will describe these backgrounds, their rates relative to signal, and their associated rate uncertainties.

Accidental Backgrounds

Accidental backgrounds are caused by coincidences between uncorrelated prompt-like and delayed-like triggers that accidentally pass all IBD selection cuts. The spectrum and rate of these triggers were shown previously in Figure 8.5. The prompt-like singles are largely caused by intrinsic radioactive backgrounds in and around the detector, whereas the delayed-like singles are mainly caused by muon-induced radioactivity and by neutrons from the AmC source interacting with materials in the detector.

The total accidental background rate can be calculated by determining the probability of time overlap between these uncorrelated singles in a 199 μs window using Poisson statistics:

$$R_{acc} = R_p \cdot R_d \cdot 199\mu s \tag{8.4}$$

where R_p and R_d are the rate of prompt and delayed singles, respectively. The total accidental background rate as a function of time for the first two ADs can be seen in Figure 8.11. After correcting for muon and multiplicity veto efficiencies, the total estimated number of accidental background events expected in the IBD candidate set is 552 and 576 for ADs 1 and 2, respectively. The uncertainties are determined mainly by the statistical uncertainty in the total number of delayed-like singles, which is around 1%, or approximately 6 accidental coincidences.

^{8}He/^{9}Li

Muons traversing and interacting inelastically with the AD can produce long-lived radioisotopes. Two such isotopes are ^{9}Li and ^{8}He, with half-lives of 178.3 ms and 118.5 ms, respectively, which beta-decay and produce an electron and a daughter that disintegrates to often produce a neutron:

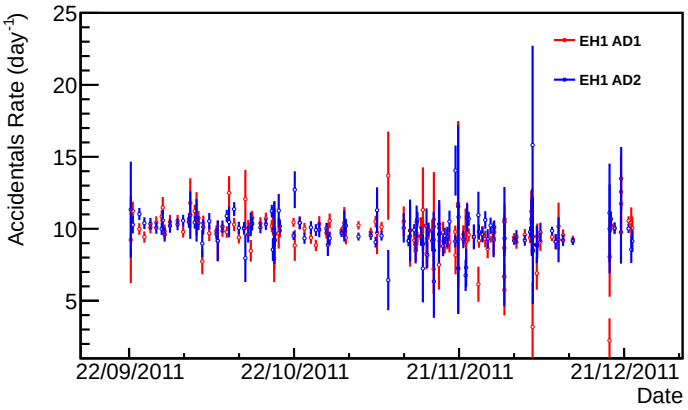

Figure 8.11: The calculated accidental background rate in AD1 and AD2 for each physics run as a function of time. Muon and multiplicity efficiencies must be applied to these values to determine the total accidental background contribution to the IBD candidate dataset.

$$^{9}Li \rightarrow^{9} Be + e^{-} \rightarrow^{8} Be + e^{-} + n \tag{8.5}$$

$$^{8}He \rightarrow^{8} Li + e^{-} \rightarrow^{7} Li + e^{-} + n \tag{8.6}$$

With Q-values of 13.6 MeV and 10.7 MeV, respectively, the betas will produce prompt-like singles, with the product neutron capturing to create a delayed signal. These backgrounds are correlated with muons, but only at very long timescales. Thus, long veto times must be used to remove them.

Previous experiments, such as KamLAND, have demonstrated that a majority of ^{8}He/^{9}Li are created by muons that deposit large amounts of energy in the detector, also called showering muons. This has also been observed in the Daya Bay ADs, as demonstrated qualitatively in Figure 7.4. Figure 8.12 shows for each IBD candidate the time since last AD muon depositing more than 1.75 GeV. A clear exponential tail is visible that matches the half-life of these isotopes. The normalization of this fit indicates 336±54 and 324±58 ^{9}Li/^{8}He events in this sample for AD1 and AD2,

respectively. The ratio between ^{9}Li and ^{8}He is 2.5. By vetoing all triggers less than 400 ms after a muon with greater than 1.75 GeV, one can expect to remove around 80%±2% of the events in this sample, reducing this background to 67±10 and 65±10, respectively. Veto of the IBD events that form the underlying background in Figure 8.12 results in an approximate 5% IBD inefficiency. As described in the muon veto section, the showering muon cut efficiency is different between detectors by approximately 0.3%, a result of imperfect PMT calibration at high charge. This explains the difference in IBD candidates between ADs visible in Figure 8.12.

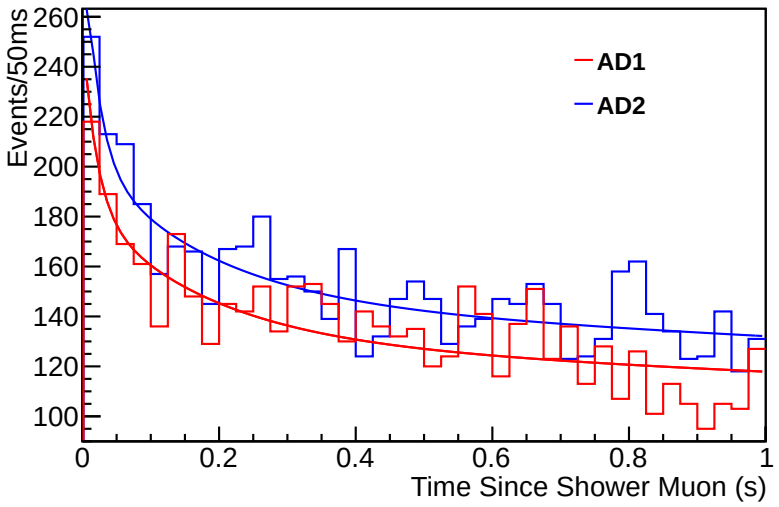

Figure 8.12: Time since muon for all inverse beta candidates within 1 s of an AD muon with >3e5 PE. The showering muon cut is not applied. One can see an exponential tail consistent with the half-life of ^{8}He/^{9}Li. Also present is ^{12}B, another cosmogenically-produced isotope of half-life 20 ms that provides a source of uncorrelated high-energy background. A cut on all events below 0.4 s removes a significant portion of the ^{8}He/^{9}Li and ^{12}B backgrounds.

The ^{8}He and ^{9}Li created by muons with less than 1.75 GeV will not be vetoed by this cut and contribute directly to the IBD background. A fit to the time since AD muon below 1.75 GeV yields an approximate value of 109/AD [137]. The total background from this source is summarized in Table 8.3. The fitted ^{8}He/^{9}Li background

rates in AD1 and AD2 are consistent between ADs, as one would expect from two detectors in the same underground location.

Muon Energy	Events, No Cut	Events, After Cut	B:S (%)	Unc. (%)
>1.75 GeV	336/324	67/65	0.20	0.03
<1.75 GeV	109	109	0.34	0.12
Total	425/413	176/174	0.54	0.12

Table 8.3: The contribution of various muon energy types to the ^{8}He/^{9}Li background. The total estimated number of detected Li/He events is listed, along with the expected event number, signal:background ratio, and associated uncertainty after showering muon cut. The two numbers in the first two columns correspond to AD1 and AD2, respectively.

Fast Neutrons

If one extends the cut on the prompt energy far above the cutoff of the expected reactor spectrum, to 18 MeV, as in Figure 8.13 one can see a relatively flat high-energy tail. This tail is caused by high-energy neutrons created by muons untagged by the water veto system; these can be muons that passed through the rock surrounding the water pool, or ones that have clipped the pool's edge and not passed the hit PMT requirement applied during event selection. These neutrons can travel many meters before thermalizing or capturing, allowing a small number of them to create signals in the AD. The signal consists of a delayed neutron capture and a prompt signal from energy transfer between the neutron and protons in the target.

One can estimate this continuum background beneath the IBD signal by fitting the high-energy background between 10 and 18 MeV with a flat line and extrapolating to lower energies. The results of this method of estimation are 35 and 36 events for AD1 and AD2, respectively. These untagged fast neutron background values match well with MC simulations of muon products produced in or near the rock surrounding the detector. The absolute uncertainties associated with this background

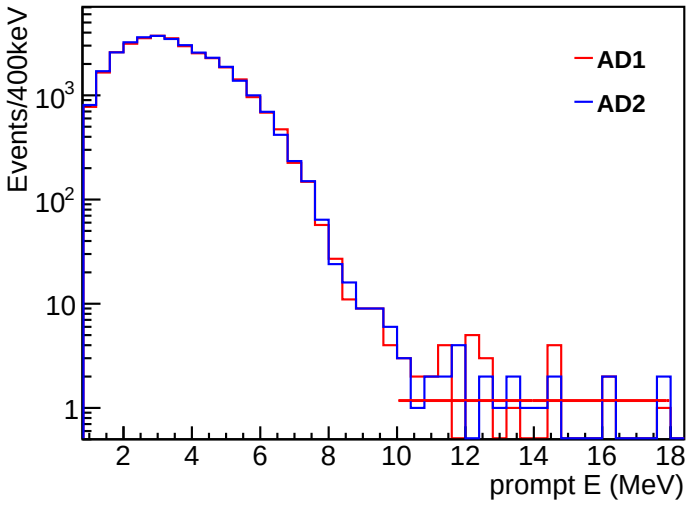

Figure 8.13: The IBD prompt spectrum, extended to high energies. One can see the extending tail beyond 12 MeV, which appears roughly flat, although low statistics make the exact shape hard to estimate. Also shown is the flat-background fit for AD1.

will be conservatively estimated at 100%. As with the ^{8}He/^{9}Li background, since both detectors are located at the same site, the fast neutron background between detectors is highly correlated, contributing <0.01% relative uncertainty in the measured IBD rate between detectors.

The assumption of flat fast neutron spectral shape at low energies can be tested by observing the spectrum of fast neutrons whose parent muon was tagged by the water pool. This spectrum is obtained by applying all IBD selection cuts with the exception of the water pool veto cut. Instead, a coincidence is required to have a prompt energy within 300 ns of a water pool muon, which should be true for neutrons travelling at a significant fraction of the speed of light. To remove Michel electrons from muon decay from this coincidence set, which will not provide a background for IBD selection, coincidences with a decay time of <12 μs are omitted. The resultant prompt energy spectrum of the remaining candidates, shown in Figure 8.14, fit the

flat spectral shape assumption very well. A similar candidate set in coincidence with the RPCs, rather than the water pool, shows the same energy distribution.

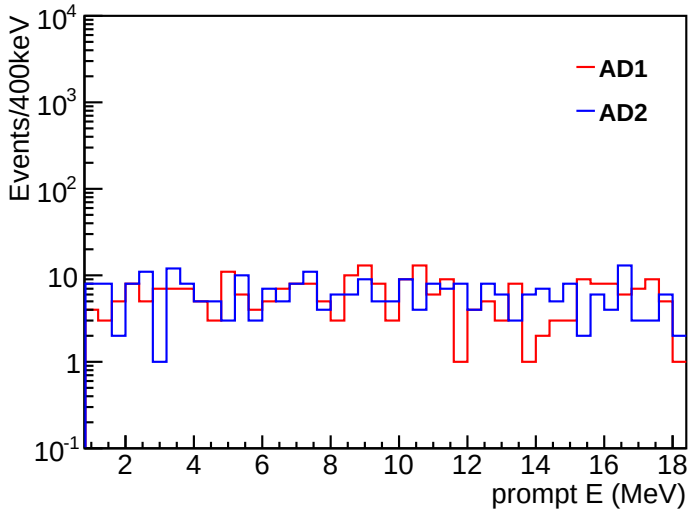

Figure 8.14: The prompt spectrum of water pool tagged fast neutron candidates. The spectrum is clearly flat as a function of energy. This indicates that the untagged fast neutron background will also be flat.

AmC Source Background

Fast neutrons are also emitted from the AmC calibration source located in the ACUs. Neutrons can double-scatter in the metal shielding underneath the ACUs, creating high-energy correlated gamma rays that can deposit some of their energy in the detector. MC simulations have limited this background to 0.03% of signal with a conservative 0.03% associated uncertainty [138]. As all AmC source activities are similar to $\pm$10%, this background is highly correlated between all detectors, and thus contributes a relative uncertainty between detectors of 0.03%.

8.4 Near-Site AD1/AD2 Detection Ratio

These calculated efficiencies, backgrounds, and their associated relative uncertainties can now be used as inputs to make a precise comparison of IBD detection rates between the two near site ADs.

Summary of Inputs and Raw IBD Ratio

Table 8.4 provides an overview of all the inputs necessary to determine the IBD detection rate ratio between the near site ADs. One can see that the raw IBD candidate ratio between detectors is 0.991. To provide a more standardized unit of comparison between ADs, corrected IBD rates can be calculated by taking the number of raw IBD candidates, subtracting the backgrounds in each AD, and dividing by the total number of live days. Since the backgrounds between detectors are similar to less than 1%, they only provide a small corrections to the raw IBD candidate ratio. In addition, muon efficiencies, which differ slightly between AD1 and AD2 should also be corrected for. For other detector efficiency uncertainties, no relative efficiency differences between ADs greater than their associated systematic uncertainties were observed. After the application of these corrections, the daily detected IBD ratio between detectors is 0.987.

The statistical uncertainty on this ratio is 0.8%. Table 8.5 provides an overview of the systematics and background uncertainties associated with the AD1/AD2 ratio measurement, with a total relative uncertainty of 0.2% per AD, which leads to a 0.3% total uncertainty in the AD1/AD2 ratio. Since all backgrounds and reactor sampling ratios are highly correlated between detectors, this detector-related uncertainty dominates the total systematic uncertainty of the measurement.

For identical detectors in an identical position, one would naively expect an IBD

Input Type	Analysis Input	EH1 Detector	
		AD1	AD2
Raw Values	$\overline{\nu}_e$ candidates [events]	32701	33006
	Statistical Uncertainty [%]	0.55	0.55
	Live Time [days]	70.311	70.311
Efficiencies	Muon [%]	0.813	0.810
	Multiplicity [%]	0.974	0.974
Backgrounds	Accidentals [events]	551	549
	Fast Neutrons [events]	34	35
	^{8}He/^{9}Li [events]	176	174
	AmC Source [events]	9	9
Corrected Values	$\overline{\nu}_e$ Candidates [events]	31931	32240
	$\overline{\nu}_e$ Detection Rate [evt/day]	559	566

Table 8.4: Total number of $\overline{\nu}_e$ candidates in each detector, before and after background, live time and muon efficiency corrections.

Category	Input	EH1 Relative Uncertainty (%)
Statistics	-	0.8
Efficiency	Flasher Cuts	0.04
	Muon Veto Cuts	0.1
	Multiplicity	<0.01
	Prompt Energy Cuts	0.02
	Delayed Energy Cuts	0.12
	Timing Cuts	0.02
	Gd-Capture Ratio	0.10
	Spill-in/out Effect	0.02
	Total Detector	0.21
Backgrounds	Accidentals	0.02
	Fast Neutrons	<0.01
	^{8}He/^{9}Li	<0.01
	AmC Source	0.03
	Total Background	0.04

Table 8.5: A summary of statistical, background, and detector relative uncertainties in the measurement of the IBD rate ratio between ADs. This table demonstrates that the AD1/AD2 comparison is limited in its precision by statistics.

event ratio of 1. However, difference in reactor-detector baselines and target mass for each detector, as well as variations in reactor, power can alter this expected ratio.

The following section will provide an accurate expected ratio based on knowledge of these parameters.

Baseline Effects

The position of the EH1 ADs with respect to the various reactors is shown in Figure 8.15; reactor baselines are measured using a combination of GPS and total station surveys accurate to 28 mm. Exact baseline values from each detector to all reactors are listed in Table 8.6. From each reactor core, one expects the detected IBD ratio between detectors to scale by the inverse squared ratio of the baselines. To aid in the calculation of this ratio, a weighted baseline is calculated to determine an 'average' baseline for the neutrinos interacting in each detector:

$$L_{eff} = \sum_i \omega_i L_i, \tag{8.7}$$

where ω_i is the percentage of the total flux at the detector from reactor i assuming equal core powers:

$$\omega_i = \frac{\sum_i L_i^2}{L_i^2} \tag{8.8}$$

	AD1	AD2
D1	362.38	357.94
D2	371.76	368.41
L1	903.47	903.35
L2	817.16	816.90
L3	1353.62	1354.23
L4	1265.32	1265.89
Weighted Baseline	496.6	494.3

Table 8.6: Distances from each reactor to each EH1 detector in meters. Reactor labels are illustrated in Figure 8.15. Also listed is the weighted baseline for each detector, as described by equation 8.7.

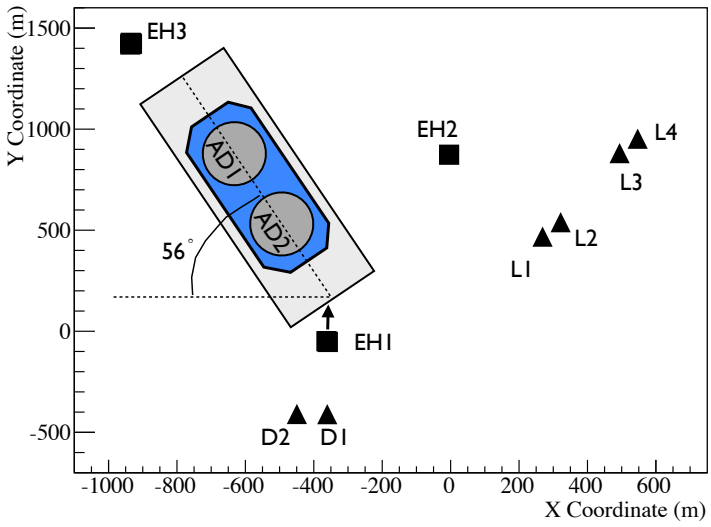

Figure 8.15: Reactor (triangle) and detector (square) locations. The orientation of AD1 and AD2 in EH1 is illustrated in the zoomed figure inlay. The 'L' cores are four Ling Ao reactors, and the 'D' cores are the two Daya Bay reactors.

Accounting for these differences in weighted baseline, The total expected AD1/AD2 IBD event ratio is 0.991. A relative uncertainty in this ratio of of 0.02% is introduced by the precision of the baseline aforementioned measurements, 28 mm.

Reactor Information Effects

Figure 8.16 shows the AD1 and AD2 IBD event rates and IBD event rate ratios for each physics run as a function of time. This ratio exhibits some unusual features, particularly some sudden jumps in rate. These jumps can be caused by changes in the operating thermal power of each reactor core. The previous calculation of weighted baselines assumes that all reactors produce an equal number of neutrinos. If reactors are shut off or run at reduced power, this will not be the case; rather, differing total neutrino production from the various reactors will alter the effective baselines used to determine the total expected event rate ratio. If realistic neutrino production rates

are included for each reactor to correct for changes in thermal output and fuel burnup over time, the expected AD1/AD2 IBD event ratio becomes 0.982.

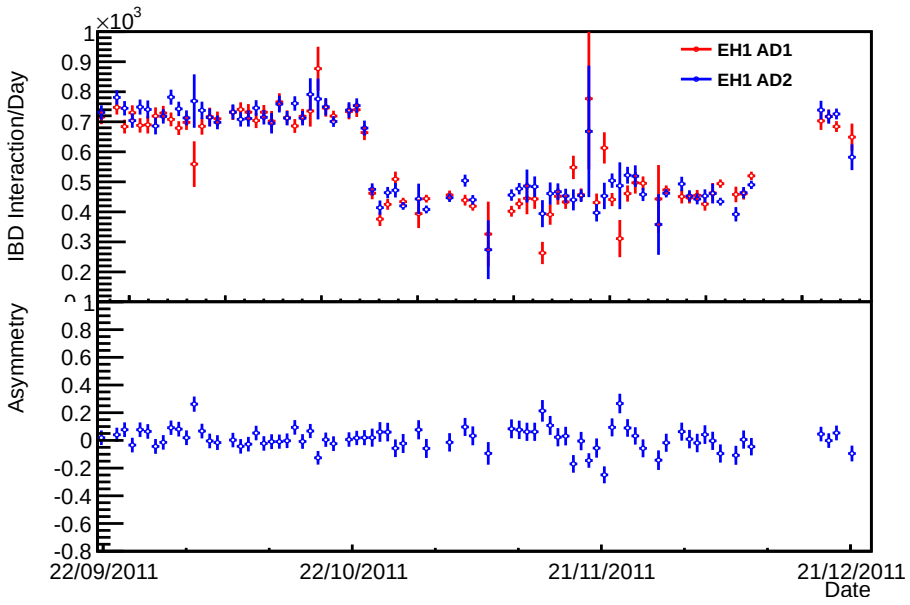

Figure 8.16: Daily IBD candidate detection rates over time for each physics run number. Rates are corrected for muon and multiplicity efficiency, but not background-subtracted. Abrupt changes in the detection rate correspond to periods of reactor shut-down and turn-on.

Target Mass Effects

A difference in the number of target protons between detectors can also alter the AD1/AD2 event rate ratio. As discussed in Chapter 6, the total number of protons per unit mass should be identical between detectors, since both detectors are filled with the same liquid. However, the total mass of liquid in each AD can vary from the small but known differences in detector geometries, and in particular variations in the AV, described in Chapter 5.

For this reason, liquid masses were measured with great precision using a target mass measurement system and corresponding liquid level sensor system in the overflow tanks. These mass measurement systems were developed, tested, and overseen

by colleagues at UW-Madison. During detector filling, GdLS from five storage tanks is pumped into a common tank that is placed on scales with a measured long-term precision of 0.015%. The mass is measured before and after detector filling, with the difference between those values determining the total AD liquid mass. The liquid volume in the overflow tank is then calculated utilizing the liquid level sensor values and surveys of the overflow tank and bellow geometry. The target mass is calculated by subtracting the overflow and connection bellow liquid mass from the total AD liquid mass. The time-averaged target masses are 19941 kg and 19966 kg for AD1 and AD2, respectively, leading to a 0.1% AD1/AD2 rate correction for a total expected ratio of 0.981. Associated uncertainties are shown in Table 8.7, and were provided along with the target mass numbers, by [139, 140].

Quantity	Corr. Unc. (%)	Uncorr. Unc. (%)
Free protons/kg	0.47	negl.
Density (kg/L)	negl.	negl.
Total GdLS Mass	0.1	0.015
Overflow tank geometry	0.0066	0.0066
Overflow sensor calibration	0.0057	0.0057
Overflow tank tilt	0.0068	0.0068
Bellows capacity	0.0025	0.0025
Total Free Protons	0.48	0.02

Table 8.7: A summary of uncertainties in the measurement of relative target proton ratio between EH1 detectors. Errors come from the total GdLS mass measurement and the measurement of the total bellows and overflow tank liquid volume. As great pains have been taken to ensure identical GdLS properties, uncertainties from relative proton density differences between detectors are negligible.

8.5 Summary

An analysis was done to select a high-purity inverse beta decay candidate set in the EH1 antineutrino detectors. Utilizing target mass, baseline, and reactor information,

the expected AD1/AD2 IBD detection ratio is calculated to be 0.981. After background subtraction, the measured IBD detection ratio is 0.986. The difference in the detected and expected IBD ratios between the two near sites ADs is then:

$$D = \frac{N_{AD1} - N_{AD2}}{\frac{1}{2}(N_{AD1} + N_{AD2})} = /0.005 \pm 0.008(stat) \pm 0.003(sys). \tag{8.9}$$

The expected and detected values show excellent agreement and demonstrate a proper understanding of the detector systematics in the Daya Bay experiment to sub-percent precision. In addition to the agreement in the total antineutrino detection rate, the detectors also show excellent agreement in their singles and IBD candidate energy spectra. Further accumulation of statistics can significantly improve the precision of this side-by-side comparison.

With proper understanding of detector systematics demonstrated, the Daya Bay experiment can reliably move forward with a sub-percent precision measurement of near-far reactor antineutrino disappearance in the search for θ_{13}. With identical antineutrino detection rates demonstrated between ADs, a significant observation of a relative rate deficit between near and far detectors can now be convincingly attributed to neutrino oscillations from θ_{13}.

Chapter 9

A Relative Rate Measurement of θ_{13}

9.1 Introduction

The previous chapter demonstrated how a high-purity sample of inverse beta detections can be gleaned from the Daya Bay detector data. In addition, it was shown that inverse beta candidate datasets from different detectors can be compared with sub-percent systematic uncertainty. This same analysis can be used on data from all three Daya Bay experimental halls to provide the rate of neutrino detection in each detector. The ratio of measured to expected IBD interactions can then be calculated for each detector and compared between detectors. By considering differences in these ratios between experimental halls in the context of neutrino oscillation theory, one can constrain the range of the neutrino oscillation parameter θ_{13}. This process is called a *rate* analysis, as only rate, not spectral information, is used to constrain the neutrino oscillation parameters.

A relative rate analysis with multiple detectors and baselines has the benefit

of cancellation of correlated uncertainties. Correlated uncertainties in the absolute expected IBD candidates will cause a shift in the measured:expected ratio that is similar for all detectors. With multiple detectors and baselines, this scenario can be easily separated from one in which shifts in this ratio are different for different detectors. Different ratios between near and far detectors provide convincing evidence that oscillation effects are non-zero.

Predicted and measured signal rates, background estimates, efficiencies, and systematic uncertainties for each detector can be used as inputs to a χ^2 analysis to fit for a most probable value of the oscillation parameter $\sin^2 2\theta_{13}$. The χ^2 model, many of the inputs (as described in the previous chapter), and the minimization procedure presented in this rate-only analysis were independently developed; their final form appears similar to those given in the collaboration's first $\overline{\nu}_e$ disappearance result [141].

9.2 Analysis Inputs

Antineutrino data was collected with six installed Daya Bay detectors from December 24, 2011 to February 17, 2011. In addition to the first two Daya Bay near site detectors described in Chapter 8, three detectors were installed at the far site and one at the Ling Ao near site. The dataset includes mainly physics runs in which all six ADs are simultaneously running, meaning that any changes in reactor power and spectrum will be represented equally in the datasets of all detectors. The total physics data live time is around 50 days for each detector.

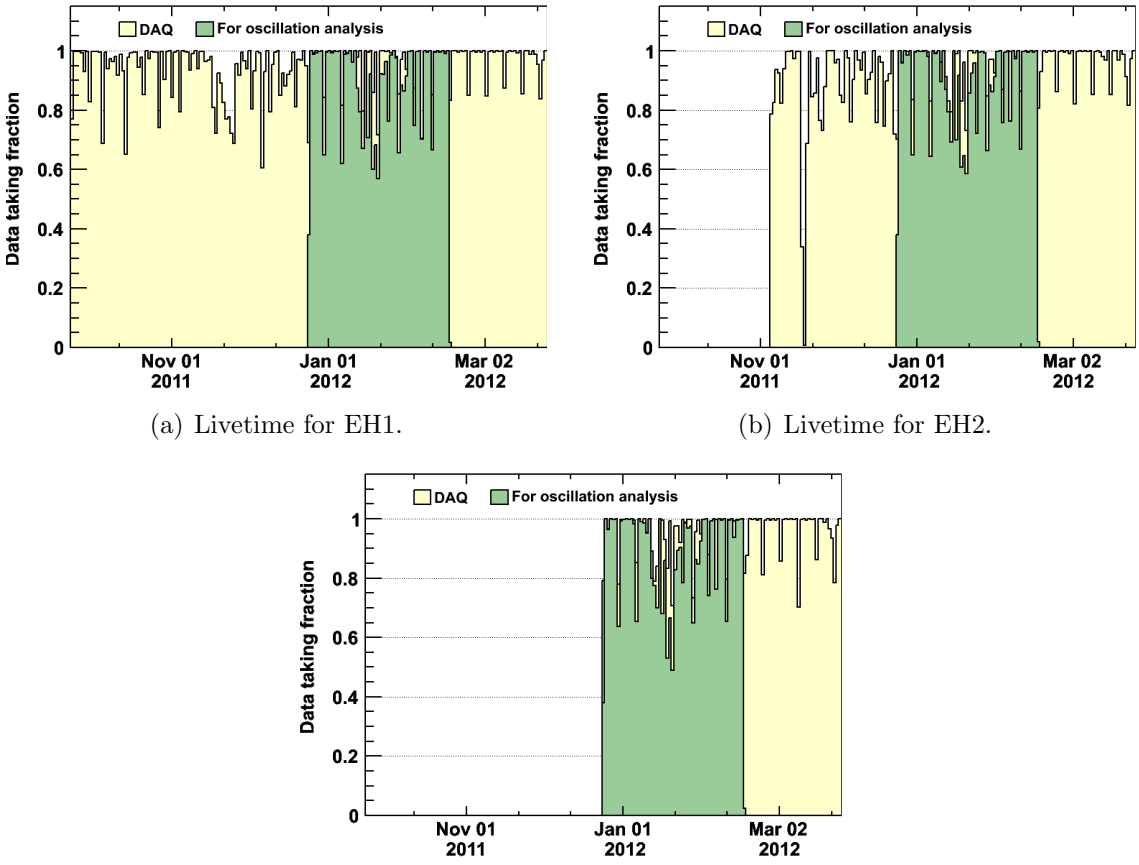

(a) Livetime for EH1.

(b) Livetime for EH2.

(c) Livetime for EH3

Figure 9.1: Data period used for the three-site θ_{13} analysis, shown as the green region. The yellow region preceding the green data region in EH1 was used for the AD1/AD2 comparison described in the previous chapter. Provided by [136].

Measured IBD Rates

To perform a three-site IBD analysis, the IBD analysis cuts used in the AD1/AD2 comparison of Chapter 8 are applied to all detectors for the θ_{13} physics running period data. The resultant candidate rates, background rates, and efficiencies are shown in Table 9.1.

One can notice a number of significant differences in these values between detectors that arise from baseline and overburden differences for the various sites. Candidate event rates are significantly lower at the far site because of a longer weighted base-

AD	Daya Bay		Ling Ao	Far		
	AD1	AD2	AD1	AD1	AD2	AD3
Live Time	49.55		49.48	48.95		
$\overline{\nu}_e$ Candidates	28703	28868	22169	3537	3465	3461
Accidentals	377	382	320	161	165	154
^{8}He/^{9}Li	108	108	59	8	8	8
Fast Neutrons	24	24	19	3	3	3
AmC Source	8	8	8	9	9	9
Total B.G. Events	516	520	405	181	186	175
Total B.G. Unc.	30	30	28	10	10	10
Measured $\overline{\nu}_e$	28186	28345	21762	3356	3280	3287
Measured $\overline{\nu}_e$/day	568	572	439	68.6	67.0	67.1
Statistical Uncertainty (%)	0.60	0.59	0.68	1.73	1.76	1.74
Background Uncertainty (%)	0.10	0.10	0.17	0.30	0.30	0.30

Table 9.1: Total number of inverse beta decay candidates and background events, as well as absolute detection efficiencies for all six detectors. Daily IBD interaction rates are calculated by subtracting backgrounds and correcting for detection efficiencies and livetime.

line for the detectors at that site. With additional overburden, detectors at the far site also experience a lower absolute rate of ^{8}He/^{9}Li, fast neutron, and accidental backgrounds. Given the decreased IBD event rate with increased baseline at the far site, the fractional contribution of the background and the associated fractional uncertainty is, however, higher at the far site than the near site. The total statistical uncertainties are also shown in Table 9.1; the total statistical uncertainty for all three far site ADs combined is 1.04%.

Expected IBD Rates

The expected event rate in each detector j, can be calculated using the following formula,

$$N_{det,j} = N_{p,j} \sum_i \frac{1}{4\pi L_{ij}^2} \int \epsilon_j \sigma P_{sur} S_i dE, \tag{9.1}$$

where N_p is the effective number of protons in the target, L_{ij} is the baseline to reactor i, ϵ_j is the detection efficiency, σ is the inverse beta decay cross section, S_i is the $\overline{\nu}_e$ flux from reactor i, and P_{sur} is the neutrino oscillation survival probability:

$$P_{sur} = 1 - \sin^2 2\theta_{13} \sin^2 \left(\frac{1.27 \Delta m^2_{31} L_{ij}}{E} \right). \tag{9.2}$$

The full form of the survival probability will be considered later in this chapter. The various inputs to the expected rate calculations to Equation 9.1, absent neutrino oscillations, are shown in Table 9.2. Also included is the total expected number of neutrino interactions for each AD, normalized to achieve a 1:1 ratio between detected and expected event rates in AD1; as we will be performing a near-far relative analysis, this overall normalization is not particularly important. Each of these inputs is overviewed in the following sections.

Proton Number

The number of target protons in each AD is calculated by the multiplying measured mass of the target, described in Section 8.4, by the proton density per kg GdLS mass, which was measured via combustion analysis to a precision of 0.47%.

This target mass must be corrected to account for $\overline{\nu}_e$ interactions outside the GdLS whose neutrons spill in and capture on Gd, and for target $\overline{\nu}_e$ interactions whose neutrons exit the target region. The net scaling resulting from spill-in/out effects was calculated via Monte Carlo to be 1.032.

Relative and absolute uncertainties in the proton number are presented in Figure 8.7. Relative proton number uncertainties arise mainly from uncertainties in the target mass of each detector. Spill-in/out effects are almost entirely correlated between detectors, with a remaining 0.02% uncorrelated uncertainty between detectors, as shown in Table 8.4.

Category	Input	Daya Bay		Ling Ao	Far		
		AD1	AD2	AD1	AD1	AD2	AD3
Protons	Target Mass (kg)	19941	19966	19891	19913	19991	19892
	Spill-in/out Scaling	103.2					
Baseline	D1	362	358	1332	1920	1918	1925
	D2	372	368	1358	1894	1892	1900
	L1	903	903	468	1533	1535	1539
	L2	817	817	490	1534	1535	1539
	L3	1354	1354	558	1551	1555	1556
	L4	1265	1266	499	1525	1528	1530
Reactor	$\overline{\nu}_e$ Prod. Fraction	0.188	0.202	0.109	0.124	0.188	0.186
	Weighted Baseline (m)	473	466	575	1645	1645	1648
Expected IBD Interactions		44252	45273	33257	4641	4650	4604
Efficiency	Multiplicity	0.974	0.975	0.975	0.973	0.973	0.973
	Muon Veto	0.814	0.811	0.845	0.981	0.980	0.981
	Time Cut	0.986					
	Prompt Energy Cut	0.999					
	Delayed Energy Cut	0.920					
	Gd-capture Fraction	0.856					
	Flasher Cut	0.999					

Table 9.2: Inputs to the calculation of expected number of detected $\overline{\nu}_e$. Inputs are separated into sections corresponding to the various terms in Equation 9.1. Total expected $\overline{\nu}_e$ interactions are normalized so that the detected to expected IBD rate in AD1 will be 1.

Baselines, Cross-section and Reactor Flux

Baselines between all reactors and detectors are listed in Table 9.1. As mentioned in Section 8.4, baselines are measured to a precision of 28 mm, providing a negligible contribution to any absolute or relative systematics.

Cross-sections for inverse beta decay interaction are pictured in 3.1. Cross-section uncertainties, which are on the order of 0.1%, will be fully correlated between all detectors.

The effect of baselines and reactor normalization and spectral shape can be sum-

marized in a single weighted baseline for each detector:

$$L_{j,eff} = \sum_i \omega_{ij} L_{ij}, \text{ with } \omega_{ij} = \frac{S_i}{L_{ij}^2} \sum_i \frac{L_{ij}^2}{S_i}, \tag{9.3}$$

where the jth detector's baseline is represented to reactor i by and L_{ij} and the ith reactor's flux contribution to total $\overline{\nu}_e$ production is represented by S_i/S_{tot}:

$$S_i = \frac{W_i}{\sum_j (f_{ij}/F) e_j} \sum_j^{isotopes} (f_{ij}/F) \int S_j(E_\nu), \tag{9.4}$$

where W_i and f_{ij}/F are the thermal output and fission fractions of each reactor, and e_j and S_j are energy per fission and $\overline{\nu}_e$ spectrum of each fission isotope j. This relative $\overline{\nu}_e$ production fraction is determined mainly by each reactor's up-time and degree of burn-up. Values of S_i/S_{tot} are given in Table 8.4 for each reactor. All reactor normalization and shape inputs, as well as all target masses, were provided by [140]. The magnitude of the associated correlated and uncorrelated reactor uncertainties are given in Table 9.3.

Input	Description	Correlated Unc. (%)	Uncorrelated Unc. (%)
W_i	Reactor Power		0.5
f_{ij}/F	Fission Fractions		0.6
e_j	Energy/Fission	0.2	
$S_j(E_{\overline{\nu}_e})$	$\overline{\nu}_e$/Fission	3.0	
Total		3	0.8

Table 9.3: Total reactor systematics for all six detectors. Uncertainties correlated between all reactors will fully cancel in a relative rate measurement of θ_{13}. Uncorrelated reactor uncertainties will also largely cancel because of common reactor sampling between near and far detectors.

Using these reactor and baseline values, weighted baselines were calculated and are given in Table 8.4. These weighted baseline values contain all the baseline and reactor information necessary to calculate expected event rates for each detector.

Efficiencies

Detector efficiencies must be properly applied for each AD in order to convert from expected inverse beta decay interactions to expected inverse beta decay detections. The absolute detection efficiencies are shown in Table 9.2, and their associated uncertainties are listed in Table 9.4.

Category	Absolute Unc. (%)	Relative Unc. (%)
Flasher Cut	0.04	0.04
Multiplicity Cut	0.01	0.01
Muon Cut	0.1	0.1
Prompt Energy Cut	0.1	0.02
Delayed Energy Cut	0.6	0.15
Coincidence Time Cut	0.1	<0.01
Gd-Capture Percentage	0.5	0.1
Spill-in/out Effects	1.5	0.02
Total	1.8	0.23

Table 9.4: Total cut efficiency absolute and relative systematics for all six detectors. Relative systematics are all evaluated based on calibration and inverse beta decay data, while absolute systematics are evaluated using data and Monte Carlo simulation.

As described in Chapter 8, muon and multiplicity efficiencies can be calculated absolutely for each detector. In addition, the absolute n-Gd capture percentage can be calculated by measuring the H/Gd ratio of the AmC source deployed at the detector center to an uncertainty of 0.5%. The remaining energy and timing cut absolute efficiencies and uncertainties were estimated using Monte Carlo simulations of the detectors.

Relative differences in the efficiencies of each cut between detectors were calculated for all six ADs in an identical manner to that discussed in detail in Chapter 7. Relative efficiency differences were only identified for the muon and multiplicity cut efficiencies, as shown in Table 9.2. The relative uncertainties for each cut are also listed in Table 9.4. As with the AD1/AD2 comparison, the largest contributing systematics

were those associated with the delayed energy cut and the Gd-capture percentage. Calculation of these relative systematics was redone for all six ADs, and found to be of similar magnitude. In particular, the energy scale uncertainty was increased slightly to 0.5%, leading to a slightly larger energy cut uncertainty of 0.15%.

9.3 $\overline{\nu}_e$ Candidate Events

After correcting the candidate dataset for the various cut efficiencies, estimating backgrounds, and calculating expected event rates, the candidate events can be compared for all detectors and sites. The background-subtracted prompt spectra for all three sites is shown in Figure 9.2. As expected, rates and spectral shapes are similar for ADs in EH3, reinforcing the conclusion from AD1 and AD2 that all detectors have identical response to neutrino interactions.

The reconstructed position distribution of the inverse beta candidates is shown in Figure 9.3. Candidate events appear to have uniform distributions throughout the target region in all ADs, as one would expect. Small variations in z- and r-uniformity exist as a result of spill-in/out effects and changes in efficiency with detector position. Most importantly, position distributions are consistent between all detectors.

The prompt spectra can be combined at each individual site and then compared between sites to identify spectral shape differences. In order to make the comparison as direct as possible, the near site spectra are scaled by the ratio of predicted IBD rates between far and near detectors. The result of this scaling is shown in Figure 9.4. One can see that spectral differences between the two near site EHs are much smaller than those seen between near and far EHs, indicating that these large spectral differences are unrelated to differences in backgrounds or reactor $\overline{\nu}_e$ spectra from individual reactors. Thus, these near-far spectral shape differences strongly hint at an energy-

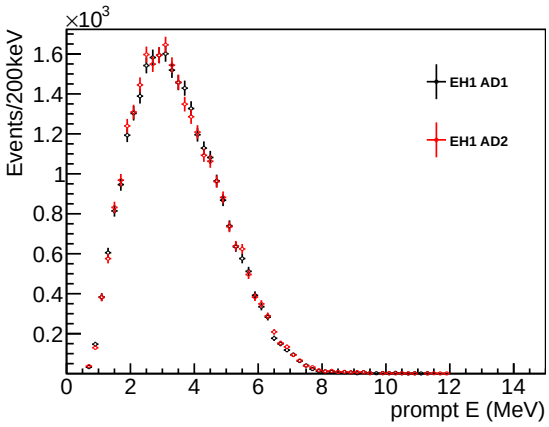

(a) Prompt E_{rec} Spectrum for EH1 ADs.

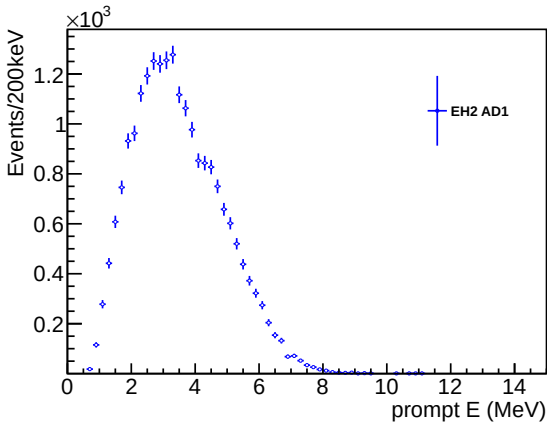

(b) Prompt E_{rec} Spectrum for EH2 ADs.

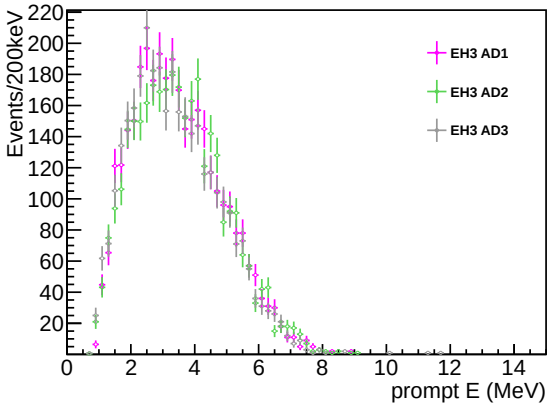

(c) Prompt E_{rec} Spectrum for EH3 ADs.

Figure 9.2: Background-subtracted prompt spectra for all ADs. One can see the similarity in shape between the two ADs in EH1, and between the three ADs in EH3.

and baseline-dependent disappearance of reactor $\overline{\nu}$.

By integrating the positron energy spectrum for each AD, one can compare the detected number of $\overline{\nu}_e$ to the expected number calculated in Section 9.2. These ratios for each AD are shown in Figure 9.5. One can see a relative difference in these ratios between near and far detectors of:

$$D = 0.061 \pm 0.011(stat) \pm 0.005(syst). \tag{9.5}$$

This deficit provides an unambiguous rate-based indication of $\overline{\nu}_e$ disappearance. If

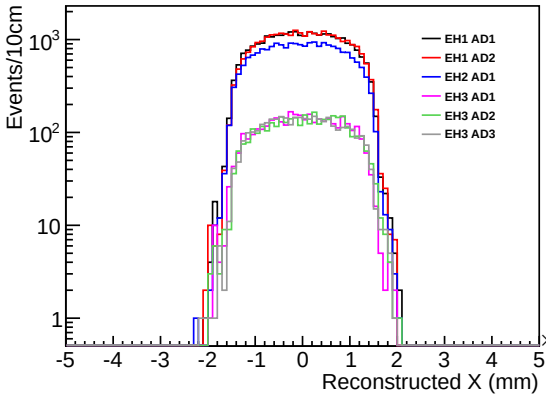

(a) X_{rec} for all ADs.

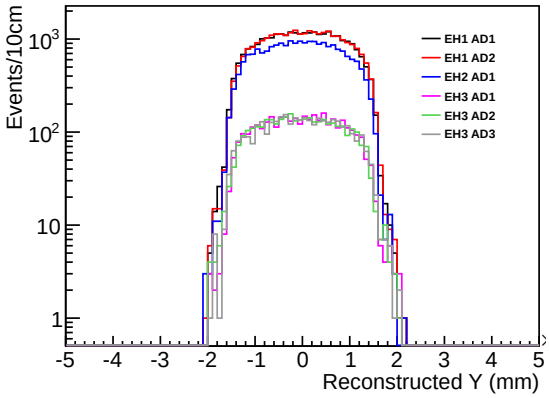

(b) Y_{rec} for all ADs.

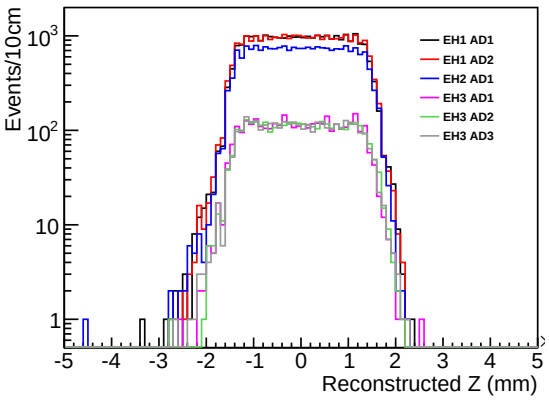

(c) Z_{rec} for all ADs.

Figure 9.3: Reconstructed X, Y, and Z positions for all inverse beta candidates. There is clear agreement in position distribution between all ADs. All distributions are largely symmetric with the exception of the Z-distribution, which arises because of the extra target from the conical GdLS and LS tops at negative Z positions and because the top and bottom reflector positions are not symmetric in Z. These distributions also demonstrate the rarity of position reconstruction inefficiency, when the reconstructed position is outside the physically allowed region.

this deficit is interpreted as the product of neutrino oscillations in a 3-neutrino framework, it can be used to determine a best-fit value for the parameter θ_{13}.

The precision of this ratio comparison is limited currently by statistics, which will be significantly improved with further data taking. In addition, systematic uncertainty is calculated assuming fully uncorrelated background uncertainties, a relatively

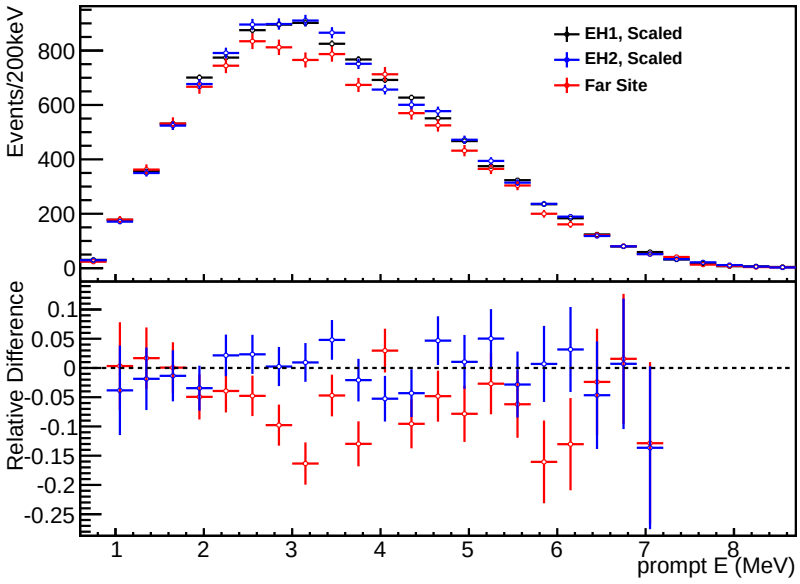

Figure 9.4: Comparison of spectra and spectral differences at the three experimental halls. EH1 and EH2 spectra appear very similar, while EH3 shows a significant deficit at the spectral peak, where oscillation effects are expected to be maximal.

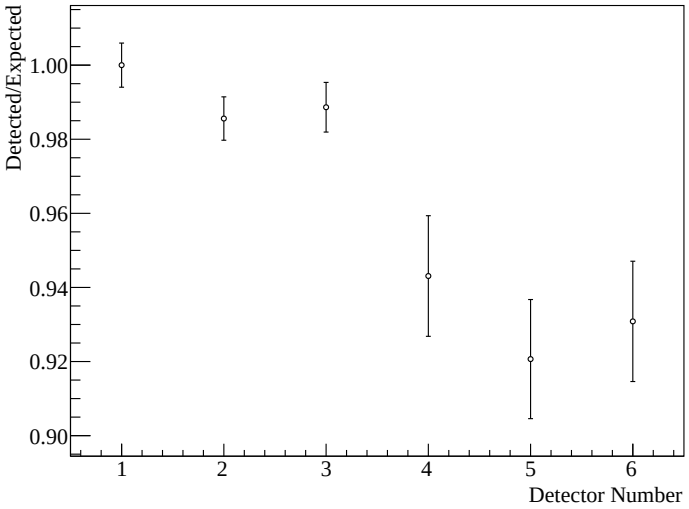

Figure 9.5: The ratio between the detected and predicted event rate for all six ADs. Error bars indicate statistical uncertainty only. Correlated uncertainties related to the neutrino flux normalization, cross-section, and detection efficiency will shift all of these points up and down equally.

conservative assumption. With more refined studies of systematics and backgrounds and further data taking, the precision of this measurement will increase significantly.

9.4 χ^2 Analysis Model

In a rate analysis of θ_{13} for the Daya Bay experiment, we begin with six $\overline{\nu}_e$ rate measurements M_i, one for each AD. The measurements are statistically independent and follow some probability density function $f(x_i|\theta_{13})$ that depends on the unknown neutrino mixing parameter θ_{13}. The probability of obtaining the six measured values, or likelihood function, is then

$$L(x_i|\theta_{13}) = \prod_i f(M_i|\theta_{13}). \tag{9.6}$$

Based on these six measurements, the best estimate of the true value of θ_{13} is the one that maximizes the value of this likelihood function.

As these are assumed to be independent measurements statistically distributed about a mean $f(M_i|\theta_{13})$, it is valid and convenient to minimize the function

$$\chi^2(M_i|\theta_{13}) = -2\ln L(M_i|\theta_{13}) = \sum_i \frac{(M_i - B_i - T_i(\theta_{13}))^2}{M_i} \tag{9.7}$$

instead, where M_i, B_i, and T_i are the total measured signal, estimated background, and predicted signal (Equation 9.1) for detector i. The value of θ_{13} that maximizes L will minimize χ^2. To accommodate each systematic uncertainty in each measurement that results in additional Gaussian fluctuations of each measured rate about the p.d.f mean, a nuisance parameter can be added to the χ^2 whose magnitude is constrained by the value of that parameter's systematic uncertainty. Considering all contributing systematics and backgrounds, the following χ^2 function is constructed:

$$\chi^2 = \sum_{A=1}^{6} \frac{\left[M_A - T_A(1 + \sum_r \omega_r^A \eta_r + \alpha + \epsilon_d^A) - B^A(1 + \epsilon_b^A)\right]^2}{T^A} + \frac{\alpha^2}{\sigma^2} + \sum_r \frac{\eta_r^2}{\sigma_r^2} + \sum_{A=1}^{6} \left[\left(\frac{\epsilon_d^A}{\sigma_d}\right)^2 + \left(\frac{\epsilon_b^A}{\sigma_b^A}\right)^2 \right]. \quad (9.8)$$

This equation sums over A detectors and r reactors, and can be minimized with respect to θ_{13} and to the nuisance parameters $\{\alpha, \eta_r, \epsilon_d^A, \epsilon_r^A\}$ describing the systematic uncertainties, with standard deviations $\{\sigma, \sigma_r, \sigma_d, \sigma_b^A\}$. The various input parameters and their assigned values are overviewed in Table 9.5. Correlated detector and reactor systematics are combined to give one normalization parameter, α. Uncorrelated reactor and detector parameters, η_r and ϵ_d^A, are also included. Backgrounds of all types are conservatively assumed to be uncorrelated between all detectors to simplify the fitting subroutine; this is reflected in the parameters ϵ_b^A. In reality, some backgrounds, particularly the AmC source background, are almost fully correlated between detectors. However, given the small contribution of the background uncertainties to the total detection rate uncertainties, this assumption should have only a small impact on the significance of the θ_{13} fitting. One should also note the constraints on the background and uncorrelated detector systematics receive the same treatment in the χ^2, and thus can be effectively treated as one term ϵ^A for each detector in the minimization procedure.

For a relative rate analysis of near and far detectors, reactor and detector normalization information should not be utilized. This is implemented by assigning an infinite value to the total correlated uncertainty σ. This allows the normalization minimization parameter α to float freely, effectively scaling the expected signal rate of all detectors evenly without penalty. This removes the ability of a difference in detected and measured rates common among ADs to have an impact on the θ_{13} fitting; only relative differences between ADs will help determine θ_{13}.

In order to calculate the oscillated T_A, the oscillation probability P_{sur} must be pre-

Fit Parameter	σ (%)	Description	Number of Parameters
$\sin^2 2\theta_{13}$	-	Neutrino osc. amplitude parameter	1
α	∞	Corr. Variation in $\overline{\nu}_e$ Detection Rate	1
ϵ_d^A	0.23	Uncorr. variation in $\overline{\nu}_e$ rate for AD A	6
ϵ_b^A	0.1/0.17/0.30	Uncorr. variation in background rate for AD A	6
η_r	0.8	Uncorr. variation in $\overline{\nu}_e$ flux for reactor r	6

Table 9.5: Input minimization parameters to the χ^2 model. The value of $\sin^2 2\theta_{13}$ is minimized along with nuisance parameters allowing for proper treatment of correlated and uncorrelated reactor, detector, and background systematic uncertainties, whose estimated magnitudes are listed. Three values are given for the background nuisance parameter's σ, one for EH1, EH2, and EH3, respectively.

cisely defined. The full oscillation probability equation for Daya Bay was previously given by Equation 2.31:

$$\begin{aligned} P_{sur} &= 1 - \cos^2(\theta_{12})\sin^2(2\theta_{13})\sin^2\left(\frac{1.27\Delta m^2_{31}L}{E}\right) \\ &- \sin^2(\theta_{12})\sin^2(2\theta_{13})\sin^2\left(\frac{1.27\Delta m^2_{32}L}{E}\right) \\ &- \sin^2(2\theta_{12})\cos^4(\theta_{13})\sin^2\left(\frac{1.27\Delta m^2_{21}L}{E}\right) \end{aligned} \tag{9.9}$$

$$\simeq 1 - \sin^2(2\theta_{13})\sin^2\left(\tfrac{1.27\Delta m^2_{32}L}{E}\right) - \sin^2(2\theta_{12})\cos^4(\theta_{13})\sin^2\left(\tfrac{1.27\Delta m^2_{21}L}{E}\right) \tag{9.10}$$

The behavior of this function is largely determined by the parameters θ_{13}, which is allowed to float freely in the χ^2, and Δm^2_{31}, which is assigned the fixed global best-fit value of 2.45×10^{-3} eV^2 [40]. This equation can be simplified to Equation 9.10, since $\Delta m^2_{32} \sim \Delta m^2_{31}$. Figure 9.6 shows the effect of this approximation on the oscillation probability in the case of inverted and normal mass hierarchy. As this effect changes the oscillation probability by $<<0.1\%$, Equation 9.10 is used to calculate T_A. Effects from longer-baseline Δm^2_{21} oscillations are small but non-negligible at the km scale, as shown in Figure 9.6, and were included in the calculation of T_A. The global best-fit

values of Δm^2_{31}, Δm^2_{21} and θ_{12} from Table 2.2 were used, and were not allowed to vary in the minimization procedure.

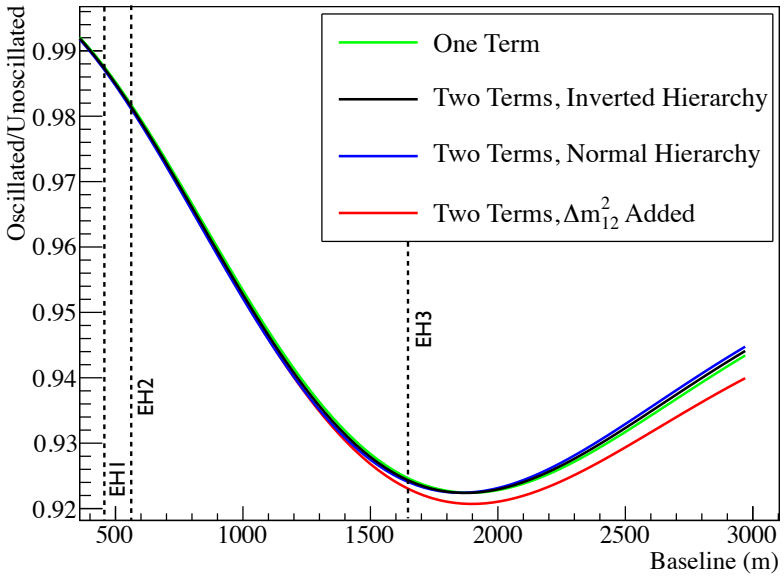

Figure 9.6: Various components of the reactor $\overline{\nu}_e$ survival probability at km baselines: Δm^2_{31}-only mixing assuming $\Delta m^2_{31} = \Delta m^2_{31}$ (black); Δm^2_{32}-only mixing without this assumption for normal (blue) and inverted (green) hierarchies, and all mixing types assuming $\Delta m^2_{31} = \Delta m^2_{32}$ (red). The last case is utilized in the χ^2.

9.5 Relative Rate Analysis

Minimization of the χ^2 was done using GSL minimization libraries [142]. The best-fit parameters from the minimization are shown in Table 9.6. The value of the oscillation parameter with the minimum χ^2 was

$$\sin^2 2\theta_{13} = 0.095 \pm 0.017(stat) \pm 0.006(syst). \tag{9.11}$$

The χ^2 can be seen in Figure 9.7. The minimum χ^2/ndf was found to be 2.8, which, given the number of degrees of freedom, indicates an excellent fit between the hypothesized oscillation model and the data. By looking along the χ^2, one can

Parameter	Best Fit Value (%)	Input σ (%)
$\sin^2 2\theta_{13}$	0.095	-
α	0.73	∞
ϵ^1	0.11	0.22
ϵ^2	-0.11	0.22
ϵ^3	0.01	0.26
ϵ^4	0.05	0.36
ϵ^5	-0.56	0.36
ϵ^6	-0.01	0.36
η_1	-0.01	0.8
η_2	-0.01	0.8
η_3	0.01	0.8
η_4	0.01	0.8
η_5	0.01	0.8
η_6	0.01	0.8

Table 9.6: The best-fit θ_{13} and nuisance parameters for the rate-only χ^2 analysis. Note that all parameters are near or within their associated uncertainties, and well within statistical uncertainties.

see that the 5σ confidence region of $\sin^2 2\theta_{13}$ ranges from 0.005 to 0.18, effectively excluding the no-oscillation hypothesis at high significance.

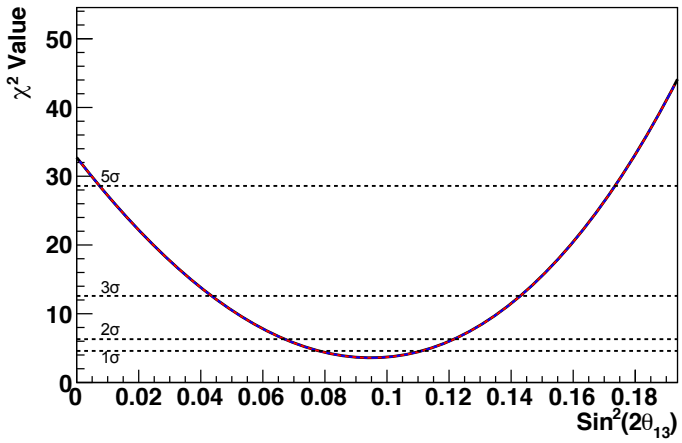

Figure 9.7: Minimized χ^2 versus $\sin^2 2\theta_{13}$. The dotted horizontal lines indicate, from bottom to top, the 1, 2, 3, and 5-σ confidence regions. The χ^2 is minimized at a value of 0.095, and zero is excluded by more than five standard deviations.

Figure 9.8 shows the appearance of the detected-to-expected ratios as a function of weighted baseline using the best-fit nuisance parameters with and without inclusion of the oscillation parameters. One can see in this comparison that the proper inclusion of oscillation effects completely removes the deficit seen at the far site.

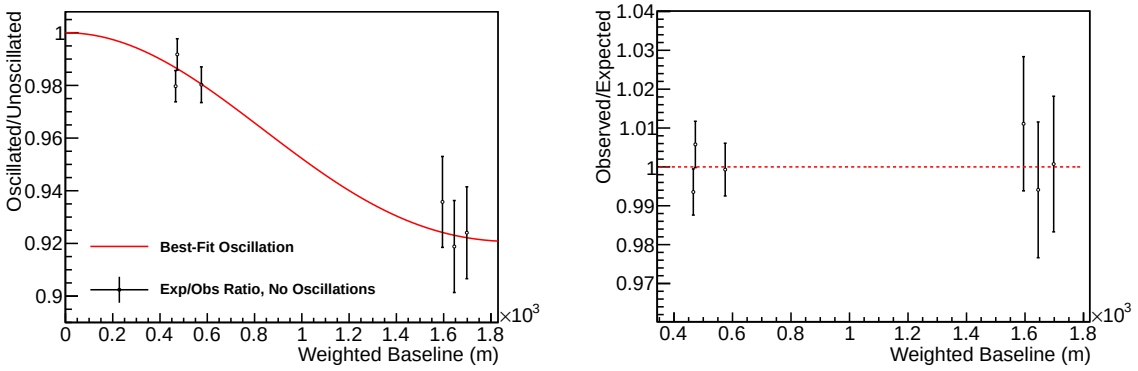

(a) Observed/expected ratios with no oscillations. Also shown is the expected oscillation from the best-fit $\sin^2 2\theta_{13}$.

(b) Observed/expected ratios with best-fit oscillation included in prediction.

Figure 9.8: Ratios between the detected and predicted event rates for all six ADs as a function of weighted baseline, including the best-fit nuisance and $\sin^2 2\theta_{13}$ parameters from the χ^2. Weighted baselines for two of the far site detectors are artificially altered by 50 m to make each data point more visible. One can see that the observed deficit agrees well with the best-fit oscillation parameters, and reduces to near 1 for all detectors when oscillations are included in the prediction.

Chapter 10

Conclusion

10.1 Summary of Thesis Results

Daya Bay is a high-statistics experiment designed to probe the value of θ_{13} as precisely as one possibly can with reactor $\overline{\nu}_e$. Through the comparison of Daya Bay's first two near-site detectors presented in this thesis, it has been demonstrated that the Daya Bay experiment is well on its way to achieving this goal. More importantly, Daya Bay's high statistics and low systematics measurement method has allowed it to make the first unambiguous measurement of a large θ_{13} value with only a few months of data.

The Daya Bay experiment has utilized one of the most powerful reactor complexes in the world as a source to measure reactor $\overline{\nu}_e$ fluxes at near and far baselines. The total rate of inverse beta decay interactions at near and far baselines were measured and compared to predictions based on precise measurements of reactor power, baselines, detector target masses and detection efficiencies. The ratios between expected and predicted rates were then compared between detectors to search for any relative differences that would indicate $\overline{\nu}_e$ disappearance. Such a difference was measured be-

tween near and far baseline detectors in 50 days of data taking, with with a relative deficit at the far site of:

$$D = 0.061 \pm 0.011(stat) \pm 0.005(syst). \tag{10.1}$$

This relative rate deficit is an unambiguous signature of reactor $\overline{\nu}_e$ disappearance. If this deficit is interpreted within the existing framework of neutrino oscillations, it indicates a non-zero value of θ_{13} at greater than 5σ confidence level, with an exact value of

$$\sin^2 2\theta_{13} = 0.095 \pm 0.017(stat) \pm 0.006(syst). \tag{10.2}$$

The unparalleled sensitivity of Daya Bay's first θ_{13} measurement is the result of systematic uncertainties lower than any previously achieved in a neutrino physics experiment. This unique ability stems from making a relative measurement using functionally identical detectors at near and far baselines. These systematics claims have been thoroughly justified over the course of this thesis. Characterization studies done during design, construction and assembly were presented to demonstrate the degree of physical identicalness achieved among all ADs. Simulations studies were then recounted to convey how little detector response was expected to vary based on the physical similarity of the ADs. Finally, three months of neutrino data taken with two side-by-side near site detectors were analyzed to provide a direct comparison of detection rates in the absence of oscillation and relative background effects. With 70 days of near site-only data-taking prior to the three-site data period, the difference in the detected and expected ratios between the near site ADs is:

$$D = 0.004 \pm 0.008(stat) \pm 0.003(syst). \tag{10.3}$$

This agreement demonstrates the identical response of the detectors to neutrinos, as well as proper understanding of detector systematics. Future experimentalists can use

Daya Bay as a successful demonstration of and inspiration for future use of identical detectors in precision particle physics experiments.

10.2 Implications and Future Prospects

The Daya Bay oscillation result presented in this thesis has significant implications, both in theoretical and experimental neutrino physics. The most direct impact is that Daya Bay has vastly improved the global knowledge of the value of $\sin^2 2\theta_{13}$, as illustrated in Figure 10.1. Daya Bay provides the highest-significance result, and agrees well with the result of previous reported values from Double Chooz [89], MINOS [82], and T2K [87], as well as a subsequent measurement by RENO [110].

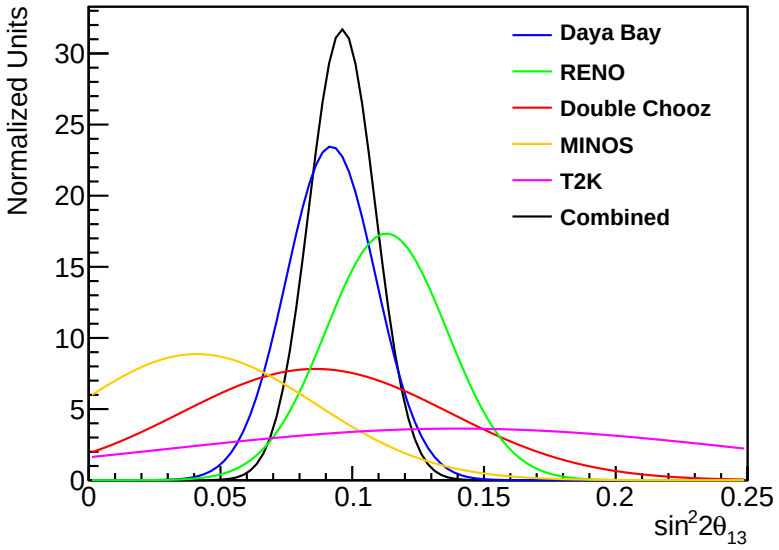

Figure 10.1: Reported $\sin^2 2\theta_{13}$ measured values and uncertainties from all experiments claiming a non-zero result: Daya Bay [141], Double Chooz [89], RENO [110], MINOS [82], and T2K [87]. Each Gaussian peak represents the best-fit value of that experiment, while the width indicates the combined statistical and systematic uncertainty. The combined Gaussian from all results is also shown, which assumes that the uncertainties of all experiments are uncorrelated and normally distributed. Daya Bay greatly improves upon the significance of previous results, giving a clear rejection of the null hypothesis.

The large value of $\sin^2 2\theta_{13}$ reported in this thesis also significantly brightens the prospects for future accelerator neutrino experiments, as demonstrated in Figure 10.2. In the shorter term, NOνA [143], an long-baseline, off-axis accelerator neutrino experiment currently being constructed to utilize the same NuMI beamline as MINOS, will have the ability to detect the neutrino mass hierarchy for roughly 20% of the possible phase space of δ_{CP}. If this is not the case, the next generation of long-baseline experiments, such as LBNE [144], LENA [145], and HyperK [146], are guaranteed to be able to measure the mass hierarchy at all possible δ_{CP} values.

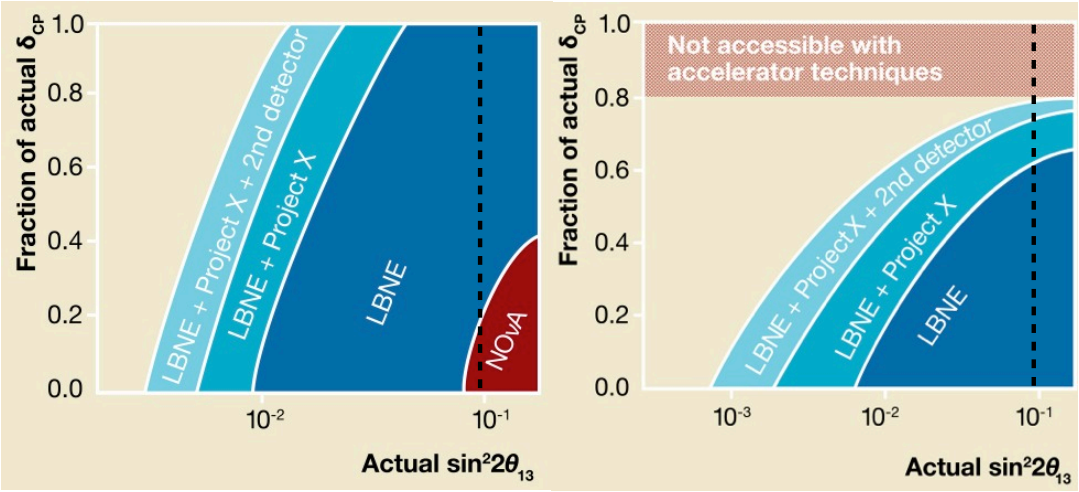

Figure 10.2: Discovery potential of future US-based accelerator experiments for the neutrino mass hierarchy (left figure) and δ_{CP} (right figure). The value of θ_{13} measured at Daya Bay is indicated by the vertical dashed lines. Daya Bay's measurement of a large mixing angle indicates the likely discovery of the mass hierarchy by LBNE or NOνA, as well as the probing of a majority of δ_{CP} parameter space by LBNE with the need for accelerator upgrades. Original figure from [147].

Given the large measured value of θ_{13}, these next-generation experiments will also be able to make great strides forward in the measurement of leptonic CP-violation. As demonstrated in Figure 10.2, even without an upgrade at Fermilab to the ambitious high-intensity Project X beamline [148], a large, long-baseline experiment such as

LBNE can rule out a majority of CP-violation phase space.

The impact of Daya Bay's measurement of θ_{13} is also felt widely in theoretical neutrino physics. As shown in Figure 10.3, with $\sin^2 2\theta_{13}$=0.95 ($\sin^2\theta_{13}$ = 0.025), the number of neutrino mass and mixing models in agreement with experimental data is greatly reduced, from upwards of 40 flavor symmetries and GUT models, to around 7 and 5, respectively. In addition, previously favored tri-bimaximal mixing schemes, which require a null or near-null value of θ_{13}, are rejected by this result. The significant constraints on CP-violation and the mass hierarchy expected from future experiments because of a large θ_{13} will further reduce this number.

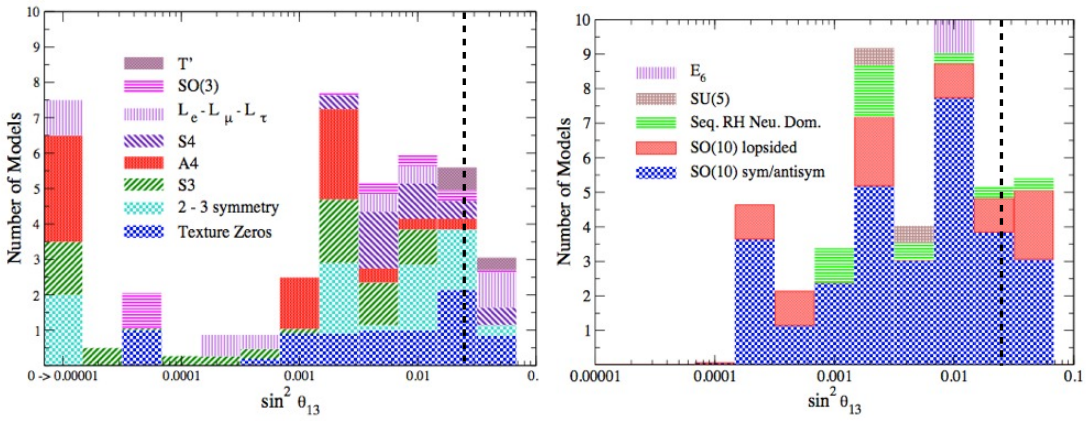

Figure 10.3: Predictions of $\sin^2 2\theta_{13}$ for a variety of lepton flavor symmetry (left plot) and GUT (right plot) models. The $\sin^2 2\theta_{13}$=0.095 ($\sin^2\theta_{13}$=0.025) value measured by Daya Bay is represented by the vertical dashed lines. Daya Bay's result constrains the number of allowed neutrino mixing models. Adapted from [149]

Accumulation of physics data at Daya Bay in the coming years will only increase the experiment's world-leading precision in measuring θ_{13}. Increased statistics will also allow the collaboration to examine with greater statistical precision the identical behavior of the Daya Bay detectors. Once the last two detectors are installed, a full eight-detector deployment will provide another set of near-site side-by-side detectors for systematic comparison, as well as an additional far site detector for increased

statistics.

In the next few years, the large value of θ_{13} and a future spectral analysis of the Daya Bay results should yield further constraints on $|\Delta m^2_{32}|$, complimenting previous measurement by accelerator experiments. In addition, an absolute measurement of the Daya Bay flux and spectrum at the Daya Bay near sites can provide new information about neutrino production in nuclear reactors and address the reactor antineutrino anomaly, which is discussed in the Appendix. The current measurement of θ_{13} already provides the basis for future experiments. After three years of data taking, Daya Bay will have a precise value of θ_{13} that can provide the basis with which to tackle the next great unanswered questions in neutrino physics, CP violation and the mass hierarchy.

Bibliography

[1] W. Pauli, *Letter to a physicist's gathering at tubingen, december 4, 1930*, in *Wolfgang Pauli, Collected Writings* (K. R. and V. Weisskopf, eds.). (Interscience: New York, 1964).

[2] F. A. Scott *Phys. Rev.* **48** 391, (1935).

[3] F. Reines and C. Cowan *Phys. Rev.* **92** 830, (1953).

[4] F. Reines and C. Cowan *Nature* **178** 446, (1956).

[5] E. Commins and P. Bucksbaum, *Weak Interactions of Leptons and Quarks*. (Cambridge University Press: Cambridge, 1983).

[6] C. Wu *Phys. Rev.* **105** 1413, (1957).

[7] N. Cooper *et. al.*, *Celebrating the neutrino*, *Los Alamos Science* **25** (1997).

[8] S. Weinberg *Phys. Rev. Lett.* **19** 1264, (1967).

[9] B. Pontecorvo *Sov. Phys. JETP* **6** 429, (1958).

[10] Z. Maki *et. al. Prog. Theor. Phys.* **28** 870, (1962).

[11] V. Gribov and B. Pontecorvo *Phys. Lett.* **28B** 493, (1969).

[12] T. Pinch, *Confronting Nature: The Sociology of Solar-Neutrino Detection*. (D. Reidel Publishing Company: Dordrecht, Holland, 1986).

[13] H. D. Davis, R. and K. Hoffman *Phys. Rev. Lett.* **20** 1205, (1968).

[14] **SAGE** Collaboration, A. Abazov *et. al. Phys. Rev. Lett.* **67** 3332, (1991).

[15] P. Anselmann *et. al. Phys. Lett.* **B285** 376, [hep-ex/1001.2731], (1992).

[16] B. Cleveland *et. al. Astrophys. J.* **486** 505, (1998).

[17] **SNO** Collaboration, Q. R. Ahmad *et. al. Phys Rev. C* **81** 055504, [nucl-ex/0910.2984], (2010).

[18] **Super-Kamiokande** Collaboration, K. Abe *et. al.* [hep-ex/1010.0118], (2010).

[19] **Borexino** Collaboration, C. Arpesella *et. al. Phys. Lett.* **B658** 101, [hep-ex/0708.2551], (2008).

[20] **Kamiokande** Collaboration, K. Hirata *et. al. Phys. Lett.* **B205** 416, (1988).

[21] **Super-Kamiokande** Collaboration, J. Hosaka *et. al. Phys. Rev. D* **74** 032002, [hep-ex/0604011], (2006).

[22] **Chooz** Collaboration, M. Apollonio *et. al. Eur. Phys. J.* **C27** 331–374, [hep-ex/0301017], (2003).

[23] **Palo Verde** Collaboration, F. Boehm *et. al. Phys. Rev.* **D64** 112001, (2001).

[24] **KamLAND** Collaboration *Phys Rev. Lett.* **100** 221803, [hep-ex/0801.4589], (2008).

[25] **MINOS** Collaboration, P. Adamson *et. al. Phys. Rev. Lett.* **101** 131802, [hep-ex/0806.2237], (2008).

[26] **K2K** Collaboration, M. Ahn *et. al. Phys. Rev.* **D74** 072003, [hep-ex/0606032], (2006).

[27] **ALEPH, DELPHI, L3, OPAL, SLD, and LEP** Collaboration *Phys. Reports* **427** 257, (2006).

[28] B. Ackhar *et. al. Phys. Lett.* **B338** 383, (1994).

[29] A. Balantekin *Phys. Rev.* **D77** 013007, (2008).

[30] **MEG** Collaboration *Phys. Rev. Lett* **107** 171801, (2011).

[31] J. Kopp *et. al. Phys. Rev.* **D77** 013007, (2008).

[32] **Super-Kamiokande** Collaboration, G. Mitsuka *et. al. Phys. Rev.* **D84** 113008, (2011).

[33] S. Gninenko *Phys. Lett.* **B710** 86, (2012).

[34] F. Boehm and P. Vogel, *Physics of Massive Neutrinos.* (Cambridge University Press: Cambridge, 1987).

[35] M. Gell-Mann *et. al.* in *Supergravity* (D. Freedman, ed.). (North Holland: Netherlands, 1979).

[36] T. Yanagida *Prog. Theor. Phys.* **64** 1103, (1980).

[37] R. Mohapatra *et. al.*, *Theory of neutrinos: A white paper*, [hep-ph/0510213], (2005).

[38] **Particle Data Group** Collaboration, K. Nakamura *et. al. J. Phys. G* **37** 075021, (2010).

[39] R. McKeown and P. Vogel *Phys. Rept.* **394** 315, (2004).

[40] T. Schwetz, M. Tortola, and J. Valle [hep-ph/1103.0734], (2011).

[41] L. Wolfenstein *Phys. Rev.* **D17** 2369, (1978).

[42] S. Mikheev and A. Smirnov *Sov. J. Nucl. Phys.* **42** 913, (1985).

[43] P. Huber *et. al. JHEP* **0911:044** [hep-ph/0907.1896], (2009).

[44] F. Reines *et. al. Phys. Rev. Lett.* **32** 180, (1974).

[45] F. Reines *et. al. Phys. Rev. Lett.* **37** 315, (1976).

[46] F. Reines *et. al. Phys. Rev. Lett.* **45** 1307, (1980).

[47] S. E. Willis *et. al. Phys. Rev. Lett.* **44** 522, (1980).

[48] H. Kwon *et. al. Phys. Rev.* **D24** 1097, (1981).

[49] J. Vuilleumier *et. al. Phys. Lett.* **B114** 298, (1982).

[50] G. K. *et. al. Phys. Lett* **B138** 449, (1984).

[51] G. Zacek *et. al. Phys. Rev.* **D34** 2621, (1986).

[52] B. Ackhar *et. al. Nucl. Phys.* **B434** 503, (1995).

[53] A. Afonin *et. al. JETP Lett.* **41** 435, (1985).

[54] A. Afonin *et. al. JETP Lett.* **45** 247, (1987).

[55] A. Afonin *et. al. JETP Lett.* **54** 253, (1991).

[56] G. Vidyakin *et. al. JETP Lett.* **59** 390, (1994).

[57] **Chooz** Collaboration, M. Apollonio *et. al. Phys. Lett.* **B420** 397, [hep-ex/9907037], (1998).

[58] **Chooz** Collaboration, M. Apollonio *et. al. Phys. Lett.* **B466** 415, [hep-ex/9711002], (1999).

[59] **Palo Verde** Collaboration, F. Boehm *et. al. Prog. Part. Nucl. Phys.* **40** 253, (1998).

[60] K. Schreckenbach *et. al. Phys. Lett.* **B99** 251, (1981).

[61] K. Schreckenbach *et. al. Phys. Lett.* **B160** 325, (1985).

[62] K. Schreckenbach *et. al. Phys. Lett.* **B218** 365, (1989).

[63] P. Vogel and J. Engel *Phys. Rev.* **D39** 3378, (1989).

[64] P. Vogel and J. Beacom *Phys. Rev.* **D60** 053003, (1999).

[65] A. Afonin *et. al. JETP Lett.* **37** 150, (1983).

[66] A. Afonin *et. al. JETP Lett.* **38** 436, (1983).

[67] **IMB** Collaboration, T. Haines *et. al. Phys. Rev. Lett.* **57** 1986, (1986).

[68] **Frejus** Collaboration, C. Berger *et. al. Phys. Lett.* **B227** 305, (1990).

[69] **NUSEX** Collaboration, M. Aglietta *et. al. Europhys. Lett.* **15** 559, (1991).

[70] **Kamiokande** Collaboration, Y. Fukuda *et. al. Phys. Lett.* **B335** 237, (1994).

[71] **Kamiokande** Collaboration, E. Beier *et. al. Phys. Lett.* **B283** 446, (1992).

[72] **Kamiokande** Collaboration, S. Hatakeyama *et. al. Phys. Rev. Lett* **81** 2016, (1998).

[73] **MACRO** Collaboration, S. Ahlen *et. al. Phys. Lett.* **B357** 481, (1995).

[74] **Soudan-2** Collaboration, W. Allison *et. al. Phys. Lett.* **B391** 491, (1997).

[75] **Soudan-2** Collaboration, W. Allison *et. al. Phys. Lett.* **B449** 137, (1999).

[76] **Super-Kamiokande** Collaboration *Phys. Rev. Lett.* **81** 1562, [hep-ex/9807003], (1998).

[77] **Super-Kamiokande** Collaboration *Phys. Rev. Lett.* **93** 101801, [hep-ex/0404034], (2004).

[78] **IMB** Collaboration, Y. Fukuda *et. al. Phys. Lett.* **69** 1010, (1992).

[79] **Frejus** Collaboration, C. Berger *et. al. Phys. Lett.* **B245** 489, (1989).

[80] B. Ackhar *et. al. Phys. Lett.* **B148** 393, (1984).

[81] **Super-Kamiokande** Collaboration, Y. Fukuda *et. al. Nucl. Inst. Meth.* **A501** 418, (2003).

[82] **MINOS** Collaboration, P. Adamson *et. al. Phys. Rev.* **D82** 051102, [hep-ex/1006.0996], (2010).

[83] **K2K** Collaboration, M. Ahn *et. al. Phys. Rev. Lett.* **96** 181801, [hep-ex/0603004], (2006).

[84] T. M. Schwetz, T. and J. Valle [hep-ph/1108.1376], (2011).

[85] P. Machado *et. al.* [hep-ph/1111.3330], (2011).

[86] A. Balantekin and D. Yilmaz *J. Phys.* **G35** 075007, [hep-ph/0804.3345], (2008).

[87] **T2K** Collaboration, A. K. *et. al. Phys. Rev. Lett.* **107** 041801, [hep-ex/1106.2822], (2011).

[88] **MINOS** Collaboration, P. Adamson *et. al. Phys. Rev. Lett.* **107** 181802, [hep-ex/1108.0015], (2011).

[89] **Double Chooz** Collaboration, Y. Abe *et. al. Phys. Rev. Lett.* **108** 131801, [hep-ex/1112.6353], (2012).

[90] G. H. and S. Glashow *Phys. Rev. Lett.* **32** 438, (1974).

[91] K. Babu and R. Mohapatra *Phys. Rev. Lett.* **70** 2845, (1993).

[92] K. Babu and S. Barr *Phys. Lett.* **B381** 202, (1996).

[93] P. Harrison, D. Perkins, and W. Scott *Phys. Lett.* **B530** 167, (2002).

[94] C. Albright and M. Chen *Phys. Rev.* **D74** 113006, (2006).

[95] C. Albright [hep-ph/0905.0146], (2009).

[96] **Daya Bay** Collaboration [hep-ex/0701029], (2007).

[97] Z. Wang *et. al. Nucl. Inst. Meth.* **A602** 489, (2009).

[98] M. Yeh *et. al. Nucl. Inst. Meth.* **A578** 329, (2007).

[99] Y. Ding *et. al. Nucl. Inst. Meth.* **A584** 238, (2008).

[100] H. Band *et. al.* [ins-det/1101.0126], (2012).

[101] Hamamatsu Photonics, Electron Tube Divison. 314-5 Shimokanzo, Iwata City, Shizuoka Pref., Japan, http://www.hamamatsu.com/.

[102] L. Wen *et. al. Nucl. Inst. Meth.* **A629** 296, (2011).

[103] H. Gong *et. al. Nucl. Inst. Meth.* **A637** 138, (2011).

[104] **Daya Bay** Collaboration, F. An *et. al.* [det-ins/1202.6181], (2012).

[105] Q. Zhang *et. al. Nucl. Inst. Meth.* **A583** 278, (2007).

[106] L. Ma *et. al. Nucl. Inst. Meth.* **A659** 154, (2011).

[107] L. Mikaelyan and V. Sinev *Phys. Atom. Nucl.* **63** 1002, [hep-ex/9908047], (2000).

[108] **Double Chooz** Collaboration [hep-ex/0606025], (2006).

[109] **RENO** Collaboration [hep-ex/1003.1391], (2010).

[110] **RENO** Collaboration [hep-ex/1204.0626], (2012).

[111] **SNO** Collaboration, Q. R. Ahmad *et. al. Nucl. Inst. Meth.* **A449** 172, [nucl-ex/9910016], (2000).

[112] B. Littlejohn *et. al. JINST* **4** T09001, (2009).

[113] SI Photonics, Inc. 1870 W. Prince Rd., Ste. 38, Tucson, AZ 85705 USA, http://www.si-photonics.com/.

[114] Chan, Yuen-Dat. personal communication.

[115] J. D. Shachiw, *Handbook of Acrylics for Submersibles, Hyperbaric Chamber, and Aquaria*. (Best Publishing Company: Flagstaff, AZ, 2003).

[116] Reynolds Polymer Technology, Inc. 607 Hollingsworth St. Grand Junction, CO 81505 USA, http://www.reynoldspolymer.com/.

[117] Spartech Polycast. 70 Carlisle Place, Stamford, CT 06902 USA, http://www.spartech.com/polycast.html.

[118] Nakano International Limited. No. 3, Ln. 483, Sec. 2, Zhongshan Rd., Taishan Township, Taipei County 243, Taiwan (R.O.C).

[119] Coroplast. 5001 Spring Valley Road Suite 400 East, Dallas, Texas 75244 USA, http://www.coroplast.com/.

[120] MSR Electronics GmbH. Oberwilerstrasse 16, CH-8444 Henggart Switzerland, http://www.msr.ch/en/.

[121] Telespial Systems, Inc. 827 Hollywood Way, Burbank, CA 91505 USA, http://www.trackstick.com/.

[122] Instrumented Sensor Technology, Inc. 4704 Moore Street, Okemos, MI 48864 USA, http://www.isthq.com/.

[123] Onset Computer Corporation. 470 MacArthur Boulevard, Bourne, MA 02532 USA, http://www.onsetcomp.com/.

[124] Leica Geosystems AG. Heinrich Wild Strasse, CH-9435 Heerbrugg, St. Gallen Switzerland, http://www.leica-geosystems.com/en/.

[125] The GAUDI Project. http://proj-gaudi.web.cern.ch/proj-gaudi/.

[126] Geant4: A Toolkit for the Simulation of the Passage of Particles Through Matter. http://geant4.cern.ch/.

[127] Zhan, Liang. personal communication.

[128] Perkin Elmer, Inc. 940 Winter Street, Waltham, MA 02451 USA, http://www.perkinelmer.com/.

[129] D. W. Zwinkels, J. C. and C. Dodd *Applied Optics* **29** 3240, (1990).

[130] Schott North America, Inc. 555 Taxter Rd., Elmsford, NY 10523 USA, http://www.us.schott.com/.

[131] Wen, Liangjian. personal communication.

[132] Zhong, Weili. personal communication.

[133] Whitehead, Lisa. personal communication.

[134] V. Guiseppe *et. al.* [nucl-ex/1101.0126], (2010).

[135] NIST Center for Neutron Research. Neutron Scattering Length Database, http://www.ncnr.nist.gov/resources/n-lengths/.

[136] Liu, Yingbiao. personal communication.

[137] Ling, Jiajie. personal communication.

[138] Gu, Wenqiang. personal communication.

[139] Webber, David. personal communication.

[140] Lewis, Christine. personal communication.

[141] **Daya Bay** Collaboration, F. An *et. al. Phys. Rev. Lett* **108** 171803, [hep-ex/1203.1669], (2012).

[142] GNU Scientific Library. http://www.gnu.org/software/gsl/.

[143] **NOvA** Collaboration [hep-ex/0708.2551], (2005).

[144] LBNE Collaboration. http://lbne.fnal.gov.

[145] M. Wurm *et. al.* [astro-ph/1104.5620], (2011).

[146] K. Abe *et. al.* [hep-ex/1109.3262], (2011).

[147] Fermilab National Accelerator Laboratory. (2012), http://www.fnal.gov/directorate/plan_for_discovery/.

[148] R. Tschirhart [hep-ex/1109.3500], (2012).

[149] C. Albright [hep-ph/0905.0146], (2009).

Appendix A

What Can Daya Bay Say About Sterile Neutrinos?

A.1 Sterile Neutrino Introduction

Neutrino mass and mixing are usually incorporated in the generalization of the Standard Model by assuming that the three neutrino states of a given flavor, ν_e, ν_μ and ν_τ, are superpositions of the three mass eigenstates ν_i,

$$|\nu_l\rangle = \sum_i U_{li} |\nu_i\rangle \ . \tag{A.1}$$

Here $U_{l,i}$ is the unitary 3×3 neutrino mixing matrix. This assumption makes it possible to consistently describe most data from solar, atmospheric, reactor and accelerator neutrino experiments. The values of the mixing angles in $U_{l,i}$ as well as of the mass square differences Δm^2_{21} and $|\Delta m^2_{31}|$ can be deduced from analysis of these data [1].

However, several recent experiments indicate that this picture might be incomplete, although the statistical significance is limited. See [2] and references therein. They suggest that one or more sterile neutrinos, which weakly couple to the active neutrinos, might exist. In particular, the "reactor anomaly" [3], based on the reevaluation of the nuclear reactor $\overline{\nu}_e$ flux [4], suggests that the $\overline{\nu}_e$ produced in reactor cores oscillate into some sterile neutrino species at distances of less than ∼10 m from the reactor core. This would reduce the active $\overline{\nu}_e$ flux observed by experiments at distances greater than 10 m from the reactor.

With the modified reactor flux model of Ref. [4], the simplest 3+1 sterile neutrino model was used to analyze the existing results from reactor experiments, GALLEX and SAGE calibration sources, and MiniBooNE [3]. Other similar analyses included a reanalysis of the MiniBooNE experiment [5] and the results of the ILL reactor experiment [6]. The resulting best fit sterile neutrino oscillation parameters are $|\Delta m^2_{\rm new}| = 2.35 \pm 0.1$ eV^2 (68% C.L.) and $\sin^2(2\theta_{\rm new}) = 0.165 \pm 0.04$ (68% C.L.). The region of these parameters compatible at 95% C.L. with all the analyzed experiments is constrained by $|\Delta m^2_{\rm new}| > 1.5$ eV^2 and $\sin^2(2\theta_{\rm new}) = 0.17 \pm 0.09$. A recent

analysis of short-baseline neutrino oscillation data in the framework of 3+1 neutrino mixing including the update of MiniBooNE antineutrino data and the MINOS results [2] yields best-fit values from around $\Delta m^2_{41} \approx 1$ eV^2 up to ≈ 5.6 eV^2, where Δm^2_{41} corresponds to the new mass splitting $\Delta m^2_{\rm new}$ in the 3+1 model.

The existing data do not provide a fully convincing picture of sterile neutrino oscillations. In particular, evidence from reactor $\overline{\nu}_e$ experiments relies on a complex calculation of absolute reactor flux to posit a measured absolute rate deficit from sterile oscillations. In addition to an absolute rate deficit, observation of $\overline{\nu}_e$ disappearance as a function of energy and baseline consistent with a new Δm^2 would provide very convincing demonstration of oscillation into sterile neutrinos. The Daya Bay experiment's near sites, as currently deployed, can provide additional high-statistics measurements of the absolute $\overline{\nu}_e$ flux at multiple sub-km baselines, providing a precise absolute check on the reactor $\overline{\nu}_e$ anomaly. The Daya Bay far site, if outfitted with a high-intensity $\overline{\nu}_e$ source, can provide a definitive test of the reactor $\overline{\nu}_e$ anomaly by searching for baseline-dependent $\overline{\nu}_e$ disappearance. The purpose of the appendix is to discuss further these Daya Bay-based searches for sterile neutrino oscillations.

A.2 Testing the Reactor $\overline{\nu}_e$ Anomaly with the Daya Bay Near Sites

Introduction

As discussed in Chapter 2, many experiments over the past three decades have measured reactor $\overline{\nu}_e$ fluxes at short baselines. The results from these measurements are shown in Figure A.1, using the newly calculated reactor fluxes from [4]. These results show a deficit in the measured number of $\overline{\nu}_e$, with general agreement between most experiments and large associated uncertainties.

The Daya Bay near detectors provide a measurement of $\overline{\nu}_e$ relatively unoscillated from Δm_{31} (of order 1% $\overline{\nu}_e \rightarrow \overline{\nu}_x$) mixing with respect to the far site detectors. The near site data can be used to make an absolute measurement of the $\overline{\nu}_e$ flux, providing further measurements of absolute rate deficits at baselines not yet probed by previous experiments. These longer baseline measurements, as with those in Figure A.1, will have no power to distinguish spectral or baseline distortions from a multi-eV^2 Δm^2, but can provide a high-statistics check on the reactor $\overline{\nu}_e$ deficit derived from previous reactor experiments.

The Daya Bay near site detectors will accrue inverse beta statistics higher than any previous experiment. In one year of data taking at EH1, each detector's IBD data will have an overall statistical uncertainty of less than 0.3%; three years of planned data-taking will result in roughly 1×10^6 inverse beta detections at each near site, giving three times the statistics per site than the Bugey experiment [7]. Given this prolific amount of data, the precision of a measurement of the absolute reactor flux at Daya Bay will be limited by the absolute systematics of the experiment. The

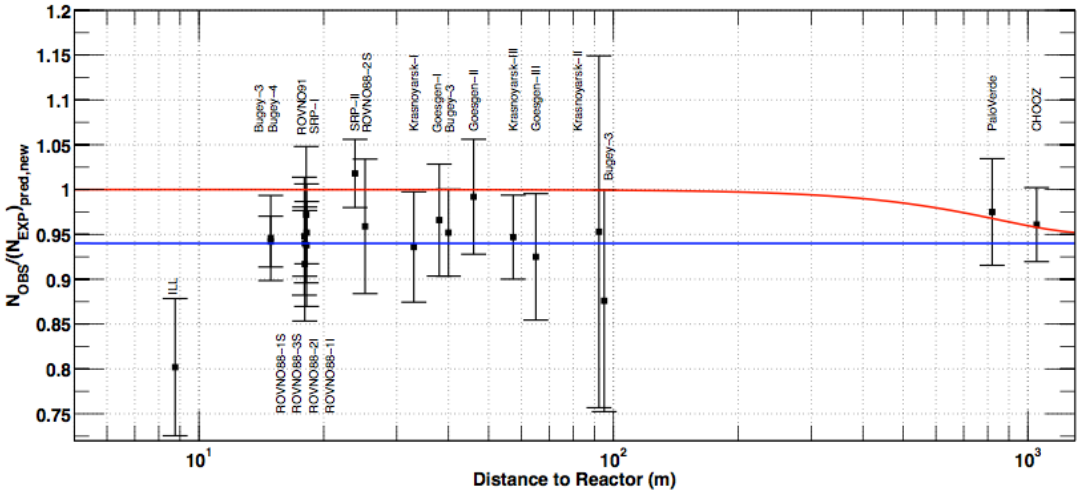

Figure A.1: Past measurements of the reactor $\overline{\nu}_e$ deficit, using the predicted reactor $\overline{\nu}_e$ calculated in [4]. The red line illustrates the effect of a θ_{13} oscillation, while the blue line shows the effect of oscillation from a new $\Delta m^2 >> 1$ eV^2. Daya Bay's near site ADs will provide measurements at two new long baselines in the vicinity of 300-600 m. From [3].

relative systematics of the Daya Bay experiment are already well-characterized to well below the percent level. In order to achieve sub-percent absolute systematics for a flux measurement, absolute detector systematics must be well-characterized through extensive detector calibration, and detailed reactor information must be gathered and properly treated to produce a low-uncertainty flux prediction for each of the six Day Bay reactors.

Establishing Absolute Reactor $\overline{\nu}_e$ Flux Predictions

As discussed in Chapter 8, the neutrino flux from each reactor i can be described by the following equation:

$$S_i = \left(\frac{W_i}{\sum_j (f_{ij}/F) e_j} \sum_j^{isotopes} (f_{ij}/F) \int S_j(E_\nu) \right), \tag{A.2}$$

where W_i and f_{ij}/F are the thermal output and fission fractions of each reactor, and e_j and S_j are energy per fission and $\overline{\nu}_e$ spectrum of each fission isotope j. By using the same values e_j and S_j used in [4], a common comparison can be made between Daya Bay's observed flux and that of the other re-analyzed short-baseline experiments.

The thermal power, W_i, is provided by the Daya Bay reactor company, and has an associated absolute uncertainty of 0.5%. The fission fractions as a function of burnup are also provided by the reactor company, with an absolute uncertainty of ∼5% for

each isotope. These fission fractions can be studied further with a reactor simulation code, such as DRAGON [8], to identify correlations between the fission rates of the different isotopes. As shown in Table 9.3 of Chapter 8, this simulation has identified correlations that reduce the overall uncertainty from this source to 0.6% per reactor. Future improvements in thermal power measurement techniques and reporting and in reactor simulation may marginally decrease the size of these current absolute reactor systematics.

Establishing Absolute Detector Systematics

Current calibration efforts at Daya Bay have principally focused on quantifying relative differences in detection efficiency and target mass between detectors, in the effort to precisely measure relative disappearance between near and far detectors from Δm^2_{31} oscillations. For an absolute flux measurement at the near site detectors, absolute detection efficiencies and effective proton numbers must be measured.

The effective absolute number of target protons is determined principally by the GdLS target mass and the proton density per unit mass. As described in Chapter 8, the absolute target mass is known to 0.019%. The proton density, also referred to as the H/C ratio, has been measured via combustion analysis, a standard chemistry laboratory method, to a precision of 0.47%.

In addition to the protons in the GdLS, protons in the IAV and LS can also serve as $\overline{\nu}_e$ interaction targets: if neutrons from $\overline{\nu}_e$ interactions in these other regions travel into the GdLS, they can create a detectable inverse beta decay signature. We have estimated using Monte Carlo simulations that this effect increases the effective target volume by $5.0 \pm 1.5\%$ [9]. This large associated uncertainty can be reduced though calibration of the spill-in effect using high intensity neutron sources in the LS along the ACUC calibration axis. The number of neutron captures on Gd can be used to calculate the magnitude of the spill-in effect at various points along the ACUC axis, providing a baseline on which to tune the spill-in effect in Monte Carlo simulation. Through this calibration regimen and associated improvement in the Monte Carlo, we hope to reduce this systematic to less than that contributed by the combustion analysis.

A plan for such a calibration has been proposed and developed by Daya Bay collaborators: an ACU with specially produced neutron and gamma sources of high intensity has been assembled, and will be installed and operated on at least one near-site AD. Since relative differences between ADs are well-understood, and, for spill-in effects, known to be negligibly small, deployment on one AD should be sufficient for precise understanding of spill-in effects in all near-site ADs.

The absolute neutron detection efficiency must also be more accurately measured to reduce the systematics of an absolute $\overline{\nu}_e$ flux measurement. Part of the neutron detection inefficiency stems from neutron captures on hydrogen, which are vetoed completely by the 6 MeV delayed energy cut. The absolute Gd/H capture ratio has been measured using a low-intensity AmC source at the detector center with

0.5% precision. This precision can be improved by deploying a high-intensity source at various positions in each detector. This will be achieved by deploying a special 'manual calibration system' on one near-site AD that will deploy a PuC neutron source throughout the target region utilizing an articulating arm.

The absolute neutron detection efficiency is also dependent on the uncertainty in absolute energy scale calibration. The absolute energy scale will be precisely calibrated to a goal precision of 1% utilizing an array of special calibration sources. By deploying multiple sources of varying energy at the detector center utilizing the aforementioned special ACU, energy non-linearity effects can be precisely measured. The manual calibration system can be used to determine the non-linearity of the energy scale with position to high precision. By combining these two calibration regimens, the location of the 6 MeV cut should be established to $\pm 1\%$, leading to a neutron detection efficiency uncertainty of approximately 0.3%.

Conclusion

The current estimates of absolute reactor and detector systematics for a near site $\overline{\nu}_e$ flux measurement are listed in Table A.1. Without further improvement of systematics, Daya Bay will be able to make a flux measurement with 1.9% precision relative to previous measurements utilizing similar $\overline{\nu}_e$ spectrum and normalization assumptions. Improvements to detector systematics are expected from further studies of the absolute energy scale and detection efficiencies, as well as from more complete absolute calibration data from special full-volume and high-intensity calibration runs. Systematic uncertainties can optimistically be reduced to the sub-percent level with precise study of these additional detector calibrations. The resultant Daya Bay absolute $\overline{\nu}_e$ flux measurement can be compared with previous short-baseline reactor neutrino results to provide the highest-statistics test of the reactor $\overline{\nu}_e$ anomaly yet recorded.

Category	Input	Absolute Unc. (%)
Detector	H/Gd n-Capture Ratio	0.5
	Delayed Energy	0.6
	H/C Ratio	0.47
	Spill-in Effects	1.5
Reactor	Thermal Power	0.5
	Fission Fraction	0.6
Total		1.9

Table A.1: Current absolute systematics for an $\overline{\nu}_e$ flux measurement at the Daya Bay near sites. The uncertainty in the number of spill-in inverse beta detections is currently the dominant systematic. Many of the calibration-related uncertainties will reduce further with improvements in effective target mass and energy calibration.

A.3 Sterile Search With an $\overline{\nu}_e$ Source

To unambiguously test the hypothesis of a short distance oscillation into a sterile neutrino state ideally one would like to place a $\overline{\nu}_e$ detector near the distance

$$L_{optim} = \frac{L_{osc}[\mathrm{m}]}{2} = 1.24 \frac{E_{\overline{\nu}_e}[\mathrm{MeV}]}{\Delta m^2_{\mathrm{new}}[\mathrm{eV}^2]} \tag{A.3}$$

and observe the $L/E_{\overline{\nu}_e}$ variation of the observed signal.

Oscillations over this baseline can be tested through the deployment of a "point-like" radioactive antineutrino source in the Daya Bay far site water pool [10, 11] outside the ADs. The small extent of such a source would minimize the smearing and averaging of the oscillation signature with baseline. Such minimal smearing will be difficult to achieve at proposed very short baseline reactor experiments [12, 13, 14, 15] because of the finite size of reactor cores, which can vary in diameter from 0.5-5 m. A Daya Bay point source deployment also would provide access to meter-scale oscillation lengths without disturbing the well-understood and calibrated far site ADs, an advantage over other proposed experiments in which a point-like source is lowered into the target region of a detector such as KamLAND or SNO [11].

Experimental Setup

Three possible source positions in the Daya Bay far site water pool have been studied for source deployment: In the center, i.e. equally distant from all four detectors (position A), on one of the sides equally spaced between the centers of two of the detectors (position B), and at the closest point to one of the antineutrino detectors (position C). Given the symmetry of the detector arrangements, positions B' and C' have the same physics capabilities as positions B and C. With a sufficiently strong source or multiple sources one can consider swapping the source between positions B and B' or C and C' respectively to better reduce and understand detector systematics. Fig. A.2 illustrates the locations of these source positions.

A proposed source is ^{144}Ce, with an intensity of 500 kCi (1.85×10^{15} Bq). For a spherical source of that strength the radius will be about 8 cm. This isotope decays into the unstable daughter ^{144}Pr which, in turn, decays into the stable ^{144}Nd with the Q-value of 2.996 MeV. The ^{144}Pr decay produces antineutrinos above the 1.8 MeV threshold for inverse neutron beta decay. The half-life of ^{144}Ce is 285 days and of its daughter ^{144}Pr only 17.3 minutes, so that the latter decay remains in equilibrium at all times. Since $A = 144$ is near the top of the fission yield curve, the isotope ^{144}Ce is contained in considerable quantities of several percent in the fission fragments of spent nuclear fuel. Many PBq of Ce are typically contained in one fuel rod at full burn-up.

In order to shield the γ radiation from the 1% branch to the 1^- excited state at 2.185 MeV in ^{144}Nd, as well as the Bremsstrahlung accompanying the β-decay, the compact source will be surrounded by some 37 cm of shielding; 35 cm of W and an

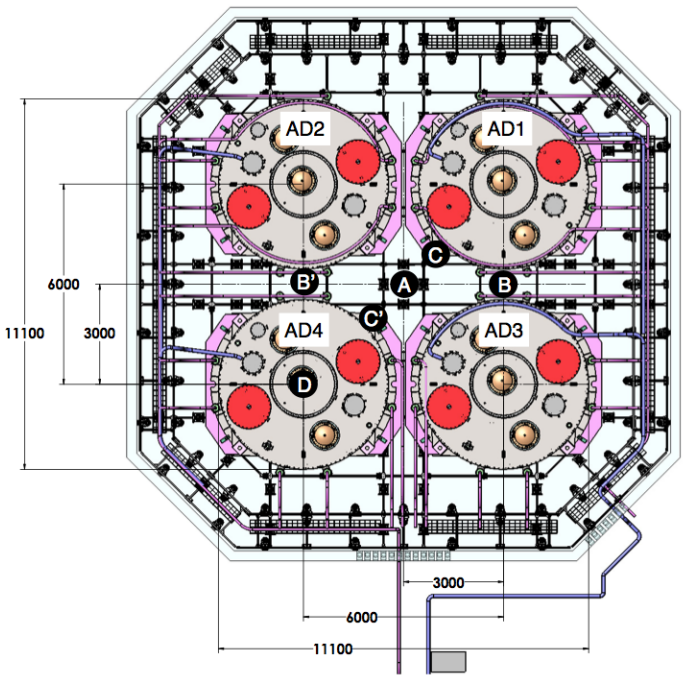

Figure A.2: Top view of the Daya Bay Far Hall with water pool (octagonal frame), four antineutrino detectors (grey cylinders) on their support stands (pink), and water cosmic ray veto photomultipliers and support structure (small black features). *A*, *B*, and *C*, mark possible antineutrino source locations. Positions *B'* and *C'* are symmetric to *B* and *C* and can be used as cross-checks and for systematic studies. Detector dimensions are given in mm. Figures adapted from Ref. [16, 17].

additional 2 cm of Cu. Such a source enclosure would reduce gamma backgrounds by a factor of 2×10^{-10} to $\sim$4 kBq. Neutron backgrounds from such a source would be mitigated through extreme purification and removal of spontaneous fission isotopes from the source material. The source locations proposed here allow the use of additional shielding if necessary.

The physical outer dimensions of the antineutrino detectors and the source geometry define the minimum distance between the source material and the active antineutrino detector region. When the source including its shielding is placed directly in contact with the outer stainless vessel of the antineutrino detectors the minimum distance between the active source material and the active detector region is about $\sim$1.3 m.

Figure A.3 illustrates the oscillation pattern in the Daya Bay Far Hall for $\overline{\nu}_e \rightarrow \nu_s$ oscillation into sterile species for source positions *C* (left) and *B* (right). For the purpose of this illustration we assume a sterile oscillation with Δm^2_{14}= 1 eV^2 and $\sin^2 2\theta_{14}$=0.1. The figure shows the color-coded disappearance probability and the positions of the active regions of the antineutrino detectors. The active regions of

the source and detectors are shown in solid red and grey color respectively, while the physical outer dimensions of the source and detectors are indicated by the dashed lines.

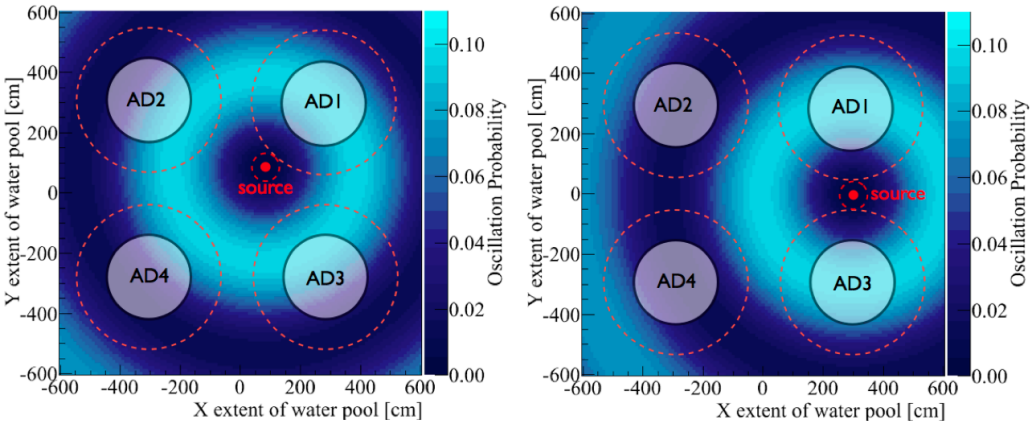

Figure A.3: Illustration of sterile neutrino oscillation in the Daya Bay Far Hall and top view of the geometric arrangement of the antineutrino detectors and the $\overline{\nu}_e$ source. Left: Source at position *C*. Right: Source at position *B*. Figures show an overlay of the positions of the active regions of the antineutrino detectors with the disappearance probability for $\overline{\nu}_e \rightarrow \nu_s$ oscillation with Δm^2_{41}=1 eV^2 and $\sin^2 2\theta_{14}$=0.1 into sterile species. Active regions of the source and detectors are shown in solid red and grey color respectively, while the physical outer dimensions of the source and detectors are indicated by the dashed lines.

Oscillation Signature

In our proposed source experiment a spectrum of $\overline{\nu}_e$ is emitted from an almost point-like source. The antineutrinos travel a range of distances determined by the layout of the detector arrangement and the cylindrical symmetry of the detectors before they interact in the Daya Bay antineutrino detectors. The typical distance traveled from the source to the detector ranges from ~1.5-8 m. The energy spectrum is determined by the ^{144}Ce source. The energy and distance traveled determine the oscillation probability of the $\overline{\nu}_e$ flux. Figure A.4 shows the effect of $\overline{\nu}_e \rightarrow \nu_s$ oscillation as a function of energy and distance from the source and illustrates the fractional oscillation effect normalized to the expected, unoscillated event rate.

To understand the physics potential of the proposed source experiment we have calculated the predicted number of events and the energy spectrum for two source positions, C and B, in the absence of sterile neutrino oscillation and compared to oscillation into sterile species. For all results shown here we assume a mass splitting of Δm_{41}=1 eV^2 and a mixing angle of $\sin^2\theta_{14}$=0.1. We analyze the rate and energy of the detected events as a function of baseline from the source. While the antineutrino

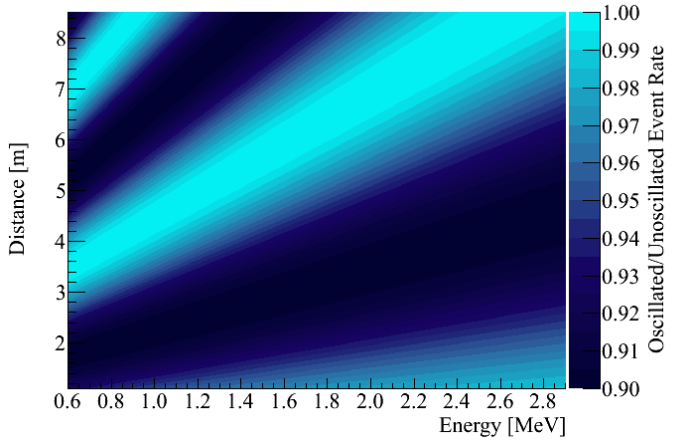

Figure A.4: Example oscillation effect as a function of energy and distance from the $\overline{\nu}_e$ source for $\Delta m_{41} = 1$ eV^2 and $\sin^2\theta_{14}$=0.1.The figure shows the ratio of the oscillated over the unoscillated event rate.

detectors at Daya Bay can in principle make a measurement of θ_{13} without position reconstruction of events, position reconstruction is necessary for a sterile neutrino search. A position resolution of 15 cm is assumed to correlate the reconstructed events with the distance from the $\overline{\nu}_e$ source. With moderate position reconstruction the Daya Bay antineutrino detectors will allow us to determine the integral event rate of all energies observed as a function of baseline and the integral event rate of all baselines as a function of energy. We can then deduce the absolute event rate as a function of energy and baseline.

Figure A.5 shows the energy and position dependence of the event rates in the antineutrino detectors for source positions C and B. The bottom row shows the 2-dimensional distributions of event rate versus energy and distance from source. Top and middle rows are the 1-dimensions projections of expected events versus energy (top) and distance from source (middle) for the case of no oscillation (black histogram), the observed event rate in case of $\overline{\nu}_e \rightarrow \nu_s$ oscillation (red points), and the reactor $\overline{\nu}_e$ background. Left panels correspond to source position C while right panels are for source position B. Source position B provides the highest statistics of events as it utilizes the two-fold symmetry of the detector arrangements. With source position B we essentially have a near and far detector arrangements with two primary baselines and two detectors at each baseline.

Backgrounds

A number of backgrounds will mask the oscillation signal from the proposed source measurement. Correlated and accidental backgrounds to the inverse beta decay signature in the antineutrino detectors are well known to the Daya Bay experiment and

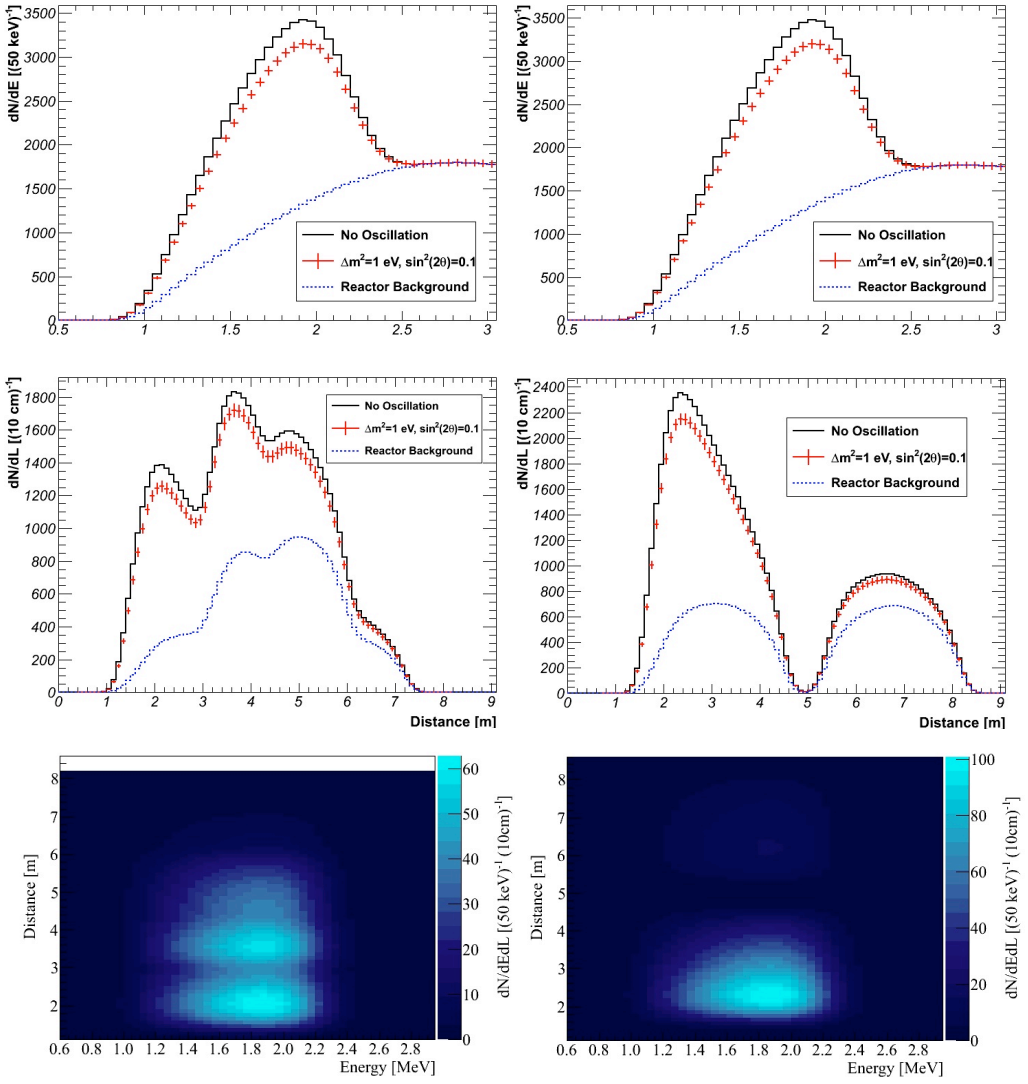

Figure A.5: Energy and position dependence of the event rates in the antineutrino detectors. The bottom row shows the 2-dimensional distributions of event rate versus energy and distance from source. Top and middle rows are the 1-dimensions projections of expected events versus energy (top) and distance from source (middle) for the case of no oscillation (black histogram), the observed event rate in case of $\overline{\nu}_e \rightarrow \nu_s$ oscillation (red points), and the reactor $\overline{\nu}_e$ background (blue dots). Left panels correspond to source position C while right panels are for source position B.

will have been studied in great detail before this source measurement is made. In the context of this proposed sterile neutrino search with a radioactive source we consider only two additional backgrounds: The reactor $\overline{\nu}_e$ background from the Daya Bay reactor complex and source-intrinsic backgrounds.

At distances of about ∼1600-2000 m to the detectors, the Daya Bay and Ling Ao nuclear reactors will be a source of considerable $\overline{\nu}_e$ background. The size of the reactor background will depend on the energy window under consideration. In the energy range of 1 to 2.2 MeV or 1 to 2.5 MeV respectively of the positron energy (plus the annihilation γ), the reactor $\overline{\nu}_e$ background will range from ∼22,000 events per year (1-2.2 MeV) to 32,000 (1-2.5 MeV) while the signal from a 500 kCi ^{144}Ce source will be 31,000 per year for source position A and ∼38,000 and ∼37,000 per year for positions B or C respectively. However, since the shape of the reactor signal will be well measured and monitored by the detectors near the reactors, we need to worry mostly only about the statistical fluctuations of the reactor signal. The contributions of the reactor background to the observed signal is shown in Figure A.5.

Backgrounds from the antineutrino source itself may also become a concern. While direct γ backgrounds can be reduced sufficiently with a W shield around the source, neutrons may become an issue for experiments with sources inside the active detector region. A ^{144}Ce source can be made by reprocessing of spent nuclear fuel. Along with the production of ^{144}Ce, ^{244}Cm is produced in the burnup of nuclear reactor fuel [18, 19]. We estimate that one spent nuclear fuel rod contains approximately 100 g of ^{144}Ce and 5 g of ^{244}Cm. With half lives of 284.91 days (^{144}Ce) and 18.1 years (^{244}Cm) respectively and a spontaneous fission branching fraction of 1.3 $\times 10^{-6}$ the estimated activities in one spent nuclear fuel rod are ∼11 PBq (^{144}Ce) and 21 MBq (^{244}Cm, spontaneous fission only). For a ^{144}Ce source produced from nuclear fuel, reprocessing would need to have a very high efficiency for rejection of ^{244}Cm from ^{144}Ce. Even if reprocessing had 100% efficiency for accepting ^{144}Ce, and only a 10^{-6} probability for introducing ^{244}Cm, there would still be a 21 Bq ^{244}Cm fission rate (for a ^{144}Ce source corresponding to one spent nuclear fuel rod).

Sensitivity

Considering the three source positions A, B and C at Daya Bay we have analyzed the sensitivity of the proposed experimental arrangement to the parameters $\Delta m^2_{\rm new}$ and $\sin^2 2\theta_{\rm new}$. We computed the sensitivity of a source experiment at Daya Bay assuming a 18.5 PBq ^{144}Ce source corresponding to an intensity of 500 kCi. The decrease in the antineutrino source activity over the measurement period of 1 year was estimated to be 66.3% and taken into account. We found the highest sensitivity for source position B due to the event statistics. For source positions A, B, and C the total event rates summed over all detectors are ∼31,000, 38,000, and 37,000 respectively. In comparison, the reactor background is estimated to be between ∼22,000-32,000 events depending on the energy window. See Figure A.5.

The sensitivity was determined using a χ^2 approach. We assume a 1% ^{144}Ce source normalization uncertainty σ_s, a 1% reactor normalization uncertainty σ_r, a 0.5% detector-to-detector relative uncertainty σ_{AD}, and a 2% bin-to-bin uncertainty

σ_b. The statistics corresponds to 1 year of running. The resulting χ^2 is,

$$\chi^2 = \sum_{AD}\sum_{i}\sum_{j}\frac{\left(N_{obs}^{AD,i,j} - N_{exp}^{AD,i,j}\right)^2}{N_{exp}^{AD,i,j}(1+\sigma_b^2 N_{exp}^{AD,i,j})} + \left(\frac{\alpha_s}{\sigma_s}\right)^2 + \left(\frac{\alpha_r}{\sigma_r}\right)^2 + \sum_{AD}\left(\frac{\alpha_{AD}}{\sigma_{AD}}\right)^2. \quad \text{(A.4)}$$

The χ^2 first includes a sum over each antineutrino detector. The indices i and j refer to bins in detected energy and position. $N_{obs}^{AD,i,j}$ is the number of antineutrino events detected in each bin, including possible sterile neutrino oscillation. The expected number of events assuming no oscillation, $N_{exp}^{AD,i,j}$, is the sum of events from the ^{144}Ce source, $S_{exp}^{AD,i,j}$, and the background from reactor antineutrinos, $R_{exp}^{AD,i,j}$,

$$N_{exp}^{AD,i,j} = (1+\alpha_{AD})\left((1+\alpha_s)\,S_{exp}^{AD,i,j} + (1+\alpha_r)\,R_{exp}^{AD,i,j}\right). \quad \text{(A.5)}$$

The expected number of events is allowed to vary within the systematic uncertainties via nuisance parameters; α_{AD} accounts for efficiency variation between antineutrino detectors, while α_s and α_r account for the ^{144}Ce source and reactor normalization uncertainties.

For the Daya Bay detector, we assume detector energy and position resolutions of $9\%/\sqrt{E(MeV)}$ and 15 cm respectively. This is slightly worse than the 7.5% energy resolution reported in [20]. A target proton density of 6.4×10^{28} m^{-3} was estimated for the Gd-loaded scintillator. An antineutrino detector efficiency of 70% was assumed; dominated by the efficiency for delayed neutron capture on Gd to produce a signal above 6 MeV. The results of our sensitivity calculation for source position B are shown in Fig. A.6 which overlays the Daya Bay sensitivity to $\Delta m^2_{\rm new}$ and $\sin^2 2\theta_{\rm new}$ with the Δm^2_{41} vs $\sin^2 2\theta_{14}$ preferred regions of the reactor anomaly and a 3+1 global fit.

The exclusion of the Δm^2_{41} and $\sin^2 2\theta_{14}$ parameter space is based on the dependence of the signal on L/E_ν, where L coverage is approximately 1-8 m, and the E_ν is between 1.8 and 3 MeV. Both variations of the $\overline{\nu}_e$ rate with distance, L, and energy, E_ν, are essential. In fact, by considering the "rate only" analysis (i.e. integrating over energies and distance L) the exclusion region in $\sin^2 2\theta_{14}$ is reduced considerably. The energy and position determination of antineutrino interactions is an important part of the analysis.

The $\overline{\nu}_e$ background from the Daya Bay nuclear power plant is an irreducible background to the source $\overline{\nu}_e$ signal. It would be favorable, of course, to build a source experiment with antineutrino detectors in an underground location far from nuclear reactors; but this may not be feasible. The advantage of the proposed source experiment at Daya Bay is the existence of multiple antineutrino detectors in an underground water pool with the access and infrastructure needed for a source deployment. Our calculations show that in the absence of a reactor $\overline{\nu}_e$ background and with a 500 kCi source we would reach $\sin^2 2\theta_{14} \geq 0.06$ compared with $\sin^2 2\theta_{\rm new} \geq 0.07$ for the case with the reactor background (see Fig. A.6). At half of the source strength the sensitivity in the presence of the $\overline{\nu}_e$ reactor background would decrease from $\sin^2 2\theta_{14} \geq 0.07$ to about $\sin^2 2\theta_{14} \geq 0.08$.

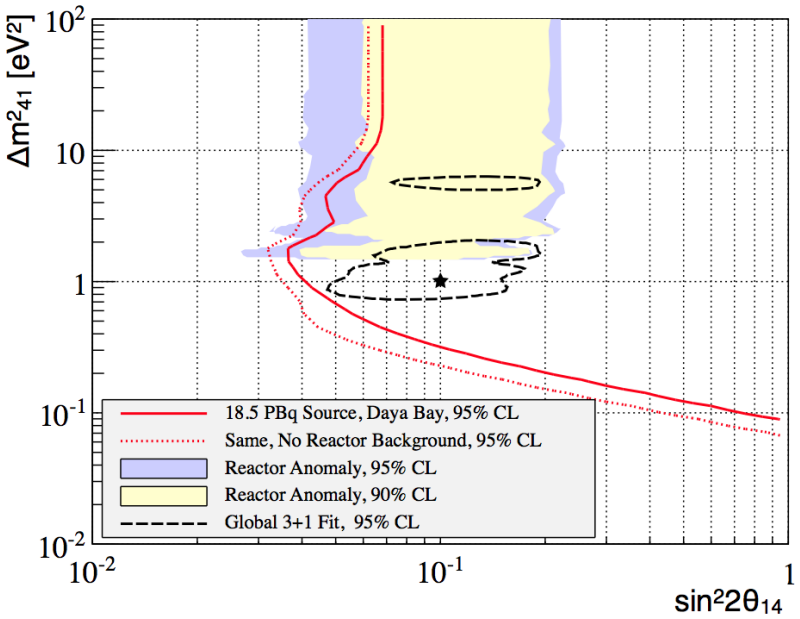

Figure A.6: Sensitivity of a $\overline{\nu}_e$ search at Daya Bay to the oscillation parameters Δm^2_{41} and $\sin^2 2\theta_{14}$ assuming a 500 kCi ^{144}Ce source at position B in the Daya Bay Far Hall. We show the 95% C.L. sensitivity of the Daya Bay source experiment with reactor background (red solid) and without (red dashed), the 90% and 95% C.L. preferred regions of the reactor anomaly (shaded yellow and blue) [3], and the 95% best-fit region from a 3+1 global fit to all neutrino data (dashed black) [2]. The parameter space to the left and above the Daya Bay sensitivity curve will be excluded at 95% C.L. The star indicates the oscillation parameters Δm^2_{41} and $\sin^2 2\theta_{14}$ used in Figures A.4 and A.5 for the study in this paper.

The multiple antineutrino detectors at the Daya Bay Far Hall provide a unique laboratory for the measurement of antineutrinos. Exploiting the symmetric positions of the detectors relative to the ^{144}Ce source will provide further constraints on systematic uncertainties, and placing a source at multiple locations could improve the sensitivity further.

Bibliography

[1] K. Nakamura *et al.* J. Phys. G. **37**, 075021 (2010).

[2] C. Giunti and M. Laveder, arXiv:1109.4033 (2011)

[3] G. Mention *et al.*, Phys. Rev. D **83**, 073006(2011).

[4] Th. Mueller *et al.*, Phys. Rev. C **83**, 054615(2011).

[5] C. Giunti and M. Laveder, Phys. Rev. D **82**, 053005(2010).

[6] H. Kwon *et al.*, Phys. Rev. D **24**, 1097(1981).

[7] Y. Declais *et al.*, Phys. Lett. B **338**, 383(1994).

[8] R. R. G. Marleau *et al.*, A User Guide for DRAGON, Report IGE-236 Rev. 1 (2011).

[9] G. Cao, personal communication.

[10] D. Dwyer *et al.*, arXiv:1109.6036[hep-ex].

[11] M. Cribier *et al.*, arXiv:1107.2335[hep-ex].

[12] V. Egorov *et al.*, *Status of the DANSS Project*, TAUP2011, Munich, Germany, September 2011,
`http://taup2011.mpp.mpg.de/?pg=Agenda&topic=4`

[13] A. Cucoanes *et al.*, *The NUCIFER Experiment*, TAUP2011, Munich, Germany, September 2011,
`http://taup2011.mpp.mpg.de/?pg=Agenda&topic=4`

[14] N. Bowden, *Future Reactor Neutrino Experiments*, Short Baseline Neutrino Workshop (SBNW11), FNAL, USA, May 2011, https://indico.fnal.gov/conferenceDisplay.py?ovw=True&confId=4157

[15] O. Yasuda, arXiv:1107.4766[Hep-ph].

[16] X. Guo *et al.* (Daya Bay Collaboration), arXiv:hep-ex/0701029.

[17] K.M. Heeger *et al.* (Daya Bay Collaboration), *First Data with the Daya Bay Antineutrino Detectors*, TAUP2011, Munich, Germany, September 2011, http://taup2011.mpp.mpg.de/?pg=Agenda&topic=4

[18] M. DeHart and O.W. Hermann, *An Extension of the Validation of SCALE (SAS2H) Isotopic Predictions for PWR Spent Fuel*, ORNL/TM-13317, 1996

[19] Y. Ham *et al.*, *Monte Carlo Characterization of Pressurized Water Reactor Spent Fuel Assembly for the Development of a New Instrument for Pin Diversion Detection*, INMM06, Nashville, TN, USA, July 2006

[20] F.P. An *et al.* (Daya Bay Collaboration), arXiv:1202.6181[ins-det]